Matthias Leuschner

Numerically efficient computational homogenization: Fourier-accelerated nodal solvers and reduced basis model order reduction

1
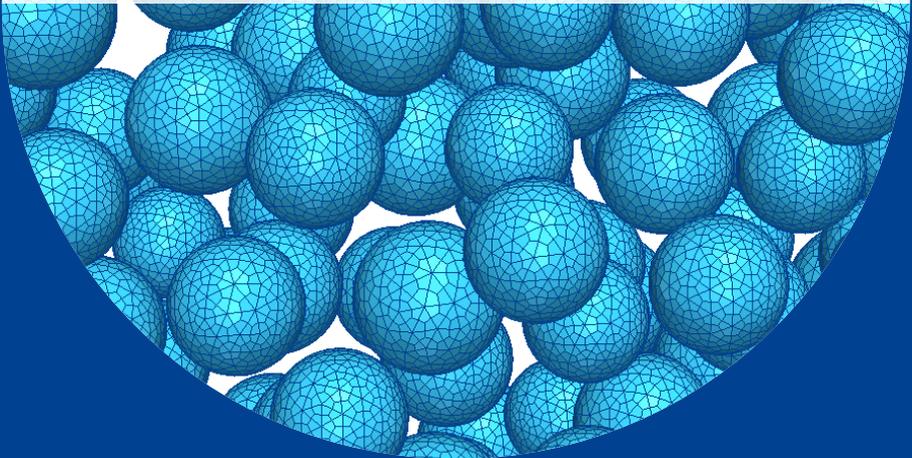
Numerically efficient computational homogenization: Fourier-accelerated nodal solvers and reduced basis model order reduction

Von der Fakultät Bau- und Umweltingenieurwissenschaften
der Universität Stuttgart zur Erlangung der Würde
eines Doktor-Ingenieurs (Dr.-Ing.)
genehmigte Abhandlung

Vorgelegt von

Dipl.-Math. techn. Matthias Leuschner

aus Hoya/Weser

Hauptberichter:	Dr.-Ing. Dipl.-Math. techn. Felix Fritzen
1. Mitberichter:	Prof. Dr.-Ing. Dr. h. c. Wolfgang Ehlers
2. Mitberichter:	Prof. Dr. Bernard Haasdonk
3. Mitberichter:	Prof. Dr.-Ing. Stefanie Reese
4. Mitberichter:	Prof. Dr.-Ing. David Ryckelynck

Tag der mündlichen Prüfung: 21. Juni 2018

Institut für Mechanik (Bauwesen) der Universität Stuttgart
Lehrstuhl für Kontinuumsmechanik, Prof. Dr.-Ing. H. Steeb

2018

Editors:

Prof. Dr.-Ing. Dr. h. c. W. Ehlers
Dr.-Ing. Dipl.-Math. techn. F. Fritzen
Jun.-Prof. Dr.-Ing. M.-A. Keip
Prof. Dr.-Ing. H. Steeb

Acknowledgements

Stuttgart, June 2018   Matthias Leuschner

Moral character is assessed not by what one knows but by what one loves

Augustine of Hippo, Letter 155

Contents

List of Acronyms

CERR	critical energy release rate
CG	conjugate gradients
CuLF	copper lead frame
CZM	cohesive zone model
DCB	double cantilever beam
DFT	discrete Fourier transform
DOF	degrees of freedom
ELS	end loaded split
ENF	end notched flexure
FANS	Fourier-accelerated nodal solvers
FE	finite element
FE^2	FE square
FEM	FE method
FF	full-field
FFT	fast Fourier transform
FP	fixed point
GPU	graphics processing unit
GSM	generalized standard material
HBM	homogenization of bulk materials
HTL	homogenization of thin layers
LEFM	linear elastic fracture mechanics
LKH	linear kinematic hardening
MCE	molding compound epoxy
MGO	modified Green's operator
MMB	mixed mode bending
MMMB	miniature MMB
MOR	model order reduction
NLKH	nonlinear kinematic hardening
NMF	non-negative matrix factorization
NTFA	nonuniform TFA
ODE	ordinary differential equation

PBC	periodic boundary conditions
PDE	partial differential equation
POD	proper orthogonal decomposition
pRBMOR	potential-based reduced basis model order reduction
RB	reduced basis
ROM	reduced order model
RVE	representative volume element
SDCZ	standard dissipative cohesive zone
SiP	system in package
SLI	standard linear interface
SLS	standard linear solid
SPCZ	single potential cohesive zone
SVD	singular value decomposition
TFA	transformation field analysis
TSO	tangent second order
UKBC	uniform kinematic boundary conditions

Zusammenfassung

Natürliche und künstliche Werkstoffe weisen heterogene Mikrostrukturen auf, werden auf einer deutlich gröberen Makroskala im Allgemeinen aber als homogen betrachtet. Für die meisten Ingenieuranwendungen ist das effektive makroskopische Materialverhalten von hauptsächlichem Interesse. Dieses hängt in nichttrivialer Weise von der Morphologie der Mikrostruktur und von den Eigenschaften der Materialbestandteile ab und wird vielfach durch Homogenisierungsmethoden ermittelt. Grenzschichten und -flächen an den Phasengrenzen können die Gesamteigenschaften von Verbundwerkstoffen und anderen Mehrphasenmaterialien wesentlich beeinflussen und müssen gegebenenfalls durch Homogenisierungsmethoden berücksichtigt werden.

Computerbasierte Homogenisierungsverfahren kommen zum Einsatz, wenn (semi-) analytische Ansätze, beispielsweise aufgrund zu komplexer Nichtlinearitäten oder Anisotropien, nicht angewendet werden können oder wenn physikalische Phänomene auf der Mikroskala untersucht werden sollen. Abgesehen von der vielseitig einsetzbaren Finite-Elemente-Methode sind Fourier-basierte Homogenisierungsmethoden, welche auf Pixel- oder Voxeldaten agieren, die am häufigsten eingesetzten Vollfeld-Löser. Der in dieser Arbeit beschriebene FANS-Ansatz („Fourier-accelerated nodal solvers") vereint Aspekte dieser beiden Gruppen von Methoden: es wird eine uniforme Finite-Elemente-Diskretisierung auf einem regulären Gitter verwendet und diskrete periodische Faltungen werden effizient im Fourier-Raum berechnet. Durch eine im Vergleich zu anderen Fourier-basierten Homogenisierungsmethoden geringere Anzahl von Rechenoperationen pro Iteration bei höherem Initialisierungsaufwand eignen sich FANS-Algorithmen insbesondere für Probleme, die viele Iterationen erfordern, beispielsweise aufgrund stark unterschiedlicher Konstitutiveigenschaften der einzelnen Bestandteile von Mehrphasenmaterialien. Das FANS-Schema wurde als einfacher Fixpunkt-Algorithmus und als CG-Verfahren mit Vorkonditionierung umgesetzt. Numerische Beispiele werden sowohl für Wärmeleitungsprobleme als auch für lineare und nichtlineare mechanische Homogenisierungsprobleme vorgestellt. Hierbei liegt das Augenmerk hauptsächlich auf Konvergenzstudien und auf möglichen diskretisierungsbedingten Artefakten, die ein bekanntes Problem im Bereich der Fourier-basierten Homogenisierung darstellen. Dank der Verwendung von Finite-Elemente-Ansätzen mit vollem Gaußschem Quadraturschema sind FANS-Lösungen glatt und weisen keine störenden Artefakte auf.

Hohe numerische Kosten und/oder hoher Speicherbedarf beschränken die Tauglichkeit von Vollfeld-Lösern für Anwendungen, bei denen Homogenisierungsroutinen sehr oft ausgeführt werden müssen, wie beispielsweise für Mehrskalensimulationen oder inverse Parameteridentifikation. Dies motiviert die Nutzung von Modellreduktionsverfahren, deren Ziel die Reduktion der algorithmischen Komplexität und des Speicherbedarfs bei nur geringen Einbußen hinsichtlich der Genauigkeit ist. Es wird eine weiterentwickelte Version der pRBMOR-Methode („potential-based reduced basis model order reduction")

für dissipative Verbundwerkstoffe mit dissipativen Grenzflächen an den Phasengrenzen vorgestellt. Reduzierte Basen für alle Felder innerer Zustandsvariablen, wie beispielsweise plastischer Dehnungen, sind integrale Bestandteile des pRBMOR-Konzepts. Für Mikrostrukturen mit singulären Flächen kommt eine zusätzliche reduzierte Basis für das Feld des Verschiebungssprungs zum Tragen. Die Koeffizienten zu den einzelnen Basisfunktionen entsprechen globalen Zustandsvariablen der homogenisierten Konstitutivmodelle. Sie werden durch ein Variationsprinzip ermittelt, für das vorausgesetzt wird, dass die zugrunde liegenden Materialmodelle ratenabhängige generalisierte Standardmaterialien sind, die durch ein Potential der freien Energie und durch ein Dissipationspotential bestimmt werden. Zusätzlich muss das Konstitutivverhalten möglicher Grenzflächen in entsprechender Weise durch Potentiale definiert sein. Neben dem mit periodischen Randbedingungen umgesetzten Standardfall der Homogenisierung von Volumenmaterialien wird die pRBMOR-Technik auch zur Homogenisierung dünner Schichten erweitert, die aus der makroskopischen Perspektive als idealisierte Grenzflächen betrachtet werden. Dabei werden kombinierte uniform-periodische Randbedingungen eingesetzt, um fehlender Skalenseparierbarkeit senkrecht zur Schicht Rechnung zu tragen.

Für drei elastische Mikrostrukturen mit reibungsfreiem Kontakt an den Phasengrenzen wird pRBMOR mit Kernel-Interpolation verglichen. Hier lassen sich mit dem pRBMOR-Ansatz bessere Approximationen für Validierungslastfälle erzielen. In einem weiteren Beispiel wird ein unidirektionales faserverstärktes Kompositmaterial mit viskoelastischen Grenzflächen und einer Matrix aus Epoxidharz untersucht. Das Matrixmaterial wird durch ein viskoplastisches Perzyna-Modell mit sättigender isotroper Verfestigung sowie linearer und nichtlinearer kinematischer Verfestigung beschrieben. Die Modellparameter wurden anhand experimenteller Daten von zyklischen Zugversuchen aus der Literatur festgelegt. Durch systematische Trainings- und Validierungsprozeduren wird der prädiktive Charakter des reduzierten Modells hinsichtlich Veränderungen der Lastrichtungen, der Dehnraten und konstitutiver Eigenschaften untersucht. In einem dritten Beispiel wird die pRBMOR-Technik eingesetzt, um die homogenisierten Grenzflächeneigenschaften einer dünnen partikelverstärkten Klebeschicht zu berechnen.

In einem Kapitel zur Kohäsivzonenmodellierung werden phänomenologische Grenzflächenmodelle behandelt. Es wird ein allgemeiner Überblick zur genannten Thematik mit besonderer Berücksichtigung von Anisotropien vermittelt und ein Grenzflächenschädigungsmodell vorgestellt, das den Kriterien eines generalisierten Standardmaterials genügt. Mit diesem Modell wurden Finite-Elemente-Simulationen eines Versuchs zur Ermittlung anisotroper Grenzflächeneigenschaften durchgeführt, die einen direkten Vergleich mit experimentellen Daten ermöglichen.

Summary

Natural and artificial materials exhibit heterogeneities at the microscopic scale but are generally considered to be homogeneous at a much coarser macroscale. The effective macroscopic material behavior is of principal interest in most engineering applications. It depends on the microstructural morphology and on the local behavior of the material constituents in a nontrivial way and is commonly determined by homogenization methods. Interphases and imperfect interfaces at phase boundaries can significantly affect the overall constitutive response of some composite materials or other multiphase materials and must be taken into account by appropriate homogenization schemes.

Computational homogenization methods are used when (semi-) analytical approaches are unsuitable, e.g., due to overly complex nonlinearities or anisotropies, or in order to gain insight into physical phenomena at the microscale. Aside from the versatile finite element method, Fourier-based homogenization schemes operating on pixel/voxel data are the most frequently used full-field solvers. Fourier-accelerated nodal solvers (FANS) are presented which combine aspects of both concepts: a finite element discretization on a regular grid is assumed, and discrete periodic convolutions with a fundamental solution are efficiently computed in Fourier space. With a higher initialization effort but less numerical operations per iteration compared to other Fourier-based homogenization methods, FANS are advantageous with regard to numerical cost especially for homogenization problems that require many iterations, e.g., because of strongly different constitutive properties in the individual constituents of a multiphase material. The FANS scheme has been implemented as a simple fixed-point algorithm and as a preconditioned conjugate gradient method. Numerical examples are given for thermal as well as for linear and nonlinear mechanical problems. The focus is put on convergence studies and on possible discretization-induced artifacts, which are a much-noticed issue of Fourier-based homogenization. Thanks to the use of finite element discretizations with full Gaussian integration, FANS solutions are smooth and exhibit no spurious artifacts.

High numerical cost and/or memory demand restrict the suitability of full-field solvers for applications that require numerous executions of a homogenization routine, such as concurrent two-scale simulations or inverse parameter identification procedures. This is the motivation for the development of model order reduction techniques, which aim at reduced computational complexity and reduced memory requirement while retaining reasonable levels of accuracy. An advanced version of the potential-based reduced basis model order reduction (pRBMOR) method for dissipative composite materials with dissipative imperfect interfaces at the phase boundaries is presented. Reduced bases for all fields of internal state variables, such as the plastic strain, are an essential part of the pRBMOR concept. An additional reduced basis for the displacement jump field is used for microstructures with imperfect interfaces. The reduced basis coefficients correspond to global state variables of the homogenized constitutive models.

They are determined by means of an incremental variational principle, which requires that the underlying material models are rate-dependent generalized standard materials specified by a free Helmholtz energy density and a (dual) dissipation potential and that the interface models are formulated in a similar potential-based manner. Beyond the standard case of homogenization of bulk materials, which is implemented with periodic boundary conditions, the pRBMOR technique is extended towards homogenization of heterogeneous thin layers that can be considered as imperfect interfaces from the macroscopic perspective. Hybrid uniform-periodic boundary conditions are utilized in order to take into account missing separation of length scales in the out-of-plane direction.

A comparison of pRBMOR with interpolation based in Gaussian kernels is presented for three microstructures with linear elastic constituents and unilateral contact without friction at the phase boundaries. It is found that the pRBMOR approach can provide more accurate predictions for validation load cases than the kernel method. In another example, a unidirectional fiber-reinforced composite with viscoelastic interfaces and an epoxy resin matrix is considered. A Perzyna-type viscoplastic standard material with saturating isotropic hardening as well as linear and nonlinear kinematic hardening is used to model the matrix material. The model parameters were calibrated with experimental data from the literature which have been obtained in cyclic tensile tests. Systematic training–validation procedures are conducted in order to assess the predictive capabilities of the reduced order model concerning variations of load directions, load rates, and constitutive properties. In a third numerical example, pRBMOR is used to determine the homogenized traction–separation behavior of a thin layer of an epoxy-based adhesive reinforced with glass powder.

Phenomenological traction–separation laws for imperfect interfaces are addressed in a separate Chapter on cohesive zone modeling. A general overview on the topic is given with special consideration of the mixed-mode behavior of anisotropic interfaces, and a damage model which is potential-based in the sense of generalized standard materials is presented. The damage model is incorporated in finite element simulations of mixed mode bending tests in order to assess its capability to replicate experimental findings.

Chapter 1:
Introduction and overview

With ongoing progress of computer engineering, numerical methods have gained increasing importance in the field of engineering mechanics and are now omnipresent in scientific as well as in industrial applications. In the industrial environment, computer-aided engineering (CAE) is widely utilized for the purpose of virtual prototyping, which can completely or partially replace physical prototypes in order to save costs. Among the most important simulation techniques grouped under the label CAE is the finite element analysis (FEA). FEA is mostly associated with simulations of the deformations of solid structures, although the *finite element method* (FEM) is a versatile numerical technique which is also applicable to boundary value problems arising in various other contexts.

Besides universal governing equations and problem-specific boundary conditions, FEM simulations require constitutive models that describe the properties of particular materials. The choice of suitable material models generally depends on several aspects and can require a substantial amount of expert knowledge, especially when nonlinear mechanical properties of materials must be considered. In the simplest case, the mechanical behavior of a material can be described by a phenomenological model whose parameters are identifiable from experimental data. However, this approach may be unfeasible either because experimental data are unavailable or available only at high expense, or because a model that captures all relevant phenomena is not at hand. Both problems emerge frequently in practice, e.g., when developing new materials.

Composite materials are artificial materials consisting of two or more distinct phases and are designed for various engineering applications such as microelectronics, lightweight construction, or adhesive bonding. Heterogeneous at the material length scale, composite materials are often considered homogeneous at the much coarser scale of structural parts or adhesive layers made thereof. Typically, the homogenized constitutive behavior, also referred to as effective or overall response, is of principal interest. It depends on the properties of the individual phases and on the morphology at the fine scale (i.e., on the microstructure) in a nontrivial manner and is determined by so-called homogenization methods. With proposals ranging from simple analytic estimates to involved computational schemes, homogenization was and still is a broad topic of research. Roughly speaking, it can be stated that the computational effort grows as the problem complexity, e.g., in terms of nonlinearities or anisotropy, increases. A more detailed introduction to homogenization and associated fundamental equations are given in Chapter 5.

Apart from solely predicting the effective response of composite materials, many computational homogenization schemes are useful to analyze physical phenomena at the small scale. Also, their applicability is not restricted to composite materials

but extends to other heterogeneous natural or engineered materials such as biological tissue or polycrystalline metals. Consequently, computational homogenization plays a central role in the field of mechanics of materials. The most considered full-field approaches are FEM-based and Fourier-based solution schemes. By the use of *fast Fourier transform* (FFT) algorithms, Fourier-based homogenization can achieve good numerical efficiency for heterogeneous materials represented by pixel or voxel images. The Fourier-accelerated nodal solvers (FANS) presented in Chapter 6 combine ideas of FFT-based homogenization with uniform FEM discretizations in order to obtain reliable, artifact-free simulation results at the small scale with good numerical efficiency. FANS are first discussed for the technically simpler case of steady-state heat conduction and are thereafter extended to mechanical applications. Numerical examples are given for linear elastic and plastic composite materials as well as for thermal problems, including a comparison with other Fourier-based homogenization methods and with a closed-form solution.

Even for comparatively efficient full-field homogenization methods, the associated numerical effort can be tremendous. Concurrent multiscale simulations and parametric studies, which require numerous executions of a homogenization procedure, can therefore become unfeasible with full-field approaches. In such situations, reduced order homogenization schemes are adequate. Considering small approximation errors to be acceptable, reduced order modeling generally aims at distinct reductions of computational cost and/or memory demand. In order to achieve this objective in the *online phase*, a *reduced order model* (ROM) is usually trained in a preceding *offline phase*. The sometimes high cost associated with the offline phase pays off when many repetitions of the online procedure are demanded. An important class of ROMs are *reduced basis* (RB) methods, which operate according to the following principle: in the offline phase, training data are generated using full-field simulations, whose results are understood as high fidelity solutions. Subsequently, a low-dimensional reduced basis is identified which spans a subspace of the high fidelity solution space and can reproduce the training data with minor approximation errors. The online procedure operates with the reduced basis and is assumed to provide good predictions for scenarios different from but similar to the ones covered by the training data. Good numerical efficiency is expected since the low dimension of the reduced basis corresponds to a low number of degrees of freedom (DOF).

The main part of this thesis is Chapter 7, which presents the potential-based reduced basis model order reduction (pRBMOR) technique for nonlinear homogenization problems descending from the nonuniform transformation field analysis (NTFA) proposed by Michel et al. [2000], Michel & Suquet [2003, 2004]. Two causes of nonlinearities are considered: physically nonlinear behavior of the material (e.g., due to viscoplasticity), and imperfect interfaces in the microstructure, corresponding to surfaces where the displacement field is discontinuous. By considering imperfect interfaces, mechanical effects at phase boundaries are taken into account, which can massively affect the overall response of composite materials. pRBMOR is presented for homogenization of bulk materials (HBM), which corresponds to the "standard" case, as well as for homogenization of thin layers (HTL) that can be idealized as imperfect interfaces from

the perspective of scales much coarser than the layer thickness. Numerical examples are presented for both types of homogenization and include particle- and fiber-reinforced composites.

As reflected in its name, the pRBMOR technique rests upon potential-based descriptions of the constitutive behavior of materials and of imperfect interfaces. More precisely, constitutive models defined by a free energy potential and by a dissipation potential are assumed. The approach is known under the name *generalized standard materials* (GSMs) for bulk materials. Chapter 3 presents the GSM framework with examples of different types of material models and with information concerning algorithmic implementation. Also, two specific GSMs calibrated for the description of different epoxy resins are given, which have been employed within present or past applications of the pRBMOR scheme.

The GSM concept can be straightforwardly transferred to the constitutive modeling of imperfect interfaces. The class of such potential-based interface models is referred to as *standard dissipative cohesive zones* (SDCZs) throughout this work. *Cohesive zone models* (CZMs) have been originally introduced for the description of fracture process zones but can be understood as constitutive models for cohesive interfaces in a more general sense. Chapter 4 gives an introduction to the modeling of cohesive interfaces, elucidates some important aspects to be considered at that, and introduces several approaches from the literature. Further, the SDCZ framework and an SDCZ damage model are presented. Different numerical examples are included where the damage model is compared to experimental results and to another interface model.

To get started, Chapter 2 introduces basic equations of continuum mechanics for solids with imperfect interfaces, which provide the theoretical foundation for the following Chapters. Here, the balance equations for points in the bulk material and for points on the imperfect interface deserve special mention. A rather unusual formulation is decided on, where bulk and interface balance equations are written analogously to a large extend. More familiar standard formulations are obtained as special or limit cases.

Chapter 2:
Basic equations of continuum mechanics

2.1 Reference configuration of a solid with interfaces

A solid body is considered within the time interval $\mathbb{T} = [t_0, T]$. At the initial time t_0, the body is assumed to be in a relaxed (i.e., stress-free) and void-free reference configuration where it is described by the totally bounded, simply connected subdomain $\mathscr{B}_0$ of the three-dimensional Euclidean space $\mathbb{E}^3$. Any material point of the body is characterized by its position $\boldsymbol{X} \in \mathscr{B}_0$ in the reference configuration. An interface $\mathscr{I}_0 \subset \mathscr{B}_0$ is introduced which does not move independently of the surrounding bulk material and is therefore called a *material interface* [cf. Javili et al., 2013]. Mathematically speaking, $\mathscr{I}_0$ is characterized as the closure (within $\mathscr{B}_0$) of the union of a finite number of topological surfaces, which is not required to be connected. The bulk material is then described by an open set $\Omega_0 = \mathscr{B}_0 \setminus \mathscr{I}_0$. A positive and a negative side are assigned to the interface $\mathscr{I}_0$, and the unit normal vector $\boldsymbol{N}$ heading to the positive side is introduced on $\mathscr{I}_0$ (cf. Figure 2.1).

The tensor notation used in this work is specified in Appendix A.1, and the set of tensors of order n is denoted $\mathscr{L}^n$. Let

$$\begin{aligned} \boldsymbol{f} : \Omega_0 \times \mathbb{T} &\rightarrow \mathscr{L}^n \\ (\boldsymbol{X}, t) &\mapsto \boldsymbol{f}(\boldsymbol{X}, t) \end{aligned} \tag{2.1}$$

be a time-dependent tensor field of order $n \geq 0$ defined in the bulk that is uniformly continuous with respect to the spatial argument. The notation $\boldsymbol{f}^{\pm}$ is introduced for the limits at both sides of the interface

$$\begin{aligned} \boldsymbol{f}^{\pm} : \mathscr{I}_0 \times \mathbb{T} &\rightarrow \mathscr{L}^n \\ (\boldsymbol{X}, t) &\mapsto \lim_{\mu \searrow 0} \boldsymbol{f}\left(\boldsymbol{X} \pm \mu \boldsymbol{N}(\boldsymbol{X}), t\right). \end{aligned} \tag{2.2}$$

The jump discontinuity $[\![\boldsymbol{f}]\!]$ of the field $\boldsymbol{f}$ at the interface is then defined by

$$\begin{aligned} [\![\boldsymbol{f}]\!] : \mathscr{I}_0 \times \mathbb{T} &\rightarrow \mathscr{L}^n \\ (\boldsymbol{X}, t) &\mapsto \boldsymbol{f}^+(\boldsymbol{X}, t) - \boldsymbol{f}^-(\boldsymbol{X}, t). \end{aligned} \tag{2.3}$$
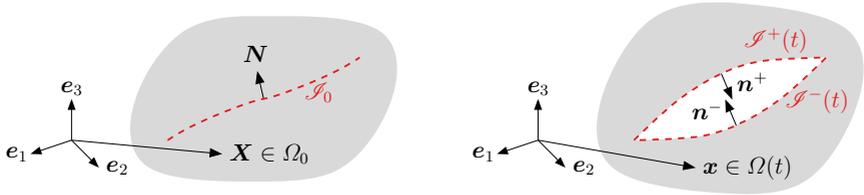
Figure 2.1: Reference configuration *(left)* and current configuration *(right)* of a solid body with a material interface.

In a similar fashion, the mean value $\langle\!\langle \boldsymbol{f} \rangle\!\rangle$ across the interface is introduced according to

$$\langle\!\langle \boldsymbol{f} \rangle\!\rangle : \mathscr{I}_0 \times \mathbb{T} \to \mathscr{L}^n$$
$$(\boldsymbol{X}, t) \mapsto \frac{1}{2} \left(\boldsymbol{f}^+(\boldsymbol{X}, t) + \boldsymbol{f}^-(\boldsymbol{X}, t) \right). \tag{2.4}$$

All considered fields are assumed to be smooth (at least uniformly continuous) in the bulk, i.e., at all points of the body except for the interface, which is therefore called a *singular surface*. E.g., the temperature in the bulk is given as a uniformly continuous scalar field

$$\theta : \Omega_0 \times \mathbb{T} \to \mathbb{R}_{>0}, \tag{2.5}$$

and in the notation introduced above, $[\![\theta]\!]$ describes the discontinuity of the temperature at the interface.

2.2 Kinematics

The motion of the bulk is expressed by the function

$$\boldsymbol{\chi} : \ \Omega_0 \times \mathbb{T} \to \mathbb{E}^3$$
$$(\boldsymbol{X}, t) \mapsto \boldsymbol{x}, \tag{2.6}$$

which maps any material point identified by its initial position $\boldsymbol{X} \in \Omega_0$ to its current position $\boldsymbol{x}$ at time $t \in \mathbb{T}$. The bulk of the body at time $t \in \mathbb{T}$ is expressed by the image of Ω_0 under the motion $\boldsymbol{\chi}$

$$\Omega(t) = \boldsymbol{\chi}(\Omega_0, t). \tag{2.7}$$

The motion function $\boldsymbol{\chi}$ is assumed to be injective with respect to $\boldsymbol{X}$, uniformly continuous with respect to $\boldsymbol{X}$, twice continuously differentiable with respect to $\boldsymbol{X}$ almost everywhere, and twice continuously differentiable with respect to t at almost every time. Here, the terms *almost everywhere* and *at almost every time* refer to the Lebesgue measures on $\mathbb{E}^3$ and on $\mathbb{T}$, respectively. The injectivity requirement is equivalent to

preclusion of material interpenetration[1]. The displacement field in the bulk of the body is introduced according to

$$\boldsymbol{u} \colon \Omega_0 \times \mathbb{T} \to \mathbb{E}^3$$
$$(\boldsymbol{X}, t) \mapsto \boldsymbol{\chi}(\boldsymbol{X}, t) - \boldsymbol{X}. \tag{2.8}$$

On the interface, the displacement jump is defined as the vector field

$$\boldsymbol{\delta} \colon \mathscr{I}_0 \times \mathbb{T} \to \mathbb{E}^3$$
$$(\boldsymbol{X}, t) \mapsto \boldsymbol{u}^+(\boldsymbol{X}, t) - \boldsymbol{u}^-(\boldsymbol{X}, t) = [\![\boldsymbol{u}(\boldsymbol{X}, t)]\!] \tag{2.9}$$

using the notation from (2.2) and (2.3). In the current state at time $t \in \mathbb{T}$, the interface has two surfaces which are specified as the images of $\mathscr{I}_0$ under $\boldsymbol{\chi}^\pm$

$$\mathscr{I}^+(t) = \boldsymbol{\chi}^+(\mathscr{I}_0, t), \qquad\qquad \mathscr{I}^-(t) = \boldsymbol{\chi}^-(\mathscr{I}_0, t). \tag{2.10}$$

For any $(\boldsymbol{X}, t) \in \mathscr{I}_0 \times \mathbb{T}$, the outer unit normal vectors on the surfaces $\mathscr{I}^+$ and $\mathscr{I}^-$ are denoted by $\boldsymbol{n}^+(\boldsymbol{X}, t)$ and by $\boldsymbol{n}^-(\boldsymbol{X}, t)$, respectively, as shown on the right-hand side of Figure 2.1. Here, the notion *outer* refers to the case where the interface is opened and forms a void, which can be characterized by

$$\boldsymbol{n}^+(\boldsymbol{X}, t) \cdot \boldsymbol{\delta}(\boldsymbol{X}, t) < 0, \qquad\qquad \boldsymbol{n}^-(\boldsymbol{X}, t) \cdot \boldsymbol{\delta}(\boldsymbol{X}, t) > 0. \tag{2.11}$$

Clearly, $\boldsymbol{n}^\pm$ are related to the normal $\boldsymbol{N}$ in the reference configuration (cf. Section 2.1) via

$$\boldsymbol{N}(\boldsymbol{X}) = \boldsymbol{n}^-(\boldsymbol{X}, t_0) = -\boldsymbol{n}^+(\boldsymbol{X}, t_0) \qquad (\boldsymbol{X} \in \mathscr{I}_0). \tag{2.12}$$

The fact that $\boldsymbol{N}$ coincides with the outer unit normal vector on the negative side of the interface in the undeformed state can be interpreted as considering the negative side as the master surface and the positive side as the corresponding slave surface.

2.3   Basic interface modeling

Interfaces where displacement discontinuities may occur are also called *imperfect interfaces* in the following[2]. With regard to the modeling of the considered body, one might wish to suppose that only a part of the interface $\mathscr{I}_0$ is imperfect in that sense. This can be easily attained by an additional kinematic constraint on the motion $\boldsymbol{\chi}$. However, this case is not treated explicitly hereafter, i.e., the entire interface $\mathscr{I}_0$ is assumed to be imperfect. Imperfect interfaces differ from other types of interfaces by the fact that they have two sides which generally do not coincide in the deformed state. Hence, a deformed

---

[1]The requirement of the motion being injective with respect to $\boldsymbol{X}$ is slightly relaxed later on. Instead of this kinematic condition, the interface is equipped with constitutive relations that penalize material interpenetration (cf. Section 4.1).

[2]This terminology should not be confused with the one used by Needleman [1990a,b], who refers to non-bonded areas of an otherwise bonded interface as imperfections.

imperfect interface is actually no longer a singular surface, and a proper concept is necessary in order to treat it like one nonetheless. The deformed interface at time $t \in \mathbb{T}$ is represented by an imaginary surface defined as the image $\mathscr{I}(t) = \breve{\boldsymbol{\chi}}_\vartheta(\mathscr{I}_0, t)$ of $\mathscr{I}_0$ under the parameterized function

$$\begin{aligned} \breve{\boldsymbol{\chi}}_\vartheta \colon \mathscr{I}_0 \times \mathbb{T} &\to \mathbb{E}^3 \\ (\boldsymbol{X}, t) &\mapsto (1 - \vartheta)\boldsymbol{\chi}^-(\boldsymbol{X}, t) + \vartheta \boldsymbol{\chi}^+(\boldsymbol{X}, t). \end{aligned} \tag{2.13}$$

The parameter $\vartheta \in [0, 1]$ specifies the so-called *intermediate configuration* which is controversially discussed in the literature [cf. Mosler & Scheider, 2011, for instance]. It will be set to $\vartheta = \frac{1}{2}$ in Section 2.7.4, corresponding to a centered interface position, but remains unspecified for now. The mapping $\breve{\boldsymbol{\chi}}_\vartheta$ also provides an implicit link of a point on the imaginary surface $\breve{\boldsymbol{x}} \in \mathscr{I}(t)$ to its counterparts $\boldsymbol{x}^\pm \in \mathscr{I}^\pm(t)$ on both sides of the interface via their common position in the reference configuration $\boldsymbol{X} \in \mathscr{I}_0$. Quantities defined on the interface are denoted with a breve according to $\breve{\bullet}$. The unit normal vector on the imaginary surface heading towards the positive side of the interface is denoted $\breve{\boldsymbol{n}}$. An important assumption made throughout this work is that the normal vectors $\boldsymbol{n}^\pm$ on both sides of the imperfect interface are collinear, which is expressed by

$$\breve{\boldsymbol{n}}(\boldsymbol{X}, t) = \boldsymbol{n}^-(\boldsymbol{X}, t) = -\boldsymbol{n}^+(\boldsymbol{X}, t) \qquad \text{for all } (\boldsymbol{X}, t) \in \mathscr{I}_0 \times \mathbb{T}. \tag{2.14}$$

These equalities are satisfied approximately under the assumption of small deformations made in Section 2.5. Hence, no further kinematic constraint is imposed on the motion $\boldsymbol{\chi}$ to prevent relative rotations[3] of both sides of the interface. The interface normal $\breve{\boldsymbol{n}}$ is used to define the projectors onto the interface normal and onto the tangential plane

$$\breve{\boldsymbol{P}}_\perp = \breve{\boldsymbol{n}} \otimes \breve{\boldsymbol{n}}, \qquad\qquad \breve{\boldsymbol{P}}_\parallel = \boldsymbol{I} - \breve{\boldsymbol{n}} \otimes \breve{\boldsymbol{n}}. \tag{2.15}$$

Any vector field $\breve{\boldsymbol{f}}$ defined at the interface can be decomposed into the tangential component and the normal out-of-plane component according to

$$\breve{\boldsymbol{f}} = \breve{\boldsymbol{f}}_\perp + \breve{\boldsymbol{f}}_\parallel \qquad \text{with} \quad \breve{\boldsymbol{f}}_\perp = \breve{\boldsymbol{P}}_\perp \cdot \breve{\boldsymbol{f}} \quad \text{and} \quad \breve{\boldsymbol{f}}_\parallel = \breve{\boldsymbol{P}}_\parallel \cdot \breve{\boldsymbol{f}}. \tag{2.16}$$

At times it is convenient to make use of the abbreviations

$$\breve{f}_\perp = \breve{\boldsymbol{n}} \cdot \breve{\boldsymbol{f}}, \qquad\qquad \breve{f}_\parallel = \left\| \breve{\boldsymbol{f}}_\parallel \right\|_2. \tag{2.17}$$

The general modeling of interfaces in this work combines ideas of Moeckel [1975] with classical assumptions for cohesive zones, following the seminal works of Barenblatt [1959, 1962] and Dugdale [1960]. Interfaces are assigned their own distinct quantities and behaviors, thus, in the terminology of Marsden & Hughes [1994], they are no simple discontinuity surfaces, but exhibit additional properties similar to shells. The aim is to present a thermodynamically consistent framework for the constitutive modeling of interfaces involving surface energies [cf. the review by Javili et al., 2013]. Following Moeckel [1975], the interface is equipped with a mass per unit area density $\breve{\varrho}$. This is

---

[3]It is worth noting that the limitation of rotations both in the bulk and at the interface is the main reason for the assumption of small deformations.

unusual for cohesive zones but allows to derive equilibrium conditions for interfaces in a similar way as for the bulk. Thus, equilibrium conditions at interfaces will be understood as additional balance equations rather than as jump conditions (see Section 2.7). Generally, such balance equations for interfaces involve intrinsic interface fluxes, such as surface/membrane stresses or in-plane interfacial heat fluxes. However, surface/membrane stresses are neglected in the following, which complies with "an implicit assumption in the classical theory [of cohesive zones] that is seldom explicitly stated" [quote from Ottosen et al., 2015, p. 71].

2.4 Lagrangian and Eulerian representation

So far, all quantities defined on the body or on subdomains thereof have been expressed with a material point's initial position $\boldsymbol{X}$ as the spatial argument. This representation, referred to as Lagrangian or material description, is commonly used for mechanical problems. In contrast, a quantity defined with the current position $\boldsymbol{x}$ as the spatial argument is said to be denoted in its Eulerian or spatial representation. Often, the notation of both representations of one quantity is only distinguished by the spatial argument itself.

2.4.1 Derivatives for bulk quantities

Let $\boldsymbol{f}$ be a sufficiently smooth tensor field of arbitrary order defined in the bulk. Its right gradient is defined as the Fréchet derivative with respect to the spatial argument, and it is denoted

$$\text{Grad}\,(\boldsymbol{f}(\boldsymbol{X},t)) = \frac{\partial \boldsymbol{f}(\boldsymbol{X},t)}{\partial \boldsymbol{X}}, \qquad\qquad \text{grad}\,(\boldsymbol{f}(\boldsymbol{x},t)) = \frac{\partial \boldsymbol{f}(\boldsymbol{x},t)}{\partial \boldsymbol{x}} \qquad (2.18)$$

for the Lagrangian and for the Eulerian representation, respectively. If the tensor order is at least one, the divergence of $\boldsymbol{f}$ is defined for either representation according to

$$\text{Div}\,(\boldsymbol{f}(\boldsymbol{X},t)) = \text{Grad}\,(\boldsymbol{f}(\boldsymbol{X},t)) : \boldsymbol{I}, \quad \text{div}(\boldsymbol{f}(\boldsymbol{x},t)) = \text{grad}\,(\boldsymbol{f}(\boldsymbol{x},t)) : \boldsymbol{I}, \quad (2.19)$$

respectively. If $\boldsymbol{f}$ is smooth with respect to the temporal argument, the material time derivative is introduced as the partial derivative with respect to time in the Lagrangian description

$$\dot{\boldsymbol{f}}(\boldsymbol{X},t) = \frac{\partial \boldsymbol{f}(\boldsymbol{X},t)}{\partial t}. \qquad (2.20)$$

For example, the velocity field is defined as the material time derivative of the displacement

$$\boldsymbol{v}(\boldsymbol{X},t) = \dot{\boldsymbol{u}}(\boldsymbol{X},t) = \dot{\boldsymbol{\chi}}(\boldsymbol{X},t) = \frac{\partial \boldsymbol{u}(\boldsymbol{X},t)}{\partial t} = \frac{\partial \boldsymbol{\chi}(\boldsymbol{X},t)}{\partial t}. \qquad (2.21)$$

In the Eulerian representation, the material time derivative of the field $\boldsymbol{f}$ is obtained as the sum of a local and a convective term according to

$$\dot{\boldsymbol{f}}(\boldsymbol{x}, t) = \frac{\partial \boldsymbol{f}(\boldsymbol{x}, t)}{\partial t} + \mathrm{grad}\,(\boldsymbol{f}(\boldsymbol{x}, t)) \cdot \boldsymbol{v}(\boldsymbol{x}, t). \tag{2.22}$$

2.4.2 Derivatives for interface quantities

By means of Riemannian geometry, derivatives of a sufficiently smooth quantity $\breve{\boldsymbol{f}}$ given at the interface are defined in a similar way as for the bulk. For any point of the interface, let $\left\{\boldsymbol{e}_1^{\mathrm{t}}, \boldsymbol{e}_2^{\mathrm{t}}\right\}$ be an orthonormal basis of the adjacent tangent plane. Further, let $\mathrm{D}_\alpha^{\mathrm{t}} \breve{\boldsymbol{f}}$ and $\mathrm{d}_\alpha^{\mathrm{t}} \breve{\boldsymbol{f}}$ denote the Lagrangian and the Eulerian representation of the covariant derivative in the direction of the basis vector $\boldsymbol{e}_\alpha^{\mathrm{t}}$ $(\alpha = 1, 2)$. For arbitrary tensor orders of $\breve{\boldsymbol{f}}$, the Lagrangian and the Eulerian representation of the intrinsic surface gradient are given by [cf. Steinmann & Häsner, 2005]

$$\breve{\mathrm{Grad}}(\breve{\boldsymbol{f}}(\boldsymbol{X}, t)) = \sum_{\alpha=1}^{2} \left(\mathrm{D}_\alpha^{\mathrm{t}} \breve{\boldsymbol{f}}(\boldsymbol{X}, t) \right) \otimes \boldsymbol{e}_\alpha^{\mathrm{t}}, \tag{2.23}$$

$$\breve{\mathrm{grad}}(\breve{\boldsymbol{f}}(\boldsymbol{x}, t)) = \sum_{\alpha=1}^{2} \left(\mathrm{d}_\alpha^{\mathrm{t}} \breve{\boldsymbol{f}}(\boldsymbol{x}, t) \right) \otimes \boldsymbol{e}_\alpha^{\mathrm{t}}. \tag{2.24}$$

If the tensor order of $\breve{\boldsymbol{f}}$ is at least one, the intrinsic surface divergence is defined and has the Lagrangian/Eulerian representation

$$\breve{\mathrm{Div}}(\breve{\boldsymbol{f}}(\boldsymbol{X}, t)) = \breve{\mathrm{Grad}}(\breve{\boldsymbol{f}}(\boldsymbol{X}, t)) : \boldsymbol{I}, \quad \breve{\mathrm{div}}(\breve{\boldsymbol{f}}(\boldsymbol{x}, t)) = \breve{\mathrm{grad}}(\breve{\boldsymbol{f}}(\boldsymbol{x}, t)) : \boldsymbol{I}. \tag{2.25}$$

If $\breve{\boldsymbol{f}}$ is a vector field, the surface divergence is split according to

$$\breve{\mathrm{Div}}(\breve{\boldsymbol{f}}(\boldsymbol{X}, t)) = \breve{\mathrm{Div}}(\breve{\boldsymbol{f}}_{\|}(\boldsymbol{X}, t)) + 2\breve{H}(\boldsymbol{X}, t)\, \breve{f}_\perp(\boldsymbol{X}, t), \tag{2.26}$$

$$\breve{\mathrm{div}}(\breve{\boldsymbol{f}}(\boldsymbol{x}, t)) = \breve{\mathrm{div}}(\breve{\boldsymbol{f}}_{\|}(\boldsymbol{x}, t)) + 2\breve{H}(\boldsymbol{x}, t)\, \breve{f}_\perp(\boldsymbol{x}, t) \tag{2.27}$$

by use of the decomposition (2.16). Note that different conventions for the sign of the mean curvature

$$\breve{H}(\boldsymbol{X}, t) = \frac{1}{2}\breve{\mathrm{Div}}(\breve{\boldsymbol{n}}(\boldsymbol{X}, t)) \tag{2.28}$$

are common in the literature. The velocity of the interface is defined as

$$\breve{\boldsymbol{v}}(\boldsymbol{X}, t) = \dot{\breve{\boldsymbol{\chi}}}_\vartheta(\boldsymbol{X}, t) = \frac{\partial \breve{\boldsymbol{\chi}}_\vartheta(\boldsymbol{X}, t)}{\partial t} \tag{2.29}$$

and allows to expand the Eulerian representation of the total derivative of $\breve{\boldsymbol{f}}$ with respect to time according to

$$\dot{\breve{\boldsymbol{f}}}(\boldsymbol{x},t) = \frac{\partial \breve{\boldsymbol{f}}(\boldsymbol{x},t)}{\partial t} + \breve{\mathrm{grad}}\big(\breve{\boldsymbol{f}}(\boldsymbol{x},t)\big) \cdot \breve{\boldsymbol{v}}(\boldsymbol{x},t). \tag{2.30}$$

2.5 Deformation measures

The selection of a quantity describing the kinematic state at a material point is elementary for modeling the mechanical constitutive behavior of materials or imperfect interfaces. Kinematic state variables are generally defined based on the motion $\boldsymbol{\chi}$. The kinematic variable used for interface models throughout this work is the displacement jump $\boldsymbol{\delta}$ defined in (2.9). Concerning constitutive models for the bulk material, various deformation measures are established in continuum mechanics. To begin with, the deformation gradient tensor

$$\boldsymbol{F}(\boldsymbol{X},t) = \mathrm{Grad}\,(\boldsymbol{\chi}(\boldsymbol{X},t)) = \frac{\partial \boldsymbol{\chi}(\boldsymbol{X},t)}{\partial \boldsymbol{X}} \tag{2.31}$$

is introduced. Similarly, the gradient of the displacement is defined by

$$\boldsymbol{H}(\boldsymbol{X},t) = \mathrm{Grad}\,(\boldsymbol{u}(\boldsymbol{X},t)) = \frac{\partial \boldsymbol{u}(\boldsymbol{X},t)}{\partial \boldsymbol{X}} = \boldsymbol{F}(\boldsymbol{X},t) - \boldsymbol{I}. \tag{2.32}$$

Introducing its symmetric and skew-symmetric parts (cf. Appendix A.1.2)

$$\boldsymbol{\varepsilon}(\boldsymbol{X},t) = \mathrm{sym}\,(\boldsymbol{H}(\boldsymbol{X},t)), \qquad\qquad \boldsymbol{\omega}(\boldsymbol{X},t) = \mathrm{skw}(\boldsymbol{H}(\boldsymbol{X},t)), \tag{2.33}$$

the displacement gradient is additively decomposed according to

$$\boldsymbol{H}(\boldsymbol{X},t) = \boldsymbol{\varepsilon}(\boldsymbol{X},t) + \boldsymbol{\omega}(\boldsymbol{X},t). \tag{2.34}$$

The deformation gradient and the displacement gradient are used to define strain tensors, which are essential for the description of the mechanical behavior of materials. Among infinitely many possible strain tensors, one prominent example is specified here, namely the Green–Lagrangian strain tensor

$$\boldsymbol{E}(\boldsymbol{X},t) = \frac{1}{2}\left(\boldsymbol{H}(\boldsymbol{X},t) + \boldsymbol{H}^{\mathsf{T}}(\boldsymbol{X},t) + \boldsymbol{H}^{\mathsf{T}}(\boldsymbol{X},t)\boldsymbol{H}(\boldsymbol{X},t)\right). \tag{2.35}$$

Assumption of small deformations. Throughout this work, the infinitesimal strain theory is adopted, which is based on the condition that the displacement gradient is small

$$\|\boldsymbol{H}(\boldsymbol{X},t)\|_2 \ll 1 \qquad \text{for all } (\boldsymbol{X},t) \in \Omega_0 \times \mathbb{T}. \tag{2.36}$$

Consequently, the deformations (i.e., strains and rotations) in each point of the considered body are small, and higher order terms out of $\mathcal{O}\big(\|\boldsymbol{H}\|_2^2\big)$ are considered negligible as opposed to terms that are linear in $\|\boldsymbol{H}\|_2$ [cf. Bertram, 2008]. The *infinitesimal strain tensor* $\boldsymbol{\varepsilon}$ defined in (2.33) is used as a deformation measure. Since $\boldsymbol{\varepsilon}$ is the linearization

of the Green–Lagrangian strain tensor $\boldsymbol{E}$ as well as of any other possible strain tensor, it is also referred to as *linear strain tensor*.

Within the infinitesimal strain theory, also known as *geometrically linear theory* or as *theory of small deformations*, it is common to not distinguish between the Lagrangian and the Eulerian representation because the difference between the material coordinate $\boldsymbol{X}$ and the spatial coordinate $\boldsymbol{x}$ is assumed to be small. Note that this assumption is not justified by (2.36) on its own but requires the additional condition that the displacement $\boldsymbol{u}(\boldsymbol{X}, t)$ is small for all $(\boldsymbol{X}, t) \in \Omega_0 \times \mathbb{T}$.

2.6   Forces and stresses

Forces and force-like quantities are essential elements of continuum mechanics, but of "all the axioms of mechanics, those for systems of forces and torques are the most difficult to formulate" [quote from Truesdell, 1966, p. 26]. Stresses are force-per-unit-area quantities, and their relevance in continuum mechanics is underlined by the following quote from Marsden & Hughes [1994, p. 132], who state that the "concept which sets continuum mechanics apart from particle mechanics is that of stress". An extensive introduction to the topic is avoided here, and the reader is referred to the given references for details. Throughout this work, the Euler–Cauchy stress principle is adopted, which is called "the keystone of classical continuum mechanics" by Truesdell [1966, p. 29]. Non-classical concepts involving couple stresses or body moments, such as Cosserat continua [cf. Cosserat & Cosserat, 1909], are therefore not considered in the following.

The Euler–Cauchy stress principle is based on the *Cauchy stress vector* $\boldsymbol{t}(\boldsymbol{x}, t, \boldsymbol{n})$, which is also called *traction vector* and is defined on the outer surface of a body as well as on material interfaces and on imaginary (oriented) surfaces in the bulk, whose orientation is specified via the unit normal vector $\boldsymbol{n}$. For the material interface and for the outer surface, the orientation is fixed such that the argument $\boldsymbol{n}$ is superfluous and can be dropped. In contrast, for imaginary surfaces inside the bulk it was pointed out by Lubliner [2008, p. 27] that the traction "is not a vector field because it depends not only on position but also on the local orientation of the surface element", as defined by $\boldsymbol{n}$. Cauchy's fundamental lemma (also called Cauchy's stress theorem) states that the traction depends linearly on $\boldsymbol{n}$ as expressed through

$$\boldsymbol{t}(\boldsymbol{x}, t, \boldsymbol{n}) = \boldsymbol{\sigma}(\boldsymbol{x}, t) \, \boldsymbol{n}. \tag{2.37}$$

The linear operator $\boldsymbol{\sigma}$ is a second order tensor and is called the *Cauchy stress tensor*. Other than body moments, body forces are included in classical continuum mechanics theory and allow to account for external forces, e.g., due to a gravitation field. The specific body forces in the bulk and at the interface are in the following denoted $\boldsymbol{b}$ and $\boldsymbol{\breve{b}}$, respectively. It is recalled from Section 2.3 that no intrinsic surface stresses at the imperfect interface are considered within this work.
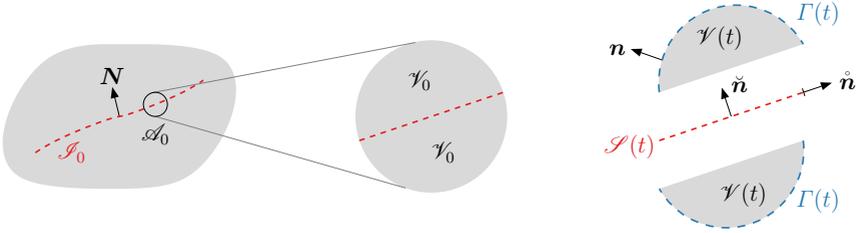
Figure 2.2: A solid body in the reference configuration *(left)* with a selected control volume in the reference configuration *(middle)* and in the current configuration *(right)*.

2.7 Bulk and interface balance equations

2.7.1 Preliminaries

A material control volume within the solid body is considered, which is described by an arbitrary, simply connected open subset $\mathscr{A}_0 \subset \mathscr{B}_0$ in the reference configuration. The subset of regular (bulk) points where all considered fields are smooth is denoted $\mathscr{V}_0 = \mathscr{A}_0 \setminus \mathscr{I}_0$ (see Figure 2.2). At time $t \in \mathbb{T}$, the set of regular points is described by $\mathscr{V}(t) = \boldsymbol{\chi}(\mathscr{V}_0, t)$. The part of the deformed interface $\mathscr{I}(t)$ which is enclosed by the control volume $\mathscr{V}(t)$ is expressed by $\mathscr{S}(t)$, and the outward boundary of $\mathscr{V}(t)$ is defined as $\Gamma(t) = \partial \mathscr{V}(t) \setminus \left(\mathscr{I}^+(t) \cup \mathscr{I}^-(t) \right)$. The unit normal on the outward boundary $\Gamma(t)$ is hereafter denoted $\boldsymbol{n}$. Further, the boundary of the deformed interface within the control volume is a curve, i.e., a one-dimensional manifold denoted $\partial \mathscr{S}(t)$. The outer unit normal on $\partial \mathscr{S}(t)$ is denoted $\mathring{\boldsymbol{n}}$. Other than in Javili et al. [2013], the interface boundary curve is not assigned its own lower-dimensional energies or other distinct quantities.

The balance equations are presented in the Eulerian description in a rather concise manner. More detailed information is found in various textbooks [see, e.g., Marsden & Hughes, 1994, Gupta & Steigmann, 2011]. The spatial argument $\boldsymbol{x}$ and the temporal argument t are dropped in the remainder of Section 2.7 for notational brevity. To start with, three theorems are presented which are crucial for the subsequent formulation of balance equations. Note that the assumption expressed by (2.14), i.e., collinearity of the surface normals on both sides of an imperfect interface, is exploited here.

Gauss's theorem. Gauss's theorem is also known as *divergence theorem*. For a sufficiently smooth vector field or tensor field of higher order $\boldsymbol{f}$ defined in the bulk, it reads

$$\int_{\mathscr{V}} \operatorname{div}(\boldsymbol{f}) \, \mathrm{d}V + \int_{\mathscr{S}} [\![\boldsymbol{f}]\!] \cdot \mathring{\boldsymbol{n}} \, \mathrm{d}A = \int_{\Gamma} \boldsymbol{f} \cdot \boldsymbol{n} \, \mathrm{d}A. \tag{2.38}$$

A corollary of this statement which is useful in the context of homogenization reads

$$\int_{\mathscr{V}} \operatorname{grad}(\boldsymbol{f}) \, \mathrm{d}V + \int_{\mathscr{S}} [\![\boldsymbol{f}]\!] \otimes \check{\boldsymbol{n}} \, \mathrm{d}A = \int_{\Gamma} \boldsymbol{f} \otimes \boldsymbol{n} \, \mathrm{d}A. \tag{2.39}$$

This result is also valid for a scalar field $\boldsymbol{f}$ and is obtained from (2.38) by inserting $\boldsymbol{f} = \boldsymbol{g} \cdot \boldsymbol{A}$ with a fixed but arbitrary tensor $\boldsymbol{A}$ of order one or higher. For a vector field or a tensor field of higher order $\check{\boldsymbol{f}}$ defined on the interface, Gauss's theorem states that

$$\int_{\mathscr{S}} \check{\operatorname{div}}(\check{\boldsymbol{f}}) \, \mathrm{d}V = \int_{\partial\mathscr{S}} \check{\boldsymbol{f}} \cdot \mathring{\boldsymbol{n}} \, \mathrm{d}L \tag{2.40}$$

holds [cf. Steinmann & Häsner, 2005].

Reynolds transport theorem. For a scalar field or vector field $\boldsymbol{f}$ defined in the bulk, the transport theorem states

$$\frac{\mathrm{d}}{\mathrm{d}t} \int_{\mathscr{V}} \boldsymbol{f} \, \mathrm{d}V = \int_{\mathscr{V}} \frac{\partial \boldsymbol{f}}{\partial t} \, \mathrm{d}V + \int_{\Gamma} (\boldsymbol{f} \otimes \boldsymbol{v}) \cdot \boldsymbol{n} \, \mathrm{d}A - \int_{\mathscr{S}} [\![\boldsymbol{f} \otimes \boldsymbol{v}]\!] \cdot \check{\boldsymbol{n}} \, \mathrm{d}A \tag{2.41}$$

$$= \int_{\mathscr{V}} \left(\dot{\boldsymbol{f}} + \operatorname{div}(\boldsymbol{v}) \, \boldsymbol{f} \right) \mathrm{d}V. \tag{2.42}$$

The transition between (2.41) and (2.42) is obtained with Gauss's theorem and (2.22).

Transport theorem for interfaces. Similar to the preceding theorem for bulk quantities, a transport theorem can be formulated for interfaces [e.g., Moeckel, 1975, Marsden & Hughes, 1994]. For a scalar field or vector field $\check{\boldsymbol{f}}$ defined on the interface, the theorem is expressed in terms of definitions from Section 2.4.2 according to

$$\frac{\mathrm{d}}{\mathrm{d}t} \int_{\mathscr{S}} \check{\boldsymbol{f}} \, \mathrm{d}A = \int_{\mathscr{S}} \frac{\partial \check{\boldsymbol{f}}}{\partial t} \, \mathrm{d}A + \int_{\partial\mathscr{S}} \left(\check{\boldsymbol{f}} \otimes \check{\boldsymbol{v}} \right) \cdot \mathring{\boldsymbol{n}} \, \mathrm{d}L \tag{2.43}$$

$$= \int_{\mathscr{S}} \left(\dot{\check{\boldsymbol{f}}} + \left(\check{\operatorname{div}}(\check{\boldsymbol{v}}_{\|}) + 2\check{H}\check{v}_{\perp} \right) \check{\boldsymbol{f}} \right) \mathrm{d}A. \tag{2.44}$$

The transition between (2.43) and (2.44) is obtained with Gauss's theorem and with (2.27) and (2.30).

2.7.2 Master balance equations

For a conserved scalar or vector-valued quantity, let $\boldsymbol{f}$ be the volumetric density in the bulk and $\check{\boldsymbol{f}}$ the areal density at the interface. Further, let $\boldsymbol{p}$, $\boldsymbol{s}$, and $\boldsymbol{Q}$ be the related

production, supply, and flux in the bulk, and let $\breve{p}$, $\breve{s}$, and $\breve{Q}$ denote the corresponding production, supply, and flux at the interface. The master balance equation is a postulate for the time derivative of the conserved quantity under consideration, which reads

$$\frac{\mathrm{d}}{\mathrm{d}t} \int_{\mathcal{V}} \boldsymbol{f} \, \mathrm{d}V + \frac{\mathrm{d}}{\mathrm{d}t} \int_{\mathcal{S}} \breve{\boldsymbol{f}} \, \mathrm{d}A = \int_{\mathcal{V}} (\boldsymbol{p} + \boldsymbol{s}) \, \mathrm{d}V + \int_{\mathcal{S}} (\breve{\boldsymbol{p}} + \breve{\boldsymbol{s}}) \, \mathrm{d}A \tag{2.45}$$

$$- \int_{\Gamma} \boldsymbol{Q} \cdot \boldsymbol{n} \, \mathrm{d}A - \int_{\partial\mathcal{S}} \breve{\boldsymbol{Q}} \cdot \hat{\boldsymbol{n}} \, \mathrm{d}L. \tag{2.46}$$

By combination with the theorems from Section 2.7.1, the integral equation

$$\int_{\mathcal{V}} \left(\dot{\boldsymbol{f}} + \mathrm{div}(\boldsymbol{v}) \, \boldsymbol{f} \right) \mathrm{d}V + \int_{\mathcal{S}} \left(\overset{\diamond}{\boldsymbol{f}} + \left(\breve{\mathrm{div}}(\breve{\boldsymbol{v}}_{\parallel}) + 2\breve{H}\breve{v}_{\perp} \right) \breve{\boldsymbol{f}} \right) \mathrm{d}A \tag{2.47}$$

$$= \int_{\mathcal{V}} (\boldsymbol{p} + \boldsymbol{s} - \mathrm{div}(\boldsymbol{Q})) \, \mathrm{d}V + \int_{\mathcal{S}} (\breve{\boldsymbol{p}} + \breve{\boldsymbol{s}} - \breve{\mathrm{div}}(\breve{\boldsymbol{Q}}) - [\![\boldsymbol{Q}]\!] \cdot \breve{\boldsymbol{n}}) \, \mathrm{d}A \tag{2.48}$$

is attained, which yields the local master balance equation for regular points

$$\dot{\boldsymbol{f}} + \mathrm{div}(\boldsymbol{v}) \, \boldsymbol{f} = \boldsymbol{p} + \boldsymbol{s} - \mathrm{div}(\boldsymbol{Q}) \qquad \text{for any } \boldsymbol{x} \in \Omega \tag{2.49}$$

and the local master equilibrium condition at the interface

$$\overset{\diamond}{\boldsymbol{f}} + \left(\breve{\mathrm{div}}(\breve{\boldsymbol{v}}_{\parallel}) + 2\breve{H}\breve{v}_{\perp} \right) \breve{\boldsymbol{f}} = \breve{\boldsymbol{p}} + \breve{\boldsymbol{s}} - \breve{\mathrm{div}}(\breve{\boldsymbol{Q}}) - [\![\boldsymbol{Q}]\!] \cdot \breve{\boldsymbol{n}} \qquad \text{for any } \boldsymbol{x} \in \mathcal{I}, \tag{2.50}$$

since the control volume $\mathcal{A}_0$, and thereby also $\mathcal{V}$ and $\mathcal{S}$, can be chosen arbitrarily. The argument exploited here is called *localization*, and with regard to interfaces it is also known as the *pillbox argument*.

2.7.3 Particularized balance equations

The balance equations for mass, linear and angular momentum, energy, and entropy are deduced from the master balance equations by insertion of the appropriate specific densities, production and supply terms, and fluxes. Table 2.1 summarizes all involved quantities.

Balance of mass. Production and supply of mass, as well as mass flux, are usually excluded in continuum mechanics of solids. Inserting the volumetric mass density $\boldsymbol{f} = \varrho$ and the areal mass density $\breve{\boldsymbol{f}} = \breve{\varrho}$ into the master balance equations immediately yields the balance of mass in regular points

$$\dot{\varrho} + \varrho \, \mathrm{div}(\boldsymbol{v}) = 0 \tag{2.51}$$

	balance of...	mass	linear momentum	angular momentum	total energy	entropy
bulk	vol. density $\boldsymbol{f}$	ϱ	$\varrho\boldsymbol{v}$	$\boldsymbol{x}\times\varrho\boldsymbol{v}$	$\varrho\left(e+\frac{1}{2}\boldsymbol{v}\cdot\boldsymbol{v}\right)$	$\varrho\eta$
	production $\boldsymbol{p}$	0	$\mathbf{0}$	$\mathbf{0}$	0	$\varrho\gamma$
	supply $\boldsymbol{s}$	0	$\varrho\boldsymbol{b}$	$\boldsymbol{x}\times\varrho\boldsymbol{b}$	$\varrho\left(h+\boldsymbol{b}\cdot\boldsymbol{v}\right)$	$\varrho h\theta^{-1}$
	flux $\boldsymbol{Q}$	$\mathbf{0}$	$-\boldsymbol{\sigma}$	$-\boldsymbol{x}\times\boldsymbol{\sigma}$	$\boldsymbol{q}-\boldsymbol{\sigma}\boldsymbol{v}$	$\theta^{-1}\boldsymbol{q}$
interface	areal density $\breve{\boldsymbol{f}}$	$\breve{\varrho}$	$\breve{\varrho}\breve{\boldsymbol{v}}$	$\breve{\boldsymbol{x}}\times\breve{\varrho}\breve{\boldsymbol{v}}$	$\breve{\varrho}\left(\breve{e}+\frac{1}{2}\breve{\boldsymbol{v}}\cdot\breve{\boldsymbol{v}}\right)$	$\breve{\varrho}\breve{\eta}$
	production $\breve{\boldsymbol{p}}$	0	$\mathbf{0}$	$\mathbf{0}$	0	$\breve{\varrho}\breve{\gamma}$
	supply $\breve{\boldsymbol{s}}$	0	$\breve{\varrho}\breve{\boldsymbol{b}}$	$\breve{\boldsymbol{x}}\times\breve{\varrho}\breve{\boldsymbol{b}}$	$\breve{\varrho}\left(\breve{h}+\breve{\boldsymbol{b}}\cdot\breve{\boldsymbol{v}}\right)$	$\breve{\varrho}\breve{h}\breve{\theta}^{-1}$
	flux $\breve{\boldsymbol{Q}}$	$\mathbf{0}$	$\mathbf{0}$	$\mathbf{0}$	$\breve{\boldsymbol{q}}$	$\breve{\theta}^{-1}\breve{\boldsymbol{q}}$

Table 2.1: Overview of the quantities involved in the derivations of the balance equations for mass, linear momentum, angular momentum, total energy, and entropy (see Section 2.7.3).

and the corresponding equilibrium condition at the interface

$$\dot{\breve{\varrho}}+\breve{\varrho}\left(\breve{\mathrm{div}}\left(\breve{\boldsymbol{v}}_{\|}\right)+2\breve{H}\breve{v}_{\perp}\right)=0. \tag{2.52}$$

The two equalities (2.51) and (2.52) are exploited to obtain the condensed representations of all balance equations discussed hereafter.

Balance of linear momentum. The local balance of linear momentum in regular points is also known as *Cauchy's first law of motion* and reads

$$\varrho\dot{\boldsymbol{v}}=\varrho\boldsymbol{b}+\mathrm{div}\left(\boldsymbol{\sigma}\right). \tag{2.53}$$

Taking into account Cauchy's fundamental lemma (2.37), the equilibrium condition derived for the interface from the balance of linear momentum is expressed as

$$\breve{\varrho}\dot{\breve{\boldsymbol{v}}}=\breve{\varrho}\breve{\boldsymbol{b}}+[\![\boldsymbol{t}]\!]. \tag{2.54}$$

Balance of angular momentum. The balance of angular momentum at regular points is also referred to as *Cauchy's second law of motion* and requires that Cauchy's stress tensor $\boldsymbol{\sigma}$ is symmetric. To derive this result from the master equation, the angular momentum per unit volume $\boldsymbol{f}=\boldsymbol{x}\times\varrho\boldsymbol{v}$ and the angular momentum per unit volume due to external body forces $\boldsymbol{s}=\boldsymbol{x}\times\varrho\boldsymbol{b}$ are considered. The corresponding flux $\boldsymbol{Q}=-\boldsymbol{x}\times\boldsymbol{\sigma}=-\boldsymbol{\epsilon}:(\boldsymbol{x}\otimes\boldsymbol{\sigma})$ is expressed by a generalization of the cross product for a pair of a vector and a second order tensor, where $\boldsymbol{\epsilon}$ denotes the Levi–Civita symbol for three dimensions defined in (A.5) in Appendix A.1.1. Inserting these quantities into

the master equation (2.49), taking into account the balance equations (2.51) and (2.53), and making use of the result

$$\mathrm{div}(\boldsymbol{Q}) = \boldsymbol{\epsilon} : \boldsymbol{\sigma} - \boldsymbol{x} \times \mathrm{div}(\boldsymbol{\sigma}) \tag{2.55}$$

following from a straightforward calculation yields the assertion

$$\boldsymbol{\epsilon} : \boldsymbol{\sigma} = \boldsymbol{0} \quad \Leftrightarrow \quad \boldsymbol{\sigma} = \boldsymbol{\sigma}^{\mathsf{T}}. \tag{2.56}$$

Likewise, the equilibrium condition at the interface due to the balance of angular momentum

$$[\![(\boldsymbol{x} - \breve{\boldsymbol{x}}) \times \boldsymbol{t}]\!] = \boldsymbol{0}. \tag{2.57}$$

is obtained from the master equation (2.50) by exploitation of (2.52) and (2.54).

Balance of energy. Let e and $\breve{e}$ denote the internal energy per unit mass in the bulk and at the interface, respectively. Further, let h and $\breve{h}$ be the specific heat supply in the bulk and at the interface due to thermal radiation, and let $\boldsymbol{q}$ and $\breve{\boldsymbol{q}}$ denote the heat flux in the bulk and at the interface. The balance of total energy in regular points

$$\varrho\left(\dot{e} + \dot{\boldsymbol{v}} \cdot \boldsymbol{v}\right) = \varrho\left(h + \boldsymbol{b} \cdot \boldsymbol{v}\right) - \mathrm{div}(\boldsymbol{q}) + \mathrm{div}(\boldsymbol{\sigma}) \cdot \boldsymbol{v} + \boldsymbol{\sigma} : \boldsymbol{D} \tag{2.58}$$

is obtained by insertion of the appropriate quantities from Table 2.1 into the master equation (2.49). Here, the symmetric part of the velocity gradient is denoted $\boldsymbol{D}$. The corresponding interface equilibrium condition is

$$\breve{\varrho}\left(\dot{\breve{e}} + \dot{\breve{\boldsymbol{v}}} \cdot \breve{\boldsymbol{v}}\right) = \breve{\varrho}\left(\breve{h} + \breve{\boldsymbol{b}} \cdot \breve{\boldsymbol{v}}\right) - \breve{\mathrm{div}}(\breve{\boldsymbol{q}}) - [\![\boldsymbol{q}]\!] \cdot \breve{\boldsymbol{n}} + [\![\boldsymbol{t} \cdot \boldsymbol{v}]\!]. \tag{2.59}$$

Total energy is the sum of kinetic and internal energy, and the balance equations for total energy can be decomposed accordingly. Kinetic and internal energy are no conservative quantities and do not have independent balance equations. In fact, the balance equations for kinetic energy are deduced from those for linear momentum by scalar multiplications of (2.53) and (2.54) with the velocities $\boldsymbol{v}$ and $\breve{\boldsymbol{v}}$, respectively. The balance of internal energy is then described by the remaining terms of (2.58) and (2.59), which amounts to

$$\varrho\dot{e} = \varrho h - \mathrm{div}(\boldsymbol{q}) + \boldsymbol{\sigma} : \boldsymbol{D} \tag{2.60}$$

for points in the bulk and

$$\breve{\varrho}\dot{\breve{e}} = \breve{\varrho}\breve{h} - \breve{\mathrm{div}}(\breve{\boldsymbol{q}}) - [\![\boldsymbol{q}]\!] \cdot \breve{\boldsymbol{n}} + [\![\boldsymbol{t} \cdot (\boldsymbol{v} - \breve{\boldsymbol{v}})]\!] \tag{2.61}$$

for points on the interface.

Balance of entropy. Let θ, η and γ be the temperature, the specific entropy, and the specific entropy production in the bulk. The corresponding quantities at the interface are denoted $\breve{\theta}$, $\breve{\eta}$ and $\breve{\gamma}$. In accordance with the early work of Clausius [1865], the standard constitutive assumption $\boldsymbol{Q} = \theta^{-1}\boldsymbol{q}$ is made for the flux of entropy in the bulk, and,

similarly, $\breve{\boldsymbol{Q}} = \breve{\theta}^{-1}\breve{\boldsymbol{q}}$ is adopted for the flux of entropy within the interface. With the supply terms $s = \varrho h \theta^{-1}$ and $\breve{s} = \breve{\varrho}\breve{h}\breve{\theta}^{-1}$, the equilibrium condition for the bulk reads

$$\varrho\dot{\eta} = \varrho\gamma + \frac{1}{\theta}\left(\varrho h + \frac{1}{\theta}\boldsymbol{q}\cdot\boldsymbol{g} - \mathrm{div}(\boldsymbol{q})\right),\tag{2.62}$$

and the corresponding interface condition is

$$\breve{\varrho}\dot{\breve{\eta}} = \breve{\varrho}\breve{\gamma} + \frac{1}{\breve{\theta}}\left(\breve{\varrho}\breve{h} + \frac{1}{\breve{\theta}}\breve{\boldsymbol{q}}\cdot\breve{\boldsymbol{g}} - \breve{\mathrm{div}}(\breve{\boldsymbol{q}})\right) - \left[\!\!\left[\frac{\boldsymbol{q}}{\theta}\right]\!\!\right]\cdot\breve{\boldsymbol{n}},\tag{2.63}$$

where the temperature gradients in the bulk and within the interface are defined by

$$\boldsymbol{g} = \mathrm{grad}\left(\theta\right),\qquad\qquad\qquad \breve{\boldsymbol{g}} = \breve{\mathrm{grad}}\left(\breve{\theta}\right).\tag{2.64}$$

2.7.4 Centered interface position

Hereafter, the common assumption is made that the fictitious surface $\mathscr{I}$ is placed in the middle between both sides of the interface, i.e., the parameter $\vartheta = \frac{1}{2}$ is chosen in (2.13). As a consequence, the identities

$$\breve{\boldsymbol{x}} = \langle\!\langle\boldsymbol{x}\rangle\!\rangle,\qquad\qquad \breve{\boldsymbol{v}} = \langle\!\langle\boldsymbol{v}\rangle\!\rangle,\qquad\qquad \dot{\breve{\boldsymbol{v}}} = \langle\!\langle\dot{\boldsymbol{v}}\rangle\!\rangle\tag{2.65}$$

are obtained, where the interface average $\langle\!\langle\bullet\rangle\!\rangle$ introduced in (2.4) is used. For the centered interface position, the additional assumptions

$$\breve{\boldsymbol{t}} = \langle\!\langle\boldsymbol{t}\rangle\!\rangle,\qquad\qquad\qquad \breve{\theta} = \langle\!\langle\theta\rangle\!\rangle\tag{2.66}$$

seem natural and are adopted. The interface condition due to the balance of angular momentum (2.57) can then be reformulated according to

$$\boldsymbol{\delta}\times\breve{\boldsymbol{t}} = \boldsymbol{0}.\tag{2.67}$$

It is concluded hereof that the displacement jump and the interface traction $\breve{\boldsymbol{t}}$ are required to be collinear. This is a severe limitation for interfaces at finite strains, as pointed out, e.g., by Vossen et al. [2013] and Ottosen et al. [2015]. However, under the assumption of small deformations, $\left\|\boldsymbol{\delta}\times\breve{\boldsymbol{t}}\right\|$ is considered to be negligibly small. The balance of internal energy at the interface is given by

$$\breve{\varrho}\dot{\breve{e}} = \breve{\varrho}\breve{h} - \breve{\mathrm{div}}(\breve{\boldsymbol{q}}) - [\![\boldsymbol{q}]\!]\cdot\breve{\boldsymbol{n}} + \breve{\boldsymbol{t}}\cdot\dot{\boldsymbol{\delta}}\tag{2.68}$$

under the assumption of a centered interface position. The term $\breve{\boldsymbol{t}}\cdot\dot{\boldsymbol{\delta}}$ corresponds to the mechanical power per unit area of the interface.

2.8   Thermodynamics

2.8.1   First law of thermodynamics

The balance of total energy principle, or the balance of internal energy derived thereof, is widely known as the first law of thermodynamics. Combining (2.60) and (2.68) with the results for the balance of entropy (2.62) and (2.63) yields the equalities

$$\varrho \left(\dot{e} - \dot{\eta}\theta \right) = \boldsymbol{\sigma} : \boldsymbol{D} - \varrho\theta\gamma - \frac{1}{\theta}\boldsymbol{q} \cdot \boldsymbol{g}, \tag{2.69}$$

$$\breve{\varrho} \left(\dot{\breve{e}} - \dot{\breve{\eta}}\breve{\theta} \right) = \breve{\boldsymbol{t}} \cdot \dot{\boldsymbol{\delta}} - \breve{\varrho}\breve{\theta}\breve{\gamma} - \frac{1}{\breve{\theta}}\breve{\boldsymbol{q}} \cdot \breve{\boldsymbol{g}} - [\![\theta]\!] \left\langle\!\!\left\langle \frac{\boldsymbol{q}}{\theta} \right\rangle\!\!\right\rangle \cdot \breve{\boldsymbol{n}}. \tag{2.70}$$

2.8.2   Second law of thermodynamics

The second law of thermodynamics states that the rate of entropy production in the bulk and at the interface must be non-negative. Together with (2.69) and (2.70), this requirement yields the *Clausius–Duhem inequality* for regular points in the bulk

$$\boldsymbol{\sigma} : \boldsymbol{D} - \varrho \left(\dot{e} - \dot{\eta}\,\theta \right) - \frac{1}{\theta}\boldsymbol{q} \cdot \boldsymbol{g} \geq 0 \tag{2.71}$$

and its counterpart for the interface

$$\breve{\boldsymbol{t}} \cdot \dot{\boldsymbol{\delta}} - \breve{\varrho} \left(\dot{\breve{e}} - \dot{\breve{\eta}}\,\breve{\theta} \right) - \frac{1}{\breve{\theta}}\breve{\boldsymbol{q}} \cdot \breve{\boldsymbol{g}} - [\![\theta]\!] \left\langle\!\!\left\langle \frac{\boldsymbol{q}}{\theta} \right\rangle\!\!\right\rangle \cdot \breve{\boldsymbol{n}} \geq 0. \tag{2.72}$$

At this point, it is useful to introduce the specific Helmholtz free energies in the bulk and at the interface

$$\Psi = e - \eta\,\theta, \qquad\qquad \breve{\Psi} = \breve{e} - \breve{\eta}\,\breve{\theta}. \tag{2.73}$$

The inequalities (2.71) and (2.72) are reformulated according to

$$\mathscr{D} \geq 0 \qquad \text{with } \mathscr{D} = \boldsymbol{\sigma} : \dot{\boldsymbol{\varepsilon}} - \varrho \left(\dot{\Psi} + \eta\,\dot{\theta} \right) - \frac{1}{\theta}\boldsymbol{q} \cdot \boldsymbol{g}, \tag{2.74}$$

$$\breve{\mathscr{D}} \geq 0 \qquad \text{with } \breve{\mathscr{D}} = \breve{\boldsymbol{t}} \cdot \dot{\boldsymbol{\delta}} - \breve{\varrho} \left(\dot{\breve{\Psi}} + \breve{\eta}\,\dot{\breve{\theta}} \right) - \frac{1}{\breve{\theta}}\breve{\boldsymbol{q}} \cdot \breve{\boldsymbol{g}} - [\![\theta]\!] \left\langle\!\!\left\langle \frac{\boldsymbol{q}}{\theta} \right\rangle\!\!\right\rangle \cdot \breve{\boldsymbol{n}}, \tag{2.75}$$

where $\mathscr{D}$ and $\breve{\mathscr{D}}$ denote the (total) dissipation per unit volume/area in the bulk/at the interface. For the bulk inequality (2.74), the approximation $\dot{\boldsymbol{\varepsilon}} \approx \boldsymbol{D}$ has been exploited, which is permissible at small deformations, The term $\boldsymbol{\sigma} : \dot{\boldsymbol{\varepsilon}}$ represents the density of mechanical power per unit volume of the bulk.

2.8.3 Consequences of the second law

Following Coleman & Gurtin [1967], a thermodynamic state is characterized by the kinematic state, temperature, and internal state variables, which are denoted by the generalized vectors $\boldsymbol{\mathcal{I}}$ and $\boldsymbol{\breve{\mathcal{I}}}$ for the bulk and for the interface, respectively. This implies

$$\Psi \equiv \Psi(\boldsymbol{\varepsilon}, \theta, \boldsymbol{\mathcal{I}}), \qquad\qquad \breve{\Psi} \equiv \breve{\Psi}(\boldsymbol{\delta}, \breve{\theta}, \boldsymbol{\breve{\mathcal{I}}}) \tag{2.76}$$

for the specific free energies and thus

$$\dot{\Psi} = \frac{\partial \Psi}{\partial \boldsymbol{\varepsilon}} : \dot{\boldsymbol{\varepsilon}} + \frac{\partial \Psi}{\partial \theta} \dot{\theta} + \frac{\partial \Psi}{\partial \boldsymbol{\mathcal{I}}} \cdot \dot{\boldsymbol{\mathcal{I}}}, \qquad \dot{\breve{\Psi}} = \frac{\partial \breve{\Psi}}{\partial \boldsymbol{\delta}} \cdot \dot{\boldsymbol{\delta}} + \frac{\partial \breve{\Psi}}{\partial \breve{\theta}} \dot{\breve{\theta}} + \frac{\partial \breve{\Psi}}{\partial \boldsymbol{\breve{\mathcal{I}}}} \cdot \dot{\boldsymbol{\breve{\mathcal{I}}}} \tag{2.77}$$

for their material time derivatives. Insertion of these representations into the dissipation inequalities (2.74) and (2.75) leads to another formulation of the second law, namely

$$\left(\boldsymbol{\sigma} - \varrho \frac{\partial \Psi}{\partial \boldsymbol{\varepsilon}} \right) : \dot{\boldsymbol{\varepsilon}} - \varrho \left(\eta + \frac{\partial \Psi}{\partial \theta} \right) \dot{\theta} - \varrho \frac{\partial \Psi}{\partial \boldsymbol{\mathcal{I}}} \cdot \dot{\boldsymbol{\mathcal{I}}} - \frac{1}{\theta} \boldsymbol{q} \cdot \boldsymbol{g} \geq 0, \quad (2.78)$$

$$\left(\boldsymbol{\breve{t}} - \breve{\varrho} \frac{\partial \breve{\Psi}}{\partial \boldsymbol{\delta}} \right) \cdot \dot{\boldsymbol{\delta}} - \breve{\varrho} \left(\breve{\eta} + \frac{\partial \breve{\Psi}}{\partial \breve{\theta}} \right) \dot{\breve{\theta}} - \breve{\varrho} \frac{\partial \breve{\Psi}}{\partial \boldsymbol{\breve{\mathcal{I}}}} \cdot \dot{\boldsymbol{\breve{\mathcal{I}}}} - \frac{1}{\breve{\theta}} \boldsymbol{\breve{q}} \cdot \boldsymbol{\breve{g}} - [\![\theta]\!] \left\langle\!\left\langle \frac{\boldsymbol{q}}{\theta} \right\rangle\!\right\rangle \cdot \boldsymbol{\breve{n}} \geq 0, \quad (2.79)$$

which must be satisfied for every admissible thermodynamic process. Simplifying the similar, more detailed reasoning for bulk quantities in Coleman & Gurtin [1967], one can, broadly speaking, say that (2.78) and (2.79) must be satisfied for arbitrary rates $\dot{\boldsymbol{\varepsilon}}$, $\dot{\theta}$, $\dot{\boldsymbol{\delta}}$, and $\dot{\breve{\theta}}$, and thus the conclusion is drawn that the following equalities and inequalities must hold:

$$\boldsymbol{\sigma} = \varrho \frac{\partial \Psi}{\partial \boldsymbol{\varepsilon}}, \qquad \eta = -\frac{\partial \Psi}{\partial \theta}, \qquad\qquad -\varrho \frac{\partial \Psi}{\partial \boldsymbol{\mathcal{I}}} \cdot \dot{\boldsymbol{\mathcal{I}}} - \frac{1}{\theta} \boldsymbol{q} \cdot \boldsymbol{g} \geq 0, \qquad (2.80)$$

$$\boldsymbol{\breve{t}} = \breve{\varrho} \frac{\partial \breve{\Psi}}{\partial \boldsymbol{\delta}}, \qquad \breve{\eta} = -\frac{\partial \breve{\Psi}}{\partial \breve{\theta}}, \qquad -\breve{\varrho} \frac{\partial \breve{\Psi}}{\partial \boldsymbol{\breve{\mathcal{I}}}} \cdot \dot{\boldsymbol{\breve{\mathcal{I}}}} - \frac{1}{\breve{\theta}} \boldsymbol{\breve{q}} \cdot \boldsymbol{\breve{g}} - [\![\theta]\!] \left\langle\!\left\langle \frac{\boldsymbol{q}}{\theta} \right\rangle\!\right\rangle \cdot \boldsymbol{\breve{n}} \geq 0. \qquad (2.81)$$

In respect of the equalities in (2.80) and (2.81), the couples $(\boldsymbol{\varepsilon}, \boldsymbol{\sigma})$, (θ, η), $(\boldsymbol{\delta}, \boldsymbol{\breve{t}})$, and $(\breve{\theta}, \breve{\eta})$ are called thermodynamic conjugate pairs of (primal) state variables and associate thermodynamic (dual) driving forces. Introducing the generalized force vectors

$$\boldsymbol{\mathcal{F}} = -\varrho \frac{\partial \Psi}{\partial \boldsymbol{\mathcal{I}}}, \qquad\qquad \boldsymbol{\breve{\mathcal{F}}} = -\breve{\varrho} \frac{\partial \breve{\Psi}}{\partial \boldsymbol{\breve{\mathcal{I}}}}, \tag{2.82}$$

conjugate pairs $(\boldsymbol{\mathcal{I}}, \boldsymbol{\mathcal{F}})$ and $(\boldsymbol{\breve{\mathcal{I}}}, \boldsymbol{\breve{\mathcal{F}}})$ are obtained for the internal state variables as well. Both the total dissipation in the bulk and the total dissipation at the interface can be decomposed into an intrinsic part and a thermal part, which can now be expressed by

$$\mathscr{D} = \mathscr{D}_{\mathrm{i}} + \mathscr{D}_{\theta} \geq 0, \qquad \mathscr{D}_{\mathrm{i}} = \boldsymbol{\mathcal{F}} \cdot \dot{\boldsymbol{\mathcal{I}}}, \qquad \mathscr{D}_{\theta} = -\frac{1}{\theta} \boldsymbol{q} \cdot \boldsymbol{g}, \tag{2.83}$$

$$\breve{\mathscr{D}} = \breve{\mathscr{D}}_{\mathrm{i}} + \breve{\mathscr{D}}_{\theta} \geq 0, \qquad \breve{\mathscr{D}}_{\mathrm{i}} = \boldsymbol{\breve{\mathcal{F}}} \cdot \dot{\boldsymbol{\breve{\mathcal{I}}}}, \qquad \breve{\mathscr{D}}_{\theta} = -\frac{1}{\breve{\theta}} \boldsymbol{\breve{q}} \cdot \boldsymbol{\breve{g}} - [\![\theta]\!] \left\langle\!\left\langle \frac{\boldsymbol{q}}{\theta} \right\rangle\!\right\rangle \cdot \boldsymbol{\breve{n}}. \tag{2.84}$$

Many times it is assumed that intrinsic and thermal dissipation are decoupled

$$\mathscr{D}_i \geq 0, \qquad \mathscr{D}_\theta \geq 0, \qquad \breve{\mathscr{D}}_i \geq 0, \qquad \breve{\mathscr{D}}_\theta \geq 0, \qquad (2.85)$$

which does not mean that mechanical and thermal effects are required to be decoupled, as noted by Halphen & Nguyen [1975]. It is worth mentioning that the first relation in (2.85) is also known as the *Clausius–Planck inequality*.

2.8.4   Classification of thermodynamic processes

A thermodynamic process is called *isothermal* if the temperature is constant in time at every point of the considered body. On the other hand, a body with spatially homogeneous temperature is said to have *uniform* temperature. Processes with constant deformations are called *static*. For a static process, the velocities v and $\breve{v}$ vanish, such that the equilibrium conditions due to the balance of linear momentum reduce to

$$\varrho b + \mathrm{div}(\boldsymbol{\sigma}) = \mathbf{0}, \qquad\qquad \breve{\varrho}\breve{b} + [\![t]\!] = \mathbf{0}. \qquad (2.86)$$

These equations also apply to *quasistatic* processes, for which the simplifying assumption is made that inertia can be neglected. If, in addition, the body forces $\breve{\varrho}\breve{b}$ acting on the interface are negligible, then the condition concerning the interface reduces to the requirement that the Cauchy traction t is continuous across the interface, which is well-known from the classical cohesive zone framework. Then, the interface traction $\breve{t}$ is uniquely defined as the surface traction on the negative (master) side of the interface such that the choice in (2.66) becomes irrelevant.

The term *steady state* refers to situations where none of the variables describing the thermodynamic state changes in time. Consequently, the rates $\dot{e}$ and $\breve{\dot{e}}$ of internal energy in the bulk and at the interface vanish and deformations of the body are constant. As a result, the equations (2.60) and (2.68) for balance of internal energy reduce to

$$\varrho h - \mathrm{div}(q) = 0, \qquad\qquad \breve{\varrho}\breve{h} - \breve{\mathrm{div}}(\breve{q}) - [\![q]\!] \cdot \breve{n} = 0. \qquad (2.87)$$

It is worth noting that an isothermal quasistatic process is in general not in steady state because of possible changes of internal state variables (e.g., consider relaxation tests of viscous materials). In the words of Germain et al. [1983, p. 1014], internal variables "may change without changes in the surroundings, and usually the observer is not able to control their value". The purpose of internal state variables is to capture path-dependent phenomena. A process is called *elastic* while intrinsic dissipation due to evolution of internal variables vanishes, otherwise it is *inelastic*. Further, a process is called *dissipative* or *irreversible* if the integral of total dissipation over time is strictly positive. No thermal dissipation occurs if the temperature is assumed to be uniform. Thus, total dissipation consists only of intrinsic dissipation in that particular case, and irreversibility is then tantamount to path-dependence and to inelastic behavior. It should be mentioned that thermal dissipation is often (sometimes tacitly) neglected for isothermal problems [cf. Germain et al., 1983].

This work is mainly concerned with quasistatic isothermal mechanical problems, but steady state heat conduction will also be treated in Chapters 5 and 6. However, thermomechanically coupled problems will not be addressed, hence the decoupling assumption expressed through (2.85) is trivially satisfied in all considered cases.

Chapter 3:
Generalized standard materials

3.1 Introduction

Thermomechanical problems are characterized by balance equations (see Section 2.7) supplemented with boundary conditions and with constitutive equations that describe the behavior of the bulk material and of the interfaces in the considered solid. With attention limited to isothermal mechanical problems, the present Chapter addresses phenomenological models which are suited to describe relevant continuum mechanical properties of bulk materials[4]. The first objective of such models is to establish relations between the (primal) state variables and the associate (dual) conjugate forces. In particular, stress–strain relations are sought-after. From a technical point of view, and in respect of (2.80) and (2.82), this is accomplished by specifying the Helmholtz free energy in (2.76), whose temperature argument is dropped in the present isothermal case. Secondly, if internal state variables are involved in the modeling, their evolution in time must be described by constitutive laws.

As stated before, internal variables are required to capture path-dependence of inelastic bulk or interface behavior. Within this work, they are assumed to vanish in the initial configuration at time t_0. Inelastic behavior can be classified as either rate-dependent or rate-independent. In the latter case, the evolution of internal variables depends only on the loading path, but not on the loading rates. The main interest lays on rate-dependent models in the following because rate-dependence is required for the reduced basis method presented in Chapter 7. It is noted that rate-dependent models are generally formulated with parameters that allow to control the degree of rate-dependence, such that rate-independent behavior can be viewed as a limit case. However, approximating rate-independent behavior with a rate-dependent model is usually challenging from a numerical point of view.

3.2 Theoretical framework

All bulk materials considered throughout this work belong to the class of generalized standard materials (GSMs), also known as *generalized standard media*, *standard dissipative solids*, or simply *standard materials*. The GSM framework was first presented by Halphen & Nguyen [1975], but key concepts of the theory were published earlier by Biot [1954, 1965] and Ziegler [1963]. Another recommendable paper on the topic which

---

[4]Constitutive phenomenological relations describing the mechanics of interfaces are introduced separately in Chapter 4

also addresses homogenization is the one of Suquet [1985]. GSMs exhibit a special structure that allows for variational treatment [e.g., Ortiz & Stainier, 1999, Miehe, 2002], which is not only handy from a mathematical point of view but also fundamental to applications such as the reduced order homogenization scheme presented in Chapter 7. A GSM model is described in terms of two thermodynamic potentials:

- a Helmholtz free energy volumetric density $\psi(\boldsymbol{\varepsilon}, \boldsymbol{\mathcal{I}})$, and

- a volumetric (primal) dissipation (pseudo-) potential $\phi(\dot{\boldsymbol{\mathcal{I}}})$.

Both potentials are required to be non-negative and convex and must contain the origin, i.e., $\psi(\mathbf{0}, \mathbf{0}) = \phi(\mathbf{0}) = 0$ must be fulfilled. The free energy density is sometimes also called *energy storage function* [e.g., Miehe, 2002]. While the original GSM formulation of Halphen & Nguyen [1975] is expressed in terms of the specific free energy per unit mass Ψ introduced in Section 2.8, the alternative utilization of the corresponding volumetric density ψ [in line with, e.g., Chaboche & Jung, 1997, Chaboche, 2002] appears to be more convenient in what follows, and it yields the relationships

$$\boldsymbol{\sigma} = \frac{\partial \psi}{\partial \boldsymbol{\varepsilon}}, \qquad\qquad \boldsymbol{\mathcal{F}} = -\frac{\partial \psi}{\partial \boldsymbol{\mathcal{I}}}. \tag{3.1}$$

Partial derivatives of the potentials ψ and ϕ have to be understood as elements of subgradients in the sense of convex analysis [cf. Rockafellar, 1970] because no differentiability has been postulated. Whereas thermodynamically consistent material models generally involve a Helmholtz free energy, the postulate that dissipation is governed by a (pseudo-) potential $\phi(\dot{\boldsymbol{\mathcal{I}}})$ is a characteristic of the GSM framework. With the primal dissipation potential ϕ, the evolution of internal variables is implicitly described via

$$\boldsymbol{\mathcal{F}} = \frac{\partial \phi}{\partial \dot{\boldsymbol{\mathcal{I}}}}. \tag{3.2}$$

Combining this relationship with the second equality in (3.1), the dissipative mechanism is summarized as a system of implicit ordinary differential equations (ODEs)

$$\frac{\partial \psi}{\partial \boldsymbol{\mathcal{I}}} + \frac{\partial \phi}{\partial \dot{\boldsymbol{\mathcal{I}}}} = \mathbf{0}, \tag{3.3}$$

which can be understood as Lagrange's equations of the second kind [cf. Biot, 1954] when considering the Lagrangian $L = \psi - \int \phi \, \mathrm{d}t$. The Legendre–Fenchel transform

$$\phi^*(\boldsymbol{\mathcal{F}}) = \sup_{\dot{\boldsymbol{\mathcal{I}}}} \left\{ \dot{\boldsymbol{\mathcal{I}}} \cdot \boldsymbol{\mathcal{F}} - \phi(\dot{\boldsymbol{\mathcal{I}}}) \right\} \tag{3.4}$$

of the primal potential ϕ is called *dual dissipation potential* or *force potential*. The dual potential ϕ^* is again non-negative, convex, and contains the origin. For rate-dependent material models, it provides the explicit description of the evolution of internal variables

$$\dot{\boldsymbol{\mathcal{I}}} = \frac{\partial \phi^*}{\partial \boldsymbol{\mathcal{F}}} \tag{3.5}$$

as a counterpart to (3.2). The Legendre–Fenchel transform of the dual dissipation potential is, in turn, the primal dissipation potential

$$\phi(\dot{\boldsymbol{\mathcal{I}}}) = \sup_{\boldsymbol{\mathcal{F}}} \left\{ \dot{\boldsymbol{\mathcal{I}}} \cdot \boldsymbol{\mathcal{F}} - \phi^*(\boldsymbol{\mathcal{F}}) \right\}. \tag{3.6}$$

GSMs are typically given in terms of the free energy density ψ and the dual dissipation potential ϕ^*, because closed-form representations of the primal dissipation potential ϕ are not at hand in most cases. This is because many dissipative mechanisms are modeled via level set functions $\varphi(\boldsymbol{\mathcal{F}})$ expressed in terms of thermodynamic forces (e.g., yield criteria). An exception are the linear viscoelastic models given in Section 3.3.2, whose potentials ϕ and ϕ^* are both known in closed form.

It is pointed out that the existence of a dissipation potential is necessary but not sufficient for GSM models. In fact, it is required that ϕ^* has the vector of generalized forces $\boldsymbol{\mathcal{F}}$ conjugate to the internal variables $\boldsymbol{\mathcal{I}}$ as its sole argument. This restriction is sometimes relaxed such that ϕ^* is also allowed to depend on the internal variables themselves, which must then be considered as parameters [see Germain et al., 1983]. Such an approach violates the variational structure of the original GSM formulation and is not further treated within this work.

From (3.2) it is concluded that the intrinsic dissipation in the bulk introduced in (2.83) can be expressed via

$$\mathscr{D}_{\mathrm{i}} = \boldsymbol{\mathcal{F}} \cdot \dot{\boldsymbol{\mathcal{I}}} = \frac{\partial \phi}{\partial \dot{\boldsymbol{\mathcal{I}}}} \cdot \dot{\boldsymbol{\mathcal{I}}}. \tag{3.7}$$

Since the primal dissipation potential is convex and contains the origin, it follows from (3.7) that the Clausius–Planck inequality (and thereby the second law of thermodynamics) is satisfied. Thus, GSMs are thermodynamically consistent material models.

3.3 Examples

3.3.1 Plasticity and viscoplasticity

The term *viscoplasticity* refers to rate-dependent plasticity, while rate-independent plasticity is usually simply called "plasticity". For an extensive introduction to the topic, see, e.g., the much-noticed book of Lubliner [2008]. At small deformations, (visco-) plasticity in the bulk is modeled via an additive decomposition of the infinitesimal strain tensor

$$\boldsymbol{\varepsilon} = \boldsymbol{\varepsilon}_{\mathrm{e}} + \boldsymbol{\varepsilon}_{\mathrm{p}} \tag{3.8}$$

into an elastic part $\boldsymbol{\varepsilon}_{\mathrm{e}}$ and into an internal variable $\boldsymbol{\varepsilon}_{\mathrm{p}}$ called *plastic strain*. A linear relation between the Cauchy stress and the elastic strain is assumed, which is expressed by the generalized Hooke's law

$$\boldsymbol{\sigma} = \mathbb{C} : \boldsymbol{\varepsilon}_{\mathrm{e}} = \mathbb{C} : (\boldsymbol{\varepsilon} - \boldsymbol{\varepsilon}_{\mathrm{p}}). \tag{3.9}$$
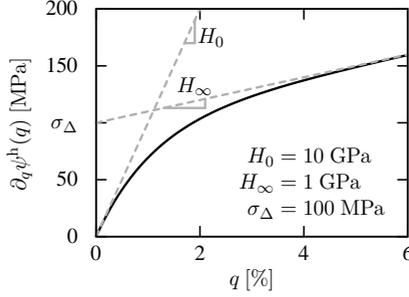
Figure 3.1: Illustration of a Voce-type isotropic hardening law.

Here, $\mathbb{C} \in \mathscr{L}^4$ denotes a stiffness tensor (cf. Appendix A.3). Stiffness tensors are not required to be constant in general. For instance, damage corresponds to degradation of the stiffness and is typically modeled via a damage internal variable $D \in [0, 1]$ according to

$$\mathbb{C}(D) = (1 - D)\mathbb{C}_0, \tag{3.10}$$

where $\mathbb{C}_0 \in \mathscr{L}^4$ is a constant stiffness tensor. Damage and plasticity can be coupled [e.g., Einav et al., 2007], but damage within bulk materials is not treated in this work, and all bulk stiffness tensors are assumed to be constant hereafter.

Helmholtz free energy density. In the following, a rather general GSM formulation of single-surface (visco-) plasticity with isotropic hardening as well as linear and nonlinear kinematic hardening (LKH/NLKH) is presented. Isotropic hardening, also known as *strain hardening,* is modeled with a potential ψ^{h} that depends only on one scalar argument q called *isotropic hardening internal variable* with a conjugate force denoted r. Two types of isotropic hardening potentials are considered: a quadratic potential

$$\psi^{\mathrm{h}}(q) = \frac{H}{2}q^2 \tag{3.11}$$

with the hardening modulus $H \geq 0$, and an exponential potential

$$\psi^{\mathrm{h}}(q) = \frac{H_\infty}{2}q^2 + \sigma_\Delta \left(q - \frac{\sigma_\Delta}{H_0 - H_\infty} \left(1 - \exp\left(-\frac{H_0 - H_\infty}{\sigma_\Delta}q \right) \right) \right) \tag{3.12}$$

with the parameters $H_0 > H_\infty \geq 0$ and $\sigma_\Delta > 0$, which converges pointwise to a quadratic form like (3.11) for $H_0 \to H_\infty$ or for $\sigma_\Delta \to 0$. When using a standard formulation of the yield stress, as specified later on in (3.23), the first kind of potential describes linear isotropic hardening and the second one describes hardening according to Voce [1955]. An illustration of the Voce-type hardening law is presented in Figure 3.1.

Linear kinematic hardening as proposed by Prager [1949] is easily incorporated via a quadratic term in the Helmholtz free energy density which depends on the plastic strain $\boldsymbol{\varepsilon}_{\mathrm{p}}$ but on no other state variables. The conjugate force to the plastic strain is denoted $\boldsymbol{\sigma}_{\mathbf{P}}$ and coincides with the Cauchy stress tensor $\boldsymbol{\sigma}$ when no linear kinematic hardening occurs.

Following Chaboche [1991], nonlinear kinematic hardening is modeled with $M \in \mathbb{N}_0$ internal deviatoric stress tensors $\boldsymbol{\chi}^{(1)}, \ldots, \boldsymbol{\chi}^{(M)}$ and with the associated internal state variables $\boldsymbol{\alpha}^{(1)}, \ldots, \boldsymbol{\alpha}^{(M)}$ which define M NLKH elements. All involved internal variables and conjugate forces are summarized according to

$$\boldsymbol{\mathcal{I}} = \left(\boldsymbol{\varepsilon}_{\mathrm{p}}, \boldsymbol{\alpha}^{(1)}, \ldots, \boldsymbol{\alpha}^{(M)}, q\right), \qquad \boldsymbol{\mathcal{F}} = \left(\boldsymbol{\sigma}_{\mathbf{P}}, -\boldsymbol{\chi}^{(1)}, \ldots, -\boldsymbol{\chi}^{(M)}, r\right), \tag{3.13}$$

and the general form of the Helmholtz free energy density is

$$\psi(\boldsymbol{\varepsilon}, \boldsymbol{\mathcal{I}}) = \frac{1}{2}\left(\boldsymbol{\varepsilon} - \boldsymbol{\varepsilon}_{\mathrm{p}}\right) : \mathbb{C} : \left(\boldsymbol{\varepsilon} - \boldsymbol{\varepsilon}_{\mathrm{p}}\right) + \psi^{\mathrm{h}}(q) + \frac{1}{2}\boldsymbol{\varepsilon}_{\mathrm{p}} : \mathbb{K}_{\mathrm{l}} : \boldsymbol{\varepsilon}_{\mathrm{p}} \tag{3.14}$$

$$+ \frac{1}{3}\sum_{i=1}^{M} \boldsymbol{\alpha}^{(i)} : \mathbb{K}^{(i)} : \boldsymbol{\alpha}^{(i)}. \tag{3.15}$$

The stiffness tensors related to kinematic hardening are assumed to be isotropic, i.e., they are multiples of the second isotropic projector $\mathbb{P}_2^{\mathrm{iso}}$ (defined in (A.19) in Appendix A.1.2)

$$\mathbb{K}_{\mathrm{l}} = K_{\mathrm{l}}\,\mathbb{P}_2^{\mathrm{iso}}, \qquad\qquad \mathbb{K}^{(i)} = K^{(i)}\,\mathbb{P}_2^{\mathrm{iso}} \qquad (i = 1, \ldots, M) \tag{3.16}$$

with a non-negative linear kinematic hardening modulus K_{l} and positive nonlinear kinematic hardening moduli $K^{(1)}, \ldots, K^{(M)}$. The internal stress $\boldsymbol{\chi}_{\mathrm{l}}$ related to linear kinematic hardening and the back stress $\boldsymbol{\chi}$ are defined according to

$$\boldsymbol{\chi}_{\mathrm{l}} = K_{\mathrm{l}}\,\boldsymbol{\varepsilon}_{\mathrm{p}}, \qquad\qquad \boldsymbol{\chi} = \boldsymbol{\chi}_{\mathrm{l}} + \sum_{i=1}^{M} \boldsymbol{\chi}^{(i)}. \tag{3.17}$$

Evaluating the GSM relations (3.1) for the specific choice of the free energy density in (3.14) and (3.15), the generalized Hooke's law (3.9) is recovered and

$$\boldsymbol{\sigma}_{\mathbf{P}} = \boldsymbol{\sigma} - \boldsymbol{\chi}_{\mathrm{l}}, \qquad\qquad \boldsymbol{\chi}^{(i)} = \frac{2}{3}K^{(i)}\boldsymbol{\alpha}^{(i)} \qquad (i = 1, \ldots, M), \tag{3.18}$$

as well as either

$$-r = Hq \qquad \text{or} \qquad -r = H_\infty q + \sigma_\Delta \left(1 - \exp\left(-\frac{H_0 - H_\infty}{\sigma_\Delta}q\right)\right) \tag{3.19}$$

are obtained, depending on the choice of the isotropic hardening potential.

Von Mises yield criterion.   The von Mises yield criterion postulates the existence of
a yield surface which is implicitly defined by

$$\varphi(\boldsymbol{\mathcal{F}}) = 0, \tag{3.20}$$

where the yield surface function (also: threshold function) has the form[5]

$$\varphi(\boldsymbol{\mathcal{F}}) = \sqrt{\frac{3}{2}} \left\| \boldsymbol{\sigma}' - \boldsymbol{\chi} \right\|_2 - \sigma_{\mathrm{y}}(\boldsymbol{\mathcal{F}}) = \sqrt{\frac{3}{2}} \left\| \boldsymbol{\sigma}'_{\mathrm{p}} - \sum_{i=1}^{M} \boldsymbol{\chi}^{(i)} \right\|_2 - \sigma_{\mathrm{y}}(\boldsymbol{\mathcal{F}}). \tag{3.21}$$

Following Gourgues & Andrieu [2003] and Besson et al. [2009], the current yield
stress σ_{y} is assumed to be of the general non-classical form

$$\sigma_{\mathrm{y}}(\boldsymbol{\mathcal{F}}) = \sigma_{\mathrm{y}}^0 - r - \frac{Q}{2}r^2 - \frac{3}{4}\sum_{i=1}^{M} \frac{D^{(i)}}{K^{(i)}} \boldsymbol{\chi}^{(i)} : \mathbb{P}_2^{\mathrm{iso}} : \boldsymbol{\chi}^{(i)}. \tag{3.22}$$

Here, $\sigma_{\mathrm{y}}^0 > 0$ represents the initial yield stress, and the coefficients Q and $D^{(1)}, \ldots, D^{(M)}$
of the non-classical quadratic terms in (3.22) are assumed to be non-negative. The
quadratic terms involving internal stresses $\boldsymbol{\chi}^{(i)}$ allow for evolution laws in accordance
with the classical approach of Armstrong & Frederick [1966], which are otherwise not
possible in the GSM framework. On the other hand, the quadratic term controlled by
the parameter Q allows for a description of saturating isotropic hardening even if the
quadratic hardening potential (3.11), otherwise associated with linear isotropic hard-
ening, is incorporated in the Helmholtz free energy density. Thus, while technically
possible, it appears unreasonable to choose the non-quadratic hardening potential (3.12)
when Q is chosen to be strictly positive. Clearly, when Q is set to zero and nonlinear
kinematic hardening is disregarded (i.e., $M = 0$), then the classical formulation

$$\varphi(\boldsymbol{\mathcal{F}}) = \sqrt{\frac{3}{2}} \left\| \boldsymbol{\sigma}'_{\mathrm{p}} \right\|_2 - \sigma_{\mathrm{y}}(r) \qquad \text{with } \sigma_{\mathrm{y}}(r) = \sigma_{\mathrm{y}}^0 - r \tag{3.23}$$

is obtained. For later use, the gradients of the (general) yield function are listed

$$\frac{\partial\varphi}{\partial\boldsymbol{\sigma}_{\mathbf{P}}} = \sqrt{\frac{3}{2}} \frac{\boldsymbol{\sigma}' - \boldsymbol{\chi}}{\left\| \boldsymbol{\sigma}' - \boldsymbol{\chi} \right\|_2}, \tag{3.24}$$

$$-\frac{\partial\varphi}{\partial\boldsymbol{\chi}^{(i)}} = \frac{\partial\varphi}{\partial\boldsymbol{\sigma}_{\mathbf{P}}} - \frac{3D^{(i)}}{2K^{(i)}} \boldsymbol{\chi}^{(i)} \qquad (i = 1, \ldots, M), \tag{3.25}$$

$$\frac{\partial\varphi}{\partial r} = 1 + Qr. \tag{3.26}$$

---

[5]Here and hereafter, the deviatoric part of a second order tensor is denoted using the prime symbol
according to (A.18) in Appendix A.1.

Rate-independent plasticity and Perzyna-type viscoplasticity. For rate-independent plasticity, the dual dissipation potential has the form [cf. Fritzen, 2011]

$$\phi^*(\boldsymbol{\mathcal{F}}) = \begin{cases} 0, & \varphi(\boldsymbol{\mathcal{F}}) \leq 0; \\ \infty, & \text{otherwise,} \end{cases} \tag{3.27}$$

and the rates of internal variables are expressed in terms of a Lagrange multiplier $\dot{\lambda}_{\mathrm{p}} \geq 0$, also known as *plastic multiplier*, by

$$\dot{\boldsymbol{\mathcal{I}}} = \dot{\lambda}_{\mathrm{p}} \frac{\partial \varphi(\boldsymbol{\mathcal{F}})}{\partial \boldsymbol{\mathcal{F}}}. \tag{3.28}$$

On the other hand, the dual dissipation potential[6]

$$\phi^*(\boldsymbol{\mathcal{F}}) = \sqrt{\frac{2}{3}} \frac{\dot{\varepsilon}_0 \, \sigma_{\mathrm{d}}}{m+1} \left(\frac{\langle \varphi(\boldsymbol{\mathcal{F}}) \rangle_+}{\sigma_{\mathrm{d}}} \right)^{m+1}, \tag{3.29}$$

with the reference rate $\dot{\varepsilon}_0 > 0$, the drag stress $\sigma_{\mathrm{d}} > 0$, and the viscosity exponent $m \geq 1$ describes Perzyna-type viscoplasticity [Perzyna, 1963, 1966]. It is worth mentioning that several models with non-constant drag stresses are found in the literature [e.g., Chaboche & Jung, 1997, Chaboche, 2008], but σ_{d} will be considered as a constant parameter within this work. The evolution of the internal state variables is then described by

$$\dot{\boldsymbol{\mathcal{I}}} = \dot{\lambda}_{\mathrm{v}} \frac{\partial \varphi(\boldsymbol{\mathcal{F}})}{\partial \boldsymbol{\mathcal{F}}} \qquad \text{with} \quad \dot{\lambda}_{\mathrm{v}} = \sqrt{\frac{2}{3}} \dot{\varepsilon}_0 \left(\frac{\langle \varphi(\boldsymbol{\mathcal{F}}) \rangle_+}{\sigma_{\mathrm{d}}} \right)^m \geq 0, \tag{3.30}$$

where $\dot{\lambda}_{\mathrm{v}}$ can be understood as a viscoplastic multiplier. Obviously, the evolution laws for rate-independent plasticity and for Perzyna-type viscoplasticity are structurally similar and can be written

$$\dot{\boldsymbol{\varepsilon}}_{\mathrm{p}} = \dot{\lambda} \sqrt{\frac{3}{2}} \frac{\boldsymbol{\sigma}' - \boldsymbol{\chi}}{\|\boldsymbol{\sigma}' - \boldsymbol{\chi}\|_2}, \tag{3.31}$$

$$\dot{\boldsymbol{\alpha}}^{(i)} = \dot{\boldsymbol{\varepsilon}}_{\mathrm{p}} - \dot{\lambda} D^{(i)} \boldsymbol{\alpha}^{(i)} \qquad (i = 1, \ldots, M), \tag{3.32}$$

$$\dot{q} = \dot{\lambda} \left(1 + Qr \right). \tag{3.33}$$

Here, $\dot{\lambda}$ is either the plastic multiplier $\dot{\lambda}_{\mathrm{p}}$ or the viscoplastic multiplier $\dot{\lambda}_{\mathrm{v}}$, and

$$\lambda = \int_{t_0}^{t} \dot{\lambda} \, \mathrm{d}\tilde{t} = \sqrt{\frac{2}{3}} \int_{t_0}^{t} \|\dot{\boldsymbol{\varepsilon}}_{\mathrm{p}}\|_2 \, \mathrm{d}\tilde{t} \tag{3.34}$$

is the *accumulated plastic strain* which coincides with the isotropic hardening variable q under the classical assumption $Q = 0$. When the quadratic hardening potential (3.11) is chosen, (3.33) can be reformulated as

$$\dot{r} = -\dot{\lambda} H \left(1 + Qr \right), \tag{3.35}$$

---

[6]Here, $\langle \bullet \rangle_+$ denotes Macauley brackets (cf. Appendix A.5).

and if, in addition, the parameter Q is strictly positive, integration of the previous equation yields the explicit formula [cf. Besson et al., 2009]

$$r = \frac{1}{Q} \left(\exp\left(-QH\lambda\right) - 1 \right). \tag{3.36}$$

By insertion of this result into the definition of the yield stress (3.22) it is found that a quadratic isotropic hardening potential with hardening modulus H combined with a coefficient $Q > 0$ is equivalent to a special case of saturating Voce-type hardening with $H_\infty = 0$, $H_0 = H$, and $\sigma_\Delta = 1/(2Q)$. Combining (3.32) with (3.18), the rates of the internal stresses related to nonlinear kinematic hardening are obtained as

$$\dot{\boldsymbol{\chi}}^{(i)} = \frac{2}{3} K^{(i)} \dot{\boldsymbol{\varepsilon}}_\mathrm{p} - \dot{\lambda} D^{(i)} \boldsymbol{\chi}^{(i)} \qquad (i = 1, \ldots, M), \tag{3.37}$$

i.e., they are given by Armstrong–Frederick-type evolution laws [cf. Frederick & Armstrong, 2007]. Note that the rate-independent model is obtained as a limit case of the Perzyna-type viscoplastic model when the drag stress tends towards zero or when the viscosity exponent tends towards infinity [cf. Chaboche, 2008].

Norton-type viscoplasticity. In the absence of nonlinear kinematic hardening and under the additional assumption $Q = 0$ with regard to isotropic hardening, the von Mises yield criterion has the classical form expressed through (3.20) and (3.23) and can be rewritten

$$\sqrt{\frac{3}{2}} \frac{\left\| \boldsymbol{\sigma}'_\mathrm{p} \right\|_2}{\sigma_\mathrm{y}^0 - r} = 1. \tag{3.38}$$

This relation is the basis for the formulation of Norton-type viscoplasticity, which is defined via the dual dissipation potential [e.g., Fritzen et al., 2014]

$$\phi^*(\boldsymbol{\mathcal{F}}) = \sqrt{\frac{2}{3}} \frac{\dot{\varepsilon}_0}{m+1} \left(\sigma_\mathrm{y}^0 - r\right) \left(\sqrt{\frac{3}{2}} \frac{\left\| \boldsymbol{\sigma}'_\mathrm{p} \right\|_2}{\sigma_\mathrm{y}^0 - r} \right)^{m+1}. \tag{3.39}$$

By application of the general explicit evolution law (3.5), the rates of the internal variables are obtained as

$$\dot{\boldsymbol{\varepsilon}}_\mathrm{p} = \dot{\varepsilon}_0 \left(\sqrt{\frac{3}{2}} \frac{\left\| \boldsymbol{\sigma}'_\mathrm{p} \right\|_2}{\sigma_\mathrm{y}^0 - r} \right)^{m} \frac{\boldsymbol{\sigma}'_\mathrm{p}}{\left\| \boldsymbol{\sigma}'_\mathrm{p} \right\|_2}, \quad \dot{q} = \sqrt{\frac{2}{3}} \frac{\dot{\varepsilon}_0\, m}{m+1} \left(\sqrt{\frac{3}{2}} \frac{\left\| \boldsymbol{\sigma}'_\mathrm{p} \right\|_2}{\sigma_\mathrm{y}^0 - r} \right)^{m+1}. \tag{3.40}$$

In contrast to rate-independent plasticity and Perzyna-type viscoplasticity, Norton-type viscoplasticity has no elastic range in a strict sense. However, rate-independent behavior can be approximated by taking large values for the viscosity exponent m, and a domain where the material behaves almost elastically exists then. On the other hand, when the smallest admissible exponent $m = 1$ is chosen and when the yield stress is assumed to be constant (as for ideal plasticity), a special case of viscoelasticity is obtained (cf. Section 3.3.2). It should be noted that a Norton-type model has a more pronounced rate-

dependence and is numerically easier to handle than the corresponding Perzyna-type model with the same viscosity exponent.

3.3.2 Linear viscoelasticity

A well-known rather general formulation of linear viscoelasticity is the *generalized Maxwell model* or *Maxwell–Wiechert model*, which is rheologically represented by a parallel assembly of one elastic spring and $M \in \mathbb{N}_{>0}$ Maxwell elements [cf. Wiechert, 1893]. The special case $M = 1$ is widely known as the *standard linear solid* (SLS) model. With the viscous strains $\boldsymbol{\varepsilon}_{\mathrm{v}}^{(1)}, \ldots, \boldsymbol{\varepsilon}_{\mathrm{v}}^{(M)}$ as internal variables, the Helmholtz free energy density reads

$$\psi\left(\boldsymbol{\varepsilon}, \boldsymbol{\varepsilon}_{\mathrm{v}}^{(1)}, \ldots, \boldsymbol{\varepsilon}_{\mathrm{v}}^{(M)}\right) = \frac{1}{2}\boldsymbol{\varepsilon} : \mathbb{C} : \boldsymbol{\varepsilon} + \sum_{i=1}^{M} G^{(i)}\left(\boldsymbol{\varepsilon} - \boldsymbol{\varepsilon}_{\mathrm{v}}^{(i)}\right) : \mathbb{P}_2^{\mathrm{iso}} : \left(\boldsymbol{\varepsilon} - \boldsymbol{\varepsilon}_{\mathrm{v}}^{(i)}\right), \tag{3.41}$$

where $\mathbb{C}$ denotes a constant stiffness tensor and $G^{(1)}, \ldots, G^{(M)}$ are the shear moduli of the Maxwell elements. The viscosity of the ith Maxwell element is expressed by $\mu^{(i)} > 0$, and the thermodynamic force conjugate to the viscous strain $\boldsymbol{\varepsilon}_{\mathrm{v}}^{(i)}$ is the viscous stress $\boldsymbol{\sigma}_{\mathrm{v}}^{(i)}$. Both the primal and the dual dissipation potential can be written in closed forms according to

$$\phi\left(\dot{\boldsymbol{\varepsilon}}_{\mathrm{v}}^{(1)}, \ldots, \dot{\boldsymbol{\varepsilon}}_{\mathrm{v}}^{(M)}\right) = \frac{1}{2}\sum_{i=1}^{M} \mu^{(i)} \dot{\boldsymbol{\varepsilon}}_{\mathrm{v}}^{(i)} : \mathbb{P}_2^{\mathrm{iso}} : \dot{\boldsymbol{\varepsilon}}_{\mathrm{v}}^{(i)}, \tag{3.42}$$

$$\phi^*\left(\boldsymbol{\sigma}_{\mathrm{v}}^{(1)}, \ldots, \boldsymbol{\sigma}_{\mathrm{v}}^{(M)}\right) = \frac{1}{2}\sum_{i=1}^{M} \frac{1}{\mu^{(i)}} \boldsymbol{\sigma}_{\mathrm{v}}^{(i)} : \mathbb{P}_2^{\mathrm{iso}} : \boldsymbol{\sigma}_{\mathrm{v}}^{(i)}. \tag{3.43}$$

From a mathematical perspective, an important property of such viscoelastic laws is that the dissipation potentials ϕ and ϕ^* as well as the Helmholtz free energy density ψ are quadratic.

3.4 Solution schemes for strain-driven processes

A process is called *strain-driven* if the loading is specified in terms of a given strain path $\boldsymbol{\varepsilon}(t)$ parameterized by time $t \in \mathbb{T}$, where $\mathbb{T} = [t_0, T]$ is the considered time interval. The evolution of internal variables is an initial value problem defined by some system of ordinary differential equations (ODEs) and by the initial condition $\boldsymbol{\mathcal{I}}(t_0) = \mathbf{0}$. Three possible kinds of systems of ODEs are presented, which are described in terms of the functions

$$\boldsymbol{f}(t, \boldsymbol{\mathcal{I}}) = -\partial_{\boldsymbol{\mathcal{I}}}\psi(\boldsymbol{\varepsilon}(t), \boldsymbol{\mathcal{I}}), \qquad \boldsymbol{g}(\dot{\boldsymbol{\mathcal{I}}}) = \partial_{\dot{\boldsymbol{\mathcal{I}}}}\phi(\dot{\boldsymbol{\mathcal{I}}}), \qquad \boldsymbol{h}(\boldsymbol{\mathcal{F}}) = \partial_{\boldsymbol{\mathcal{F}}}\phi^*(\boldsymbol{\mathcal{F}}). \tag{3.44}$$

Firstly, the implicit Biot-type equation (3.3) is recovered with

$$\boldsymbol{g}(\dot{\boldsymbol{\mathcal{I}}}) - \boldsymbol{f}(t, \boldsymbol{\mathcal{I}}) = \boldsymbol{0}. \tag{3.45}$$

Secondly, the explicit formulation (3.5) based on the dual instead of the primal dissipation potential is rewritten

$$\dot{\boldsymbol{\mathcal{I}}} = \boldsymbol{h}(\boldsymbol{f}(t, \boldsymbol{\mathcal{I}})) = (\boldsymbol{h} \circ \boldsymbol{f})(t, \boldsymbol{\mathcal{I}}). \tag{3.46}$$

Thirdly, in order to circumvent the function composition in the previous equation, on can replace (3.46) by

$$\dot{\boldsymbol{\mathcal{I}}} = \boldsymbol{h}(\boldsymbol{\mathcal{F}}), \qquad\qquad \boldsymbol{\mathcal{F}} = \boldsymbol{f}(t, \boldsymbol{\mathcal{I}}), \tag{3.47}$$

where $\boldsymbol{\mathcal{F}}$ has to be understood as a generalized vector of slack variables which are independent of $\boldsymbol{\mathcal{I}}$.

These initial value problems are generally solved by numerical methods which require a temporal discretization. The time interval $\mathbb{T}$ is discretized into $N \in \mathbb{N}_{>0}$ time steps by introducing intermediate times $t_1, \ldots, t_{N-1}$ such that

$$t_{n-1} < t_n < t_{n+1} \qquad (n \in \{1, \ldots, N-1\}) \qquad \text{with } t_N = T. \tag{3.48}$$

Hereafter, $n \in \{0, \ldots, N-1\}$ specifies the time step under consideration beginning at t_n and ending at t_{n+1}, where t_{n+1} is understood as the current time. For any time step and for a quantity denoted $\boldsymbol{a}$, the abbreviations $\Delta t = t_{n+1} - t_n$ and

$$\boldsymbol{a}_n = \boldsymbol{a}(t_n), \qquad \boldsymbol{a}_{n+1} = \boldsymbol{a}(t_{n+1}), \qquad \Delta \boldsymbol{a} = \boldsymbol{a}(t_{n+1}) - \boldsymbol{a}(t_n) \tag{3.49}$$

are introduced. All involved quantities are given at the beginning of the considered time step, while at the current time t_{n+1} only $\boldsymbol{\varepsilon}_{n+1}$ is known due to the prescribed loading. Linear temporal interpolation is adopted for the strain and the internal variables, i.e., the rates $\dot{\boldsymbol{\varepsilon}}$ and $\dot{\boldsymbol{\mathcal{I}}}$ are assumed to be constant within every time step according to

$$\dot{\boldsymbol{\varepsilon}}(t) = \frac{\Delta \boldsymbol{\varepsilon}}{\Delta t}, \qquad\qquad \dot{\boldsymbol{\mathcal{I}}}(t) = \frac{\Delta \boldsymbol{\mathcal{I}}}{\Delta t} \qquad\qquad \text{for } t \in (t_n, t_{n+1}). \tag{3.50}$$

With regard to numerical solution schemes, attention is limited to Runge–Kutta methods, which are distinguished by the way in which the function $\boldsymbol{f}$ is evaluated in (3.45)–(3.47). Three well-known examples are:

[RK1] the explicit Euler method with $\boldsymbol{f}(t, \boldsymbol{\mathcal{I}}) = \boldsymbol{f}(t_n, \boldsymbol{\mathcal{I}}_n)$,

[RK2] the implicit backward Euler method with $\boldsymbol{f}(t, \boldsymbol{\mathcal{I}}) = \boldsymbol{f}(t_{n+1}, \boldsymbol{\mathcal{I}}_{n+1})$, and

[RK3] the implicit midpoint method with $\boldsymbol{f}(t, \boldsymbol{\mathcal{I}}) = \boldsymbol{f}\left(\frac{1}{2}(t_n + t_{n+1}), \frac{1}{2}(\boldsymbol{\mathcal{I}}_n + \boldsymbol{\mathcal{I}}_{n+1})\right)$.

The backward Euler method is the standard implicit solution scheme for viscoplastic materials and is used for most applications in this work. However, it is noted that the implicit midpoint method is sometimes more efficient if the viscosity exponent m is small, or for viscoelastic models.

3.5 Variational formulation for inelastic time steps

For notational brevity, the index "$n + 1$" characterizing the current value of a quantity at time t_{n+1} according to (3.49) is dropped hereafter (except for t_{n+1} itself). Following Comi & Perego [1995] and Miehe [2002], the generalized incremental work

$$\Pi\big(\boldsymbol{\varepsilon}, \underset{\sim}{\boldsymbol{\mathcal{I}}}\big) = \int_{t_n}^{t_{n+1}} \Big(\dot{\psi}\big(\boldsymbol{\varepsilon}(t), \boldsymbol{\mathcal{I}}(t)\big) + \phi\big(\dot{\boldsymbol{\mathcal{I}}}(t)\big) \Big) \, \mathrm{d}t \tag{3.51}$$

$$= \psi(\boldsymbol{\varepsilon}, \boldsymbol{\mathcal{I}}) - \psi(\boldsymbol{\varepsilon}_n, \boldsymbol{\mathcal{I}}_n) + \int_{t_n}^{t_{n+1}} \phi\big(\dot{\boldsymbol{\mathcal{I}}}(t)\big) \, \mathrm{d}t, \tag{3.52}$$

can be introduced for GSM models. The representation $\underset{\sim}{\boldsymbol{\mathcal{I}}}$ is used for the history of the internal variables in the considered time interval $[t_n, t_{n+1}] \subset \mathbb{T}$ and underlines the variational character of the following equation. Minimizing the generalized incremental work Π with respect to $\underset{\sim}{\boldsymbol{\mathcal{I}}}$, an incremental stress potential

$$w(\boldsymbol{\varepsilon}) = \inf_{\underset{\sim}{\boldsymbol{\mathcal{I}}}} \Pi\big(\boldsymbol{\varepsilon}, \underset{\sim}{\boldsymbol{\mathcal{I}}}\big) \tag{3.53}$$

is obtained, which can be considered a quasi-hyperelastic potential, and which defines the Cauchy stress at the end of the time step according to

$$\boldsymbol{\sigma} = \partial_{\boldsymbol{\varepsilon}} w(\boldsymbol{\varepsilon}). \tag{3.54}$$

The time-discrete setting requires a discretization of the history of the internal variables. For simplicity, the standard approach based on a continuous, piecewise linear discretization is adopted here, such that the rate of internal variables $\dot{\boldsymbol{\mathcal{I}}}$ is constant within every time increment as in (3.50). The generalized incremental work Π is then replaced by

$$\Pi(\boldsymbol{\varepsilon}, \boldsymbol{\mathcal{I}}) = \psi(\boldsymbol{\varepsilon}, \boldsymbol{\mathcal{I}}) - \psi(\boldsymbol{\varepsilon}_n, \boldsymbol{\mathcal{I}}_n) + \Delta t \, \phi(\dot{\boldsymbol{\mathcal{I}}}), \tag{3.55}$$

and the corresponding incremental stress potential reads

$$W(\boldsymbol{\varepsilon}) = \inf_{\Delta \boldsymbol{\mathcal{I}}} \Pi(\boldsymbol{\varepsilon}, \boldsymbol{\mathcal{I}}). \tag{3.56}$$

The variational minimization problem described by the previous two equations (3.55) and (3.56) corresponds to a formulation of Ortiz & Stainier [1999]. This formulation based on the primal dissipation potential ϕ is subsequently replaced by a mixed primal–dual formulation [cf. Miehe, 2011, 2014] which is useful when the dual dissipation potential ϕ^* is known in closed form, while the primal potential ϕ is not. To that end, the mixed incremental potential

$$\Pi^*(\boldsymbol{\varepsilon}, \boldsymbol{\mathcal{I}}, \boldsymbol{\mathcal{F}}) = \psi(\boldsymbol{\varepsilon}, \boldsymbol{\mathcal{I}}) - \psi(\boldsymbol{\varepsilon}_n, \boldsymbol{\mathcal{I}}_n) + \Delta \boldsymbol{\mathcal{I}} \cdot \boldsymbol{\mathcal{F}} - \Delta t \, \phi^*\big(\boldsymbol{\mathcal{F}}\big) \tag{3.57}$$

is introduced, which, making use of the Legendre–Fenchel transform (3.6), allows to write

$$\Pi(\boldsymbol{\varepsilon}, \boldsymbol{\mathcal{I}}) = \sup_{\boldsymbol{\mathcal{F}}} \Pi^*(\boldsymbol{\varepsilon}, \boldsymbol{\mathcal{I}}, \boldsymbol{\mathcal{F}}). \tag{3.58}$$

Consequently, the minimization problem (3.56) can be replaced by the saddle-point problem

$$W(\varepsilon) = \inf_{\Delta \mathcal{I}} \sup_{\mathcal{F}} \Pi^*(\varepsilon, \mathcal{I}, \mathcal{F}), \tag{3.59}$$

which yields the stationarity conditions

$$\delta_{\mathcal{I}} \Pi^* = \delta \mathcal{I} \cdot (\mathcal{F} + \partial_{\mathcal{I}} \psi(\varepsilon, \mathcal{I})) \overset{!}{=} 0, \tag{3.60}$$

$$\delta_{\mathcal{F}} \Pi^* = \delta \mathcal{F} \cdot (\Delta \mathcal{I} - \Delta t \, \partial_{\mathcal{F}} \phi^*(\mathcal{F})) \overset{!}{=} 0. \tag{3.61}$$

By arguing that the variations $\delta \mathcal{I}$ and $\delta \mathcal{F}$ are arbitrary, one arrives at two necessary conditions which are equivalent to a backward Euler version of the slack variable formulation (3.47). Note that this equivalence is subject to the requirement of piecewise constant rates of internal variables (3.50).

3.6   Algorithmic treatment

Aspects regarding the implementation of constitutive subroutines for GSM models are given in the matrix–vector notation declared in Appendix A.2. Implicit time integration schemes generally require iterative numerical solution procedures (the radial return scheme for von Mises plasticity with linear isotropic hardening is an exception, cf. Appendix B.1). The standard procedure to attain the stationarity conditions (3.60) and (3.61) is to find a root of the residual function

$$\underline{f}(\Delta \mathcal{I}, \mathcal{F}) = \begin{bmatrix} \underline{\mathcal{F}} + \underline{\partial_{\mathcal{I}} \psi}(\varepsilon, \mathcal{I}) \\ \underline{\Delta \mathcal{I}} - \Delta t \, \underline{\partial_{\mathcal{F}} \phi^*}(\mathcal{F}) \end{bmatrix} \tag{3.62}$$

with the Newton–Raphson method, which involves repeated evaluations of the Jacobian

$$\underline{\underline{J}}(\Delta \mathcal{I}, \mathcal{F}) = \begin{bmatrix} \underline{\underline{\partial_{\mathcal{I}}^2 \psi}}(\varepsilon, \mathcal{I}) & \underline{\underline{I}} \\ \underline{\underline{I}} & -\Delta t \, \underline{\underline{\partial_{\mathcal{F}}^2 \phi^*}}(\mathcal{F}) \end{bmatrix}. \tag{3.63}$$

In the context of finite element simulations it is sometimes necessary to provide the *algorithmic tangent operator*, also known as *algorithmic stiffness*, which is defined as the total derivative of the Cauchy stress with respect to strain

$$\underline{\underline{C}}^{\mathrm{a}} = \frac{\mathrm{d}\underline{\sigma}}{\mathrm{d}\underline{\varepsilon}} = \frac{\partial^2 \psi}{\partial \underline{\varepsilon}^2} + \frac{\partial^2 \psi}{\partial \underline{\varepsilon} \, \partial \underline{\mathcal{I}}} \frac{\partial \underline{\mathcal{I}}}{\partial \underline{\varepsilon}}. \tag{3.64}$$

In order to find the partial derivatives of the internal variables with respect to strain $\partial \underline{\mathcal{I}}/\partial \underline{\varepsilon}$, one exploits the fact that the total derivative of the residual $\underline{f}$ with respect to strain must vanish. From the linearization

$$\frac{\mathrm{d}\underline{f}}{\mathrm{d}\underline{\varepsilon}} = \frac{\partial \underline{f}}{\partial \underline{\varepsilon}} + \frac{\partial \underline{f}}{\partial \underline{\mathcal{I}}}\frac{\partial \underline{\mathcal{I}}}{\partial \underline{\varepsilon}} + \frac{\partial \underline{f}}{\partial \underline{\mathcal{F}}}\frac{\partial \underline{\mathcal{F}}}{\partial \underline{\varepsilon}} = \begin{bmatrix} \underline{\partial^2_{\mathcal{I}\varepsilon}\psi} \\ \underline{0} \end{bmatrix} + \underline{\underline{J}}\,\frac{\partial}{\partial \underline{\varepsilon}}\begin{bmatrix} \underline{\mathcal{I}} \\ \underline{\mathcal{F}} \end{bmatrix} \overset{!}{=} 0 \tag{3.65}$$

it follows that $\partial \underline{\mathcal{I}}/\partial \underline{\varepsilon}$ can be found by solving a system of linear equations with the matrix of coefficients $\underline{\underline{J}}$. Straightforward calculations lead to the representation

$$\underline{\underline{C}}^{\mathrm{a}} = \frac{\partial^2 \psi}{\partial \underline{\varepsilon}^2} - \Delta t\,\frac{\partial^2 \psi}{\partial \underline{\varepsilon}\,\partial \underline{\mathcal{I}}}\left(\left(\frac{\partial^2 \phi^*}{\partial \underline{\mathcal{F}}^2}\right)^{-1} + \Delta t\,\frac{\partial^2 \psi}{\partial \underline{\mathcal{I}}^2}\right)^{-1}\left(\frac{\partial^2 \psi}{\partial \underline{\varepsilon}\,\partial \underline{\mathcal{I}}}\right)^{\mathsf{T}}, \tag{3.66}$$

which shows that the algorithmic tangent operator is unconditionally symmetric for any rate-dependent GSM model. Such symmetry is not guaranteed for arbitrary material models, but it is of practical importance. While the GSM framework naturally imposes restrictions on the modeling of material behavior, it has favorable theoretical properties as well as benefits with regard to numerical implementation. Aside from the just mentioned symmetry of the algorithmic stiffness, another practical advantage is that one implementation of the described Newton–Raphson scheme can be used for all GSM models and it is only necessary to provide the first and second order gradients of the respective potentials via exchangeable subroutines.

Improving the robustness of the Newton–Raphson scheme. For challenging applications, robustness of the material subroutines is crucial, but naive implementations of the Newton–Raphson scheme fail to converge quite often. Some counter-measures which have been employed for numerical examples in this work are presented in the following. First of all, error handling should involve a sub-stepping scheme, e.g., prescribed time increments that could not be solved at once can be recursively subdivided into smaller increments where convergence can be achieved. Sub-stepping generally leads to inconsistent algorithmic tangent operators. If necessary, the final result of a sub-stepping procedure can be used for an initial guess of a subsequent single-step scheme, which then yields the consistent algorithmic stiffness. A more standard predictor–corrector method also divides the desired increment into sub-steps and computes an initial guess by an explicit scheme such as the explicit Euler method. Alternatively, for some moderately complex models, it is possible to construct model-specific initial guess routines based on physical understanding of the material response.

Power-law relaxation for Perzyna-type viscoplasticity. For Perzyna-type viscoplasticity as presented in Section 3.3.1, the residual function $\underline{f}$ from (3.62) involves the gradient

$$
\frac{\partial \phi^*}{\partial \underline{\mathcal{F}}} = \sqrt{\frac{2}{3}} \dot{\varepsilon}_0 \left(\frac{\langle \varphi(\underline{\mathcal{F}}) \rangle_+}{\sigma_{\mathrm{d}}} \right)^m \frac{\partial \varphi(\underline{\mathcal{F}})}{\partial \underline{\mathcal{F}}}
\tag{3.67}
$$

of the dual dissipation potential ϕ^* from (3.29). When the viscosity exponent m is high (corresponding to weak rate-sensitivity), the standard Newton–Raphson scheme is prone to failure. In order to make the solution scheme more robust, one possible approach is to replace the system of residual functions $\underline{f}$ by an equivalent one (in the sense that it has the same root) which contains power-laws with lower exponents only. For this purpose, the original exponentiation is distributed to $L \in \mathbb{N}_{>0}$ levels with the exponent

$$
p = \sqrt[L]{m}.
\tag{3.68}
$$

Scalar slack variables are introduced for each level and are comprised in the vector $\underline{\omega} \in \mathbb{R}_{\geq 0}^L$. An additional scalar slack variable $\omega_0 \in \mathbb{R}_{\geq 0}$ is introduced, which coincides with the base of the original exponentiation at the solution point. The extended system of residual functions has $L + 1$ additional rows and is given by

$$
\underline{f}_{\mathrm{e}}\big(\Delta \underline{\mathcal{I}}, \underline{\mathcal{F}}, \omega_0, \underline{\omega}\big) =
\begin{bmatrix}
\underline{\mathcal{F}} + \underline{\partial_{\underline{\mathcal{I}}} \psi}\big(\varepsilon, \underline{\mathcal{I}}\big) \\
\Delta \underline{\mathcal{I}} - \sqrt{\frac{2}{3}} \Delta t\, \dot{\varepsilon}_0\, \omega_L\, \partial_{\underline{\mathcal{F}}} \varphi\big(\underline{\mathcal{F}}\big) \\
\sigma_{\mathrm{d}}\, \omega_0 - \langle \varphi(\underline{\mathcal{F}}) \rangle_+ \\
\omega_1 - \omega_0^p \\
\vdots \\
\omega_L - \omega_{L-1}^p
\end{bmatrix}
\begin{array}{l}
\\ \\
/\!/\, 0 \\
/\!/\, 1 \\
/\!/\, \vdots \\
/\!/\, L
\end{array} .
\tag{3.69}
$$

In contrast to the standard approach, the associated Jacobian[7]

$$
\underline{J}_{\mathrm{e}}\big(\Delta \underline{\mathcal{I}}, \underline{\mathcal{F}}, \omega_0, \underline{\omega}\big) =
\tag{3.70}
$$

$$
\begin{bmatrix}
\underline{\underline{\partial_{\underline{\mathcal{I}}}^2 \psi}} & \underline{\underline{I}} & \underline{0} & \underline{0} & \cdots & \underline{0} & \underline{0} \\
\underline{\underline{I}} & -\sqrt{\frac{2}{3}} \Delta t\, \dot{\varepsilon}_0\, \omega_L\, \partial_{\underline{\mathcal{F}}}^2 \varphi & \underline{0} & \underline{0} & \cdots & \underline{0} & \underline{0} \\
\underline{0}^{\mathsf{T}} & -\Theta(\varphi)\big(\partial_{\underline{\mathcal{F}}} \varphi\big)^{\mathsf{T}} & \sigma_{\mathrm{d}} & 0 & \cdots & 0 & 0 \\
\underline{0}^{\mathsf{T}} & \underline{0}^{\mathsf{T}} & -p\, \omega_0^{p-1} & 1 & & 0 & 0 \\
\vdots & \vdots & & \ddots & \ddots & & \vdots \\
\underline{0}^{\mathsf{T}} & \underline{0}^{\mathsf{T}} & 0 & & -p\, \omega_{L-2}^{p-1} & 1 & 0 \\
\underline{0}^{\mathsf{T}} & \underline{0}^{\mathsf{T}} & 0 & \cdots & 0 & -p\, \omega_{L-1}^{p-1} & 1
\end{bmatrix}
\begin{array}{l}
\\ \\
/\!/\, 0 \\
/\!/\, 1 \\
/\!/\, \vdots \\
/\!/\, L\!-\!1 \\
/\!/\, L
\end{array}
$$

---

[7]In (3.70), Θ denotes the Heaviside step function (cf. Appendix A.5).
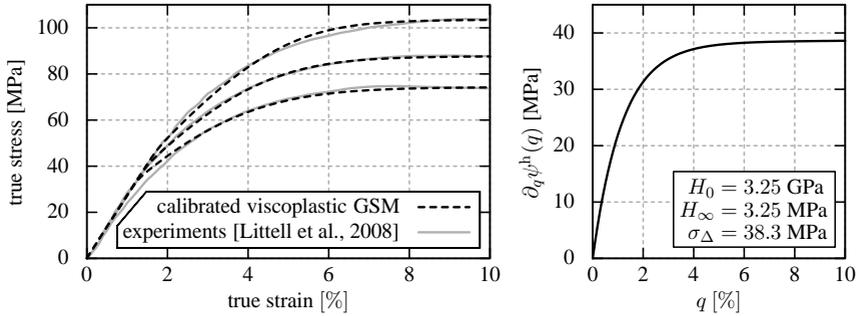
Figure 3.2: *Left:* experimental results of tensile tests on epoxy resin conducted by Littell et al. [2008] at the strain rates 10^{-5} s^{-1}, 10^{-3} s^{-1}, and 10^{-1} s^{-1} along with corresponding stress–strain curves of a viscoplastic GSM from Leuschner & Fritzen [2017] calibrated to these experimental data. *Right:* Voce-type isotropic hardening behavior of the calibrated viscoplastic GSM.

is not symmetric, but it can be used to compute the algorithmic tangent operator in a similar fashion as before.

3.7 Numerical examples

3.7.1 Modeling of epoxy resin with Voce-type isotropic hardening

In this Section, a viscoplastic model of epoxy resin is presented which has been previously employed in Leuschner & Fritzen [2017] for the modeling of a unidirectional fiber-reinforced composite material. The model has been calibrated to experimental results from tensile tests conducted by Littell et al. [2008] at three different strain rates. Both the experimental and the calibrated stress–strain curves are displayed on the left-hand side of Figure 3.2. The experimental data were collected from Figure 12 in Littell et al. [2008] and have been converted from engineering stresses and strains to true stresses and strains. Also, multiple curves from repeated tests have been merged to averaged curves.

For the GSM model, Norton-type viscoplasticity according to (3.39) and Voce-type hardening as defined in (3.12) are assumed while kinematic hardening is not incorporated. The Young's modulus 2.73 GPa and the Poisson's ratio 0.41 are taken directly from Littell et al. [2008] as average values of the isotropic elastic constants specified there. The reference strain rate $\dot{\varepsilon}_0$ is set to the lowest strain rate of the considered experiments, which is 10^{-5} s^{-1}. Since saturating hardening behavior with a vanishing asymptotic hardening modulus is observed in the experiments, it is possible to directly determine the viscosity exponent m from the plateau stresses at saturation. For this it is exploited that $\dot{\varepsilon} = \dot{\varepsilon}_p$

holds and that the driving force r conjugate to the equivalent plastic strain q remains constant in the saturating regime. Based on the evolution law of the plastic strain (3.40), the viscosity exponent is then determined via

$$m = \log\left(\frac{\dot{\varepsilon}_1}{\dot{\varepsilon}_2}\right)\left(\log\left(\frac{\sigma_1}{\sigma_2}\right)\right)^{-1} \tag{3.71}$$

given two true strain rates $\dot{\varepsilon}_1$ and $\dot{\varepsilon}_2$ and the corresponding true stresses σ_1 and σ_2 at the saturated plateaus. With this approach, the value of the viscosity exponent is estimated as 27.8 from the experimental curves displayed in Figure 3.2. Clearly, the asymptotic hardening modulus H_∞ of the Voce hardening law vanishes for saturating hardening. However, in order to guarantee that the asymptotic value of the second gradient of the hardening potential ψ^h from (3.12) remains strictly positive, H_∞ is set to a small positive value by defining the fixed ratio of hardening moduli $H_0/H_\infty = 10^3$. Three independent model parameters remain which have to be adjusted: the initial hardening modulus H_0, the initial value of the yield stress σ_y^0, and the vertical offset σ_Δ (with respect to linear hardening with modulus H_∞). These have been determined in a semi-automated optimization scheme such that the deviations of the model predictions from the three experimental stress–strain curves were simultaneously minimized in a least squares sense. The model predictions were computed for a single material point with prescribed normal strain in the tensile direction, and the remaining strain components were iteratively determined such as to attain uniaxial stress states[8]. With this procedure, the initial value of the yield stress $\sigma_y^0 = 35.2\,\mathrm{MPa}$ was obtained as well as the hardening parameters specified on the right-hand side of Figure 3.2. Comparing the experimental and the fitted stress–strain curves on the left-hand side of the same Figure, it is found that the adjusted viscoplastic GSM model is very well suited to describe the observed saturating hardening behavior and, at the same time, the experimentally determined rate-dependency.

3.7.2 Modeling of epoxy resin with linear and nonlinear kinematic hardening combined with isotropic hardening

An epoxy resin with almost rate-independent behavior has been investigated by da Costa Mattos & Martins [2013] in a stress-controlled cyclic tensile test with amplitudes increasing from 1 MPa to 5 MPa engineering stress. The resultant relation between engineering stress and engineering strain [see da Costa Mattos & Martins, 2013, Figure 2] has been transferred to true stresses and true strains and is depicted in the two plots at the bottom of Figure 3.3. Like in Section 3.7.1, the result of the experiment is numerically imitated with a viscoplastic GSM at an idealized material point loaded with uniaxial stress. The Perzyna-type formulation (3.29) is used as a viscous regularization with parameters chosen such as to account for the fact that the mate-

---

[8]For simplicity, the prescribed true strain rate was approximated by the engineering strain rate of the experiments by Littell et al. [2008]. This approximation is admissible because the observed rate-dependency is rather weak.

rial is almost rate-independent. The viscosity exponent is set to $m = 30$, the reference rate $\dot{\varepsilon}_0 = 10^{-3}$ s^{-1} corresponds to the load rate in the experiment approximately, and the drag stress is $\sigma_d = 0.1$ MPa. From the experimental data, the initial yield stress can be estimated as approximately 0.2 MPa. Since the drag stress contributes to the effective yield stress for Perzyna-type viscoplasticity, the parameter σ_y^0 is set to 0.1 MPa. For the Young's modulus of the epoxy resin, the range 1.6 ± 0.3 GPa has been specified by da Costa Mattos & Martins [2013]. Here, the minimum value $E = 1.3$ GPa is adopted. From the one-dimensional study of da Costa Mattos & Martins [2013] the Poisson's ratio is not available, hence it is chosen freely as $\nu = 0.35$, which falls into the range of rather diverse values found in the literature. The experimental stress–strain curves in Figure 3.3 exhibit hysteresis loops which are clearly due to kinematic hardening of the material. Further, growth of the elastic domain, corresponding to isotropic hardening, is observed. Appropriate modeling of combined isotropic and kinematic hardening, including calibration of the related parameters, was systematically achieved as described below.

For different numbers of NLKH elements and different types of isotropic hardening laws, an unconstrained nonlinear optimization procedure using the MATLAB function `fminsearch` has been conducted to find hardening parameters which are—at least locally—optimal in some specific sense that remains to be particularized. In all cases, LKH was enabled. Like the experiment, the numerical imitation of the tensile test using the GSM model was conducted in a stress-driven manner, and the stress levels at all load reversals have been chosen exactly as detected from the experimental data. The deviation of the numerically computed stress–strain relation from the experimental reference is then described in terms of strains. It is useful for practical reasons to consider the accumulated true stress for the whole loading process (although there is no particular physical interpretation of this quantity), and the relationship of true strain versus accumulated true stress is shown at the top of Figure 3.3. Here, the vertical deviation of the numerical curve from the experimental reference represents the relevant information to be considered in the objective function for the optimization procedure. The mean of the squared vertical deviations evaluated at 20 sample points per (un-) loading step constitutes the foundation of the objective function. Taken by itself, this approach showed a tendency towards overestimation of the experimentally observed hysteresis. Therefore, a penalization of hysteresis mismatch has been added to the objective function. More precisely, for each hysteresis loop (see bottom of Figure 3.3), the difference between experimental and numerical horizontal opening has been computed at 20 sample points, and the mean of the squared differences equipped with a positive coefficient (here: 0.5) has been added to the above-mentioned error measure.

When applied to a GSM with Voce-type isotropic hardening as described by (3.12), the automated optimization procedure always yielded very small values of the asymptotic stiffness H_∞, corresponding to saturating isotropic hardening. This is in agreement with the eventual stabilization of hysteresis loops at amplitude 5 MPa reported by da Costa Mattos & Martins [2013], also called *shakedown*. A quadratic hardening potential according to (3.11) combined with a suitable coefficient Q in the non-classical
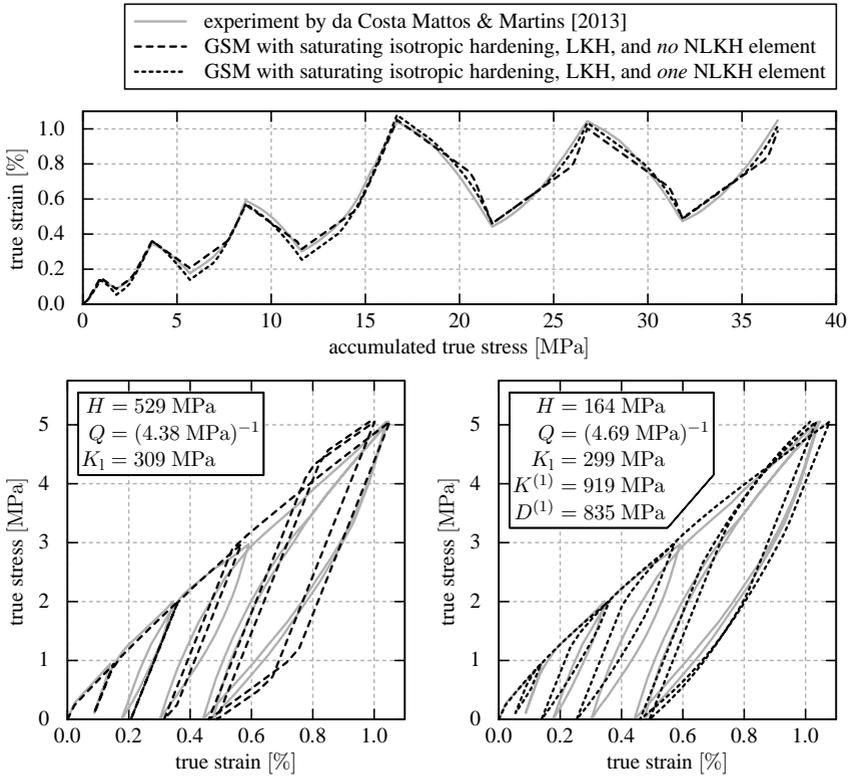
Figure 3.3: Cyclic tensile test for an almost rate-independent epoxy resin: comparison of experimental data from da Costa Mattos & Martins [2013] with numerical results for two GSMs calibrated thereto. *Top:* relationship of true strain versus true stress accumulated throughout the experiment; vertical deviations of the numerical curves from the experimental ones are considered in the error measure for the automated calibration of hardening parameters. *Bottom:* experimental stress–strain curves compared to numerical results obtained from a GSM with saturating isotropic hardening and LKH *(left)* and from a GSM with one additional NLKH element *(right)*. For either GSM, the automatically detected hardening parameters are specified in the corresponding plot.

definition of the yield stress in (3.22) is thus sufficient to capture the observed isotropic hardening (cf. (3.36) as well). Another clear outcome of the optimization procedure was that a combination of LKH and one NLKH element is most suitable to capture the hardening behavior of the epoxy resin. Incorporation of more than one NLKH element always led to a replacement of LKH (i.e., to a LKH modulus which almost vanished) by a (quasi-linear) NLKH element at no considerable improvement in terms of the objective function. In that situation it is preferable to incorporate LKH combined

with only one NLKH element because of numerical advantages. On the other hand, complete omission of NLKH appears to be inappropriate, as can be concluded from the juxtaposition in Figure 3.3, where the stress–strain behavior of a calibrated GSM with saturating isotropic hardening and LKH only is depicted at the bottom left, while another calibrated GSM which in addition also includes one NLKH element yields the stress–strain behavior displayed at the bottom right. Note that the automated parameter identification scheme generates significantly different isotropic hardening moduli H with and without consideration of NLKH. The model with consideration of NLKH and with the hardening parameters specified in Figure 3.3 is regarded as the optimal approximation of the experimental data by means of the GSM formulation of (visco-) plasticity from Section 3.3.1.

Chapter 4:
Constitutive modeling of imperfect interfaces

4.1 Fundamentals of cohesive zone modeling

The theory of cohesive zones was initiated by Barenblatt [1959, 1962] and Dugdale [1960] in order to overcome limitations of the concept of linear elastic fracture mechanics (LEFM) established by Griffith [1921]. A key feature of the framework is the incorporation of constitutive relationships between the displacement jump δ and the interface traction $\check{t}$. Such traction–separation laws for imperfect interfaces, also referred to as *bridging laws* [cf., e.g., Fett, 1995, Sørensen & Jacobsen, 1998], are the counterparts to stress–strain relations for bulk materials and are commonly referred to as cohesive zone models (CZMs). Approximately three decades after the seminal works, the cohesive zone framework attracted new attention due to contributions of, e.g., Needleman [1987, 1990a,b], Tvergaard & Hutchinson [1992, 1993], Ortiz & Suresh [1993] and Xu & Needleman [1993, 1994], in which some of the most recognized yet rather simple CZMs have been presented. Meanwhile, numerous models have been proposed, and only a few can be mentioned in what follows. Cohesive zones were originally introduced to model the formation of cracks via interfacial damage. However, the term is subsequently used in a more general sense referring to imperfect interfaces that are assigned constitutive traction–separation laws. In general, two types of mechanical problems involving cohesive interfaces have to be distinguished:

[I1] The geometry of the interface is known a priori. This situation is found, e.g., for decohesion along glued surfaces, or along phase boundaries in composite materials.

[I2] The geometry of the interface is *not* known a priori. This is the case for, e.g., crack propagation in metals, in rocks, or within matrix phases of composite materials.

From a numerical point of view, the first case is obviously easier to deal with than the latter in FEM simulations: *interface elements* (also called *cohesive elements*) are generated at the interface when the finite element mesh is created in a preprocessing step. Interface elements are generally placed at common surfaces of neighboring bulk elements and are usually assumed to have zero thickness in the undeformed state. Like for bulk elements, various basic as well as advanced element formulations exist [e.g., Schellekens & Borst, 1993, Alfano & Crisfield, 2001, Crisfield & Alfano, 2002, Samimi et al., 2009, 2013]. To deal with the case **[I2]**, interface elements "can be adaptively inserted during computational simulation[s] whenever and wherever they are needed" [quote from Park & Paulino, 2013, p. 2]. Certainly, naive approaches using fixed discretizations are only

reasonable for few selected applications. Otherwise, adaptive remeshing [e.g., Swenson & Ingraffea, 1988] is advised. For completeness it is mentioned that, instead of using interface elements, problems of type **[I2]** can alternatively be solved with partition of unity methods [Moës et al., 1999, Wells & Sluys, 2001, Fries & Belytschko, 2010, to name only a few works] or using finite elements with embedded discontinuities [e.g., Linder & Armero, 2007], which have been developed to avoid remeshing.

As far as interface element approaches are concerned, a cohesive zone is called *intrinsic* if it is of type **[I1]** or *extrinsic* if it is of type **[I2]** [Geubelle & Baylor, 1998, Seagraves & Radovitzky, 2010, Park & Paulino, 2013]. This naming is related to interfacial mechanisms ahead of a crack tip being called intrinsic, while mechanisms behind the crack tip are referred to as extrinsic. The distinction of these two cases is not only relevant with respect to numerical treatment but also affects the constitutive modeling: traction–separation laws for intrinsic cohesive zones have an elastic (or almost elastic) initial range, which is missing for extrinsic cohesive zones that are not inserted until the interface starts to behave inelastically. This implies that in "the intrinsic approach, the failure criterion is incorporated within the constitutive model of the cohesive elements" [quote from Geubelle & Baylor, 1998, p. 591], while extrinsic models need to be supplemented with an additional failure criterion formulated in the bulk. Thus, any CZM is specifically designed for either intrinsic or extrinsic cohesive zones, although this is not always stated explicitly. In the following, attention is limited to intrinsic CZMs and to the case **[I1]**. The interested reader can find examples of extrinsic CZMs in Camacho & Ortiz [1996], Zhang et al. [2007], or Park et al. [2009].

Interface separation modes, interpenetration.   In line with (2.16) and (2.17), the displacement jump at the imperfect interface has the decomposition

$$\boldsymbol{\delta} = \boldsymbol{\delta}_\parallel + \delta_\perp \check{\boldsymbol{n}}, \tag{4.1}$$

and the norm of the tangential component is denoted $\delta_\parallel = \left\| \boldsymbol{\delta}_\parallel \right\|_2$. Purely normal loadings of imperfect interfaces with $\delta_\perp \geq 0$ are referred to as *mode I* or *tensile* loadings, while purely tangential loadings are called *mode II* or *shear* loadings[9]. Superpositions of both types of interface separation modes are referred to as *mixed mode* loadings, which are further characterized by the *mode angle*, also referred to as loading angle or phase angle,

$$\alpha = \arctan\left(\frac{\delta_\parallel}{\delta_\perp}\right) = \arccos\left(\frac{\boldsymbol{\delta}}{\|\boldsymbol{\delta}\|_2} \cdot \check{\boldsymbol{n}}\right) \in (0°, 90°). \tag{4.2}$$

For mode I and mode II, the mode angle is defined as $\alpha = 0°$ and $\alpha = 90°$, respectively. Loadings with $\delta_\perp < 0$ are called *compressive* and characterize interpenetration of solid material at the imperfect interface, which is usually considered to be unphysical. One

---

[9]The interface opening modes should not be confused with the three fracture modes in LEFM, however, there is some agreement between the respective designations: mode I interface opening is found in mode I fracture, while mode II interface opening occurs in mode II and mode III fracture.

obvious way to suppress interpenetration is to impose and enforce appropriate kinematic constraints, which is common-place in the field of computational contact mechanics [see, e.g., Wriggers & Laursen, 2007, Konyukhov & Schweizerhof, 2013]. However, the standard approach for intrinsic cohesive zones, which is adopted for all applications within this work, is to penalize interpenetration by a high compressive interface stiffness. Thereby, regions with small material overlap are allowed for.

Isotropy, transverse isotropy, and isomorphy. A CZM is called *transversely isotropic* if it is isotropic in the tangential plane, i.e., if the constitutive equations depend on the norm $\delta_\parallel$ of the tangential component, but not on the direction of $\boldsymbol{\delta}_\parallel$. Most CZMs found in the literature are transversely isotropic, and, for convenience, attention is limited to such models in this work. Some CZMs that are in the following referred to as *isomorphic* are governed by a relationship between an effective scalar traction

$$\breve{t} = \left\| \boldsymbol{B}^{-1} \breve{\boldsymbol{t}} \right\|_2 \tag{4.3}$$

and an effective scalar separation

$$\delta = \left\| \boldsymbol{A} \boldsymbol{\delta} \right\|_2, \tag{4.4}$$

where $\boldsymbol{A}$ and $\boldsymbol{B}$ are dimensionless, symmetric, and positive definite second order tensors. The effective traction is assumed to depend on the interface opening $\boldsymbol{\delta}$ only via the effective separation δ, i.e., additional dependence on the mode angle α [as found, e.g., in the model used by Kolluri et al., 2012] is not allowed for. Instead of an effective scalar separation δ, which is employed, e.g., in Ortiz & Pandolfi [1999], other authors like Tvergaard [1990] prefer to use a normalized effective scalar separation

$$\lambda = \frac{\delta}{\delta^c}, \tag{4.5}$$

where δ^c represents an overall characteristic length of the interface. For a given effective scalar traction $\breve{t}$, the cohesive traction vector is obtained via

$$\breve{\boldsymbol{t}} = \frac{\breve{t}}{\delta} \boldsymbol{B} \boldsymbol{A} \boldsymbol{\delta} = \breve{t} \boldsymbol{B} \frac{\boldsymbol{A} \boldsymbol{\delta}}{\left\| \boldsymbol{A} \boldsymbol{\delta} \right\|_2} \tag{4.6}$$

for isomorphic models. The mode coupling tensors $\boldsymbol{A}$ and $\boldsymbol{B}$ often have structures that can be expressed in terms of the projectors defined in (2.15) according to

$$\boldsymbol{A} = \breve{\boldsymbol{P}}_\perp + \frac{\delta_\perp^c}{\delta_\parallel^c} \breve{\boldsymbol{P}}_\parallel, \qquad\qquad \boldsymbol{B} = \breve{\boldsymbol{P}}_\perp + b \breve{\boldsymbol{P}}_\parallel, \tag{4.7}$$

which guarantees that pure normal/tangential openings of the interface implicate pure normal/tangential cohesive tractions. Here, $\delta_\perp^c$ and $\delta_\parallel^c$ are normal and tangential characteristic lengths and b is a positive, nondimensional coupling parameter. The normal characteristic length is typically adopted as the overall characteristic length of the

interface ($\delta^c = \delta^c_\perp$). One prominent early example of an isomorphic CZM was proposed by Tvergaard [1990] based on the cubic polynomial law

$$\breve{t}(\lambda) = \begin{cases} \frac{27}{4}\,\breve{t}^\wedge \lambda \left(1 - 2\lambda + \lambda^2\right), & \lambda < 1; \\ 0, & \text{otherwise} \end{cases} \tag{4.8}$$

that was previously used by Needleman [1987] to describe pure mode I behavior and is depicted under the label **[TS8]** in Figure 4.4. The model of Tvergaard [1990] adopts the mixed mode assumption expressed through (4.7) and contains the peak effective traction $\breve{t}^\wedge$ as a parameter for the cohesive strength.

Note that the definition of isomorphy refers to loadings without interpenetration. Clearly, isomorphic CZMs can be equipped with penalizations of interpenetration. A CZM is called *isotropic* if it is isomorphic and independent of the mode angle α, which is the case if and only if $\boldsymbol{A} \sim \boldsymbol{I}$ and $\boldsymbol{B} \sim \boldsymbol{I}$ is satisfied, and it is otherwise called *anisotropic*.

Work of separation.   Complete separation at a point of a cohesive interface is defined as a constitutive state where (approximately) no cohesive traction is transferred across the interface (except for penalty traction due to interpenetration or shear traction due to friction) even if the displacement jump does not vanish. A completely separated interface that was initially bonded is said to have experienced damage either by brittle or by ductile fracture, possibly involving a softening process. As previously stated in Section 2.7.4, the mechanical power per unit area of the interface is $\breve{\boldsymbol{t}} \cdot \dot{\boldsymbol{\delta}}$, hence for any loading history $\boldsymbol{\delta}(t)$ represented by a path Δ that results in complete separation of the interface at the end of a time interval $\mathbb{T} = [t_0, T]$, the work of separation (per unit interface area) is given by

$$\breve{W}^s = \int_\Delta \breve{\boldsymbol{t}} \cdot \mathrm{d}\boldsymbol{\delta} = \int_{t_0}^{T} \breve{\boldsymbol{t}} \cdot \dot{\boldsymbol{\delta}} \,\mathrm{d}t \tag{4.9}$$

and can be decomposed into normal and tangential components according to

$$\breve{W}^s = \breve{W}^s_\perp + \breve{W}^s_\parallel \qquad \text{with} \quad \breve{W}^s_\perp = \int_{t_0}^{T} \breve{t}_\perp \dot{\delta}_\perp \,\mathrm{d}t, \quad \breve{W}^s_\parallel = \int_{t_0}^{T} \breve{\boldsymbol{t}}_\parallel \cdot \dot{\boldsymbol{\delta}}_\parallel \,\mathrm{d}t. \tag{4.10}$$

For unidirectional loadings with fixed mode angles, the work of separation $\breve{W}^s$ corresponds to the critical (strain) energy release rate (CERR)

$$G^c = G^c_\perp + G^c_\parallel \tag{4.11}$$

used for the brittle fracture criterion of Griffith [1921], which is similarly decomposed into a tensile part $G^c_\perp$ and a shear part $G^c_\parallel$. The CERR is a measure of fracture toughness and is in general anisotropic, i.e., it depends on the mode angle, and the ratios $G^c_\perp/G^c_\parallel$ and $G^c_\parallel/G^c$ are often used as measures of mode mixity.
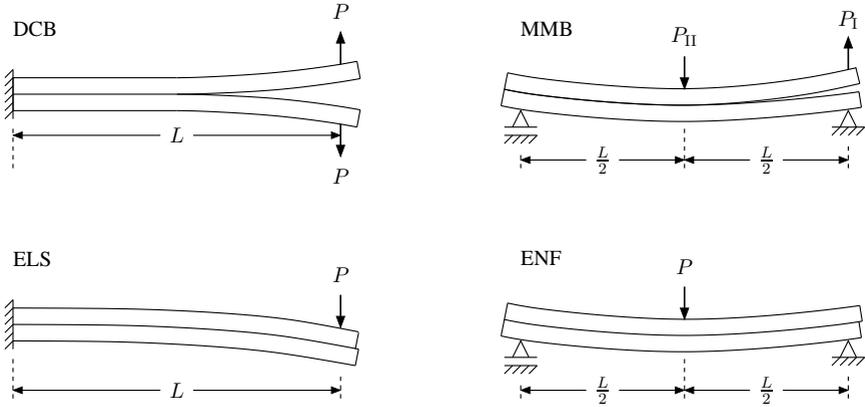
Figure 4.1: Delamination tests for different types of interface loadings (P, P_I, and P_II denote loading forces). *Top left:* double cantilever beam test (mode I). *Top right:* mixed mode bending test (mixed mode I/mode II). *Bottom left:* end loaded split test (mode II). *Bottom right:* end notched flexure test (mode II).

4.2 Experimental characterization of interfacial anisotropy

While the experimental characterization of constitutive properties of imperfect interfaces can be quite intricate, one fact that is supported by several studies [e.g., Benzeggagh & Kenane, 1996, Dollhofer et al., 2000, Warrior et al., 2003] is that many interfaces behave anisotropically. More precisely, analyses of debonding in adhesive joints or of interlaminar fracture in laminated composites show that the work of separation often depends on the mode angle α and is usually higher for mode II than for mode I. Delamination tests are used to estimate the CERR from the applied external work and from the observed crack propagation. For each test it is tried to keep the (local) mode angle α constant with respect to the position within the specimen and with respect to time. Mode I conditions are typically investigated with *double cantilever beam* (DCB) tests [e.g., Whitney et al., 1982, Keary et al., 1985], while *end loaded split* (ELS) tests [e.g., Wang & Vu-Khanh, 1996, de Moura & de Morais, 2008] or *end notched flexure* (ENF) tests [e.g., Russell, 1982, Carlsson et al., 1986] are widely used to examine mode II properties. However, it should be mentioned that compressive forces acting on the interface in ELS and ENF tests cause frictional dissipation, which leads to overestimation of the mode II CERR [see Davies, 1997, Kolluri et al., 2009]. *Mixed mode bending* (MMB) tests [e.g., Reeder & Crews, 1990, 1991, Soboyejo et al., 1999, Thijsse et al., 2008] have been developed to characterize delamination at intermediate mode angles, but are also suited for pure mode II loading with compensation of compressive forces in order to reduce disturbing friction. An MMB test can be understood as a
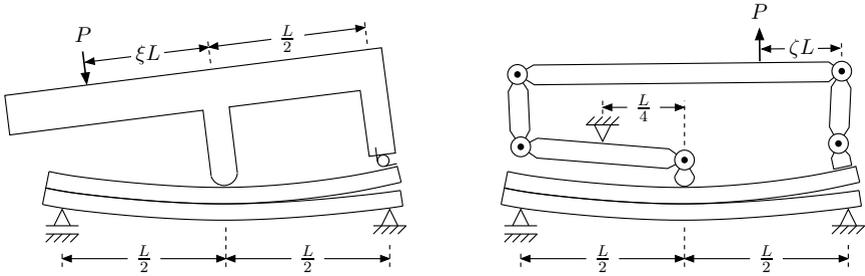
Figure 4.2: Sketches of mixed mode bending test devices. *Left:* apparatus from Reeder & Crews [1990, 1991], where the mode mixity is controlled by the attack point of the loading force P, which is parameterized by $\xi > 0$. *Right:* miniature mixed mode bending setup for in situ testing from Kolluri et al. [2009, 2011], where the loading force attack point (and thereby the mode mixity) is parameterized by $\zeta \in [0, 1]$.
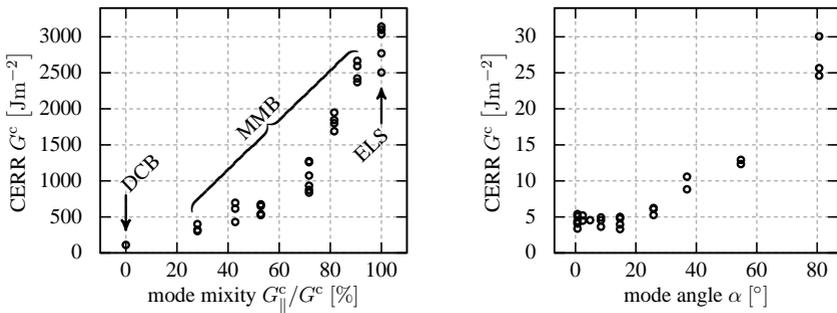
Figure 4.3: *Left:* CERR for delamination of a unidirectional glass/epoxy composite under varying mode mixity. Experimental data from DCB, MMB and ELS tests, reproduced from Benzeggagh & Kenane [1996]. *Right:* mixed mode delamination behavior of an interface between a copper lead frame and molding compound epoxy. Experimental data from (improved) MMMB tests, reproduced from Kolluri et al. [2011].

combination of DCB and ENF tests (as illustrated in Figure 4.1), and MMB experimental devices are adjustable for various mixities of mode I and mode II.

For in situ testing, a *miniature mixed mode bending* (MMMB) apparatus has been developed by Kolluri et al. [2009] and improved by Kolluri et al. [2011]. Sketches of the experimental setups for the MMB test of Reeder & Crews [1990, 1991] and of the MMMB test of Kolluri et al. [2009, 2011] are juxtaposed in Figure 4.2. The setup of Reeder & Crews [1990, 1991] is vertically oriented and allows for G_I^c/G_{II}^c ratios up to approximately five [see Reeder & Crews, 1990] but is not suited for mixed-mode conditions with a stronger mode I dominance. However, Reeder & Crews [1990] report
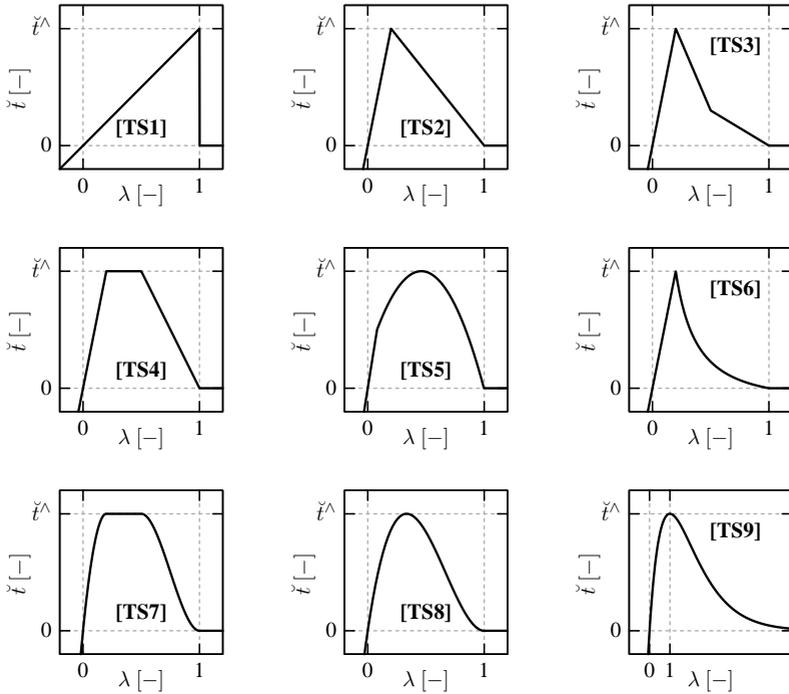
Figure 4.4: Different types of traction–separation curves for intrinsic cohesive zones: **[TS1]** perfectly brittle, **[TS2]** linear softening, **[TS3]** bilinear softening, **[TS4]** trapezoidal, **[TS5]** linear-parabolic, **[TS6]** linear-exponential, **[TS7]** smoothed trapezoidal, **[TS8]** cubic polynomial, and **[TS9]** exponential. Although specified as relationships between effective tractions $\breve{t}$ and normalized effective interface openings λ as for isomorphic models, all curves can also be used to model pure mode I or pure mode II behavior (in the latter case, only the range $\lambda \geq 0$ is considered).

that the loading device can be easily turned into a DCB test setup to investigate pure tensile loading. On the other hand, the apparatus of Kolluri et al. [2009, 2011] is suited for the whole range of mode mixities and is horizontally aligned in order to allow for in situ tests with standard microscopes. Experimental results from the literature demonstrating the anisotropy of the CERR for real interfaces are depicted in Figure 4.3.

4.3 Traction–separation curves

Figure 4.4 shows some established traction–separation curves for damage modeling with intrinsic cohesive zones:

[TS1] The linear cohesive law with abrupt failure employed in Ortiz & Suresh [1993] corresponds to perfectly brittle behavior [see also Valoroso & Champaney, 2006, Portillo & Cebon, 2013]. It can be viewed as a limit case of the linear-exponential law **[TS6]** and of

[TS2] the linear softening model [e.g., Geubelle & Baylor, 1998, Espinosa & Zavattieri, 2003, Samimi et al., 2009], which is also known as bilinear or triangular law and can in turn be understood as a limit case of the trapezoidal law **[TS4]**, or of

[TS3] the bilinear softening model [e.g., Li et al., 2006, Amidi & Wang, 2017], which is also referred to as trilinear law.

[TS4] The trapezoidal law, introduced by Tvergaard & Hutchinson [1992, 1993], is one of the most commonly used models for ductile fracture. It is sometimes also misleadingly called trilinear.

[TS5] The linear-parabolic law has been studied by Alfano [2006] as an approximate substitute of the more complex model from Allix et al. [1995] and Allix & Corigliano [1996]. A purely parabolic law without the initial linear elastic range has been considered, e.g., by Volokh [2004], who also studied a similar trigonometric law based on one half-cycle of the sine function (both not shown).

[TS6] The linear-exponential law is used to model quasi-brittle fracture [e.g., Borst et al., 2004, Portillo & Cebon, 2012, 2013]. Note that, different from the exponential law **[TS9]**, the exponential softening regime is modeled with a limited range such that complete separation is attained not only approximately but exactly.

[TS7] The smoothed trapezoidal law proposed by Scheider & Brocks [2003] is a continuously differentiable modification of the trapezoidal law **[TS4]**. Around the origin it has a quadratic polynomial regime, followed by a plateau with the maximum traction, behind which the traction decreases to zero due to softening, which is modeled by a cubic polynomial. Thus, the softening behavior corresponds to the one of

[TS8] the cubic polynomial law from (4.8) proposed by Needleman [1987].

[TS9] The exponential law [e.g., Rice & Wang, 1989, Needleman, 1990a,b] is motivated by atomistic considerations about metallic interfaces by Rose et al. [1981, 1983] and Ferrante & Smith [1985]. In contrast to the previously mentioned models **[TS1–8]**, the tractions decrease asymptotically to zero for $\lambda \to \infty$ but remain strictly positive. The characteristic length is chosen as the (unique) interface opening associated to the peak traction $\breve{t}^{\wedge}$ in this case because complete failure is never attained.

It should be mentioned that despite the one-dimensional traction–separation curves in Figure 4.4 being expressed as relationships between effective tractions and effective interface openings (as required for isomorphic models), they are not only applicable to isomorphic interface models but can also be used to model purely normal or purely

tangential behavior. Also, the normal and the tangential behavior of an interface are not necessarily characterized by the same type of traction–separation curve. For instance, Li et al. [2006] use bilinear softening for mode I and trapezoidal ductile failure for mode II in the modeling of an adhesively bonded polymer-matrix composite. The models of Needleman [1990b, 1992] and Xu & Needleman [1993] combine an exponential damage law for mode I with periodic sinusoidal behavior in shear, which amounts to a "phenomenological continuum description to reflect the lattice periodicity for atomistically sharp crystal interfaces" [quote from Needleman, 1992, p. 206].

There is quite some disagreement in the literature about the importance of the shape of traction–separation curves for the modeling of cohesive interfaces. While the work of separation, corresponding to the area under the traction–separation curve, is undoubtedly a key property to describe cohesive behavior, some authors assume that one additional quantity, more precisely, either the characteristic length [see Rahulkumar et al., 2000] or the peak traction corresponding to interfacial strength [see Hutchinson & Evans, 2000], is sufficient for the characterization of a CZM. In doing so, the detailed shape of the traction–separation curve is regarded subsidiary, which complies to a widespread opinion. On the other hand, the shape-sensitivity of CZMs has been investigated by a few studies [Chandra et al., 2002, Volokh, 2004, Alfano, 2006] which conclude that the "form of the traction–separation equations for CZMs plays a very critical role" [quote from Chandra et al., 2002, p. 2827]. However, a question which has not been sufficiently clarified to the author's knowledge is to which degree the shape-sensitivity can be attributed to relevant physical information as opposed to numerical effects. In this context it is important to keep in mind that constitutive modeling and numerical treatment are typically much more interdependent for imperfect interfaces than for bulk materials. Note though that physical relevance of the shape of a CZM is implicitly suggested by the fact that perfectly brittle behavior and ductile fracture are usually modeled with different types of traction–separation curves.

4.4 Single potential cohesive zone (SPCZ) models

Some traction–separation laws are derived from an energy storage function $\breve{\psi} \equiv \breve{\psi}(\boldsymbol{\delta})$ with $\breve{\psi}(\mathbf{0}) = 0$, which can be understood as a hyperelastic potential [cf. Costanzo, 1998] that defines a traction–separation law via the generalized gradient

$$\breve{\boldsymbol{t}} = \frac{\partial \breve{\psi}}{\partial \boldsymbol{\delta}}. \tag{4.12}$$

CZMs of this kind are in the following referred to as *single potential cohesive zone* (SPCZ) models and are path-independent (unless additional constitutive assumptions are made). From (4.12) it is concluded that the tangent $\partial \breve{\boldsymbol{t}}/\partial \boldsymbol{\delta}$ is symmetric due to Schwarz's theorem. Also, in combination with (4.9) it follows that the work of separation is given by the energy storage function

$$\breve{W}^{\mathrm{s}}(\boldsymbol{\delta}^{\mathrm{s}}) = \breve{\psi}(\boldsymbol{\delta}^{\mathrm{s}}) \tag{4.13}$$

for any point δ^{s} in a region of complete separation. A common assumption for damaging CZMs is that the interface can break by unidirectional loading at any mode angle (cf. Section 4.2), which implies the existence of one connected region of complete separation comprising all mode angles. Then, the CERR of an SPCZ must be isotropic in view of (4.13) because $\breve{\psi}$ is (approximately) constant within a region of complete separation. This is of course a severe limitation against the backdrop of experimental results elucidated in Section 4.2. Two types of approaches are found in the literature for SPCZ models to take into account anisotropy of the CERR nevertheless: on the one hand, models without a region of complete separation have been proposed [e.g., Xu & Needleman, 1993, 1994], which exhibit undesired, physically inconsistent behavior. Some of these inconsistencies have been discussed by van den Bosch et al. [2006], who proposed a modified version of the model from Xu & Needleman [1993], renouncing the idea of an SPCZ formulation. On the other hand, regions of complete or partial separation can be explicitly defined by setting all or only normal or tangential tractions to zero under certain conditions [e.g., Freed & Banks-Sills, 2008, Park et al., 2009]. Obviously, such models only stem from an energy storage function outside such regions of separation (except for trivial cases). Briefly speaking, this approach allows for anisotropy of the CERR by artificially removing path-independence which is otherwise enforced by the energy storage function.

SPCZ models are often called potential-based in the literature, even if they comprise regions of complete or partial separation which are not governed by a potential [cf. Park & Paulino, 2013]. It is important to note that the term potential-based is ambiguously used for constitutive models throughout the literature. This is because constitutive modeling based on energy storage functions is not as prevalent for imperfect interfaces as for bulk materials. Since the existence of energy storage functions is most commonly assumed for bulk materials, these are rather called potential-based if it is postulated that dissipation is controlled by additional potentials, as in the GSM framework presented in Section 3.2. In contrast, SPCZ models adopt an implicit description of dissipation, as discussed in Section 4.5.

4.5 Modeling of dissipative processes

Besides friction, softening damage is the most recognized dissipative process at imperfect interfaces and is usually assumed for CZMs if nothing else is stated. Like for bulk materials, elastic degradation can be motivated by thinking of a constitutive interface model as the homogenized response of a lower scale micromechanical model with gradually increasing micro-cracks. Pure damage shows linear elastic unloading to the origin, as illustrated on the left-hand side of Figure 4.5. On the other hand, pure plastic softening is characterized by a recovery of the initial elastic stiffness during unloading (see right-hand side of Figure 4.5). This behavior is attributed to pure ductile fracture [cf. Kolluri et al., 2014] but is hardly considered in the literature. Kolluri et al. [2014] also discuss experimental justification for combined damage-plasticity CZMs (illustrated in the middle of Figure 4.5). Such combined models have been
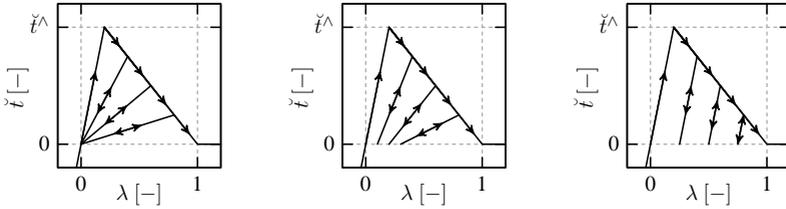
Figure 4.5: Different types of loading–unloading behavior: pure damage *(left)*, combined damage–plasticity *(middle)*, and pure plasticity *(right)*.

presented, e.g., by Marzi et al. [2009], Biel & Stigh [2010], Cazes et al. [2010], and Kolluri et al. [2014].

SPCZ models and other traction–separation laws that do not explicitly incorporate internal variables [such as the mixed mode model of van den Bosch et al., 2006] are commonly used to mimic dissipative behavior. These models comprise purely phenomenological, implicit descriptions of dissipative processes. Clearly, unless attention is restricted to simple load paths without unloading, the unloading/reloading behavior must be specified by constitutive laws. As mentioned before, pure damaging behavior is sometimes implicitly assumed. Then, for isomorphic models it is sufficient to store the maximum normalized effective separation $\lambda^\wedge$ that has been attained so far and to replace the traction–separation curve of the undamaged interface by a linear elastic slope when the current effective separation λ is smaller than $\lambda^\wedge$ [cf. Högberg, 2006]. Such replacements must be made as soon as the effective traction–separation curve becomes nonlinear since an infinitesimal increase of λ would otherwise cause a finite increase of the dissipated energy at the onset of damage. Hence, traction–separation laws without a linear initial slope (see, e.g., **[TS7–9]** in Figure 4.4) do not have an initial elastic range. In other words, such models cannot possess a nonlinear elastic range.

For interface models which are not isomorphic (and are thus anisotropic in particular), modeling of unloading/reloading behavior for arbitrary load paths is more challenging, and the rather simple treatment of dissipation described above, which is sometimes tacitly assumed, does not suffice. On the one hand, it can be quite tricky to represent the progress of damage by just one scalar variable for an anisotropic model. On the other hand, if damage is represented by more than one variable, e.g., by two variables associated to tensile and to shear behavior, respectively, the challenge is to specify a suitable coupling of those variables. In any case, it is necessary to define how incomplete damage due to loading (with subsequent unloading) in one direction effects the elastic degradation for other load directions. Moreover, it is important to ensure thermodynamic consistency, which some models proposed in the literature do not fulfill for arbitrary loadings, as pointed out by Turon et al. [2006]. Generally speaking, explicit descriptions of dissipative processes based on evolution laws for internal variables are more suitable

for the modeling of complex, non-isomorphic interfacial behavior at arbitrary load paths. Interface models that explicitly involve internal variables have been proposed by Allix et al. [1995], Allix & Corigliano [1996], Alfano & Crisfield [2001], Valoroso & Champaney [2006], and Cazes et al. [2009, 2010], for instance.

Another issue that is facilitated by involving internal variable is the modeling of rate-dependency. Just like pure damage unloading behavior, rate-independence is tacitly assumed for many CZMs in the literature. However, experimental studies such as those by Smiley & Pipes [1987], Hashemi et al. [1990], and Frassine et al. [1996] show that some interfaces have rate-dependent constitutive behavior. Rate-dependent models comprising internal variable have been proposed by, e.g., Corigliano & Mariani [2001] and Musto & Alfano [2013]. Yet, rate-dependency can also be included into rather simple interface models without internal variables, e.g., by introducing rate-dependent parameters for traction–separation curves, as done by Marzi et al. [2009].

4.6 Standard dissipative cohesive zone (SDCZ) models

The idea to model imperfect interfaces within a GSM-like framework (cf. Section 3.2) seems obvious but, to the author's knowledge, has not attracted much attention in the literature so far. One noteworthy exception is the work of Costanzo & Allen [1995] in which an uncommon additive split of cohesive tractions into an elastic part and an irreversible part is adopted. Cazes et al. [2009] also consider a cohesive zone which they claim behaves like a GSM, yet although dissipation potentials are essential for the formulation of GSMs, none is explicitly specified in that study. In the following, a variational approach for the modeling of imperfect interfaces is briefly introduced which is equivalent to the GSM framework in the original formulation of Halphen & Nguyen [1975] and has been previously considered by Leuschner et al. [2015]. Since it seems odd to use a label comprising the expression "material" for a class of interface models, the framework is hereafter referred to as *standard dissipative cohesive zones* (SDCZ) [cf. Leuschner et al., 2015], following the label "standard dissipative solids" that is alternatively used for GSMs.

Within the SDCZ framework, the state of an interface is characterized by the kinematic state specified in terms of the displacement jump $\boldsymbol{\delta}$ and by interfacial internal state variables $\breve{\mathcal{I}}$. An SDCZ model is defined by two potential functions:

- the Helmholtz free energy areal density $\breve{\psi}\big(\boldsymbol{\delta}, \breve{\mathcal{I}}\big)$, and

- either the primal dissipation potential $\breve{\phi}\big(\dot{\breve{\mathcal{I}}}\big)$ or its Legendre–Fenchel transform, the dual dissipation potential $\breve{\phi}^*\big(\breve{\mathcal{F}}\big)$, both of which are energy rate areal densities.

The potentials are non-negative and contain the origin, i.e., $\breve{\psi}(\mathbf{0}, \mathbf{0}) = \breve{\phi}(\mathbf{0}) = \breve{\phi}^*(\mathbf{0}) = 0$ holds. Moreover, both dissipation potentials are required to be convex in order to

ensure thermodynamic consistency. However, the free energy density $\breve{\psi}$ may be non-convex to enable modeling of softening behavior. Like for GSMs (cf. Section 3.2), it is usually more convenient to specify the dual dissipation potential $\breve{\phi}^*$ instead of the primal one $\breve{\phi}$. Hence, the dual potential, which explicitly defines the evolution of internal state variables $\dot{\breve{\mathcal{I}}}$, is used in most subsequent formulations. In addition to the evolution law, the constitutive equations of an SDCZ model define the dual state, i.e., the cohesive traction vector $\breve{t}$ and the generalized forces $\breve{\mathcal{F}}$ conjugate to the internal state variables. All constitutive equations are given via generalized gradients of the SDCZ potentials and are summarized according to

$$\breve{t} = \frac{\partial \breve{\psi}}{\partial \boldsymbol{\delta}}, \qquad\qquad \breve{\mathcal{F}} = -\frac{\partial \breve{\psi}}{\partial \breve{\mathcal{I}}}, \qquad\qquad \dot{\breve{\mathcal{I}}} = \frac{\partial \breve{\phi}^*}{\partial \breve{\mathcal{F}}}. \qquad (4.14)$$

Concerning the interfacial Helmholtz free energy, the representation by the areal density $\breve{\psi}$ is preferred over the mass specific counterpart $\breve{\Psi}$ introduced in Section 2.8.2. The free energy areal density can be understood as a stored energy function and is thus denoted $\breve{\psi}$ like potentials of SPCZ models (cf. Section 4.4), although internal variables $\breve{\mathcal{I}}$ are considered as arguments for SDCZ models but not for SPCZ models. Obviously, SPCZ models that are completely governed by an energy storage function (i.e., without any cut-off regions, as elucidated in Section 4.4), can be viewed as (hyper-) elastic SDCZ models as long as modeling of dissipative processes such as elastic degradation due to damage (cf. Section 4.5) is neglected.

From a numerical point of view, SDCZs are treated much like GSMs. In particular, an incremental stress potential

$$\breve{W}(\boldsymbol{\delta}) = \inf_{\Delta \breve{\mathcal{I}}} \breve{\Pi}\left(\boldsymbol{\delta}, \breve{\mathcal{I}}\right) = \inf_{\Delta \breve{\mathcal{I}}} \sup_{\breve{\mathcal{F}}} \breve{\Pi}^*\left(\boldsymbol{\delta}, \breve{\mathcal{I}}, \breve{\mathcal{F}}\right) \qquad (4.15)$$

based on the generalized incremental work

$$\breve{\Pi}\left(\boldsymbol{\delta}, \breve{\mathcal{I}}\right) = \breve{\psi}\left(\boldsymbol{\delta}, \breve{\mathcal{I}}\right) - \breve{\psi}\left(\boldsymbol{\delta}_n, \breve{\mathcal{I}}_n\right) + \Delta t\, \breve{\phi}\left(\dot{\breve{\mathcal{I}}}\right) \qquad (4.16)$$

or on the mixed incremental potential

$$\breve{\Pi}^*\left(\boldsymbol{\delta}, \breve{\mathcal{I}}, \breve{\mathcal{F}}\right) = \breve{\psi}\left(\boldsymbol{\delta}, \breve{\mathcal{I}}\right) - \breve{\psi}\left(\boldsymbol{\delta}_n, \breve{\mathcal{I}}_n\right) + \Delta\breve{\mathcal{I}} \cdot \breve{\mathcal{F}} - \Delta t\, \breve{\phi}^* \qquad (4.17)$$

can be defined in the same manner as for GSMs in a time-discrete setting (cf. Section 3.5). Since most of the content of Sections 3.4–3.6 is also applicable to SDCZ models and can be adopted in a straightforward manner, no further details concerning numerics and algorithms are discussed here.
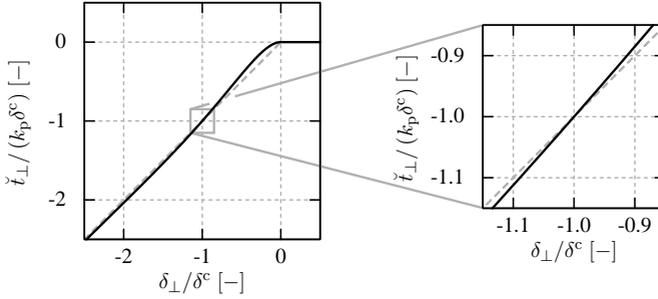
Figure 4.6: Normalized representation of the traction–separation relationship of the regularized penalty formulation for unilateral contact without friction from (4.19). The linear standard approach from (4.18) is indicated by a dashed gray line.

Example: unilateral contact without friction. Unilateral contact without friction is modeled by penalization of material interpenetration at the imperfect interface. The simplest possible choice of a penalty energy storage function is the quadratic expression

$$\breve{\psi}(\boldsymbol{\delta}) = \frac{k_\mathrm{p}}{2} \langle \boldsymbol{\delta} \cdot \breve{\boldsymbol{n}} \rangle_-^2 = \frac{k_\mathrm{p}}{2} \langle \delta_\perp \rangle_-^2 \tag{4.18}$$

with a penalty stiffness k_p, which yields linear normal penalty tractions in the compressive regime and zero cohesive tractions when the interface is opened. In some simulation situations, the nonsmoothness around the origin of the function $\breve{\psi}$ gives rise to numerical difficulties which can be moderated by regularized penalty formulations. One possible regularization is expressed via the energy storage function

$$\breve{\psi}(\boldsymbol{\delta}) = \frac{k_\mathrm{p}}{2} \langle \delta_\perp \rangle_-^2 \left(1 - \exp\left(2 \frac{\langle \delta_\perp \rangle_-}{\delta^\mathrm{c}} \right) \right), \tag{4.19}$$

where δ^c denotes a characteristic length. The resulting traction–separation law in normal direction has the asymptotic penalty stiffness k_p and is continuously differentiable. Figure 4.6 illustrates that the regularized traction–separation curve intersects with the non-regularized bilinear curve at $\delta_\perp = -\delta^\mathrm{c}$. A regularized penalty formulation of this type has been employed by Fritzen & Leuschner [2015]. Note that, like any other interface stiffness, the penalty stiffness k_p contains a length scale that introduces scale-dependence. If this is undesired, a representation of the interface stiffness that is normalized with respect to a characteristic length δ^c according to $c_\mathrm{p} = k_\mathrm{p} \delta^\mathrm{c}$ is useful.

Example: standard linear interface (SLI). The standard linear interface is a simple model of linear viscoelasticity which is structurally similar to standard linear

solids (cf. Section 3.3.2) except for a superposed penalty formulation impeding interpenetration. It is expressed in terms of the SDCZ potentials

$$\breve{\psi}(\boldsymbol{\delta}, \boldsymbol{\delta}_{\mathrm{v}}) = \frac{1}{2}\boldsymbol{\delta} \cdot \boldsymbol{K}\boldsymbol{\delta} + \frac{1}{2}\left(\boldsymbol{\delta} - \boldsymbol{\delta}_{\mathrm{v}}\right) \cdot \boldsymbol{K}_{\mathrm{v}}\left(\boldsymbol{\delta} - \boldsymbol{\delta}_{\mathrm{v}}\right) + \frac{k_{\mathrm{p}}}{2}\left\langle\boldsymbol{\delta} \cdot \breve{\boldsymbol{n}}\right\rangle_{-}^{2}, \tag{4.20}$$

$$\breve{\phi}^{*}(\boldsymbol{t}_{\mathrm{v}}) = \frac{1}{2\eta}\boldsymbol{t}_{\mathrm{v}} \cdot \boldsymbol{t}_{\mathrm{v}} \tag{4.21}$$

with the viscosity η, the viscous displacement jump $\boldsymbol{\delta}_{\mathrm{v}}$ as internal variable, and with the viscous traction $\boldsymbol{t}_{\mathrm{v}}$ as the force conjugate to $\boldsymbol{\delta}_{\mathrm{v}}$. The second order tensors $\boldsymbol{K}$ and $\boldsymbol{K}_{\mathrm{v}}$ are symmetric and positive definite and are expressed as linear combinations of the projectors from (2.15) for transversely isotropic models. Standard linear interfaces have been considered in the context of composite materials, e.g., by Gosz et al. [1991] and by Leuschner & Fritzen [2017] and are incorporated in the numerical example presented in Section 7.9.2.

4.7 Damage modeling in the SDCZ framework

As mentioned earlier in Section 4.5, a variety of damage CZMs with explicit modeling of dissipative processes via internal variables has been proposed in the literature. Most of these models do not fit into the SDCZ framework. This has motivated the development and proposal of a damage SDCZ model by Leuschner et al. [2015], which is presented in a slightly altered notation hereafter. In order to highlight some basic ideas, an isotropic model is given first, which can of course be understood as a one-dimensional model with minor technical changes. Based on the isotropic formulation, a transversely isotropic damage model is subsequently presented.

Isotropic damage SDCZ model. Isotropic damage is modeled in the SDCZ framework with a scalar damage variable d and a scalar softening variable y as internal state variables. An additive split of the Helmholtz free energy density into an elastic damageable part $\breve{\psi}^{\mathrm{d}}$, an elastic penalty part $\breve{\psi}^{\mathrm{p}}$, and a softening potential $\breve{\psi}^{\mathrm{s}}$ according to

$$\breve{\psi}(\boldsymbol{\delta}, d, y) = \breve{\psi}^{\mathrm{d}}(\boldsymbol{\delta}, d) + \breve{\psi}^{\mathrm{p}}(\boldsymbol{\delta}) + \breve{\psi}^{\mathrm{s}}(y) \tag{4.22}$$

is adopted. The softening potential $\breve{\psi}^{\mathrm{s}}$ is the only non-convex part of the damage models' potentials, and the quadratic form (4.18) is assumed for the penalty potential $\breve{\psi}^{\mathrm{p}}$. Two possible types of softening potentials are presented in the next paragraph. The elastic damageable part of the Helmholtz free energy density is chosen to be of the form

$$\breve{\psi}^{\mathrm{d}}(\boldsymbol{\delta}, d) = \frac{k}{2(1+d)}\left(\left\langle\boldsymbol{\delta} \cdot \breve{\boldsymbol{n}}\right\rangle_{+}^{2} + \boldsymbol{\delta} \cdot \breve{\boldsymbol{P}}_{\|}\boldsymbol{\delta}\right) = \frac{k}{2(1+d)}\left(\left\langle\delta_{\perp}\right\rangle_{+}^{2} + \delta_{\|}^{2}\right). \tag{4.23}$$

In many cases it seems feasible to choose coincident values for the undamaged interface stiffness k and for the penalty stiffness k_{p} (cf. **[TS1–6]** in Figure 4.4). Clearly, the damageable part of the free energy density in (4.23) becomes small but remains positive

as the damage variable d increases. In practice it is recommended to set $\breve{\psi}^{\mathrm{d}}$ to zero once d exceeds a critical value. Note that this does not violate the requirements of the SDCZ framework if the cohesive tractions are already sufficiently small when the critical value is reached. From (4.22) it follows that the cohesive traction can be additively split into a penalty traction $\breve{\boldsymbol{t}}_{\mathrm{p}}$ and into the remaining damageable traction $\breve{\boldsymbol{t}}_{\mathrm{d}}$ according to

$$\breve{\boldsymbol{t}} = \frac{\partial \breve{\psi}}{\partial \boldsymbol{\delta}} = \frac{\partial \breve{\psi}^{\mathrm{d}}}{\partial \boldsymbol{\delta}} + \frac{\partial \breve{\psi}^{\mathrm{p}}}{\partial \boldsymbol{\delta}} = \breve{\boldsymbol{t}}_{\mathrm{d}} + \breve{\boldsymbol{t}}_{\mathrm{p}} \tag{4.24}$$

with

$$\breve{\boldsymbol{t}}_{\mathrm{d}} = \frac{k}{1+d} \left(\langle \delta_{\perp} \rangle_{+} \, \breve{\boldsymbol{n}} + \boldsymbol{\delta}_{\parallel} \right), \qquad\qquad \breve{\boldsymbol{t}}_{\mathrm{p}} = k_{\mathrm{p}} \, \langle \delta_{\perp} \rangle_{-} \, \breve{\boldsymbol{n}}. \tag{4.25}$$

Any traction vector $\breve{\boldsymbol{t}}$ can be decomposed into $\breve{\boldsymbol{t}}_{\mathrm{d}}$ and $\breve{\boldsymbol{t}}_{\mathrm{p}}$ without any background knowledge other than the interface normal $\breve{\boldsymbol{n}}$. Clearly, modeling of softening behavior in terms of a damage surface is based on the norm $\left\| \breve{\boldsymbol{t}}_{\mathrm{d}} \right\|_{2}$ of the damageable traction vector. However, the dual dissipation potential $\breve{\phi}^{*} \equiv \breve{\phi}^{*}(f, z)$, through which dissipative processes are modeled, must be expressed as a function with the thermodynamic forces $\breve{\boldsymbol{\mathcal{F}}} = (f, z)$ conjugate to the internal state variables $\breve{\boldsymbol{\mathcal{I}}} = (d, y)$ as the sole arguments. Therefore, the potential $\breve{\psi}^{\mathrm{d}}$ has been deliberately chosen such that the conjugate force to the damage variable is

$$f = -\frac{\partial \breve{\psi}}{\partial d} = -\frac{\partial \breve{\psi}^{\mathrm{d}}}{\partial d} = \frac{k}{2(1+d)^{2}} \left(\langle \delta_{\perp} \rangle_{+}^{2} + \delta_{\parallel}^{2} \right), \tag{4.26}$$

which allows to recover the norm of the damageable traction from f via

$$\left\| \breve{\boldsymbol{t}}_{\mathrm{d}} \right\|_{2} = \sqrt{2kf}. \tag{4.27}$$

Note that this approach is enabled by a non-standard damage variable formulation: here, the current, damaged interface stiffness is given by the expression $k/(1+d)$, which is in contrast to representations of the form $(1-D)k$ using a classical damage variable D. The damage criterion is now expressed as $\varphi(f, z) \leq 0$ through the level set function

$$\varphi(f, z) = \sqrt{2kf} - \tau^{\mathrm{c}}(z) \qquad \text{with } \tau^{\mathrm{c}}(z) = \langle -z - \tau^{\mathrm{s}} \rangle_{+}, \tag{4.28}$$

where $\tau^{\mathrm{s}} \geq 0$ is a stopping parameter which allows to decrease the critical traction τ^{c} to zero even if z (which is alway non-positive) is strictly negative. The transition from the level set function to the dual dissipation potential is achieved in a similar way as for (visco-) plastic GSMs (cf. Section 3.3.1): rate-independent behavior is obtained with

$$\breve{\phi}^{*}(f, z) = \begin{cases} 0, & \varphi(f, z) \leq 0; \\ \infty, & \text{otherwise,} \end{cases} \tag{4.29}$$

while the Perzyna-type formulation

$$\breve{\phi}^{*}(f, z) = \frac{\dot{\delta}_{0} \, \sigma_{\mathrm{d}}}{m+1} \left(\frac{\langle \varphi(f, z) \rangle_{+}}{\sigma_{\mathrm{d}}} \right)^{m+1} \tag{4.30}$$
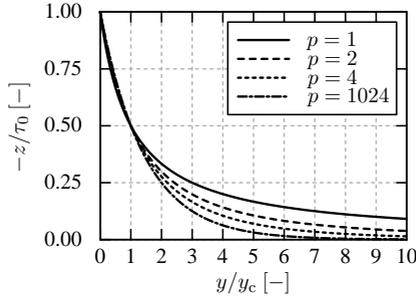
Figure 4.7: Softening of power-law type as defined in (4.31).

can be used as a viscous regularization or to model rate-dependency. The involved viscous parameters are the displacement jump reference rate $\dot{\delta}_0 > 0$, the drag stress $\sigma_d > 0$, and the viscosity exponent $m \geq 1$.

Softening potentials. Two types of softening behavior that have been used for damage SDCZ models in Leuschner et al. [2015] are briefly presented. The first one is based on a power-law approach and is defined by the softening potential

$$\check{\psi}^s(y) = \tau_0 \int_0^y (1 + \gamma v)^{-p} \, dv = \begin{cases} \dfrac{\tau_0}{(p-1)\gamma} \left(1 - (1 + \gamma y)^{1-p}\right), & p > 1; \\ \dfrac{\tau_0}{\gamma} \ln\left(1 + \gamma y\right), & p = 1 \end{cases} \tag{4.31}$$

with the parameters $p \geq 1$, $\tau_0 > 0$, and $\gamma > 0$. It can be handy to define the parameter γ as

$$\gamma = \frac{\sqrt[p]{2} - 1}{y_c}, \tag{4.32}$$

where $y_c > 0$ denotes a characteristic length that corresponds to the value of the softening variable y when $-z = \partial_y \check{\psi}^s$ has dropped from τ_0 to $\tau_0/2$. Figure 4.7 shows the softening behavior of power-law type.

The second type of softening behavior is defined by the bi-exponential expression

$$\check{\psi}^s(y) = (\tau_0 + \tau_1) \, y_0 \left(1 - \exp\left(-\frac{y}{y_0}\right)\right) + \tau_1 \, y_1 \left(\exp\left(-\frac{y}{y_1}\right) - 1\right) \tag{4.33}$$

with the parameters $y_0 > y_1 > 0$, $\tau_0 > 0$, and $\tau_1 \geq -\tau_0$. It is sometimes useful to parameterize τ_1 via the initial slope $\mu \geq -\tau_0/y_1$ of the softening curve according to

$$\tau_1 = \frac{y_0 \, y_1}{y_0 - y_1} \left(\mu + \frac{\tau_0}{y_0}\right). \tag{4.34}$$
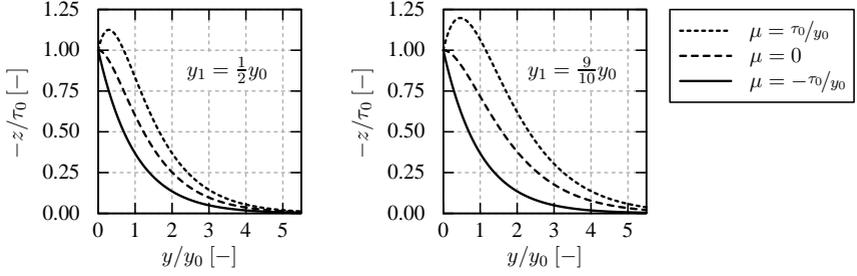
Figure 4.8: Bi-exponential softening as defined in (4.33). Notice that the softening behavior is independent of y_1 for the special case $\tau_1 = 0 \Leftrightarrow \mu = -\tau_0/y_0$.

The effects of a varying ratio y_1/y_0 and of a varying slope μ are illustrated in Figure 4.8.

Transversely isotropic damage model. According to Section 4.2, one essential requirement to transversely isotropic damage models is the description of significant anisotropy of the CERR G^c. More specifically, such models should exhibit a continuous, monotonic dependence of the CERR on the mode angle α. Within the SDCZ framework it is not possible to model such behavior with only one damage variable. Therefore, two damage variables $\underline{d} = \begin{bmatrix} d_\perp, d_\parallel \end{bmatrix}^\mathsf{T}$ and two softening variables $\underline{y} = \begin{bmatrix} y_\perp, y_\parallel \end{bmatrix}^\mathsf{T}$, corresponding to two dissipative mechanisms, are used for the transversely isotropic damage model proposed by Leuschner et al. [2015]. The thermodynamic driving forces conjugate to the internal state variables $\underline{d}$ and $\underline{y}$ are denoted $\underline{f} = \begin{bmatrix} f_\perp, f_\parallel \end{bmatrix}^\mathsf{T}$ and $\underline{z} = \begin{bmatrix} z_\perp, z_\parallel \end{bmatrix}^\mathsf{T}$, respectively. The Helmholtz free energy density of the damage model has the form

$$\breve{\psi}(\boldsymbol{\delta}, \underline{d}, \underline{y}) = \breve{\psi}^\mathrm{d}(\boldsymbol{\delta}, \underline{d}) + \breve{\psi}^\mathrm{p}(\boldsymbol{\delta}) + \breve{\psi}^\mathrm{s}_\perp(y_\perp) + \breve{\psi}^\mathrm{s}_\parallel(y_\parallel) \tag{4.35}$$

with $\breve{\psi}^\mathrm{d}(\boldsymbol{\delta}, \underline{d}) = \dfrac{k_\perp}{2\left(1 + d_\perp\right)} \left\langle \delta_\perp \right\rangle_+^2 + \dfrac{k_\parallel}{2\left(1 + d_\parallel\right)} \delta_\parallel^2,$ \hfill (4.36)

where $k_\perp > 0$ and $k_\parallel > 0$ denote the initial tensile and shear stiffness, respectively, $\breve{\psi}^\mathrm{s}_\perp$ and $\breve{\psi}^\mathrm{s}_\parallel$ are softening potentials, and the quadratic penalty potential from (4.18) is again adopted for $\breve{\psi}^\mathrm{p}$. If not stated otherwise, the penalty stiffness k_p and the undamaged tensile stiffness $k_\perp$ are assumed to be equal. For a physically reasonable modeling of elastic degradation and, eventually, complete separation of the interface, it is necessary that the evolution of both damage variables $d_\perp$ and $d_\parallel$ is coupled. In particular, it is feasible to postulate that complete separation can be caused by proportional loading in any direction. Thus, pure mode I loading must not only effect the evolution of $d_\perp$ but also the one of $d_\parallel$, while pure mode II loading is required to trigger the evolution of $d_\perp$

conversely. In addition, it is necessary that the evolution of the softening variables $y_\perp$ and $y_\parallel$ is coupled. Apparently, the four internal variables are decoupled in the definition of the Helmholtz free energy density in (4.35) and (4.36), hence the coupling of both dissipative mechanisms is left to the formulation of the dual dissipation potential. It also follows from the non-standard damage formulation (4.36) that the tensile traction and the shear traction can be described in terms of the thermodynamic driving forces $\underline{f}$ conjugate to the damage variables $\underline{d}$ via

$$\langle \breve{t}_\perp \rangle_+ = \sqrt{2k_\perp f_\perp}, \qquad\qquad \breve{t}_\parallel = \sqrt{2k_\parallel f_\parallel}. \qquad (4.37)$$

This is the point of departure for the definitions of the effective combined tractions

$$\tau_\perp\left(\underline{f}\right) = \sqrt{2\left(k_\perp f_\perp + \lambda_\perp^2 \, k_\parallel f_\parallel\right)} = \sqrt{\langle \breve{t}_\perp \rangle_+^2 + \left(\lambda_\perp \breve{t}_\parallel\right)^2}, \qquad (4.38)$$

$$\tau_\parallel\left(\underline{f}\right) = \sqrt{2\left(k_\parallel f_\parallel + \lambda_\parallel^2 k_\perp f_\perp\right)} = \sqrt{\breve{t}_\parallel^2 + \langle \lambda_\parallel \breve{t}_\perp \rangle_+^2} \qquad (4.39)$$

involving the coupling parameters $\lambda_\perp, \lambda_\parallel > 0$. As pointed out by Leuschner et al. [2015], the effective tractions are used to define the overstress functions

$$\varphi_\perp\left(\underline{f}, \underline{z}\right) = \tau_\perp\left(\underline{f}\right) - \tau_\perp^c\left(\underline{z}\right), \qquad\qquad \varphi_\parallel\left(\underline{f}, \underline{z}\right) = \tau_\parallel\left(\underline{f}\right) - \tau_\parallel^c\left(\underline{z}\right) \qquad (4.40)$$

in a way which corresponds to elliptic flow rules in bulk material plasticity [cf. Fritzen et al., 2013]. The critical tractions are specified as

$$\tau_\perp^c\left(\underline{z}\right) = \left\langle -z_\perp - \alpha_\perp z_\parallel - \tau_\perp^s \right\rangle_+, \qquad \tau_\parallel^c\left(\underline{z}\right) = \left\langle -z_\parallel - \alpha_\parallel z_\perp - \tau_\parallel^s \right\rangle_+ \qquad (4.41)$$

with the stopping parameters $\tau_\perp^s, \tau_\parallel^s \geq 0$ and with the coupling parameters $\alpha_\perp, \alpha_\parallel > 0$. The definition of the transversely isotropic SDCZ damage model is completed with the dual dissipation potential

$$\breve{\phi}^*\left(\underline{f}, \underline{z}\right) = \frac{\dot{\delta}_0 \, \sigma_d}{m+1} \left(\frac{\left\langle \varphi_\perp\left(\underline{f}, \underline{z}\right)\right\rangle_+}{\sigma_d}\right)^{m+1} + \frac{\dot{\delta}_0 \, \sigma_d}{m+1} \left(\frac{\left\langle \varphi_\parallel\left(\underline{f}, \underline{z}\right)\right\rangle_+}{\sigma_d}\right)^{m+1} \qquad (4.42)$$

with viscous regularization parameters as for the isotropic SDCZ damage model. For convenience, the same regularization is applied to both overstress functions.

4.8 Numerical examples involving SDCZ damage models

4.8.1 Large scale bridging in unidirectional fiber reinforced composites

According to Sørensen & Jacobsen [2003], cohesive zones are particularly useful for the modeling of large scale bridging, i.e., for "failure process zones that are long in one dimension but small in the perpendicular direction" [quote from Sørensen &
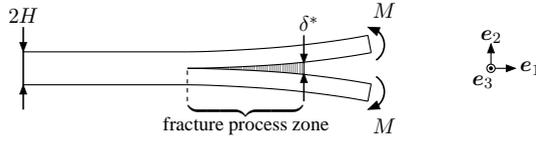
Figure 4.9: Sketch of a specimen for symmetric DCB testing with pure moment bending, as considered by Sørensen & Jacobsen [1998].

Jacobsen, 2003, p. 1842]. Large scale bridging in unidirectional carbon fiber/epoxy matrix composites has been investigated through symmetric DCB tests with pure bending moments by Sørensen & Jacobsen [1998]. A sketch of the DCB specimens used in their experiments is shown in Figure 4.9. The benefit of a symmetric DCB setup where the load is only applied in terms of a moment M is that the strain energy release rate G can be determined via a J-integral approach. Following Sørensen & Jacobsen [1998], the strain energy release rate is

$$G = 12 \left(1 - \nu_{\mathrm{lt}}\nu_{\mathrm{tl}}\right) \frac{M^2}{B^2 H^3 E_{\mathrm{l}}} \tag{4.43}$$

under the assumption of plane strain, where H and B denote half the beam height and the beam width, respectively, while E_{l}, ν_{lt}, and ν_{tl} are elastic properties of the transversely isotropic composite material (cf. Appendix A.3.2). At ongoing fracture, the strain energy release rate G coincides with the crack growth resistance G^{r}. During the experiments, G^{r} and the end-opening of the bridging zone δ^* (cf. Figure 4.9) are recorded. Two experimental G^{r}–δ^* curves from Sørensen & Jacobsen [1998] are reproduced in Figure 4.10. Following Li & Ward [1989] and Suo et al. [1992], the tensile traction–separation curve can be estimated via

$$\breve{t}_\perp(\delta^*) = \frac{\partial G^{\mathrm{r}}}{\partial \delta^*}. \tag{4.44}$$

This relation has been exploited by Leuschner et al. [2015] in order to demonstrate the capability of the isotropic SDCZ damage model (cf. Section 4.7) to describe the observed fiber cross-over bridging. The numerical results presented in this Section are reproduced from Leuschner et al. [2015]. For power-law softening as well as for bi-exponential softening, the model parameters have been adjusted such that the $\breve{W}^{\mathrm{s}}$–$\delta_\perp$ relationships (also shown in Figure 4.10) fit to the experimental G^{r}–δ^* curves. For both types of softening, the same stiffness k and the same initial critical traction τ_0 are used as well as identical viscous regularizations according to (4.30) that yield almost rate-independent behavior, and the stopping parameter τ^{s} is set to zero. All parameters of the fitted SDCZ models are given in Table C.1 in Appendix C.1. In view of Figure 4.10 it appears that both types of softening allow to approximate the experimental observation sufficiently well. However, bi-exponential softening is slightly preferable because the steady-state crack growth which is reported by Sørensen & Jacobsen [1998] for $\delta^* \geq 4\,\mathrm{mm}$ is captured better.
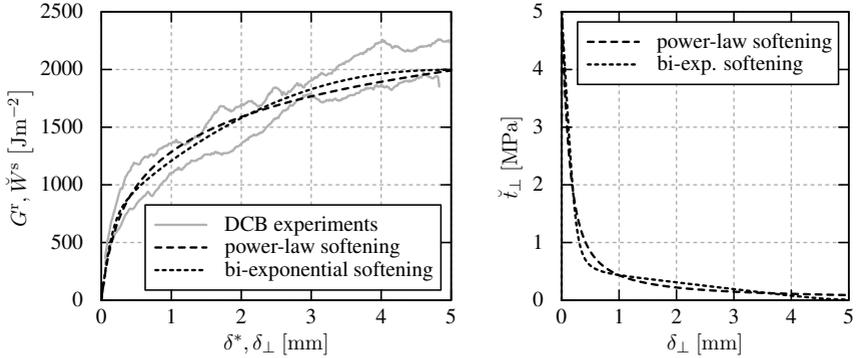
Figure 4.10: *Left:* experimentally determined G^{r}–δ^* curves for fiber cross-over bridging in a unidirectional fiber composite [reproduced from Sørensen & Jacobsen, 1998] alongside fitted $\breve{W}^{\mathrm{s}}$–δ relationships of isotropic SDCZ damage models with different types of softening behavior. *Right:* tensile traction–separation relationships corresponding to the fitted SDCZ damage models.

The traction–separation relationships obtained from the isotropic damage models fitted to the DCB experiments are displayed on the right-hand side of Figure 4.10. Note that the experimental G^{r}–δ^* curves begin at end-openings δ^* around 0.05 mm. It is stressed that for δ^* smaller than that, the shape of the traction–separation curves is thus merely hypothetical. One might assume linear elastic behavior in that range, but Sørensen & Jacobsen [1998] state that the specimen was loaded prior to the experiment in which the displayed data were collected. For this prestage they report unstable crack growth with significant load drop. Therefore, damaging behavior is assumed already for end-openings below 0.05 mm, and the initial stiffness is set to a very high value such that the initial range of (tensile) normal separations, in which the SDCZ damage models behave linearly elastic, is almost negligible.

4.8.2 Mixed mode behavior of SDCZ damage models compared to the CZM of van den Bosch et al. [2006]

One of the most recognized CZMs in the literature is the exponential model of Xu & Needleman [1993], which is an SPCZ model defined by the potential

$$\breve{\psi}(\boldsymbol{\delta}) = G_{\perp}^{\mathrm{c}} + G_{\perp}^{\mathrm{c}} \exp\left(-\frac{\delta_{\perp}}{\delta_{\perp}^{\mathrm{c}}}\right) \left[\left(1 - r + \frac{\delta_{\perp}}{\delta_{\perp}^{\mathrm{c}}}\right) \frac{1-q}{r-1} \right. \tag{4.45}$$

$$\left. - \left(q + \frac{r-q}{r-1}\frac{\delta_{\perp}}{\delta_{\perp}^{\mathrm{c}}}\right) \exp\left(-\left(\frac{\delta_{\|}}{\delta_{\|}^{\mathrm{c}}}\right)^2\right) \right]. \tag{4.46}$$

Here, $\delta_\perp^\mathrm{c}$ and $\delta_\parallel^\mathrm{c}$ are the normal and the tangential characteristic length, r and q are dimensionless coupling parameters, and $G_\perp^\mathrm{c}$ is the mode I CERR. As elucidated by van den Bosch et al. [2006], realistic coupling of normal and tangential behavior is obtained only for $q = 1$. In this case, the model is independent of r and the CERR is isotropic. This is a severe limitation in view of what has been discussed in Section 4.2, and it has motivated the proposal of an improved exponential CZM for mixed-mode decohesion by van den Bosch et al. [2006]. The improved model is obtained by setting $q = 1$ in (4.45) and (4.46), computing the tractions via (4.12), and replacing the mode I CERR $G_\perp^\mathrm{c}$ by the mode II CERR $G_\parallel^\mathrm{c}$ in the equation defining the shear tractions. The resulting traction–separation law, which is no longer an SPCZ model, reads

$$\breve{t}_\perp(\boldsymbol{\delta}) = \frac{G_\perp^\mathrm{c}}{\delta_\perp^\mathrm{c}} \frac{\delta_\perp}{\delta_\perp^\mathrm{c}} \exp\left(-\frac{\delta_\perp}{\delta_\perp^\mathrm{c}}\right) \exp\left(-\left(\frac{\delta_\parallel}{\delta_\parallel^\mathrm{c}}\right)^2\right), \tag{4.47}$$

$$\breve{t}_\parallel(\boldsymbol{\delta}) = 2\frac{G_\parallel^\mathrm{c}}{\delta_\parallel^\mathrm{c}} \frac{\delta_\parallel}{\delta_\parallel^\mathrm{c}} \left(1 + \frac{\delta_\perp}{\delta_\perp^\mathrm{c}}\right) \exp\left(-\frac{\delta_\perp}{\delta_\perp^\mathrm{c}}\right) \exp\left(-\left(\frac{\delta_\parallel}{\delta_\parallel^\mathrm{c}}\right)^2\right). \tag{4.48}$$

Both for the original model of Xu & Needleman [1993] and for the modification of van den Bosch et al. [2006] it is found that

$$\delta_\perp^\mathrm{c} = \operatorname*{argmax}_{\delta_\perp} \breve{t}_\perp(\delta_\perp \breve{\boldsymbol{n}}), \qquad\qquad \frac{\sqrt{2}}{2}\delta_\parallel^\mathrm{c} = \left\|\operatorname*{argmax}_{\boldsymbol{\delta}_\parallel} \breve{t}_\parallel\left(\boldsymbol{\delta}_\parallel\right)\right\|_2 \tag{4.49}$$

hold, i.e., the normal characteristic length is associated to the peak normal traction for purely normal loading (as mentioned in Section 4.3), but the same does not hold for the tangential direction. As discussed by Kolluri et al. [2014], this can lead to physical misinterpretation of the tangential characteristic length $\delta_\parallel^\mathrm{c}$. Therefore, Kolluri et al. [2014] use a slightly modified version of the model proposed by van den Bosch et al. [2006] where the tangential characteristic length $\delta_\parallel^\mathrm{c}$ is associated to the peak shear traction under pure mode II loading. The modified traction–separation law reads

$$\breve{t}_\perp(\boldsymbol{\delta}) = \frac{G_\perp^\mathrm{c}}{\delta_\perp^\mathrm{c}} \frac{\delta_\perp}{\delta_\perp^\mathrm{c}} \exp\left(-\frac{\delta_\perp}{\delta_\perp^\mathrm{c}}\right) \exp\left(-\frac{1}{2}\left(\frac{\delta_\parallel}{\delta_\parallel^\mathrm{c}}\right)^2\right), \tag{4.50}$$

$$\breve{t}_\parallel(\boldsymbol{\delta}) = \frac{G_\parallel^\mathrm{c}}{\delta_\parallel^\mathrm{c}} \frac{\delta_\parallel}{\delta_\parallel^\mathrm{c}} \left(1 + \frac{\delta_\perp}{\delta_\perp^\mathrm{c}}\right) \exp\left(-\frac{\delta_\perp}{\delta_\perp^\mathrm{c}}\right) \exp\left(-\frac{1}{2}\left(\frac{\delta_\parallel}{\delta_\parallel^\mathrm{c}}\right)^2\right), \tag{4.51}$$

and the characteristic lengths are related to the normal/tangential peak tractions $\breve{t}_\perp^\wedge$ and $\breve{t}_\parallel^\wedge$ via

$$\delta_\perp^\mathrm{c} = \frac{G_\perp^\mathrm{c}}{\breve{t}_\perp^\wedge} \exp\left(-1\right), \qquad\qquad \delta_\parallel^\mathrm{c} = \frac{G_\parallel^\mathrm{c}}{\breve{t}_\parallel^\wedge} \exp\left(-\frac{1}{2}\right). \tag{4.52}$$

In the following numerical example taken from Leuschner et al. [2015], the CZM from (4.50) and (4.51) is used as a theoretical reference with regard to mixed-mode

reference peak tractions			SDCZ damage model	
$\mathcal{R}^\wedge$ [−]	$\breve{t}_\perp^\wedge$ [MPa]	$\breve{t}_\parallel^\wedge$ [MPa]	$\breve{t}_\perp^\wedge$ [MPa]	$\breve{t}_\parallel^\wedge$ [MPa]
$^1/_3$	225	75	222	78
$^2/_3$	180	120	179	123
1	150	150	157	144
$^3/_2$	120	180	120	196

Table 4.1: Reference peak tractions and approximations with SDCZ damage models fitted to the mixed mode behavior of the exponential CZM of van den Bosch et al. [2006].

behavior because it has been specifically proposed for physically feasible descriptions of mode coupling. The pure mode CERRs are fixed at $G_\perp^c = 1 \text{ Jm}^{-2}$ and $G_\parallel^c = 2 \text{ Jm}^{-2}$ and the sum of the peak tractions is kept constant at $\breve{t}_\perp^\wedge + \breve{t}_\parallel^\wedge = 300$ MPa while their ratio $\mathcal{R}^\wedge = \breve{t}_\parallel^\wedge / \breve{t}_\perp^\wedge$ is varied. Four sets of parameters of the transversely isotropic SDCZ damage model have been identified in order to approximate the mixed mode behavior of the modified model from (4.50) and (4.51) for four different values of $\mathcal{R}^\wedge$. More precisely, the model parameters have been chosen such that the work of separation was approximated well for proportional loadings over the whole range of mode angles, while at the same time the reference values of the peak tensile traction and the peak shear traction were replicated approximately. These parameters are given in Table C.2 in Appendix C.1. Power-law type softening behavior as described by (4.31) has been adopted. Table 4.1 shows the reference values of the peak tractions and the approximations using the SDCZ models. It is found that the aberrations from the reference values are below 5% except for the case $\mathcal{R}^\wedge = {}^3/_2$, where the peak shear traction is approximately 9% off.

During the calibration of the SDCZ parameters, the focus has been put on the dependence of the CERR on the mode angle, which is shown at the top left of Figure 4.11. It is observed that the transversely isotropic SDCZ model can replicate the curves of the improved exponential CZM of van den Bosch et al. [2006] with quite satisfactory accuracy for all considered ratios $\mathcal{R}^\wedge$ of peak tractions. In addition to proportional loadings, the work of separation has also been evaluated for right-angled loading paths where the interface was first loaded up to the normal separation $\delta_\perp^\urcorner$ or the tangential separation $\delta_\parallel^\urcorner$ under pure mode I/mode II conditions and then broken by gradually increasing the tangential/normal separation. Illustrations of such loading paths and the corresponding results for the work of separation are displayed at the bottom of Figure 4.11. The quantitative agreement between the curves of the SDCZ model and of the reference model is not as good as for proportional loadings, which was to be expected because right-angled loading paths have not been considered for the calibration of the model parameters. However, the qualitative agreement is still quite good, and all curves exhibit smooth monotonous transitions between the pure mode I CERR and the pure mode II CERR. This kind of behavior is expected by intuition but is not found for
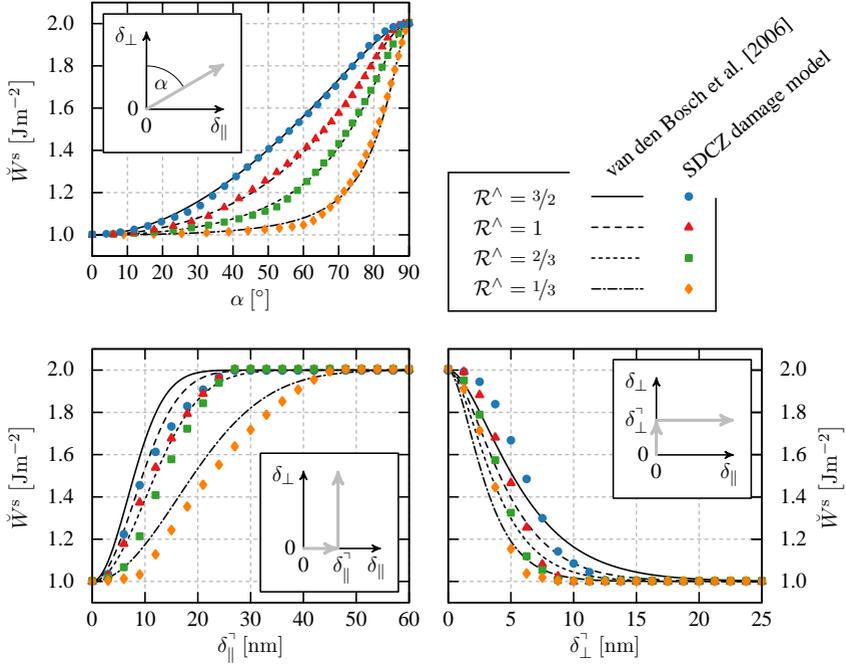
Figure 4.11: Comparison between SDCZ damage model and exponential CZM by van den Bosch et al. [2006] for different ratios $\mathcal{R}^\wedge = \breve{t}_\parallel^\wedge / \breve{t}_\perp^\wedge$ of peak tractions. *Top left:* work of separation for proportional loadings. *Bottom left:* work of separation for pure shear loading up to $\delta_\parallel^\urcorner$ followed by breaking of the interface in normal direction. *Bottom right:* work of separation for pure tensile loading up to $\delta_\perp^\urcorner$ followed by breaking of the interface in tangential direction.

the exponential CZM of Xu & Needleman [1993], as criticized by van den Bosch et al. [2006]. Thus it is concluded that the SDCZ model is able to qualitatively capture one of the main improvements that were intended by van den Bosch et al. [2006] regarding mixed mode behavior.

For completeness, the traction–separation behavior for proportional loadings is depicted in Figure 4.12 for the ratio $\mathcal{R}^\wedge = 2/3$. For the corrected, improved exponential reference model, the characteristic lengths corresponding to the separations at the peak tractions are obtained from (4.52) as $\delta_\perp^c = 2.04$ nm and $\delta_\parallel^c = 10.11$ nm. Figure 4.12 shows that the peak tractions of the SDCZ model under pure mode loadings are attained at rather similar interface separations. Overall, the regions of non-negligible cohesive tractions are shaped differently but have similar dimensions for the SDCZ model and for the reference model.
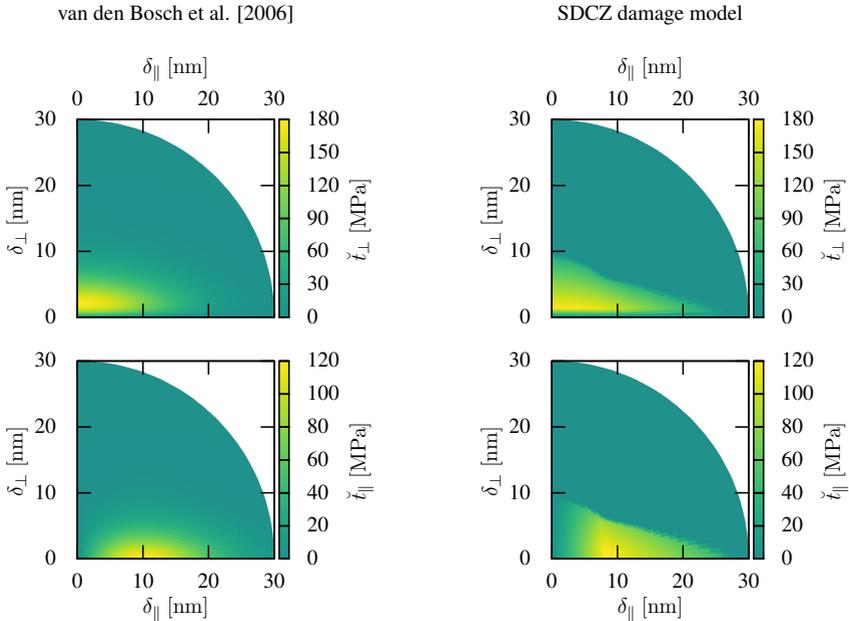
Figure 4.12: Comparison between SDCZ damage model and exponential CZM by van den Bosch et al. [2006]: traction–separation behavior for proportional loadings.

4.8.3   FE simulations of MMMB tests

To meet increasing requirements with regard to both miniaturization and versatility of electronic systems, the so-called system in package (SiP) design is used. An SiP consists of a number of electronic components that are vertically stacked, resulting in a layered structure with several interfaces between different materials. Such interfaces "are often recognized as critical regions for the reliability of these products" [quote from Kolluri et al., 2009, p. 183] because delamination induced by thermal expansion frequently occurs during manufacturing or during device operation [see also Evans & Hutchinson, 1995, Dauskardt et al., 1998]. Thus, understanding the mechanics of interfaces in SiPs is crucial to enable improvements with respect to reliability.

One specific type of interface that is relevant in SiP devices and has been much considered in the literature [see, e.g., Pan et al., 1990, Lee & Park, 2002, Thijsse et al., 2008] is the boundary layer between a copper lead frame (CuLF) and molding compound epoxy (MCE). This type of interface has also been examined by Kolluri et al. [2009, 2011] by means of in situ MMMB experiments as introduced in Section 4.2. Further, experimental–numerical comparisons involving FE simulations of MMMB tests have been presented by Kolluri et al. [2012] and by Samimi et al. [2013]. While

|	CuLF	MCE
Young's moduli	120 GPa	30 GPa
Poisson's ratios	0.33	0.25
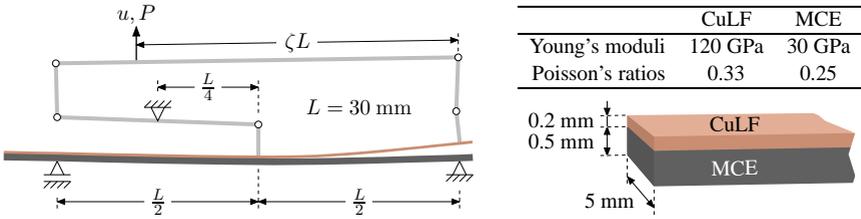
Figure 4.13: *Left:* true to scale side view of a specimen loaded at the position $\zeta = 0.8$ with sketch of the loading device. *Right:* dimensions of the bi-layer specimen and isotropic elastic properties of the layers.

a Smith–Ferrante type CZM based on an effective displacement and on an effective traction is employed by Kolluri et al. [2012], Samimi et al. [2013] make use of the improved exponential CZM of van den Bosch et al. [2006] that has been presented in Section 4.8.2. Details regarding the dimensions of the bi-layer samples as well as the elastic parameters used in the FE simulations are given in Figure 4.13. Note that the interface is comparatively weak such that the assumption of linear elastic bulk behavior is permissible. Similar FE simulations have also been run by Leuschner et al. [2015] with the transversely isotropic SDCZ damage model from Section 4.7 in order to explore the model's capability to capture experimentally determined mixed mode behavior. The commercial FE software Abaqus/Standard has been used for this purpose, and instead of employing elaborate cohesive interface elements like the enriched model of Samimi et al. [2009], the standard surface interaction implementation of Abaqus was used. Numerical artifacts like jerky detachment of pairs of opposite nodes, which is often observed at damaging interfaces, were avoided by using a rather fine discretization, and a convergence study has been conducted to ensure virtually mesh-independent simulation results. The constitutive SDCZ damage model was incorporated into the FE model via a user-defined UINTER subroutine. One set of parameters for the SDCZ damage model has been identified (see Table C.3 in Appendix C.1) which yields good accordance of simulation results and experimental data for the whole range of mode angles that has been considered in the experiments of Kolluri et al. [2011]. The bi-exponential form (4.33) was adopted for both involved softening potentials, and the special case $\tau_1 = 0$, corresponding to a formulation which is in fact "mono-exponential", was assumed for simplicity. The related numerical results from Leuschner et al. [2015] are presented in the following.

The key data collected in the MMMB experiments and in the simulations are the histories of the loading displacement u and of the associated force P (see Figure 4.13). Figure 4.14 shows P–u curves for four different loading configurations of the MMMB device. The relation between the loading position (parameterized by ζ, see Figure 4.13) and the mode angle α depends on the geometry of the specimen and on its constitutive properties and is specified for the considered CuLF–MCE samples on the left-hand side of Figure 4.15. Obviously, the limit cases $\zeta = 0$ and $\zeta = 1$ correspond to a DCB
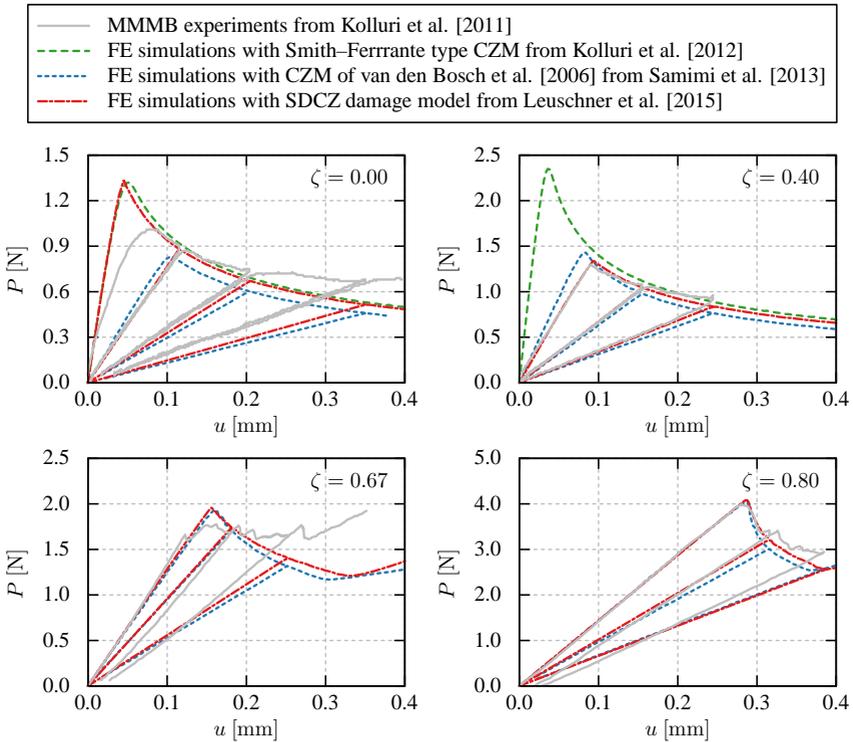
Figure 4.14: Experimental and numerical force–displacement curves for MMMB tests with the setup illustrated in Figure 4.13 for four different mode mixities controlled via the loading position ζ.

test and to an ENF test, respectively. Pure mode II conditions are already obtained at $\zeta = 0.89$, and overestimations of the CERR due to compressive forces resulting in frictional dissipation appear for values of ζ higher than that. Looking at the experimental curves in Figure 4.14, it occurs that the curve for pure mode I transitions smoothly from the almost linear initial elastic slope into the damaging regime, which is in contrast to the other mode mixities. Kolluri et al. [2011] state that this is because the pre-crack of approximately 6 mm length, which has been generated with a thin knife at one end of each sample, did at the beginning not exhibit a sharp, stable crack front normal to the crack propagation direction. This is why this first loading–unloading cycle has not been considered by Samimi et al. [2013]. Clearly, the initial elastic slopes of the force–displacement curves in Figure 4.14 are governed by the length of the pre-crack, and different assumptions regarding the length of the pre-crack also serve as an explanation for the deviation of the simulation by Kolluri et al. [2012] from the other curves for the case $\zeta = 0.4$. For the three mixed mode cases, the simulations based on the SDCZ
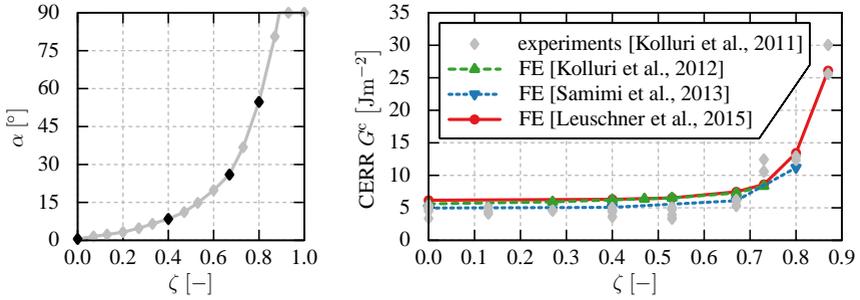
Figure 4.15: *Left:* mode angle at CuLF–MCE interface versus load configuration of MMMB device [data from Kolluri et al., 2011]. The 16 discrete possible loading positions are indicated by rhombuses, and the positions considered in Figure 4.14 are highlighted by black rhombuses. *Right:* critical energy release rate of CuLF–MCE interface at varying mode mixities: experimental data versus FE simulation results using different CZMs.

damage model yield results rather similar to the ones obtained by Samimi et al. [2013]. The agreement with the experimental curves is regarded quite satisfactory, and it is particularly convincing for $\zeta = 0.4$. In the case $\zeta = 0.67$, the non-smoothness of the experimental curve aggravates more accurate reproduction by numerical simulations. For the pure mode I case, the curve obtained with the SDCZ model is close to the one computed with the Smith–Ferrante CZM by Kolluri et al. [2012], and both match the experimental data better than the curve obtained by Samimi et al. [2013] with the CZM of van den Bosch et al. [2006]. All in all, it is concluded that the FE simulations based on the SDCZ damage model replicate the experimental force–displacement curves of Kolluri et al. [2011] at least as accurate as the simulations conducted by Kolluri et al. [2012] or Samimi et al. [2013] for all four considered mode mixities.

The mechanical work dissipated during a loading–unloading cycle of an MMMB test is represented by the area enclosed by the respective P–u curve. In order to estimate the CERR at the present mode angle, the advancement of the crack front during the loading stage of the cycle must be known. A substantial advantage of the MMMB apparatus is its suitability for in situ experiments which allows to determine the positions of the crack tip at load reversals via scanning electron microscopy. Thereby, the CERR was experimentally estimated by Kolluri et al. [2011] as shown on the right-hand side of Figure 4.15 along with the corresponding values obtained from the FE simulations. Two additional simulations for $\zeta = 0.73$ and for $\zeta = 0.87$ have been run by Leuschner et al. [2015], and for each mode mixity ζ, the CERR was computed as the average of the values obtained from the considered load cycles. Notably, the CERRs obtained with the SDCZ damage model almost coincide with those computed by Kolluri et al. [2012] using a Smith–Ferrante type CZM in the whole range of mode mixities up to $\zeta = 0.73$ that has been considered by Kolluri et al. [2012]. It appears that these two interface models were calibrated such as to slightly overestimate the experimentally determined CERRs for

values of ζ up to 0.67, and the simulation results of Samimi et al. [2013] using the CZM of van den Bosch et al. [2006] are a little closer to the experimental data in that range. However, the SDCZ model was adjusted such that the experimental results for $\zeta = 0.87$ were still captured well, and the slight overestimation of CERRs at lower mode angles is attributed to a tradeoff between the extreme mode angles.

4.9 Summary and discussion

When choosing a CZM for a specific application it is important to not only consider the physical behavior of the modeled interface but also the numerical framework that is used and the type of loadings that will be treated. Regarding numerical frameworks, attention was limited to intrinsic cohesive zones. The type of loading determines whether implicit modeling of dissipative processes at the interface in the style of hyperelastic material models is sufficient or if an explicit description of dissipation, e.g., via evolution laws for internal variables, is required. The SDCZ framework, which has been introduced in Section 4.6 for interfaces as an equivalent to the class of GSMs for bulk materials, incorporates explicit evolution laws for internal variables which are derived from a dual dissipation potential. Like GSMs, SDCZs exhibit a number of favorable properties such as a variational structure, thermodynamic consistency, a symmetric algorithmic tangent operator which is easy to compute, and the possibility of a unified implementation with the first and second order gradients of the model-specific potential functions outsourced to exchangeable subroutines.

An isotropic and a transversely isotropic SDCZ damage model proposed by Leuschner et al. [2015] were described in Section 4.7, and numerical examples of these models taken from Leuschner et al. [2015] have been presented in Section 4.8. The isotropic damage model is quite versatile with respect to the shape of the traction–separation behavior due to the possibility to incorporate different softening potentials. For the transversely isotropic damage model, this shape is much more difficult to control. Also, the relatively high number of constitutive parameters (of which some interact in a rather unintuitive manner) make the calibration of the transversely isotropic model difficult. However, despite the restrictions imposed on the modeling of mixed mode behavior by the SDCZ framework, the numerical examples demonstrated the model's capability to capture significantly anisotropic CERRs combined with a physically reasonable description of arbitrary load paths as well as its applicability in the context of FE simulations.

Chapter 5:
Homogenization of heterogeneous media

5.1   Introduction

Mathematical problems that exhibit relevant characteristics at multiple spatial and/or temporal scales are referred to as *multiscale problems* and arise in various scientific areas as well as in practical engineering applications. The scales are typically distinct to a degree which prohibits naive approaches with discretizations comprehending two or more scales (even if the same numerical methodology is applicable to each scale). Therefore, dedicated multiscale methods are required to couple separated but interacting scales. In the field of material modeling, multiscale methods have significant relevance because several length scales naturally emerge when real materials are investigated. Consequently, a large community of scientists from various disciplines like mathematics, physics, chemistry, and mechanical as well as civil engineering is concerned with research on scale-bridging methods for natural and artificial materials.

At a fundamental level, materials are investigated by molecular dynamics or atomistic simulations based on classical mechanical laws or on quantum mechanics. Several competing methods have been proposed to establish a link from such approaches to continuum theory [a short literature review can be found in Lee & Basaran, 2013]. The special case of crystal plasticity is addressed by so-called discrete dislocation dynamics (DDD) models [e.g., Zbib et al., 2005]. Above the atomistic scale, artificial as well as natural materials such as wood, biological tissue, or porous geomaterials exhibit more than one continuum scale. For many applications, phenomenological constitutive models defined at the superordinate continuum scale, referred to as *macroscale*, are sufficient. However, in other contexts like materials engineering it is necessary to resolve the smallest relevant scale called *microscale* as well as possible intermediate *mesoscales*. Multiscale approaches bridging the gap between two continuum scales are commonly referred to as *homogenization* techniques. These are particularly relevant for composite materials which are deliberately designed to have certain mechanical, thermal, or otherwise favorable properties.

5.2   Overview

Homogenization of materials with heterogeneous microstructures has a rich history beginning with the upper Voigt bound [Voigt, 1910] and the lower Reuss bound [Reuss, 1929]. Some of the most recognized analytical approaches proposed in the sequel are the Hashin–Shtrikman bounds [Hashin & Shtrikman, 1963] based on variational calculus,

so-called self-consistent schemes [Hill, 1965] derived from the solution for an ellipsoidal inclusion by Eshelby [1957, 1959], and the micromechanical model of Mori & Tanaka [1973]. While the above-mentioned homogenization principles are aimed at elastic problems, semi-analytical methods allow to estimate the effective behavior of some nonlinear inelastic composites. Besides seminal works of Ponte Castañeda [1991, 1992], the two-part study of Lahellec & Suquet [2007a,b] and recent results of Idiart & Vincent [2015] and Ponte Castañeda [2015] are worth mentioning [see also Jöchen, 2013, for an overview].

Computational homogenization techniques are brought into play when (semi-) analytical methods are too inaccurate or not applicable, e.g., due to overly complex material properties. Like many other problems arising in solid mechanics, homogenization problems are frequently solved with the finite element method. When integrated into structural FEM simulations, effective material properties predicted by FE homogenization procedures give rise to nested FE schemes widely known under the label FE^2 ["FE square", e.g., Feyel & Chaboche, 2000]. Fourier-based homogenization techniques originating from the seminal papers of Dumontet [1983] and Moulinec & Suquet [1994, 1995, 1998] constitute an alternative class of solvers for homogenization problems that have attracted increased attention in the past decade [see Lebensohn & Needleman, 2016, de Geus et al., 2017, Kochmann et al., 2018, for recent contributions]. Assuming uniform discretizations of microstructures, homogenization problems are formulated such that a substantial amount of the overall algorithmic effort arises in the form of discrete convolutions, which are efficiently computed via fast Fourier transform (FFT) algorithms. Due to their relatively good computational efficiency, such methods are particularly useful for microstructures represented by pixel/voxel data with high resolutions, as obtained from experimental imaging techniques, where already the generation of finite element meshes would pose complex tasks. However, the drawback of uniform spatial discretizations is their poor description of non-aligned surfaces, and despite proposals to face this issue, e.g., by the use of *composite voxels* [Kabel et al., 2015, 2017], FE meshes are more appropriate in that regard. Thus, homogenization problems with consideration of imperfect interfaces, e.g., at phase boundaries, are generally approached with nonuniform FE discretizations.

Standard FEM solvers and FFT-based solvers for homogenization problems are referred to as *full-field* methods because they operate in high-dimensional solution spaces which are constructed without restrictive assumptions concerning physical feasibility, i.e., background knowledge or empirical evidence about possible solutions is not exploited. Given sufficiently fine spatial discretizations, all relevant details of the solution fields are captured at the expense of vast numbers of degrees of freedom (DOF). Clearly, large numbers of DOF are associated with high computational cost, which rapidly becomes critical for applications with many queries, such as two-scale simulations of real structures. Thus, despite the permanently increasing performance of computers, two-scale simulations of real structures using full-field homogenization methods (like FE^2) remain limited to rather small-sized academic problems, or viable only for users with access to massive computing resources. These limitations have motivated the
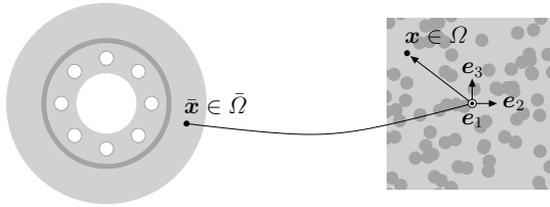
Figure 5.1: Sketch of a two-scale problem with a macroscopic structural part *(left)* with a heterogeneous microstructure represented by an RVE *(right)*.

development of computational homogenization schemes that make use of model order reduction (MOR) techniques [e.g., Yvonnet & He, 2007, Oskay & Fish, 2007, Hernández et al., 2014, Redeker & Haasdonk, 2015, Wulfinghoff et al., 2018]. One of the main topics of this thesis is a reduced basis MOR homogenization scheme for composite materials with imperfect interfaces, which is presented in Chapter 7. The remainder of the present Chapter introduces basic concepts for computational homogenization which are fundamental for the subsequent Chapters 6 and 7.

5.3 General aspects of two-scale problems

Solid structures made of heterogeneous materials pose two-scale problems when the characteristic material length $l_\mathrm{\mu}$ is much smaller than the structural characteristic length l_m. Under such circumstances, the constitutive behavior can be considered homogeneous on the macroscopic structural level but depends strongly on the heterogeneous microstructure. In order to determine the effective homogenized response, computational homogenization schemes are based on the assumption that so-called *representative volume elements* (RVEs) can be defined which capture the geometrical characteristics of the material at the small scale [see, e.g., Ostoja-Starzewski, 2006]. As in the majority of the related literature, cuboidal RVEs are assumed throughout this work, although other approaches exist [e.g., Grasset-Bourdel et al., 2011, Glüge et al., 2012]. The bulk of the macroscopic structure being denoted $\bar{\Omega} \subset \mathbb{E}^3$, every position $\bar{x} \in \bar{\Omega}$ is theoretically assigned an RVE such that the centroid of the RVE is identified with $\bar{x}$ as shown in Figure 5.1. Each RVE is decomposed into the bulk Ω and into the imperfect interface $\mathscr{I}$ in agreement with the basic assumptions from Chapter 2, and the outward boundary of the RVE is denoted Γ. Positions within the bulk or on the interface of the RVE are denoted x, $\check{x}$, respectively, and are specified with respect to a separate coordinate system defined at the microscale such that its origin coincides with the RVE's centroid. Quantities defined at the RVE level are referred to as *local*, while macroscopic quantities are called *global* and are denoted with an overbar $\bar{\bullet}$. The essential operations required to create the link between local and global quantities are volume averaging and surface averaging. For additive quantities f and $\check{f}$ defined in the bulk Ω and on the interface $\mathscr{I}$, re-

spectively, the volume averaging operator $\langle \bullet \rangle_{\Omega}$ and the surface averaging operator $\langle \bullet \rangle_{\mathscr{I}}$ are defined by

$$\left\langle \boldsymbol{f} \right\rangle_{\Omega} = \frac{1}{|\Omega|} \int\limits_{\Omega} \boldsymbol{f}(\boldsymbol{x}, \ldots) \, \mathrm{d}V, \qquad\qquad \left\langle \breve{\boldsymbol{f}} \right\rangle_{\mathscr{I}} = \frac{1}{|\Omega|} \int\limits_{\mathscr{I}} \breve{\boldsymbol{f}}(\breve{\boldsymbol{x}}, \ldots) \, \mathrm{d}A. \qquad (5.1)$$

Before addressing mechanical and thermal homogenization separately, a collection of the most important common assumptions, inspired by Fritzen [2011], is given.

[H1] The material length is clearly separated from the characteristic length of the macroscopic structure ($l_{\mu} \ll l_{\mathrm{m}}$).

[H2] A continuum description is valid at both scales, i.e., the microscopic scale is well above the atomistic length scale.

[H3] The RVE is void-free in the reference configuration (cf. Section 2.1).

[H4] The constitutive relations at the microscopic level are known.

5.4   Mechanical two-scale problems

For mechanical problems, the following additional assumptions are made.

[HM1] A geometrically linear description (cf. Section 2.5) is adopted at both scales.

[HM2] The processes are slow enough to be treated as quasistatic at both scales.

[HM3] At the microscale, body forces acting on the bulk or on the interface are negligible.

[HM4] The macroscopic displacement $\bar{\boldsymbol{u}}$ has a microscopic counterpart $\boldsymbol{u}$ that can be described by a first order Maclaurin expansion of the macroscopic displacement superposed with a displacement fluctuation field $\tilde{\boldsymbol{u}}$ which does not contribute to the effective deformation gradient $\bar{\boldsymbol{H}}$.

From the assumptions **[HM2]** and **[HM3]** it follows that the static equilibrium conditions to be considered at the RVE level are obtained from the balance of linear momentum (2.86) as[10]

$$\mathrm{div}(\boldsymbol{\sigma}) = \boldsymbol{0} \qquad \text{in } \Omega, \qquad\qquad [\![\boldsymbol{t}]\!] = \boldsymbol{0} \qquad \text{at } \mathscr{I}. \qquad (5.2)$$

Exploiting the continuity of tractions $\boldsymbol{t}$ at the interface, the effective global stress is obtained as the volume average of the stress in the bulk

$$\bar{\boldsymbol{\sigma}} = \frac{1}{|\Omega|} \int\limits_{\Gamma} \boldsymbol{t} \otimes \boldsymbol{x} \, \mathrm{d}A = \langle \boldsymbol{\sigma} \rangle_{\Omega} \qquad (5.3)$$

---

[10]Note that the static equilibrium conditions (5.2) and, thus, the considered mechanical homogenization problems, are independent of the volumetric mass density ϱ in the bulk and of the areal mass density $\breve{\varrho}$ at the interface.

using Gauss's theorem (2.38). The assumption **[HM4]** is translated into the equations

$$\boldsymbol{u}(\boldsymbol{x}) = \tilde{\boldsymbol{u}}(\boldsymbol{x}) + \bar{\boldsymbol{u}} + \bar{\boldsymbol{H}}\boldsymbol{x} + \mathcal{O}\left(\left\|\frac{\boldsymbol{x}}{l_\mu}\right\|_2^2\right), \qquad \int_\Gamma \tilde{\boldsymbol{u}} \otimes \boldsymbol{n}\, \mathrm{d}A = \boldsymbol{0} \qquad (5.4)$$

with the global displacement gradient $\bar{\boldsymbol{H}}$ given by

$$\bar{\boldsymbol{H}} = \frac{1}{|\Omega|} \int_\Gamma \boldsymbol{u} \otimes \boldsymbol{n}\, \mathrm{d}A = \langle \boldsymbol{H} \rangle_\Omega + \langle \boldsymbol{\delta} \otimes \check{\boldsymbol{n}} \rangle_{\mathscr{I}}. \qquad (5.5)$$

Here, the decomposition into bulk and interface contributions has been derived from Gauss's theorem (2.39). Since the behavior of the RVE is independent of rigid body motion, the global displacement $\bar{\boldsymbol{u}}$ is dropped in (5.7) without loss of generality. Choosing the first order Maclaurin expansion in (5.4) corresponds to the standard approach referred to as first order homogenization, which is often tacitly adopted. This linearization is justified if the macroscopic displacement field is sufficiently smooth, i.e., if its higher order gradients are small, or if the microstructure does not contain a fixed length scale. Then, an asymptotic analysis with $l_\mu/l_\mathrm{m} \to 0$, corresponding to virtual downscaling of the RVE, implies that higher order terms can be neglected in (5.4). These conditions are clearly injured by non-convex overall behavior which leads to localization and must be treated by higher order homogenization[11] methods [see, e.g., Kouznetsova et al., 2002, Geers et al., 2010, Jänicke & Steeb, 2012]. Unfortunately, these fundamental requirements are frequently violated, and many examples of first order homogenization schemes applied to damaging behavior are found in the literature.

5.4.1 Homogenization of bulk materials (HBM)

The aim of first order homogenization schemes (if nothing else is stated) is to determine the effective global response of a heterogeneous bulk material, which means that an effective stress–strain relation and, depending on the context, also an effective tangent stiffness operator are desired. From the description of the effective displacement gradient (5.5), the effective strain is immediately obtained as

$$\bar{\boldsymbol{\varepsilon}} = \frac{1}{|\Omega|} \int_\Gamma \mathrm{sym}\,(\boldsymbol{u} \otimes \boldsymbol{n})\, \mathrm{d}A = \langle \boldsymbol{\varepsilon} \rangle_\Omega + \langle \mathrm{sym}\,(\boldsymbol{\delta} \otimes \check{\boldsymbol{n}}) \rangle_{\mathscr{I}} = \mathrm{sym}\,\left(\bar{\boldsymbol{H}}\right). \qquad (5.6)$$

Attention is limited to strain-driven homogenization implemented with the common ansatz

$$\boldsymbol{u}(\boldsymbol{x}) = \tilde{\boldsymbol{u}}(\boldsymbol{x}) + \bar{\boldsymbol{\varepsilon}}\boldsymbol{x}, \qquad (5.7)$$

---

[11]This notion of higher order and, in particular, second order homogenization schemes must not be confused with the second order homogenization estimates of Ponte Castañeda [1996, 2015].
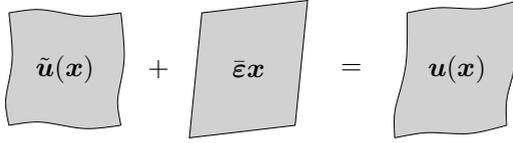
Figure 5.2: Illustration of periodic boundary conditions defined in (5.10) for HBM.

corresponding to a first order Maclaurin expansion in (5.4) with a restriction of the global displacement gradient $\bar{\boldsymbol{H}}$ to symmetric second order tensors[12]. The task for the homogenization scheme is to determine the microscopic fluctuation field $\tilde{\boldsymbol{u}}$ induced by the prescribed effective strain $\bar{\boldsymbol{\varepsilon}}$. In order to do so, the equilibrium conditions (5.2) must be supplemented with boundary conditions for the displacement fluctuation. The boundary conditions must be chosen such that the global mechanical work corresponds to the averaged mechanical work in the bulk and at the interface of the RVE

$$\bar{\boldsymbol{\sigma}} : \bar{\boldsymbol{\varepsilon}} = \langle \boldsymbol{\sigma} : \boldsymbol{\varepsilon} \rangle_\Omega + \langle \breve{\boldsymbol{t}} \cdot \boldsymbol{\delta} \rangle_{\mathscr{I}} \qquad \Leftrightarrow \qquad \int_\Gamma \boldsymbol{t} \cdot \tilde{\boldsymbol{u}} \, \mathrm{d}A = 0. \qquad (5.8)$$

This requirement is known as *Hill–Mandel condition*, and the equivalence in (5.8) is obtained with Gauss's theorem (2.38) and with the static conditions (5.2). Two types of boundary conditions which are obviously consistent with the Hill–Mandel condition and with the requirement from (5.4) are uniform kinematic boundary conditions (UKBC) defined by

$$\tilde{\boldsymbol{u}} = \boldsymbol{0} \qquad \text{on } \Gamma \qquad (5.9)$$

and *periodic boundary conditions* (PBC) characterized by

$$\tilde{\boldsymbol{u}}(\boldsymbol{x}_-) = \tilde{\boldsymbol{u}}(\boldsymbol{x}_+), \qquad\qquad \boldsymbol{t}(\boldsymbol{x}_-) = -\boldsymbol{t}(\boldsymbol{x}_+) \qquad (5.10)$$

for all pairs $\{\boldsymbol{x}_-, \boldsymbol{x}_+\} \subset \Gamma$ of opposite material points from opposing sides of the RVE (see Figure 5.2). Their main advantage being the enabling of smaller RVEs compared to UKBC [cf. Suquet, 1987], PBC are the most used type of boundary conditions and are applied in all numerical examples of homogenization for bulk materials in this work. While only applicable to periodic RVEs from a theoretical point of view, PBC are sometimes nevertheless used for arbitrary microstructures as well. When implemented in an FE framework [see, e.g., Fritzen & Böhlke, 2010], enforcement of the kinematic periodicity constraint on the displacement fluctuations $\tilde{\boldsymbol{u}}$ leads to solutions which also satisfy the anti-periodicity condition for the tractions $\boldsymbol{t}$ from (5.10) in the discretized weak form, i.e., in the sense of anti-periodic nodal forces.

---

[12]Note that (5.7) is consistent with (5.6) because of the property of the displacement fluctuation $\tilde{\boldsymbol{u}}$ postulated in (5.4). This consistency would still be fulfilled when accepting non-symmetric effective gradients satisfying $\mathrm{sym}\left(\bar{\boldsymbol{H}}\right) = \bar{\boldsymbol{\varepsilon}}$ instead of the prescribed effective strain $\bar{\boldsymbol{\varepsilon}}$ itself in (5.7).
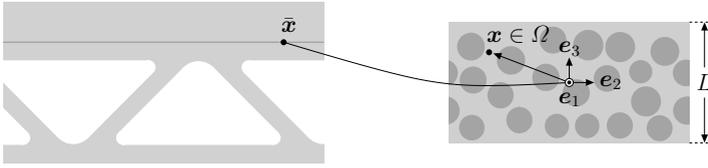
Figure 5.3: Sketch of a two-scale problem with a macroscopic structural part *(left)* comprising a heterogeneous thin layer represented by an RVE *(right)*.
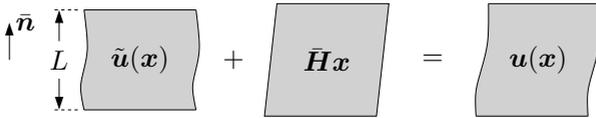
Figure 5.4: Illustration of hybrid boundary conditions for HTL.

5.4.2 Homogenization of thin layers (HTL)

The previously described homogenization approach is aimed at effective stress–strain relations. It is not applicable to a layer with a heterogeneous bulk microstructure if the characteristic length l_μ of the microstructure is not clearly separated from the layer thickness L. However, problems of this kind can be homogenized with modified boundary conditions [e.g., Matouš et al., 2008, Hirschberger et al., 2009]. If the layer thickness L is negligibly small compared to the dimensions of the surrounding structure (as illustrated in Figure 5.3), a representation of the layer's overall behavior in terms of an effective traction–separation law is feasible. Here, an approach with three independent global deformation modes governed by the global displacement jump $\bar{\delta}$ is pursued. With $\bar{n}$ denoting the unit normal on the thin layer, the ansatz for the microscopic displacement field is derived from the general formulation (5.4) according to

$$\boldsymbol{u}(\boldsymbol{x}) = \tilde{\boldsymbol{u}}(\boldsymbol{x}) + \bar{\boldsymbol{H}}\boldsymbol{x} \qquad \text{with } \bar{\boldsymbol{H}} = \frac{1}{L}\bar{\boldsymbol{\delta}} \otimes \bar{\boldsymbol{n}}. \tag{5.11}$$

In-plane stretch and in-plane shear are neglected here but could be incorporated either via prescribed global parameters in addition to $\bar{\delta}$ (corresponding to an enriched CZM) or as additional degrees of freedom (possibly resulting in a softer overall response). Hybrid boundary conditions combining the periodicity conditions from (5.10) for the in-plane directions with uniform kinematic boundary conditions (5.9) for the out-of-plane direction are imposed on the displacement fluctuations $\tilde{\boldsymbol{u}}$ (see Figure 5.4). Once the problem is solved, the desired effective traction vector $\bar{\boldsymbol{t}}$ is obtained from the effective stress $\bar{\boldsymbol{\sigma}}$ by Cauchy's fundamental lemma (2.37).

For completeness it is noted that the chosen hybrid boundary conditions are consistent with the requirement (5.4) and with the Hill–Mandel condition

$$\bar{\boldsymbol{t}} \cdot \bar{\boldsymbol{\delta}} = L\left(\langle \boldsymbol{\sigma} : \boldsymbol{\varepsilon}\rangle_{\Omega} + \langle \check{\boldsymbol{t}} \cdot \boldsymbol{\delta}\rangle_{\mathscr{I}}\right) \qquad \Leftrightarrow \qquad \int_{\Gamma} \boldsymbol{t} \cdot \tilde{\boldsymbol{u}} \, \mathrm{d}A = 0. \tag{5.12}$$

5.5 Thermal two-scale problems

For the thermal two-scale problems considered in this work, the assumptions **[H1]–[H4]** are supplemented as follows.

[HT1] No singular surfaces are considered at the microscale.

[HT2] Attention is limited to steady state processes at both scales.

[HT3] Heat supply is negligible at the microscale.

[HT4] The macroscopic temperature $\bar{\theta}$ has a microscopic counterpart θ that can be described by a first order Maclaurin expansion of the macroscopic temperature superposed with a temperature fluctuation field $\tilde{\theta}$ which does not contribute to the effective temperature gradient $\bar{\boldsymbol{g}}$.

[HT5] The constitutive behavior at the microscale is characterized by Fourier's law

$$\boldsymbol{q} = -\boldsymbol{\kappa}\boldsymbol{g}, \tag{5.13}$$

where $\boldsymbol{\kappa}$ denotes a symmetric, positive definite heat conduction tensor independent of the temperature.

With **[HT1]–[HT3]**, the equilibrium condition for the steady state heat condition problem at the microscale is derived from the balance of internal energy (2.87) as

$$\operatorname{div}(\boldsymbol{q}) = 0 \qquad \text{in } \Omega. \tag{5.14}$$

The effective heat flux is defined by

$$\bar{\boldsymbol{q}} = \int_{\Gamma} (\boldsymbol{q} \cdot \boldsymbol{n}) \, \boldsymbol{x} \, \mathrm{d}A = \langle \boldsymbol{q}\rangle_{\Omega}, \tag{5.15}$$

where the equality of the surface integral and of the volume average is obtained with Gauss's theorem (2.38) and with (5.14). Corresponding to strain-driven mechanical homogenization, the effective heat flux is sought-after for a given effective temperature gradient

$$\bar{\boldsymbol{g}} = \frac{1}{|\Omega|} \int_{\Gamma} \theta \boldsymbol{n} \, \mathrm{d}A = \langle \boldsymbol{g}\rangle_{\Omega}, \tag{5.16}$$

where the equality of both representations is obtained from Gauss's theorem (2.39). The assumption **[HT4]** is reformulated according to

$$\theta(\boldsymbol{x}) = \tilde{\theta}(\boldsymbol{x}) + \bar{\theta} + \bar{\boldsymbol{g}} \cdot \boldsymbol{x} + \mathcal{O}\left(\left\|\frac{\boldsymbol{x}}{l_\mu}\right\|_2^2\right), \qquad \int_\Gamma \tilde{\theta}\boldsymbol{n}\, dA = \boldsymbol{0}. \qquad (5.17)$$

The constitutive assumption **[HT5]** implies that the global temperature $\bar{\theta}$ does not affect the effective response, and like for mechanical problems, attention is limited to first order homogenization schemes, such that the ansatz for the local temperature field

$$\theta(\boldsymbol{x}) = \tilde{\theta}(\boldsymbol{x}) + \bar{\boldsymbol{g}} \cdot \boldsymbol{x} \qquad (5.18)$$

is made. Periodic boundary conditions which satisfy

$$\tilde{\theta}(\boldsymbol{x}_-) = \tilde{\theta}(\boldsymbol{x}_+), \qquad \boldsymbol{q}(\boldsymbol{x}_-) \cdot \boldsymbol{n}(\boldsymbol{x}_-) = -\boldsymbol{q}(\boldsymbol{x}_+) \cdot \boldsymbol{n}(\boldsymbol{x}_+) \qquad (5.19)$$

for all pairs $\{\boldsymbol{x}_-, \boldsymbol{x}_+\} \subset \Gamma$ of opposite material points on the boundary of the RVE are adopted. These boundary conditions are consistent with the requirement from (5.17) and with the Hill–Mandel condition [cf. Ostoja-Starzewski, 2002]

$$\bar{\boldsymbol{q}} \cdot \bar{\boldsymbol{g}} = \langle \boldsymbol{q} \cdot \boldsymbol{g} \rangle_\Omega \qquad \Leftrightarrow \qquad \int_\Gamma (\boldsymbol{q} \cdot \boldsymbol{n})\, \tilde{\theta}\, dA = 0, \qquad (5.20)$$

where the equivalence of both representations is obtained with Gauss's theorem (2.38) and with the equilibrium condition (5.14).

Chapter 6:
Fourier-accelerated nodal solvers (FANS) for homogenization problems

6.1 Introduction

Fourier-based homogenization schemes are iterative algorithms which are designed such that a considerable part of the numerical operations takes the form of discrete periodic convolutions with global ansatz functions (mostly fundamental solutions). By virtue of the convolution theorem, discrete periodic convolutions are computable via pointwise products in Fourier space. Thanks to fast Fourier transform (FFT) algorithms [cf. Cooley & Tukey, 1965], for which high-performance implementations are available, the necessary forward and backward discrete Fourier transform (DFT) operations can be conducted in a computationally efficient way. With the crucial involvement of discrete periodic convolutions, Fourier-based homogenization methods are generally aimed at HBM problems with periodic boundary conditions (cf. Section 5.4.1). Another requirement for convolution-based formulations are uniform discretizations of the RVEs. This renders Fourier-accelerated methods well suited for microstructures described by pixel or voxel data where the generation of nonuniform FE meshes would be cumbersome.

The development of FFT-based homogenization methods started with the pioneering works of Moulinec & Suquet [1994, 1995, 1998], in which a fixed-point scheme for the solution of periodic Lippmann–Schwinger equations was proposed. A key concept in their proposal is the introduction of a homogeneous reference material for which a fundamental solution is given in terms of a classical Green's operator. The spatially heterogeneous constitutive behavior is evaluated at collocation points arranged on a uniform grid. The original algorithm, hereafter referred to as *basic scheme*, is technically appealing and easy to implement but has two major drawbacks: firstly, the convergence properties are poor in the presence of high phase contrast, i.e., when the material properties vary significantly between the individual phases, and, secondly, the solutions exhibit spurious oscillations attributed to the Gibbs phenomenon. Numerous contributions addressing these issues are found in the literature, only a few of which can be mentioned here. Substantial progress with respect to the convergence behavior was attained when Zeman et al. [2010] pointed out that the fixed point scheme can be replaced by Krylov subspace methods that are efficiently preconditioned with a fundamental solution via FFT operations. On the other hand, the problem with spurious artifacts is closely related to the fundamental solution that is incorporated. Willot et al. [2014], Willot [2015], and Brisard & Dormieux [2010, 2012] found that improvement

in this regard can be achieved by simply substituting the classical Green's operator with modified Green's operators (MGOs), also referred to as discrete Green's operators. The MGO derived from a rotated grid approach by Willot [2015] leads to a considerable reduction of spurious artifacts and to notable improvement of the convergence behavior compared to the basic scheme.

Fourier-accelerated nodal solvers (FANS) for homogenization problems [Leuschner & Fritzen, 2018] have been developed in order to further diminish artifacts while at the same time reducing the number of operations per iteration compared to conventional Fourier-based schemes, such that the obtained algorithms are highly efficient in terms of computing times. These objectives are achieved with an FE formulation using bilinear (2D) or trilinear (3D) shape functions on a regular grid, where all operations of the iterative scheme are conducted on nodal data (e.g., nodal displacements and nodal forces in the case of mechanical problems). The number of FFT operations per iteration is thereby reduced compared to conventional Fourier-accelerated homogenization schemes acting on gradient quantities and fluxes (i.e., strains and stresses for mechanical problems), yet it shall not be concealed that this idea has been previously exploited by Willot et al. [2014], Willot [2015], and Schneider et al. [2016]. FANS are closely related to the FFT-Q_1Hex scheme recently proposed by Schneider et al. [2017]; in fact, although the two methods were developed independently, they can be considered equivalent from a theoretical point of view. Both schemes make use of the same fundamental solution, both can be implemented as fixed point (FP) schemes or as preconditioned conjugate gradient (CG) schemes, and both produce identical solutions. However, FFT-Q_1Hex and FANS differ by algorithmic aspects that have important practical consequences. Compared to FFT-Q_1Hex, the FANS concept was developed in a more classical FE style, making use of a periodized global conductance/stiffness matrix. This can become a disadvantage in view of memory limitations, but it allows for rapid FP or CG iterations. Thus, the matrix-based FANS scheme is preferred when the problem dimensions allow to store (a sophisticated representation of) the conductance/stiffness matrix. FFT-Q_1Hex or a matrix-free version of FANS can be used when the memory resources are insufficient.

Chapter 6 presents key aspects of the paper of Leuschner & Fritzen [2018], from which parts of the theoretical and methodological descriptions are taken with only minor modifications. In particular, some of the technical declarations in Section 6.2 are adopted word-for-word from Leuschner & Fritzen [2018]. As opposed to the other Chapters of the present work, attention is not restricted to three-dimensional problems, but two-dimensional problems[13] are considered as well, and the number of spatial dimensions is denoted $d \in \{2, 3\}$. Numerical examples will be presented for two-dimensional problems only in Section 6.5. However, it is worth mentioning that a three-dimensional implementation of FANS is subject of ongoing work, and a preliminary numerical example was already given in Leuschner & Fritzen [2018].

---

[13]In the two-dimensional case, the operator $\langle \bullet \rangle_\Omega$ introduced in (5.1) is understood as an area averaging operator (instead of a volume averaging operator for $d = 3$).
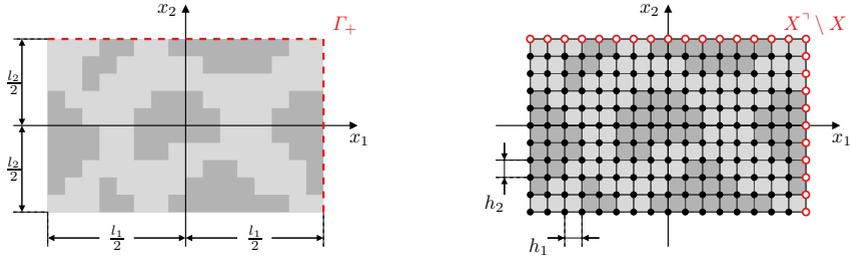
Figure 6.1: Sketch of a two-dimensional RVE *(left)* with a uniform grid discretization *(right)*. Slave nodes on the "positive" boundary Γ_+ are represented by red empty circles.

6.2 Preliminaries

A periodic microstructure is considered which is represented by an RVE whose domain Ω takes the form of a rectangle ($d = 2$) or of a rectangular cuboid ($d = 3$). A Cartesian coordinate system with coordinate axes $\boldsymbol{e}_1, \ldots, \boldsymbol{e}_d$ parallel to the RVE's edges is introduced such that the coordinate origin coincides with the centroid of the RVE (see Figure 6.1). The length of the RVE's edges in the direction of $\boldsymbol{e}_i$ is denoted l_i for $i = 1, \ldots, d$, and the diagonal

$$l_{\mathrm{c}} = \sqrt{l_1^2 + \cdots + l_d^2} \tag{6.1}$$

is chosen as the characteristic length of the RVE. A regular grid with even numbers $N_1, \ldots, N_d$ of elements along the coordinate axes $\boldsymbol{e}_1, \ldots, \boldsymbol{e}_d$ is assumed as a discretization. The dimensions of the elements, which correspond to pixels ($d = 2$) or voxels ($d = 3$), are given by

$$h_i = \frac{l_i}{N_i} \qquad (i = 1, \ldots, d). \tag{6.2}$$

The material properties are assumed to be elementwise uniform (although multiphase elements could be considered).

Node-based description. The numbers of all elements and of all nodes are denoted

$$N = \prod_{i=1}^{d} N_i, \qquad\qquad N^\urcorner = \prod_{i=1}^{d} (N_i + 1), \tag{6.3}$$

respectively. Within Chapter 6, the symbol $\bullet^\urcorner$ is used to tag quantities related to the set of all nodes

$$X^\urcorner = \left\{ \boldsymbol{x}^{[1]}, \ldots, \boldsymbol{x}^{[N^\urcorner]} \right\} \subset \Omega. \tag{6.4}$$

A node numbering denoted with superscripted square brackets has been introduced here, which defines a vector representation $\underline{a}^{\urcorner} \in \mathbb{R}^{N^{\urcorner}}$ of any scalar field $a(\boldsymbol{x})$ given on $X^{\urcorner}$ via

$$a_i^{\urcorner} = \left(\underline{a}^{\urcorner}\right)_i = a\left(\boldsymbol{x}^{[i]}\right) \qquad \left(\boldsymbol{x}^{[i]} \in X^{\urcorner}, \quad i = 1, \ldots, N^{\urcorner}\right). \tag{6.5}$$

In order to account for the periodicity of the microscopic fields, all nodes on the positive boundaries (see Figure 6.1)

$$\Gamma_+ = \left\{\boldsymbol{x} \in \Omega \,\middle|\, \boldsymbol{x} \cdot \boldsymbol{e}_1 = \frac{l_1}{2} \quad \vee \quad \ldots \quad \vee \quad \boldsymbol{x} \cdot \boldsymbol{e}_d = \frac{l_d}{2}\right\}, \tag{6.6}$$

are considered as slave nodes. The remaining free nodes are comprised in the set

$$X = X^{\urcorner} \setminus \Gamma_+ = \left\{\boldsymbol{x}^{\langle 1 \rangle}, \ldots, \boldsymbol{x}^{\langle N \rangle}\right\}, \tag{6.7}$$

where the superscripted angular brackets denote another numbering of the (free) nodes. A scalar field $b(\boldsymbol{x})$ defined on X can be expressed as a vector $\underline{b} \in \mathbb{R}^N$ according to

$$b_i = \left(\underline{b}\right)_i = b\left(\boldsymbol{x}^{\langle i \rangle}\right) \qquad \left(\boldsymbol{x}^{\langle i \rangle} \in X, \quad i = 1, \ldots, N\right). \tag{6.8}$$

With this conversion in mind, the ith unit vector of the N-dimensional standard basis can be understood as the unit impulse at the free node $\boldsymbol{x}^{\langle i \rangle} \in X$ described in terms of the Kronecker delta according to $(i = 1, \ldots, N)$

$$\begin{aligned} \delta^{\langle i \rangle} &: X \to \{0, 1\} \\ \boldsymbol{x}^{\langle j \rangle} &\mapsto \delta_{ij}. \end{aligned} \tag{6.9}$$

The discrete representation $\underline{c}^{\urcorner} \in \mathbb{R}^{N^{\urcorner}}$ of a periodic scalar field $c(\boldsymbol{x})$ defined on $X^{\urcorner}$ is fully determined by the values at the free nodes comprised in a vector $\underline{c} \in \mathbb{R}^N$, and the recovery of the full representation can be formally expressed via a periodicity constraint matrix $\underline{\underline{\mathcal{P}}} \in \mathbb{R}^{N^{\urcorner} \times N}$ according to

$$\underline{c}^{\urcorner} = \underline{\underline{\mathcal{P}}}\,\underline{c}. \tag{6.10}$$

The sparse matrix $\underline{\underline{\mathcal{P}}}$ has $N^{\urcorner}$ non-zero entries all equal to one and is introduced in favor of sleek technical descriptions; in practice, matrix–vector and matrix–matrix multiplications involving $\underline{\underline{\mathcal{P}}}$ are replaced by more efficient index operations[14].

---

[14]If the node numberings in (6.4) and in (6.7) are ordered in a consistent manner, i.e., if the implication

$$\boldsymbol{x}^{[k]} = \boldsymbol{x}^{\langle i \rangle}, \quad \boldsymbol{x}^{[l]} = \boldsymbol{x}^{\langle j \rangle}, \quad i < j \qquad\qquad \Rightarrow \qquad\qquad k < l$$

holds for all possible index pairs $i < j$, then the construction of $\underline{\underline{\mathcal{P}}}$ can be described as follows, using the $N^{\urcorner} \times N^{\urcorner}$ identity matrix as initialization: for any slave node $\overline{\boldsymbol{x}^{[s]}} \in X^{\urcorner}$ with its associated master node $\boldsymbol{x}^{[m]} \in X^{\urcorner}$, the sth column is added to the mth column. Subsequently, all columns related to slave nodes in terms of the node numbering from (6.4) are removed.
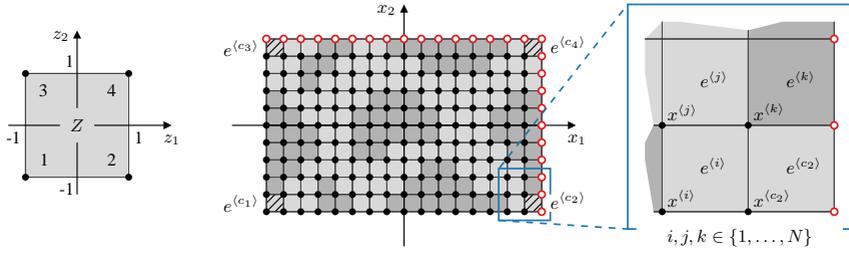
Figure 6.2: Two-dimensional reference element *(left)*, numbering of the corner elements in agreement with the node numbering in the reference element *(middle)*, and coincident numbering of the elements and their first nodes *(right)*.

For m-dimensional vector fields given on $X^\daleth$ or on X (arising, e.g., in the case of mechanical homogenization problems), the conversions (6.5) and (6.8) are applied componentwise, and the resultant m vectors are concatenated, leading to $mN^\daleth$-dimensional or mN-dimensional vector representations, respectively. For a vector-valued periodic fluctuation field of dimension m, an equivalent to (6.10) is obtained by replacing $\underline{\underline{\mathcal{P}}}$ with the block matrix

$$
\begin{array}{c}
\begin{array}{ccc} 1 & \cdots & m \end{array} \\
\begin{array}{c} 1 \\ \vdots \\ m \end{array}
\begin{bmatrix} \underline{\underline{\mathcal{P}}} & & \\ & \ddots & \\ & & \underline{\underline{\mathcal{P}}} \end{bmatrix}
\end{array}
= \underline{\underline{\mathcal{P}_m}} \in \mathbb{R}^{mN^\daleth \times mN}.
\tag{6.11}
$$

Reference element. Bilinear $(d = 2)$ or trilinear $(d = 3)$ finite element shape functions are employed and a reference element $Z = [-1, 1]^d$ is introduced (see Figure 6.2). Each node of the reference element is characterized by its position vector $\underline{\alpha} \in \{-1, 1\}^d \subset Z$. A local numbering of the 2^d nodes of each element is introduced according to

$$
\mathcal{N}(\underline{\alpha}) = 1 + \sum_{i=1}^{d} 2^{i-2} \left(1 + \alpha_i\right).
\tag{6.12}
$$

Gaussian quadrature with P integration points is utilized. The integration points and the corresponding weights are denoted

$$
\underline{z}^{(1)}, \dots, \underline{z}^{(P)} \in Z, \qquad w^{(1)}, \dots, w^{(P)} \in \mathbb{R}_{>0} \qquad \left(1 = \sum_{p=1}^{P} w^{(p)}\right).
\tag{6.13}
$$

The case $P = 1$ with $\underline{z}^{(1)} = \underline{0}$ is referred to as *reduced integration* but is not considered in the following. Instead, *full integration* is assumed with $P = 2^d$ and

$$\underline{z}^{(p)} \in \left\{ -\frac{\sqrt{3}}{3}, \frac{\sqrt{3}}{3} \right\}^d, \qquad w^{(p)} = 2^{-d} \qquad (p = 1, \dots, P). \qquad (6.14)$$

Element-based description.   The numbering of the free nodes introduced in (6.7) implicates a numbering of the elements where each element is assigned the (global) node number of its first node, as illustrated on the right-hand side of Figure 6.2. The notation $c_1, \dots, c_{2^d} \in \{1, \dots, N\}$ is introduced for the index numbers of the elements at the corners of the RVE, and the corner indices c_i are ordered in the same manner as the nodes of the reference element (see Figure 6.2, again). For a vector-valued field $\boldsymbol{a}(\boldsymbol{x})$ defined at the integration points, the jth component of the value at the pth integration point of the ith element $e^{\langle i \rangle}$ is represented by $a_j^{(p)}\big(e^{\langle i \rangle}\big)$.

Array representations.   Throughout Chapter 6, a frame $\boxed{\bullet}$ is occasionally used to denote d-dimensional $(N_1 \times \cdots \times N_d)$-arrays, and the entrywise product[15] of two such arrays is expressed by "$\odot$". Arrays with one or two additional dimensions are denoted $\boxed{\underline{\bullet}}$ and $\boxed{\underline{\underline{\bullet}}}$, respectively. E.g., any scalar field $a(\boldsymbol{x})$ defined on the set of free nodes X has a natural array representation $\boxed{a}$. Further, an m-dimensional vector field $\underline{b}(\boldsymbol{x})$ given on X can be represented by an $(N_1 \times \cdots \times N_d \times m)$-array $\boxed{\underline{b}}$, while an m-dimensional vector-field $\underline{c}(\boldsymbol{x})$ defined at the integration points has a representation in terms of an $(N_1 \times \cdots \times N_d \times P \times m)$-array $\boxed{\underline{\underline{c}}}$.

It is stressed that any scalar field $a(\boldsymbol{x})$ defined on X has an array representation $\boxed{a}$ as well as a vector representation $\underline{a}$ obtained via the node numbering from (6.7). Both representations are used interchangeably for the formulation and for the implementation of FANS. For instance, the unit impulse at the ith free node, introduced in (6.9), has the array representation $\boxed{\delta^{\langle i \rangle}}$ and the vector representation $\underline{\delta}^{\langle i \rangle}$ (which is the ith unit vector). In order to avoid memory access overhead, the vector representation should be compliant with the array storage scheme, i.e., the numbering of the free nodes should be specified accordingly.

Notation and properties of the DFT.   The d-dimensional discrete periodic Fourier transform $\mathscr{F}$ and its inverse $\mathscr{F}^{-1}$ map the real space representation $\boxed{\bullet}$ of an $(N_1 \times \cdots \times N_d)$-array to its Fourier representation or spectrum $\boxed{\widehat{\bullet}}$, and vice versa. For

---

[15]The entrywise of product of two-dimensional arrays is also known as *Hadamard product*.

arrays with additional dimensions, the forward and backward transforms are defined componentwise, e.g., according to

$$\boxed{\widehat{a_i}} = \mathscr{F}\left(\boxed{a_i}\right), \qquad \boxed{a_i} = \mathscr{F}^{-1}\left(\boxed{\widehat{a_i}}\right) \qquad (i = 1, \ldots, m) \qquad (6.15)$$

for a vector-valued field $\underline{a}(\boldsymbol{x})$ of dimension m defined on X, which has the array representations $\boxed{\underline{a}}$ and $\boxed{\underline{\widehat{a}}}$ in real space and in Fourier space, respectively. For completeness, the forward and backward DFT operations are specified in Appendix A.4. Recall that the numbers of elements $N_1, \ldots, N_d$ are assumed to be even. Then, the frequency vectors are defined as

$$\underline{\underline{\Xi}}^{(i)} = \left[0, \frac{1}{l_i}, \frac{2}{l_i}, \ldots, \frac{N_i - 2}{2\, l_i}, \frac{-N_i}{2\, l_i}, \frac{2 - N_i}{2\, l_i}, \ldots, \frac{-2}{l_i}, \frac{-1}{l_i}\right]^{\mathsf{T}} \qquad (i = 1, \ldots, d)$$
$$(6.16)$$

in accordance with the subroutine library FFTW [cf. Frigo & Johnson, 2005]. The Fourier frequency domain corresponding to the set of free nodes X is thereby defined as

$$\widehat{X} = \underline{\underline{\Xi}}^{(1)} \times \cdots \times \underline{\underline{\Xi}}^{(d)}. \qquad (6.17)$$

Note that the zero frequency $\boldsymbol{0} \in \widehat{X}$ occupies the corner of the array where all indices are one. The number[16] of the free node corresponding to this position within the array is hereafter denoted i^*. The following equalities are deduced directly from the definition of the DFT

$$\mathscr{F}\left(\underline{\delta^{\langle i^* \rangle}}\right) = \underline{1}, \qquad \mathscr{F}^{-1}\left(\underline{\delta^{\langle i^* \rangle}}\right) = N^{-1}\underline{1}, \qquad \sum_{i=1}^{N} a\left(\boldsymbol{x}^{\langle i \rangle}\right) = \widehat{a}(\boldsymbol{0}). \qquad (6.18)$$

Another equality worth mentioning is the Plancherel theorem

$$\sum_{\boldsymbol{x} \in X} \|f(\boldsymbol{x})\|_2^2 = \frac{1}{N} \sum_{\boldsymbol{\xi} \in \widehat{X}} \left\|\widehat{f}(\boldsymbol{\xi})\right\|_2^2. \qquad (6.19)$$

Discrete periodic convolution. The discrete periodic convolution $(a * b)$ of two scalar fields $a(\boldsymbol{x})$ and $b(\boldsymbol{x})$ given on the set of free nodes X is defined as

$$(a * b)(\boldsymbol{x}) = \sum_{j=1}^{N} a\left(\boldsymbol{x}^{\langle j \rangle}\right) b\left(\boldsymbol{x} - \boldsymbol{x}^{\langle j \rangle} + \boldsymbol{x}^{\langle i^* \rangle}\right) \qquad (\boldsymbol{x} \in X), \qquad (6.20)$$

---

[16]I.e., the node index in terms of the numbering of the free nodes introduced in (6.7).

where periodic continuations across the boundaries of the RVE are implicitly assumed. The convolution theorem states that the operation defined in (6.20) can be computed via an entrywise product in Fourier space according to

$$\underline{a} * \underline{b} = \mathscr{F}^{-1}\left(\widehat{\underline{a}} \odot \widehat{\underline{b}}\right) = \mathscr{F}^{-1}(\mathscr{F}(\underline{a}) \odot \mathscr{F}(\underline{b})). \tag{6.21}$$

Therefore, the convolution can be computed efficiently using FFT algorithms. It is concluded from (6.18) and (6.21) that $\underline{\delta^{\langle i^* \rangle}}$ represents the neutral element with respect to convolution.

Zero mean N-dimensional vectors.   The space of all N-dimensional vectors with zero mean is denoted $\mathbb{R}_0^N$ in the following, and the vectors

$$\underline{\delta_0^{\langle i \rangle}} = \underline{\delta^{\langle i \rangle}} - \frac{1}{N}\underline{1} \qquad (i = 1, \dots, N) \tag{6.22}$$

are introduced, which constitute a generating set of $\mathbb{R}_0^N$. Note that $\underline{\delta_0^{\langle i^* \rangle}}$ is the neutral element with respect to convolution in $\mathbb{R}_0^N$.

6.3   Steady-state heat conduction

In the following, homogenization of thermal problems as introduced in Section 5.5 is addressed. Attention is limited to steady-state isotropic heat conduction, i.e., the spatially heterogeneous conductivity tensor in Fourier's law (cf. **[HT5]**) is assumed to be of the form

$$\boldsymbol{\kappa} = \kappa \boldsymbol{I} \qquad \text{with } \kappa > 0. \tag{6.23}$$

While none of the presented algorithms is confined to isotropic local constitutive behavior, this assumption is made to simplify the following technical description and to put the focus on methodological aspects.

6.3.1   FANS basic framework

As in standard finite element formulations, a weak form of the discretized homogenization problem is expressed in terms of

- the global conductance matrix[17] $\underline{\underline{K}^{\urcorner}} \in \mathbb{R}^{N^{\urcorner} \times N^{\urcorner}}$,
- the global vector of nodal temperatures $\underline{u}^{\urcorner} \in \mathbb{R}^{N^{\urcorner}}$, and
- the global vector of nodal reactions $\underline{f}^{\urcorner} \in \mathbb{R}^{N^{\urcorner}}$

---

[17]Details on the construction of $\underline{K}^{\urcorner}$ are given in Appendix B.2.

by the requirement

$$\left(\tilde{\underline{v}}^{\urcorner}\right)^{\mathsf{T}} \underline{\underline{K}}^{\urcorner} \underline{u}^{\urcorner} = \left(\tilde{\underline{v}}^{\urcorner}\right)^{\mathsf{T}} \underline{f}^{\urcorner} \qquad \text{for all } \tilde{\underline{v}}^{\urcorner} = \underline{\underline{P}}\,\tilde{\underline{v}} \text{ with } \tilde{\underline{v}} \in \mathbb{R}^{N}. \tag{6.24}$$

Making use of the extrapolation introduced for periodic fluctuation fields in (6.10), a vector representation of the decomposition of the local temperature field (5.18) is obtained as

$$\underline{u}^{\urcorner} = \underline{u}_{0}^{\urcorner} + \underline{\underline{P}}\,\tilde{\underline{u}} \qquad \text{with } \left(\underline{u}_{0}^{\urcorner}\right)_{i} = \bar{\boldsymbol{g}} \cdot \boldsymbol{x}^{[i]} \qquad \left(i = 1, \ldots, N^{\urcorner}\right). \tag{6.25}$$

While the prescribed effective temperature gradient $\bar{\boldsymbol{g}}$ is considered via $\underline{u}_{0}^{\urcorner} \in \mathbb{R}^{N^{\urcorner}}$, the vector $\tilde{\underline{u}} \in \mathbb{R}^{N}$ comprises the degrees of freedom of the system. Combining the two previous equations (6.24) and (6.25), one arrives at

$$\underline{\underline{K}}\,\tilde{\underline{u}} = \underline{f}, \tag{6.26}$$

with the reduced conductance matrix $\underline{\underline{K}} \in \mathbb{R}^{N \times N}$ and the reduced vector[18] $\underline{f} \in \mathbb{R}^{N}$ defined by

$$\underline{\underline{K}} = \underline{\underline{P}}^{\mathsf{T}} \underline{\underline{K}}^{\urcorner} \underline{\underline{P}}, \qquad\qquad \underline{f} = \underline{\underline{P}}^{\mathsf{T}} \left(\underline{f}^{\urcorner} - \underline{\underline{K}}^{\urcorner} \underline{u}_{0}^{\urcorner}\right) = -\underline{\underline{P}}^{\mathsf{T}} \underline{\underline{K}}^{\urcorner} \underline{u}_{0}^{\urcorner}. \tag{6.27}$$

The matrix $\underline{\underline{K}}$, in the following referred to as *periodized conductance matrix*, is symmetric and positive semi-definite with rank $N - 1$, i.e., it has one zero eigenvalue. The rank deficiency is due to missing Dirichlet boundary conditions, and the additional constraint

$$\tilde{\underline{u}} \in \mathbb{R}_{0}^{N} \qquad\qquad \Leftrightarrow \qquad\qquad \left\langle \tilde{\theta} \right\rangle_{\Omega} = 0 \tag{6.28}$$

is introduced in order to make the solution of (6.26) well-defined. The vector $\underline{f}$ has also zero mean, i.e., $\underline{f} \in \mathbb{R}_{0}^{N}$ holds unconditionally.

6.3.2 Reference medium and fundamental solution

As in the majority of the literature on Fourier-based homogenization, a homogeneous reference medium with the conductivity $\kappa_{\mathrm{r}} > 0$ is introduced. The periodized conductance matrix $\underline{\underline{K}_{\mathrm{r}}} \in \mathbb{R}^{N \times N}$ for the reference medium is defined analogously to $\underline{\underline{K}}$ and has the same pattern of non-zero entries. In contrast to the original heterogeneous problem defined by (6.26) and (6.28), the homogeneous problem

$$\underline{\underline{K}_{\mathrm{r}}}\,\underline{a} = \underline{b}, \qquad \underline{a} \in \mathbb{R}_{0}^{N} \qquad\qquad\qquad \text{with } \underline{b} \in \mathbb{R}_{0}^{N} \tag{6.29}$$

---

[18]The absence of heat supply h yields $\underline{\underline{P}}^{\mathsf{T}} \underline{f}^{\urcorner} = \underline{0}$, which is exploited for the representation of $\underline{f}$ in (6.27).

has a closed-form solution. The specific structure of $\underline{\underline{K}}_{\mathrm{r}}$ allows to replace the matrix–vector product in (6.29) with a convolution according to

$$\underline{\underline{K}}_{\mathrm{r}}\,\underline{a} = \underline{k}_{\mathrm{r}} * \underline{a}, \tag{6.30}$$

where $\underline{k}_{\mathrm{r}}$ denotes the i^*th column (or row) of $\underline{\underline{K}}_{\mathrm{r}}$. The solution $\underline{k}_{\mathrm{r}}^{+} \in \mathbb{R}_0^N$ of the problem

$$\underline{k}_{\mathrm{r}} * \underline{k}_{\mathrm{r}}^{+} = \underline{\delta}_0^{\langle i^* \rangle}, \tag{6.31}$$

is referred to as *fundamental solution*, and the solution of (6.29) is thereby given through

$$\underline{a} = \underline{\delta}_0^{\langle i^* \rangle} * \underline{a} = \left(\underline{k}_{\mathrm{r}} * \underline{k}_{\mathrm{r}}^{+} \right) * \underline{a} = \underline{k}_{\mathrm{r}}^{+} * \left(\underline{k}_{\mathrm{r}} * \underline{a} \right) = \underline{k}_{\mathrm{r}}^{+} * \underline{b}, \tag{6.32}$$

where associativity and commutativity of the convolution have been exploited. Application of the DFT on (6.31) yields

$$\widehat{\underline{k}_{\mathrm{r}}} \odot \widehat{\underline{k}_{\mathrm{r}}^{+}} = \underline{1} - \underline{\widehat{\delta}^{\langle i^* \rangle}} \qquad \Leftrightarrow \qquad \begin{cases} \widehat{k}_{\mathrm{r}}(\boldsymbol{\xi})\,\widehat{k}_{\mathrm{r}}^{+}(\boldsymbol{\xi}) = 0, & \boldsymbol{\xi} = \mathbf{0}; \\ \widehat{k}_{\mathrm{r}}(\boldsymbol{\xi})\,\widehat{k}_{\mathrm{r}}^{+}(\boldsymbol{\xi}) = 1, & \boldsymbol{\xi} \in \widehat{X} \setminus \{\mathbf{0}\}, \end{cases} \tag{6.33}$$

hence the fundamental solution can be constructed frequency-wise in Fourier space via

$$\widehat{k}_{\mathrm{r}}^{+}(\boldsymbol{\xi}) = \begin{cases} 0, & \boldsymbol{\xi} = \mathbf{0}; \\ \dfrac{1}{\widehat{k}_{\mathrm{r}}(\boldsymbol{\xi})}, & \boldsymbol{\xi} \in \widehat{X} \setminus \{\mathbf{0}\}. \end{cases} \tag{6.34}$$

Altogether, the fundamental solution can be constructed easily in practice by computing $\underline{k}_{\mathrm{r}}$ in a standard finite element setting, calculating its Fourier representation $\widehat{\underline{k}_{\mathrm{r}}}$ via the DFT, and by eventually evaluating (6.34). Since the fundamental solution will always be applied in Fourier space in FANS algorithms, it is not necessary to compute the real space representation $\underline{k}_{\mathrm{r}}^{+}$ via a backward DFT. For completeness, it is noted that the matrix

$$\underline{\underline{K}}_{\mathrm{r}}^{+} = \left[\underline{\delta}^{\langle 1 \rangle} * \underline{k}_{\mathrm{r}}^{+} \mid \cdots \mid \underline{\delta}^{\langle N \rangle} * \underline{k}_{\mathrm{r}}^{+} \right] \in \mathbb{R}^{N \times N} \tag{6.35}$$

is the Moore–Penrose inverse of $\underline{\underline{K}}_{\mathrm{r}}$, and it can be used to formally express the convolution of $\underline{k}_{\mathrm{r}}^{+}$ with a vector $\underline{b} \in \mathbb{R}_0^N$ in terms of a matrix–vector product according to

$$\underline{\underline{K}}_{\mathrm{r}}^{+}\,\underline{b} = \underline{k}_{\mathrm{r}}^{+} * \underline{b}. \tag{6.36}$$

The above construction of the fundamental solution departs from the periodized homogeneous conductance matrix $\underline{\underline{K}}_{\mathrm{r}}$, which is assembled in accordance with the standard FE convention that needs no detailed description. Also, the DFT is applied in a black box manner, such that the fundamental solution can be described without too many technical details regarding FE and DFT nomenclature.
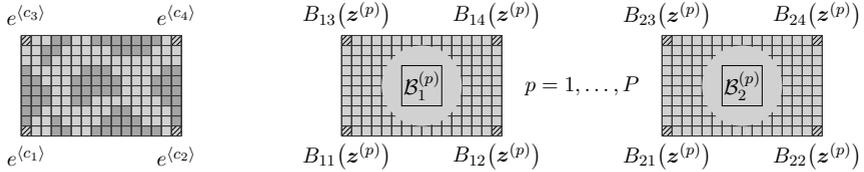
Figure 6.3: Illustration of the gradient stencil assignments (6.38) for $d = 2$.

Alternative construction of the fundamental solution. Two alternative ways to construct the fundamental solution k_{r}^{+} have been presented in Leuschner & Fritzen [2018]. One of these is reproduced hereafter because the intermediate steps will also help to describe the FFT-Q_1Quad/Hex scheme of Schneider et al. [2017] in Section 6.3.4. To begin with, it is recalled that bilinear ($d = 2$) or trilinear ($d = 3$) shape functions are used. The corresponding FE gradient operator is denoted $\underline{\underline{B}}(\underline{z}) \in \mathbb{R}^{d \times 2^d}$ and is specified for the two-dimensional case as

$$\underline{\underline{B}}(\underline{z}) = \frac{1}{2} \begin{bmatrix} h_1^{-1} & 0 \\ 0 & h_2^{-1} \end{bmatrix} \begin{bmatrix} z_2 - 1 & 1 - z_2 & -1 - z_2 & 1 + z_2 \\ z_1 - 1 & -1 - z_1 & 1 - z_1 & 1 + z_1 \end{bmatrix} \quad (\underline{z} \in Z). \quad (6.37)$$

The FE gradient operator is evaluated at all P integration points of the reference element, and the components are placed at the corners of an $(N_1 \times \cdots \times N_d \times P \times d)$-array $\boxed{\underline{\underline{\mathcal{B}}}}$ called *gradient stencil* according to

$$\mathcal{B}_i^{(p)}\left(e^{\langle c_j \rangle}\right) = B_{ij}\left(\underline{z}^{(p)}\right) \quad \left(i = 1, \ldots, d;\ j = 1, \ldots, 2^d;\ p = 1, \ldots, P\right). \quad (6.38)$$

All other entries of $\boxed{\underline{\underline{\mathcal{B}}}}$ vanish. The assignments in (6.38) are illustrated in Figure 6.3, and it is pointed out that the numbering of the corner elements must correspond to the node numbering in the reference element, as assumed in Section 6.2 (cf. Figure 6.2). The temperature gradient field $\boldsymbol{g}$ (given at the integration points) can now be derived from the temperature fluctuation field (given at the free nodes) via a convolution[19]

$$\boxed{g_i^{(p)}} = \bar{g}_i\,\boxed{1} + \boxed{\mathcal{B}_i^{(p)}} * \boxed{\tilde{u}} \quad (i = 1, \ldots, d;\ p = 1, \ldots, P). \quad (6.39)$$

The same relationship is expressed in Fourier space as

$$\widehat{\boldsymbol{g}^{(p)}}(\boldsymbol{\xi}) = \begin{cases} N\bar{\boldsymbol{g}}, & \boldsymbol{\xi} = \boldsymbol{0}; \\ \widehat{\boldsymbol{\mathcal{B}}^{(p)}}(\boldsymbol{\xi})\,\widehat{u}(\boldsymbol{\xi}), & \boldsymbol{\xi} \in \widehat{X} \setminus \{\boldsymbol{0}\} \end{cases} \quad (p = 1, \ldots, P). \quad (6.40)$$

---

[19]While the definition of the discrete periodic convolution in (6.20) is specified for two fields given on X, the convolution with $\boxed{\mathcal{B}_i^{(p)}}$ in (6.39) is implicitly determined via the one-to-one correspondence between the elements and their first nodes (cf. Figure 6.2).

Further, the negative of the conjugate transpose of the gradient stencil is the divergence operator [cf. Schneider et al., 2017], i.e.,

$$\widehat{\text{div}(\boldsymbol{q})}(\boldsymbol{\xi}) = -\sum_{p=1}^{P} w^{(p)} \left(\widehat{\boldsymbol{\mathcal{B}}^{(p)}}(\boldsymbol{\xi}) \right)^{\mathsf{H}} \widehat{\boldsymbol{q}}(\boldsymbol{\xi}) \qquad \left(\boldsymbol{\xi} \in \widehat{X} \right). \tag{6.41}$$

The Fourier representation $\underline{\underline{\widehat{\mathcal{B}}}}$ of the gradient stencil can be either computed via an FFT algorithm or can be explicitly described by

$$\widehat{\mathcal{B}_i^{(p)}}(\boldsymbol{\xi}) = \sum_{\underline{\alpha} \in \{-1,1\}^d} B_{i\mathcal{N}(\underline{\alpha})}\left(\underline{z}^{(p)} \right) \exp\left(\imath\pi \sum_{k=1}^{d} (1 + \alpha_k)\, h_k\, \xi_k \right) \qquad \begin{array}{c} (i = 1, \dots, d) \\ (p = 1, \dots, P) \\ \left(\boldsymbol{\xi} \in \widehat{X} \right) \end{array} \tag{6.42}$$

following Schneider et al. [2017], where the second index of the gradient operator $\underline{\underline{B}}$ is specified in terms of the node numbering of the reference element defined in (6.12) and where $\imath$ denotes the imaginary unit. The fundamental solution is then given by

$$\widehat{k_{\text{r}}^+}(\boldsymbol{\xi}) = \begin{cases} 0, & \boldsymbol{\xi} = \boldsymbol{0}; \\ \left(\kappa_{\text{r}} \sum_{p=1}^{P} w^{(p)} \left(\widehat{\boldsymbol{\mathcal{B}}^{(p)}}(\boldsymbol{\xi}) \right)^{\mathsf{H}} \widehat{\boldsymbol{\mathcal{B}}^{(p)}}(\boldsymbol{\xi}) \right)^{-1}, & \boldsymbol{\xi} \in \widehat{X} \setminus \{\boldsymbol{0}\}. \end{cases} \tag{6.43}$$

6.3.3   FANS algorithms

Making use of the above introduced fundamental solution, the mapping

$$F \colon \mathbb{R}_0^N \to \mathbb{R}_0^N$$
$$\underline{\tilde{u}} \mapsto \underline{\tilde{u}} + \underline{k_{\text{r}}^+} * \left(\underline{f} - \underline{\underline{K}}\, \underline{\tilde{u}} \right). \tag{6.44}$$

is defined, which has a fixed point at the solution $\underline{\tilde{u}}^*$ of the homogenization problem given by (6.26) and (6.28). The best convergence of the fixed-point FANS (FP-FANS) scheme

$$\underline{\tilde{u}}_0 = \underline{0}, \qquad\qquad \underline{\tilde{u}}_{n+1} = F\left(\underline{\tilde{u}}_n \right) \qquad (n = 0, 1, 2, \dots) \tag{6.45}$$

is observed for the reference conductivity

$$\kappa_{\text{r}} = \frac{1}{2}\left(\kappa_- + \kappa_+ \right) \qquad \text{with} \quad \kappa_- = \inf_{\boldsymbol{x} \in \Omega} \kappa(\boldsymbol{x}), \quad \kappa_+ = \sup_{\boldsymbol{x} \in \Omega} \kappa(\boldsymbol{x}), \tag{6.46}$$

following the proposal of Moulinec & Suquet [1998] for mechanical problems. Based on the norm of the current residuum, the dimensionless error measure

$$\mathcal{E}_{\text{FANS}} = \frac{\|\underline{r}\|_2}{l_{\text{c}}\, \kappa_{\text{r}} \|\bar{\underline{g}}\|_2} \qquad \text{with} \quad \underline{r} = \underline{f} - \underline{\underline{K}}\, \underline{\tilde{u}} \tag{6.47}$$

Algorithm 6.1: FP-FANS scheme for steady-state heat conduction.

---

1 load $\boxed{\widehat{k_{\mathrm{r}}^+}}$ `// get fundamental solution`

2 assemble $\underline{K}$ and $\underline{f}$

3 $\underline{r} \leftarrow \underline{f}$ and $\underline{\tilde{u}} \leftarrow \underline{0}$ `// initialization`

4 **while** $\mathcal{E}_{\mathrm{FANS}} > \epsilon$ **do** `// check convergence`

5 $\quad \widehat{\underline{r}} \leftarrow \mathscr{F}(\underline{r})$ `// forward DFT`

6 $\quad \widehat{\underline{\lambda}} \leftarrow \widehat{\underline{k_{\mathrm{r}}^+}} \odot \widehat{\underline{r}}$ `// Fourier space computation of convolution`

7 $\quad \underline{\tilde{u}} \leftarrow \underline{\tilde{u}} + \mathscr{F}^{-1}\left(\widehat{\underline{\lambda}}\right)$ `// backward DFT`

8 $\quad \underline{r} \leftarrow \underline{f} - \underline{\underline{K}}\,\underline{\tilde{u}}$ `// compute residuum`

9 **end**

---

is defined for use in a stopping criterion. Algorithm 6.1 summarizes the technical steps of the FP-FANS scheme.

While the ill-posed system of linear equations (6.26) cannot be handled with direct solvers, the application of iterative solvers that do not presuppose a regular system matrix seems natural. The preconditioned conjugate gradient (CG) method is often said to require a symmetric positive definite matrix. However, convergence is also guaranteed for a singular symmetric positive semi-definite matrix when the right-hand side vector is in the range of the matrix [cf. Kaasschieter, 1988]. This is the case for the problem at hand, as the range of $\underline{\underline{K}}$ is $\mathbb{R}_0^N$. Hence, the homogenization problem can be solved by a standard CG scheme in which the Moore–Penrose inverse of the periodized homogeneous conductance matrix $\underline{\underline{K}}_{\mathrm{r}}$ acts as preconditioner. The preconditioning is efficiently realized via Fourier-accelerated convolutions with the fundamental solution k_{r}^+, and the resulting CG-FANS scheme is shown in Algorithm 6.2. One can read off from Algorithm 6.2 that the solution found by CG-FANS satisfies the zero mean constraint (6.28). Since everything about the CG-FANS algorithm is standard except for the preconditioning part, standard implementations of the CG method may be exploited. E.g., CG-FANS algorithms are easily implemented in MATLAB using the pcg command, as shown in Figure 6.4. It is emphasized that CG-FANS fulfills the theoretical requirements of the preconditioned CG method. This is in contrast to the trigonometric collocation method of Zeman et al. [2010] for which CG iterations are found to converge despite the fact that the system is not symmetric.

6.3.4 Other Fourier-accelerated homogenization schemes

In the following, adaptations of three fixed-point schemes that were originally proposed for mechanical problems are briefly presented for steady-state heat conduction.

Algorithm 6.2: CG-FANS scheme for steady-state heat conduction.

---

1 load $\boxed{\widehat{k_r^+}}$ // get fundamental solution
2 assemble $\underline{\underline{K}}$ and $\underline{f}$
3 $\underline{r} \leftarrow \underline{f}, \; \tilde{\underline{u}} \leftarrow \underline{0}, \; \underline{d} \leftarrow \underline{0}, \;$ and $\delta \leftarrow 1$ // initialization
4 **while** $\mathcal{E}_{\text{FANS}} > \epsilon$ **do** // check convergence
5 $\quad \widehat{\underline{r}} \leftarrow \mathscr{F}(\underline{r})$ // start preconditioning
6 $\quad \widehat{\underline{\lambda}} \leftarrow \widehat{k_r^+} \odot \widehat{\underline{r}}$ // Fourier space computation of convolution
7 $\quad \underline{s} \leftarrow -\mathscr{F}^{-1}\left(\widehat{\underline{\lambda}}\right)$ // end preconditioning
8 $\quad \delta_0 \leftarrow \delta \;$ and $\delta \leftarrow \underline{r}^{\mathsf{T}}\underline{s}$
9 $\quad \underline{d} \leftarrow \underline{s} + (\delta/\delta_0)\,\underline{d}$
10 $\quad \underline{z} \leftarrow \underline{\underline{K}}\,\underline{d}$
11 $\quad \alpha \leftarrow \delta\left(\underline{d}^{\mathsf{T}}\underline{z}\right)^{-1}$
12 $\quad \tilde{\underline{u}} \leftarrow \tilde{\underline{u}} + \alpha\,\underline{d}$
13 $\quad \underline{r} \leftarrow \underline{r} - \alpha\,\underline{z}$
14 **end**

```
%% given:
% k:           Fourier representation of fundamental solution
% K, f:        periodized conductance matrix and right-hand side vector
% t:           error tolerance relative to initial error
% m:           maximum number of iterations
% N1, N2, N3:  numbers of elements along RVE edges
%% preconditioner:
P = @(r) reshape(ifftn(k.*fftn(reshape(r,N1,N2,N3))),N1*N2*N3,1);
%% CG-FANS:
u = pcg(K,f,t,m,P);
```

Figure 6.4: MATLAB implementation of CG-FANS for 3D steady-state heat conduction.

Basic scheme of Moulinec & Suquet [1994]. Fourier-accelerated computational homogenization originates from the basic scheme proposed by Moulinec & Suquet [1994, 1995, 1998]. The key ingredient of the basic scheme is an analytic Green's operator defined in Fourier space; for thermal problems, the analytic Green's function $\widehat{\mathbf{\Gamma}}$ reads

$$\widehat{\Gamma_{ij}}(\boldsymbol{\xi}) = \begin{cases} 0, & \boldsymbol{\xi} = \mathbf{0}; \\ \dfrac{-\xi_i\,\xi_j}{\kappa_r\,\|\boldsymbol{\xi}\|_2^2}, & \text{else} \end{cases} \qquad (i,j = 1,\ldots,d)\,. \tag{6.48}$$

While no particular discretization is explicitly considered in the above definition, the basic scheme acts on the discrete frequency domain $\widehat{X}$ defined in (6.17). The combination of the chosen discretization and the analytic Green's operator corresponds to a parameterization of the fields defined in the RVE in terms of trigonometric shape functions. For any vector field $\boldsymbol{f}(\boldsymbol{x})$ that can be represented as a linear combination of such shape functions, the divergence can be computed in Fourier space according to

$$\widehat{\mathrm{div}(\boldsymbol{f})}(\boldsymbol{\xi}) = \imath 2\pi\, \boldsymbol{\xi} \cdot \widehat{\boldsymbol{f}}(\boldsymbol{\xi}) \qquad \left(\boldsymbol{\xi} \in \widehat{X}\right). \tag{6.49}$$

This relation is exploited to define the error measure[20]

$$\mathcal{E}_{\mathrm{div}} = \frac{2\pi l_{\mathrm{c}}}{\|\widehat{\boldsymbol{q}}(\boldsymbol{0})\|_2} \sqrt{\sum_{\boldsymbol{\xi} \in \widehat{X}} \|\boldsymbol{\xi} \cdot \widehat{\boldsymbol{q}}(\boldsymbol{\xi})\|_2^2} \approx \frac{l_{\mathrm{c}}}{\|\overline{\boldsymbol{q}}\|_2} \sqrt{\left\langle \|\mathrm{div}(\boldsymbol{q})\|_2^2 \right\rangle_{\Omega}}. \tag{6.50}$$

The constitutive law (i.e., Fourier's law of heat conduction) is evaluated at the element centers comprised in the set $\mathcal{X}$, which serve as collocation points. The basic scheme is thus called a trigonometric collocation method [cf. Zeman et al., 2010]. Algorithm 6.3 summarizes the fixed-point iterations of the basic scheme.

Rotated grid scheme of Willot [2015]. In order to reduce discretization artifacts and improve convergence behavior compared to the basic scheme, several modified Green's operators (MGOs) have been proposed in the literature. Among the best performing MGOs is the one derived from a rotated grid scheme by Willot [2015]. The name is due to the fact that temperature gradients and heat fluxes are evaluated at the element centers $\mathcal{X}$ as in the basic scheme, whereas the temperature field and the divergence of the heat flux are computed on a superimposed rotated grid (i.e., on the nodes in the FE/FANS terminology). While square/cubic elements are assumed in the original work of Willot [2015], this assumption can be relaxed to rectangular/cuboidal shapes. A modified version of the rotated grid method applicable also to non-square/non-cubic elements is presented here. The key ingredient is a discrete gradient operator $\boldsymbol{k}(\boldsymbol{\xi})$ specified as

$$k_i(\boldsymbol{\xi}) = \frac{\imath 2}{h_i} \sin(\pi h_i \xi_i) \left(\prod_{\substack{j=1 \\ i \neq j}}^{d} \cos(\pi h_j \xi_j) \right) \prod_{j=1}^{d} \exp(\imath \pi h_j \xi_j) \quad (i = 1, \dots, d) \tag{6.51}$$

---

[20]The transition between the two expressions in (6.50) is obtained with the summation property from (6.18) and with the Plancherel theorem (6.19). Note that the Fourier space expression of $\mathcal{E}_{\mathrm{div}}$ differs from the corresponding definition in Moulinec & Suquet [1998] by the factor $2\pi\sqrt{N}$. This correction has practical relevance since high resolutions would otherwise mistakenly be favored by a stopping criterion based on $\mathcal{E}_{\mathrm{div}}$. Moreover, in contrast to the proposal of Moulinec & Suquet [1998], the characteristic length l_{c} is incorporated in the definition of $\mathcal{E}_{\mathrm{div}}$ in order to obtain a dimensionless error measure.

Algorithm 6.3: Basic scheme of Moulinec & Suquet [1994] for steady-state heat conduction.

1 load $\widehat{\boldsymbol{\Gamma}}$ // `get fundamental solution`
2 $\forall \boldsymbol{x} \in \mathcal{X} : \boldsymbol{g}(\boldsymbol{x}) \leftarrow \bar{\boldsymbol{g}}, \boldsymbol{q}(\boldsymbol{x}) \leftarrow -\kappa(\boldsymbol{x})\,\bar{\boldsymbol{g}}$ // `initialization`
3 **while** $\mathcal{E}_{\mathrm{div}} > \epsilon$ **do** // `check convergence`
4   **for** $j = 1, \ldots, d$ **do**
5          $\widehat{q_j} \leftarrow \mathscr{F}\left(\underline{q_j}\right)$ // `forward DFT`
6   **end**
7   **for** $i = 1, \ldots, d$ **do**
8          $\widehat{\underline{\lambda}} \leftarrow \underline{0}$
9   **for** $j = 1, \ldots, d$ **do**
10             $\forall \boldsymbol{\xi} \in \widehat{X} : \widehat{\lambda}(\boldsymbol{\xi}) \leftarrow \widehat{\lambda}(\boldsymbol{\xi}) - \widehat{\Gamma_{ij}}(\boldsymbol{\xi})\,\widehat{q_j}(\boldsymbol{\xi})$ // `apply Green's operator`
11   **end**
12         $\underline{g_i} \leftarrow \underline{g_i} + \mathscr{F}^{-1}\left(\widehat{\underline{\lambda}}\right)$ // `backward DFT`
13   **end**
14     $\forall \boldsymbol{x} \in \mathcal{X} : \boldsymbol{q}(\boldsymbol{x}) \leftarrow -\kappa(\boldsymbol{x})\,\boldsymbol{g}(\boldsymbol{x})$ // `evaluate constitutive model`
15 **end**

---

without reproducing details of the derivation[21]. Therewith, the MGO $\widehat{\boldsymbol{\Gamma}^{\mathrm{R}}}$ is defined as

$$\widehat{\Gamma_{ij}^{\mathrm{R}}}(\boldsymbol{\xi}) = \begin{cases} 0, & \boldsymbol{\xi} \in \{\boldsymbol{0}\} \cup \widehat{X_0^{\mathrm{R}}}; \\ \dfrac{-\mathrm{Re}\left(k_i(\boldsymbol{\xi})\overline{k_j(\boldsymbol{\xi})}\right)}{\kappa_{\mathrm{r}}\|\boldsymbol{k}(\boldsymbol{\xi})\|_2^2}, & \boldsymbol{\xi} \in \widehat{X} \setminus \left(\{\boldsymbol{0}\} \cup \widehat{X_0^{\mathrm{R}}}\right) \end{cases} \quad (i, j = 1, \ldots, d), \quad (6.52)$$

where

$$\widehat{X_0^{\mathrm{R}}} = \left\{\boldsymbol{\xi} \in \widehat{X} \setminus \{\boldsymbol{0}\} : \boldsymbol{k}(\boldsymbol{\xi}) = \boldsymbol{0}\right\} \tag{6.53}$$

$$= \left\{\boldsymbol{\xi} \in \widehat{X} : \xi_i = -\frac{1}{2h_i} \wedge \xi_j = -\frac{1}{2h_j} \quad \text{for } i \neq j \quad (i, j = 1, \ldots, d)\right\} \tag{6.54}$$

---

[21]The adaptation for non-square/non-cubic elements is achieved by the prefactor h_i^{-1} in (6.51). Moreover, the definition of the gradient operator $\boldsymbol{k}(\boldsymbol{\xi})$ has been reformulated by means of trigonometric angle sum identities compared to the original formulae of Willot [2015], which contain terms like $\tan(\pi h_i \xi_i)$ that are undefined for all $\boldsymbol{\xi} \in \widehat{X}$ with $\xi_i = -(2h_i)^{-1}$ $(i = 1, \ldots, d)$.

describes the set of frequencies where the operator $\boldsymbol{k}(\boldsymbol{\xi})$ vanishes. The consistent error measure for the Green's operator in (6.52) is

$$\mathcal{E}_{\mathrm{div}}^{\mathrm{R}} = \frac{2\pi l_{\mathrm{c}}}{\|\widehat{\boldsymbol{q}}(\boldsymbol{0})\|_2} \sqrt{\sum_{\boldsymbol{\xi}\in\widehat{X}} \|\boldsymbol{k}(\boldsymbol{\xi})\cdot\widehat{\boldsymbol{q}}(\boldsymbol{\xi})\|_2^2} \approx \frac{l_{\mathrm{c}}}{\|\bar{\boldsymbol{q}}\|_2} \sqrt{\left\langle\|\mathrm{div}(\boldsymbol{q})\|_2^2\right\rangle_{\Omega}}. \tag{6.55}$$

The rotated grid fixed-point scheme is obtained by simply replacing the Green's operator and the error measure in Algorithm 6.3.

It has been shown by Schneider et al. [2017] that the discrete gradient operator $\boldsymbol{k}(\boldsymbol{\xi})$ is equal to the gradient stencil $\widehat{\boldsymbol{\mathcal{B}}^{(1)}}(\boldsymbol{\xi})$ from (6.42) when the latter is computed with reduced integration. Therefore, the rotated grid scheme of Willot [2015] can be understood as a special case of the FFT-Q_1Quad/Hex method presented next.

FFT-Q_1Quad/Hex scheme of Schneider et al. [2017]. FFT-Q_1Hex is a Fourier-accelerated homogenization scheme based on hexahedral finite elements with trilinear shape functions that was recently proposed by Schneider et al. [2017] for three-dimensional mechanical problems. The adaptation presented for thermal problems here considers two-dimensional as well as three-dimensional problems and is thus referred to as FFT-Q_1Quad/Hex. As mentioned previously, the method has many similarities with FANS, since the same discretization and the same fundamental solution are employed. Except for the evaluation of the constitutive model, all operations of the FFT-Q_1Quad/Hex fixed-point scheme shown in Algorithm 6.4 are conducted in Fourier space. More specifically, the temperature gradient and the divergence of the heat flux are computed in Fourier space via (6.40) and (6.41). It is pointed out that this is in contrast to FANS, where only the convolution with the fundamental solution is accelerated by FFT algorithms, i.e., all other operations are performed in real space. Note also that the numerical cost of the FFT-Q_1Quad/Hex algorithm scales almost linearly with the number of integration points per element P, i.e., FFT-Q_1Quad/Hex is significantly faster with reduced integration than with full integration. When operating FFT-Q_1Quad/Hex with reduced integration (which yields the same results as the rotated grid MGO approach of Willot [2015]), the definition of the fundamental solution $\widehat{k_{\mathrm{r}}^+}(\boldsymbol{\xi})$ in (6.43) must be slightly altered to the effect that $\widehat{k_{\mathrm{r}}^+}(\boldsymbol{\xi})$ is zero for every $\boldsymbol{\xi}\in\widehat{X_0^{\mathrm{R}}}$.

While the FANS error measure defined in (6.47) could be evaluated in the FFT-Q_1Quad/Hex algorithm via the Plancherel theorem (6.19), Schneider et al. [2017] proposed to use the convergence indicator[22]

$$\mathcal{C}_{Q_1} = \|\bar{\boldsymbol{g}}\|_2^{-1}\left|\sqrt{\left\langle\|\boldsymbol{g}_n\|_2^2\right\rangle_{\Omega}} - \sqrt{\left\langle\|\boldsymbol{g}_{n-1}\|_2^2\right\rangle_{\Omega}}\right| \qquad (n=1,2,\ldots) \tag{6.56}$$

for the stopping criterion.

---

[22]A normalization with respect to the area/volume $|\Omega|$ of the RVE that is missing in the original formulation has been included in (6.56) in order to obtain a dimensionless quantity.

Algorithm 6.4: FFT-Q_1Quad/Hex proposed by Schneider et al. [2017], adapted for isotropic steady-state heat conduction.

---

1 load $\boxed{\widehat{\underline{k_r^+}}}$ // `get fundamental solution`

2 $\widehat{\widetilde{u}} \leftarrow \underline{0}$ // `initialization`

3 **while** $\mathcal{C}_{Q_1} > \epsilon$ **do** // `check convergence`

4 $\quad$ $\widehat{r} \leftarrow \underline{0}$ // `initialize residuum`

5 $\quad$ **for** $p = 1, \ldots, P$ **do** // `loop over element integration points`

6 $\quad\quad$ **for** $i = 1, \ldots, d$ **do**

7 $\quad\quad\quad$ $\forall \boldsymbol{\xi} \in \widehat{X} \setminus \{\mathbf{0}\} : \widehat{g}(\boldsymbol{\xi}) \leftarrow \widehat{\mathscr{B}_i^{(p)}}(\boldsymbol{\xi}) \, \widehat{\widetilde{u}}(\boldsymbol{\xi})$ // `compute temperature gradient`

8 $\quad\quad\quad$ $\widehat{g}(\mathbf{0}) \leftarrow N \bar{g}_i$ // `prescribed effective temperature gradient`

9 $\quad\quad\quad$ $\underline{g} \leftarrow \mathscr{F}^{-1}\big(\widehat{\underline{g}}\big)$ // `backward DFT`

10 $\quad\quad\quad$ $\underline{q} \leftarrow -\underline{\kappa} \odot \underline{g}$ // `apply constitutive law in real space`

11 $\quad\quad\quad$ $\widehat{\underline{q}} \leftarrow \mathscr{F}\big(\underline{q}\big)$ // `forward DFT`

12 $\quad\quad\quad$ $\forall \boldsymbol{\xi} \in \widehat{X} : \widehat{r}(\boldsymbol{\xi}) \leftarrow \widehat{r}(\boldsymbol{\xi}) - w^{(p)} \overline{\widehat{\mathscr{B}_i^{(p)}}}(\boldsymbol{\xi}) \, \widehat{q}(\boldsymbol{\xi})$ // `compute residuum`

13 $\quad\quad$ **end**

14 $\quad$ **end**

15 $\quad$ $\widehat{\widetilde{u}} \leftarrow \widehat{\widetilde{u}} - \widehat{\underline{k_r^+}} \odot \widehat{r}$ // `apply fundamental solution`

16 **end**

6.4   Mechanical problems

The FANS concept for thermal problems presented in Section 6.3 is transferred to linear elastic homogenization problems in a straightforward manner. For convenience, attention is limited to microstructures with isotropic individual phases again. Analogous to (6.26), the discretized homogenization problem can be expressed by a system of linear equations

$$\underline{\underline{K}} \, \tilde{\underline{u}} = \underline{f}. \tag{6.57}$$

The periodized stiffness matrix $\underline{\underline{K}} \in \mathbb{R}^{dN \times dN}$, the vector of unknowns $\tilde{\underline{u}} \in \mathbb{R}^{dN}$, and the right-hand side vector $\underline{f} \in \mathbb{R}^{dN}$ are organized according to

$$\underline{\underline{K}} = \begin{bmatrix} \underline{\underline{K}}_{11} & \cdots & \underline{\underline{K}}_{1d} \\ \vdots & \ddots & \vdots \\ \underline{\underline{K}}_{d1} & \ldots & \underline{\underline{K}}_{dd} \end{bmatrix}, \qquad \tilde{\underline{u}} = \begin{bmatrix} \tilde{\underline{u}}_1 \\ \vdots \\ \tilde{\underline{u}}_d \end{bmatrix}, \qquad \underline{f} = \begin{bmatrix} \underline{f}_1 \\ \vdots \\ \underline{f}_d \end{bmatrix} \tag{6.58}$$

with $\tilde{\underline{u}}_i$ denoting the displacement fluctuations at the free nodes in direction $\boldsymbol{e}_i$ and $\underline{f}_i$ representing the corresponding nodal forces in direction $\boldsymbol{e}_i$, through which the prescribed

effective strain $\bar{\varepsilon}$ is considered. Instead of gathering the d degrees of freedom of each node, the above representation is chosen since the arrays on which the FFT algorithm operates are thereby arranged en bloc. It is worth mentioning that not only $\underline{\underline{K}}$ is symmetric, but also each block $\underline{\underline{K}}_{ij}$ is symmetric $(i, j = 1, \ldots, d)$. A homogeneous reference medium with the corresponding periodized stiffness matrix $\underline{\underline{K}}_{\mathrm{r}}$ is introduced. The fundamental solution can be formally described as the solution of the problem

$$\underline{\underline{K}}_{\mathrm{r}} \begin{bmatrix} \underline{k}^+_{\mathrm{r},11} & \cdots & \underline{k}^+_{\mathrm{r},1d} \\ \vdots & \ddots & \vdots \\ \underline{k}^+_{\mathrm{r},d1} & \cdots & \underline{k}^+_{\mathrm{r},dd} \end{bmatrix} = \begin{bmatrix} \delta_0^{\langle i^* \rangle} & & \\ & \ddots & \\ & & \delta_0^{\langle i^* \rangle} \end{bmatrix}, \quad \underline{k}^+_{\mathrm{r},ij} \in \mathbb{R}_0^N \quad (i, j = 1, \ldots, d).$$

(6.59)

With $\underline{k}_{\mathrm{r},ij}$ denoting the i^*th column (or row) of the block $\underline{\underline{K}}_{\mathrm{r},ij}$ for $i, j = 1, \ldots, d$, the problem is reformulated in terms of convolutions according to

$$\sum_{l=1}^{d} \underline{k}_{\mathrm{r},il} * \underline{k}^+_{\mathrm{r},lj} = \begin{cases} \delta_0^{\langle i^* \rangle}, & i = j; \\ \underline{0}, & i \neq j, \end{cases} \qquad \underline{k}^+_{\mathrm{r},ij} \in \mathbb{R}_0^N \quad (i, j = 1, \ldots, d).$$

(6.60)

The corresponding Fourier representation is

$$\sum_{l=1}^{d} \widehat{\underline{k}_{\mathrm{r},il}} \odot \widehat{\underline{k}^+_{\mathrm{r},lj}} = \begin{cases} 1 - \widehat{\delta}^{\langle i^* \rangle}, & i = j; \\ \underline{0}, & i \neq j, \end{cases} \qquad \widehat{\underline{k}^+_{\mathrm{r},ij}}(\mathbf{0}) = 0 \quad (i, j = 1, \ldots, d).$$

(6.61)

Thus, the fundamental solution is obtained by solving small-sized systems of linear equations for all non-zero frequencies in Fourier space, which is equivalent to computing the inverse

$$\begin{bmatrix} \widehat{k^+_{\mathrm{r},11}}(\boldsymbol{\xi}) & \cdots & \widehat{k^+_{\mathrm{r},1d}}(\boldsymbol{\xi}) \\ & \ddots & \vdots \\ \mathrm{sym.} & & \widehat{k^+_{\mathrm{r},dd}}(\boldsymbol{\xi}) \end{bmatrix} = \begin{bmatrix} \widehat{k_{\mathrm{r},11}}(\boldsymbol{\xi}) & \cdots & \widehat{k_{\mathrm{r},1d}}(\boldsymbol{\xi}) \\ & \ddots & \vdots \\ \mathrm{sym.} & & \widehat{k_{\mathrm{r},dd}}(\boldsymbol{\xi}) \end{bmatrix}^{-1} \quad \left(\boldsymbol{\xi} \in \widehat{X} \setminus \{\mathbf{0}\} \right).$$

(6.62)

The FANS error measure for mechanical problems is defined as

$$\mathcal{E}_{\mathrm{FANS}} = \frac{\|\underline{r}\|_2}{l_{\mathrm{c}} \, \|\mathbb{C}_{\mathrm{r}} : \bar{\varepsilon}\|_2} \qquad \text{with } \underline{r} = \underline{f} - \underline{\underline{K}} \, \underline{\tilde{u}},$$

(6.63)

Algorithm 6.5: FP-FANS for linear elastostatics.

---

1   load $\boxed{\widehat{\underline{k_{\mathrm{r}}^+}}}$ // get fundamental solutions

2   assemble $\underline{\underline{K}}$ and $\underline{f}$

3   $\underline{r} \leftarrow \underline{f}$ and $\underline{\tilde{u}} \leftarrow \underline{0}$ // initialization

4   **while** $\mathcal{E}_{\mathrm{FANS}} > \epsilon$ **do** // check convergence

5   **for** $j = 1, \ldots, d$ **do**

6       $\widehat{\underline{r_j}} \leftarrow \mathscr{F}\left(\underline{r_j}\right)$ // forward DFT

7   **end**

8   **for** $i = 1, \ldots, d$ **do**

9       $\widehat{\underline{\lambda}} \leftarrow \underline{0}$

10   **for** $j = 1, \ldots, d$ **do**

11         $\widehat{\underline{\lambda}} \leftarrow \widehat{\underline{\lambda}} + \widehat{\underline{k_{\mathrm{r},ij}^+}} \odot \widehat{\underline{r_j}}$ // Fourier space computation of convolution

12   **end**

13       $\underline{\tilde{u}_i} \leftarrow \underline{\tilde{u}_i} + \mathscr{F}^{-1}\left(\widehat{\underline{\lambda}}\right)$ // backward DFT

14   **end**

15     $\underline{r} \leftarrow \underline{f} - \underline{\underline{K}}\,\underline{\tilde{u}}$ // compute residuum

16   **end**

---

where $\mathbb{C}_{\mathrm{r}}$ denotes the stiffness tensor of the reference medium. For good convergence of the FP-FANS scheme shown in Algorithm 6.5, $\mathbb{C}_{\mathrm{r}}$ is defined via the Lamé constants (cf. Appendix A.3.1)

$$\lambda_{\mathrm{r}} = \frac{1}{2}\left(\inf_{\boldsymbol{x} \in \Omega} \lambda(\boldsymbol{x}) + \sup_{\boldsymbol{x} \in \Omega} \lambda(\boldsymbol{x})\right), \qquad \mu_{\mathrm{r}} = \frac{1}{2}\left(\inf_{\boldsymbol{x} \in \Omega} \mu(\boldsymbol{x}) + \sup_{\boldsymbol{x} \in \Omega} \mu(\boldsymbol{x})\right) \qquad (6.64)$$

following the proposal of Moulinec & Suquet [1994]. CG-FANS is defined as a CG solver preconditioned by some steps similar to lines 5–14 of Algorithm 6.5 (cf. Algorithm 6.2) and is more robust with respect to the choice of the reference medium. In particular, CG-FANS is insensitive to scaling of $\mathbb{C}_{\mathrm{r}}$.

The transition from static to quasistatic problems is accomplished in the same way as for standard FE implementations and is therefore not discussed. Note that FANS can be applied to linearized problems emerging in Newton–Raphson procedures without modifications of the core algorithms.

6.5   Numerical examples

Two planar periodic microstructures are considered in the subsequent examples. The first one is represented by a quadratic unit cell containing one square inclusion with volume fraction 25% (see Figure 6.5) which has been investigated in several works on Fourier-based homogenization [e.g., Brisard & Dormieux, 2010, 2012, Willot et al., 2014, Willot, 2015]. This unit cell makes for a suitable benchmark problem in the case of thermal homogenization because a closed-form solution for (locally) isotropic heat conduction is available[23] [Obnosov, 1999]. The second microstructure is represented by a quadratic RVE taken from Willot et al. [2014] which contains 30% equal-sized, overlapping circular inclusions (see Figure 6.7).

6.5.1   Method comparison for steady-state heat conduction

The conductivities in the matrix and in the inclusions of two-phase materials are given by

$$\kappa_{\mathrm{m}} = 100\,\frac{\mathrm{W}}{\mathrm{m\,K}}, \qquad\qquad \kappa_{\mathrm{i}} = \mathcal{R}\,\kappa_{\mathrm{r}}, \qquad\qquad (6.65)$$

respectively. Different conductivity ratios $\mathcal{R} > 0$ will be considered, and $|\log(\mathcal{R})|$ is understood as a measure of phase contrast. Throughout Section 6.5.1, the prescribed effective temperature gradient is

$$\bar{\boldsymbol{g}} = 0.01\,\frac{\mathrm{K}}{\mathrm{m}}\,\boldsymbol{e}_1. \qquad\qquad (6.66)$$

Accuracy and smoothness of the local heat flux.   Attention is first directed at the benchmark unit cell problem, and the related results are taken from Leuschner & Fritzen [2018]. The resolutions 512×512, 1024×1024, and 2048×2048 are considered, and the conductivity ratio is set to $\mathcal{R} = 100$. The thermal homogenization problem has been solved with the basic scheme and with the rotated grid scheme (cf. Section 6.3.4) as well as with FP-FANS. The basic scheme was carried out until the error $\mathcal{E}_{\mathrm{div}}$ defined in (6.50) fell below the tolerance 10^{-4}. This happened after 498, 510, and 523 fixed-point iterations for the coarse, intermediate, and fine resolution, respectively. On the other hand, 100 iterations of the rotated grid scheme and of FP-FANS were executed, which sufficed for complete convergence at all resolutions. The heat flux fields computed for each of the three fixed-point schemes are compared to the closed-form solution $\boldsymbol{q}^*(\boldsymbol{x})$

---

[23]The closed-form formulation of Obnosov [1999] is a stationary, divergence-free, and curl-free solution of a heterogeneous conductivity problem. In the present case, the heat flux is curl-free because both phases are assumed to be isotropic. Interestingly, the calculation of the closed-form solution is more expensive computation-wise than any of the considered numerical approaches because the Jacobian elliptic delta function needs to be evaluated at each discretization point. For replicability of the presented results, a minor error in Obnosov [1999] is mentioned: in (3.5) therein, both denominators must be replaced by their square roots.
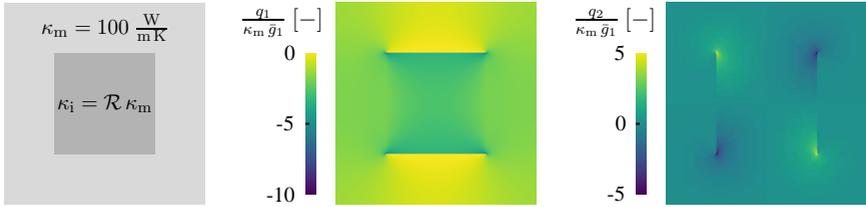
Figure 6.5: *Left:* unit cell with one square inclusion (25% volume fraction). *Middle, right:* components of the heat flux field computed with FP-FANS for $\mathcal{R} = 100$ and for the resolution 2048×2048.

resolution ($N_1 = N_2$)	512	1024	2048
basic scheme	1.881	1.176	0.736
rotated grid	0.414	0.259	0.162
FP-FANS	0.394	0.247	0.155

Table 6.1: Relative L^2-error $\mathcal{E}_{\mathrm{ref}}$ [%] of the heat flux field with respect to the closed-form solution for the benchmark problem (see Figure 6.5) [data reproduced from Leuschner & Fritzen, 2018].

derived by Obnosov [1999], which is evaluated at the element centers comprised in the set $\mathcal{X}$. The comparison is conducted via the relative L^2-error of the flux field

$$\mathcal{E}_{\mathrm{ref}} = \sqrt{\frac{\sum_{\boldsymbol{x} \in \mathcal{X}} \|\boldsymbol{q}(\boldsymbol{x}) - \boldsymbol{q}^*(\boldsymbol{x})\|_2^2}{\sum_{\boldsymbol{x} \in \mathcal{X}} \|\boldsymbol{q}^*(\boldsymbol{x})\|_2^2}} \approx \sqrt{\frac{\left\langle \|\boldsymbol{q} - \boldsymbol{q}^*\|_2^2 \right\rangle_{\Omega}}{\left\langle \|\boldsymbol{q}^*\|_2^2 \right\rangle_{\Omega}}} \tag{6.67}$$

and involves elementwise averaging of the FP-FANS results (using full integration). For the three fixed-point schemes and the three considered resolutions, the relative L^2-errors are given in Table 6.1. As expected, the errors decrease with increasing resolution for all three methods. It is found that heat flux fields computed with the rotated grid MGO approach and with FP-FANS approximate the closed-form solution much better than the basic scheme. Moreover, the errors for FP-FANS are slightly better than those obtained with the said MGO scheme at all considered resolutions.

It stands to reason that the relative errors with respect to the closed-form solution are correlated with artifacts induced by the different discretization schemes, which are expected to be most pronounced around the singularities at the corners of the inclusion. Close-ups of the region around the bottom left corner of the inclusion are shown in Figure 6.6. As expected on the basis of other works [such as Willot et al., 2014, Willot, 2015], strong spurious oscillations are observed for the basic scheme. The heat flux component $q_1(\boldsymbol{x})$ computed with the MGO approach is much smoother, but a noticeable mismatch compared to the closed-form solution is found, and a weak oscillation along
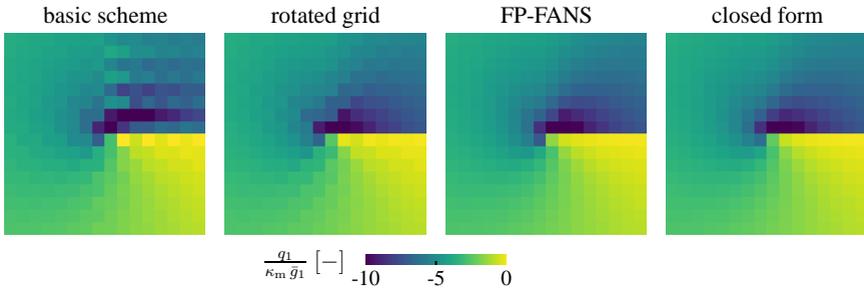
Figure 6.6: Close-ups of the heat flux component $q_1(\boldsymbol{x})$ in the region around the bottom left corner of the square inclusion (cf. Figure 6.5) for $\mathcal{R} = 100$ and 2048×2048 elements.
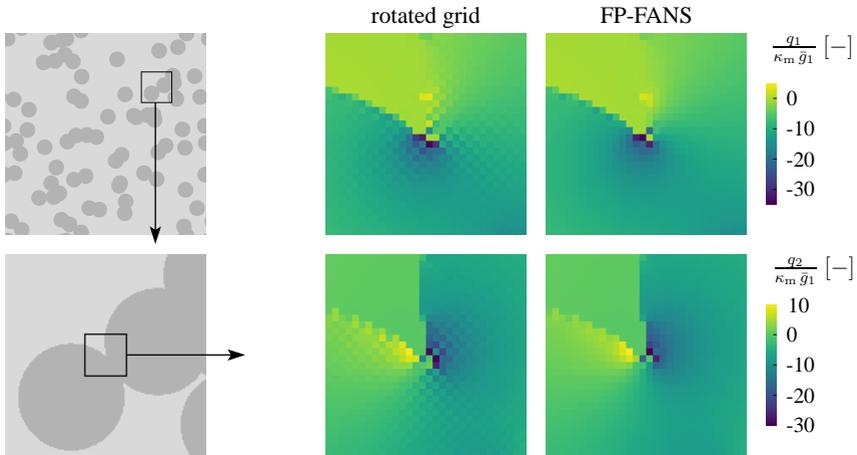

Figure 6.7: RVE with 30% circular inclusions, discretized with 1024×1024 elements, and details of numerical solutions of the heat flux field for the conductivity ratio $\mathcal{R} = 100$.

the lower boundary of the inclusion is perceivable in the matrix. In contrast, no spurious oscillations are found for the FP-FANS solution at all, and differences to the closed-form solution are barely visible.

While the benchmark problem is appealing due to the existence of a closed-form solution, it is not representative of typical applications because of its simplistic structure and the phase boundary being perfectly aligned with the uniform grid. Therefore, an otherwise equivalent homogenization problem with the random RVE with circular inclusions is considered, which is discretized with 1024×1024 elements. The problem has been solved with the rotated grid scheme and with FP-FANS, and 400 fixed-point iterations have
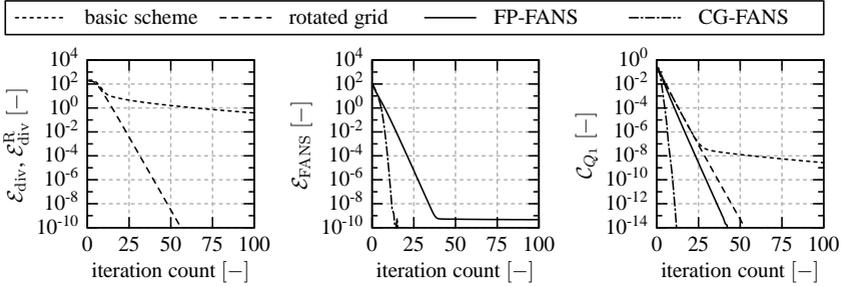
Figure 6.8: Convergence behavior of different Fourier-based schemes for the benchmark problem with a single square inclusion (see Figure 6.5) at conductivity ratio $\mathcal{R} = 100$.
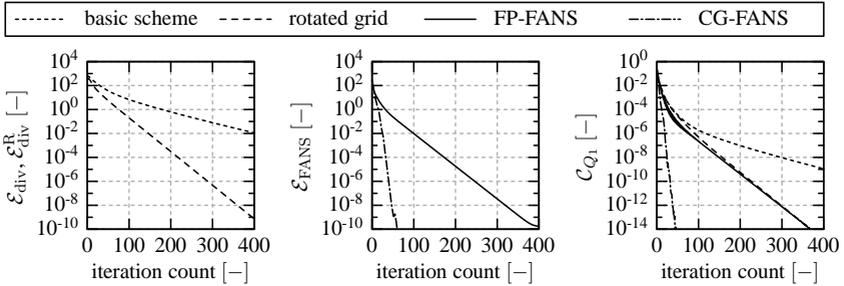

Figure 6.9: Convergence behavior of different Fourier-based schemes for the RVE with circular inclusions (see Figure 6.7) at conductivity ratio $\mathcal{R} = 100$.

been conducted for each method[24]. Figure 6.7 shows the entire RVE at the top left and a detail of the computed heat flux fields. A distinct checkerboard pattern is visible in both components of the MGO solution. On the other hand, the FP-FANS solution is as smooth as one could possibly expect from a uniform grid discretization approximating circular boundaries.

Convergence behavior. The error measures[25] $\mathcal{E}_{\mathrm{div}}$, $\mathcal{E}_{\mathrm{div}}^{\mathrm{R}}$, and $\mathcal{E}_{\mathrm{FANS}}$ are specifically designed for the basic scheme, for the rotated grid MGO scheme, and for FANS, respectively; none of them is meaningful for the other methods. Thus, a direct comparison of the convergence behavior of the three considered fixed-point schemes and of CG-FANS in terms of these error measures is not possible. The convergence indicator $\mathcal{C}_{Q_1}$ from (6.56) is therefore used as a workaround. For the fixed conductivity ratio $\mathcal{R} = 100$, the descent of the error measures and of the convergence indicator for

---

[24]From Figure 6.9 it is concluded that 400 iterations suffice for satisfactory accuracy with both methods.

[25]For the definitions of these error measures, see (6.50), (6.55), and (6.47), respectively.
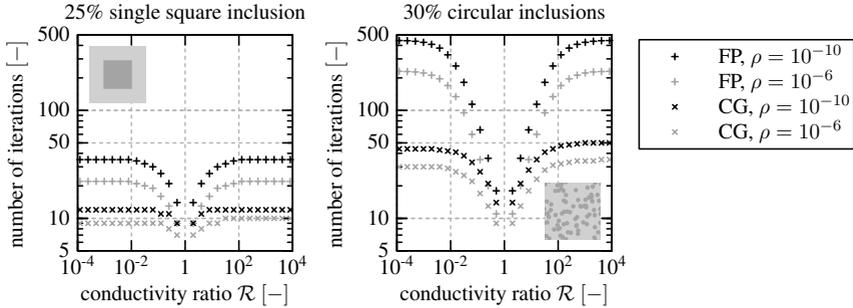
Figure 6.10: Numbers of iterations until the FANS error $\mathcal{E}_{\text{FANS}}$ drops below the fraction $\rho \in \left\{ 10^{-10}, 10^{-6} \right\}$ of its initial value. *Left:* RVE with one square inclusion (cf. Figure 6.5). *Right:* RVE with 30% circular inclusions (cf. Figure 6.7).

the Fourier-based schemes applied to the square inclusion benchmark problem with 1024×1024 elements is shown in Figure 6.8. The corresponding results for the RVE with 30% circular inclusions and resolution 1024×1024 are displayed in Figure 6.9. It is striking that all considered methods converge much faster for the benchmark problem than for the random RVE. For both microstructures, the rotated grid method is observed to converge significantly better than the basic scheme, confirming the findings reported by Willot [2015]. The comparison between the convergence of the MGO method and of FP-FANS in terms of the convergence indicator $\mathcal{C}_{Q_1}$ shows a slight advantage for FP-FANS for the benchmark problem and rather similar results for both methods for the random RVE[26]. Further, CG-FANS exhibits much better convergence than FP-FANS, and the difference is more pronounced for the random RVE.

For both microstructures, each resolved with 1024×1024 elements, a comparison of the convergence behavior of both FANS algorithms at varying conductivity ratio $\mathcal{R}$ has been conducted. Figure 6.10 shows the numbers of FANS iterations necessary to push the FANS error relative to its initial value before the first iteration below the thresholds 10⁻⁶ and 10⁻¹⁰. The special case $\mathcal{R} = 1$ corresponds to a trivial homogeneous problem and can be assigned the theoretical number of iterations "zero" (not shown). With $\mathcal{R}$ gradually diverging from the value 1, the required numbers of iterations increase monotonically, until upper limits are reached. The number of necessary CG-FANS iterations is always below the corresponding number of FP-FANS iterations. As previously observed for the case $\mathcal{R} = 100$, the advantage of CG-FANS is generally more pronounced for the random RVE than for the benchmark problem: for high phase contrasts, the number of fixed-point iterations to reach the threshold 10⁻¹⁰ is roughly ten times higher than the corresponding number of CG iterations. Also, both FANS schemes converge much faster

---

[26]For the random RVE, the convergence indicator $\mathcal{C}_{Q_1}$ oscillates slightly within the first 100 FP-FANS iterations (see right-hand side of Figure 6.9), which tells that the mean temperature gradient is not improved monotonically. However, more importantly, the FANS error $\mathcal{E}_{\text{FANS}}$ decreases monotonically.

for the benchmark problem than for the random RVE, which highlights the impact of the microstructural complexity on the numerical effort. The plots in Figure 6.10 are almost symmetric with respect to the vertical axis at $\mathcal{R} = 1$, i.e., the convergence behavior is almost independent of $\text{sign}(\log(\mathcal{R}))$. Interestingly, this symmetry is exact for FP-FANS, while for CG-FANS, minor benefits are found for the case $\mathcal{R} < 1$ (corresponding to a lower conductivity in the inclusions than in the matrix) compared to the case $\mathcal{R} > 1$.

6.5.2   Linear elastic problems with heterogeneous Poisson's ratios

The convergence of FANS for linear elastic mechanical homogenization is examined for problems characterized by the RVE with randomly distributed circular inclusions (cf. Figure 6.7). The Young's moduli in the matrix and in the circular inclusions are

$$E_\mathrm{m} = 100\,\mathrm{MPa}, \qquad\qquad E_\mathrm{i} = \mathcal{R}\,E_\mathrm{m} \qquad (\mathcal{R} > 0). \qquad\qquad (6.68)$$

Many works on Fourier-based homogenization are concerned with investigations on the impact of the ratio of Young's moduli $\mathcal{R}$ on the convergence behavior. Meanwhile, the Poisson's ratios are quite often assumed to be equal in both phases. This idealizing assumption is generally not applicable for real problems. Therefore, possible effects of dissimilar Poisson's ratios in the matrix (ν_m) and in the inclusions (ν_i) on the convergence of FANS are going to be investigated. To begin with, convergence in dependence on the ratio $\mathcal{R}$ is studied for $2\nu_\mathrm{m} = \nu_\mathrm{i} = 0.4$ and is compared to the simple standard case $\nu_\mathrm{m} = \nu_\mathrm{i} = 0.25$. For this comparison, the RVE discretized with 512×512 elements is loaded with 1% effective normal strain in direction $\boldsymbol{e}_1$ under plane strain conditions. Figure 6.11 shows the numbers of FP-FANS and CG-FANS iterations required to reduce the FANS error relative to its initial value

$$\mathcal{E}_\mathrm{FANS}^\mathrm{rel} = \frac{\|r\|_2}{\|\underline{f}\|_2} \qquad\qquad (6.69)$$

below certain thresholds. As for thermal homogenization, FP-FANS is found to be inappropriate for high contrasts of Young's moduli $|\log(\mathcal{R})|$, and CG-FANS shows better convergence already for low contrasts. The convergence of CG-FANS is affected by the choice of Poisson's ratios and is clearly decelerated in the case $2\nu_\mathrm{m} = \nu_\mathrm{i} = 0.4$ for moderate and high phase contrasts $|\log_{10}(\mathcal{R})| \geq 2.5$ compared to the case of a uniform Poisson's ratio $\nu = 0.25$. Figure 6.12 highlights the differences of the local normal stress fields $\sigma_{22}(\boldsymbol{x})$ perpendicular to the load direction obtained for the different choices of Poisson's ratios.

For the above example, the reference medium was defined in accordance with (6.64), following Moulinec & Suquet [1994]. While the proposal of Moulinec & Suquet [1994] was made for a fixed-point scheme and is suitable for FP-FANS, the question arises how the reference medium should be selected for CG-FANS. More specifically, since the preconditioned CG scheme is invariant to the reference medium's Young's modulus E_r,
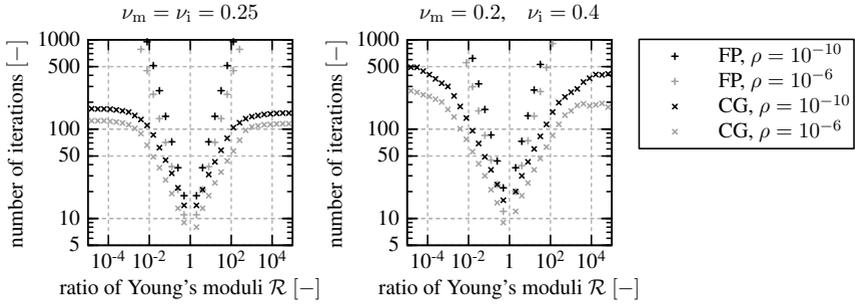
Figure 6.11: Numbers of iterations until the relative FANS error $\mathcal{E}_{\mathrm{FANS}}^{\mathrm{rel}}$ drops below the threshold $\rho \in \left\{10^{-10}, 10^{-6}\right\}$. Results for the RVE with 30% circular inclusions (cf. Figure 6.7) at resolution 512×512, loaded with $\bar{\varepsilon} = 0.01\, \boldsymbol{e}_1 \otimes \boldsymbol{e}_1$ under the assumption of plane strain.
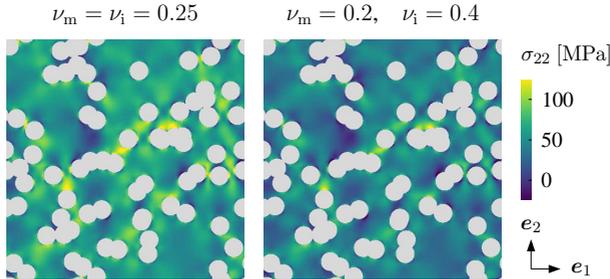

Figure 6.12: Normal stresses $\sigma_{22}(\boldsymbol{x})$ in the matrix material for the ratio of Young's moduli $\mathcal{R} = 1000$ and for different Poisson's ratios.

the question is how the Poisson's ratio of the reference medium ν_{r} should be chosen in situations with $\nu_{\mathrm{m}} \neq \nu_{\mathrm{i}}$. In the following, the three alternatives

$$\nu_{\mathrm{r}}^{(1)} = \nu_{\mathrm{f}}, \qquad \nu_{\mathrm{r}}^{(2)} = 0.25, \qquad \nu_{\mathrm{r}}^{(3)} = \nu_{-} = \begin{cases} \nu_{\mathrm{m}}, & \mathcal{R} > 1; \\ \nu_{\mathrm{i}}, & \mathcal{R} < 1 \end{cases} \tag{6.70}$$

will be compared for $\mathcal{R} = 10^{\pm 3}$, where the Poisson's ratio stemming from (6.64) is denoted ν_{f} while ν_{-} represents the Poisson's ratio of the softer phase. Note that the third alternative in (6.70) can be understood as the counterpart to the first one, because ν_{f} is approximately equal to the Poisson's ratio of the stiffer phase when the contrast $|\log(\mathcal{R})|$ is high. Further, both choices are equivalent when $\nu_{\mathrm{m}} = \nu_{\mathrm{i}}$. The convergence of CG-FANS with the three different approaches to define the fundamental solution is investigated for 16×16 combinations of Poisson's ratios $(\nu_{\mathrm{m}}, \nu_{\mathrm{i}}) \in [0, 0.5]^2$. For this purpose, the RVE with randomly distributed circular inclusions from Figure 6.7 is considered at the resolution 256×256. Results for shear loading under the assumption
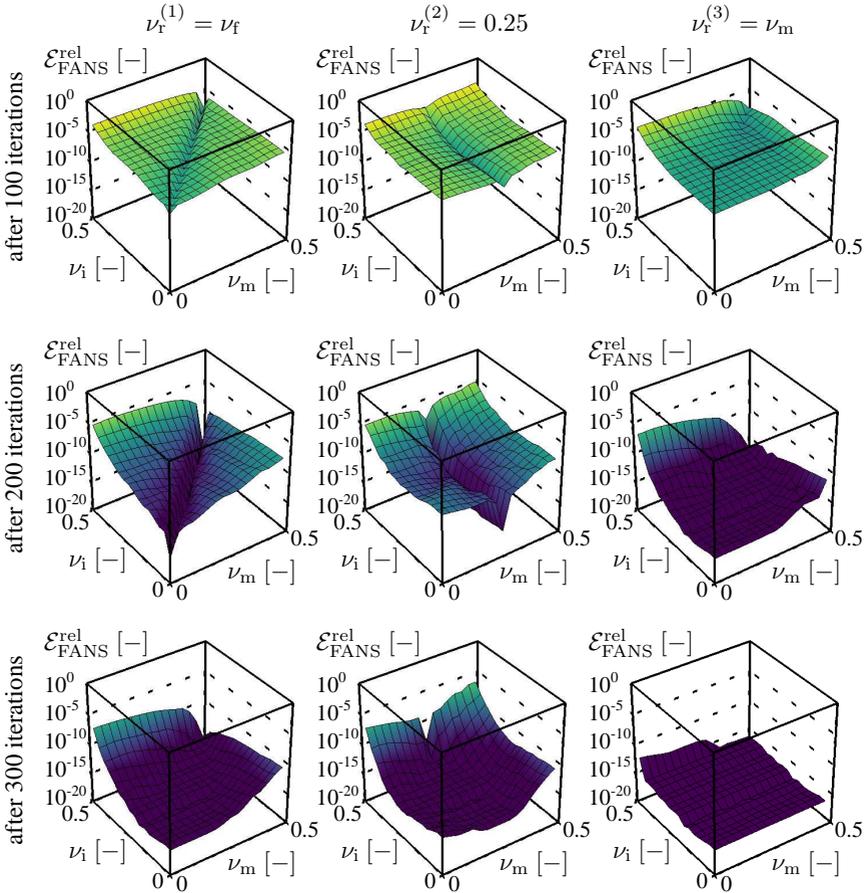
Figure 6.13: Convergence behavior of CG-FANS for fundamental solutions with different Poisson's ratios ν_r at a fixed ratio of Young's moduli $\mathcal{R} = 10^3$. The results were obtained for shear loading under the assumption of plane strain. The FANS error relative to its value before the first iteration is shown for different combinations of Poisson's ratios in the matrix and in the inclusions.

of plane strain at $\mathcal{R} = 10^3$ are given in Figure 6.13. Figure 6.14 shows similar results for the ratio $\mathcal{R} = 10^{-3}$ and uniaxial loading $\bar{\varepsilon} = 0.01\,\boldsymbol{e}_1 \otimes \boldsymbol{e}_1$ under the plane stress assumption. Both examples confirm that the best convergence rate of CG-FANS with $\nu_r^{(1)} = \nu_f$ is found for problems with homogeneous Poisson's ratio (i.e., at the diagonal line $\nu_m = \nu_i$). For fundamental solutions computed with a fixed Poisson's ratio $\nu_r^{(2)} = 0.25$, the best convergence rates are observed along the line characterized by $\nu_- = 0.25$. It is pointed out that the third alternative $\nu_r^{(3)} = \nu_-$ recovers the "sweet
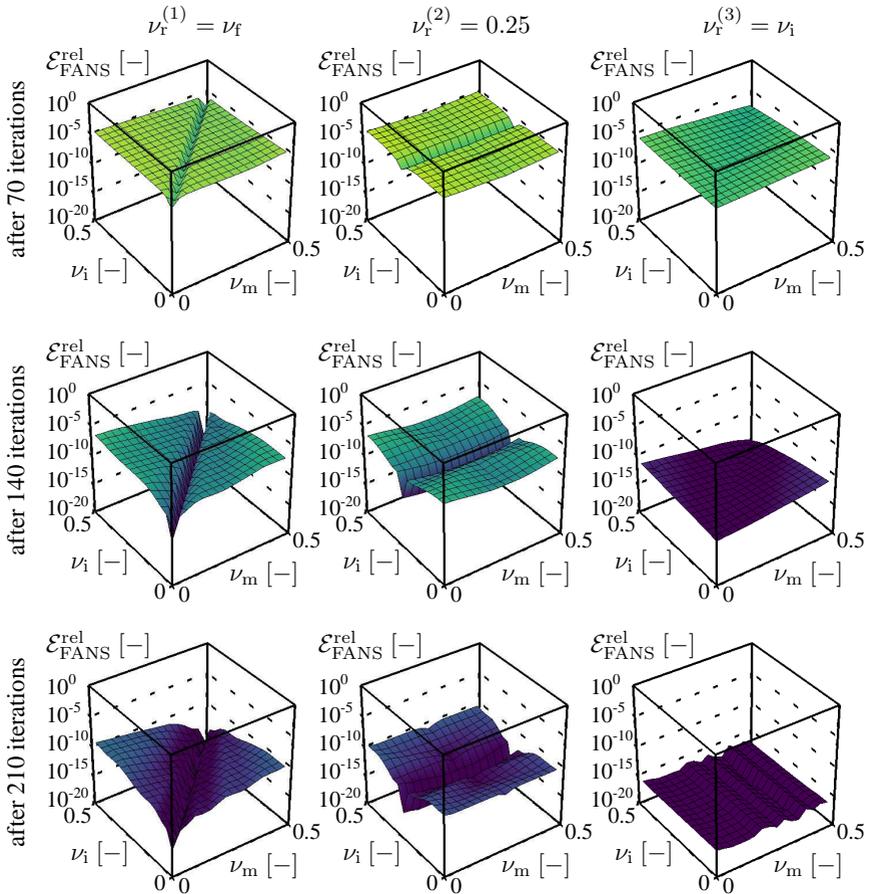
Figure 6.14: Convergence behavior of CG-FANS for fundamental solutions with different Poisson's ratios ν_r at a fixed ratio of Young's moduli $\mathcal{R} = 10^{-3}$. The results were obtained for uniaxial loading under the assumption of plane stress. The FANS error relative to its value before the first iteration is shown for different combinations of Poisson's ratios in the matrix and in the inclusions.

spot" lines detected for both previous choices $\nu_r^{(1)} = \nu_f$ and $\nu_r^{(2)} = 0.25$. Moreover, better convergence than in the first two cases is observed for other combinations of Poisson's ratios off those lines. Despite the fact that different loading conditions have been considered, the results displayed in Figures 6.13 and 6.14 are in good qualitative agreement concerning the suggestion that out of the three considered alternatives, the third one $\nu_r^{(3)} = \nu_-$ yields the best convergence of CG-FANS. The findings are also in line with results of a similar study for the benchmark unit cell previously presented

in Leuschner & Fritzen [2018] and with additional unpublished data. It should be mentioned that the merits of the choice $\nu_{\mathrm{r}}^{(3)} = \nu_-$ compared to $\nu_{\mathrm{r}}^{(1)} = \nu_{\mathrm{f}}$ are under some circumstances not as significant as in the cases considered here (e.g., for smaller values of $|\log(\mathcal{R})|$). However, the convergence of CG-FANS with fundamental solutions computed for the Poisson's ratio of the softer phase is at least as good as with the classical choice $\nu_{\mathrm{r}}^{(1)} = \nu_{\mathrm{f}}$ in all known examples of linear elastic mechanical homogenization problems.

6.5.3   Nonlinear homogenization with von Mises plasticity

Since nonlinear problems constitute the main scope of application of computational homogenization methods, the applicability of CG-FANS to nonlinear problems is briefly demonstrated for a composite material with von Mises plasticity in the matrix. The numerical example is based on the RVE with 30% circular inclusions (see Figure 6.7) at the resolution 1024×1024 and is otherwise equal to an example presented in Leuschner & Fritzen [2018] for a unit cell with a single square inclusion. The material properties are defined correspondent to an Al/SiC metal matrix composite with isotropic linear elastic particles characterized by the Young's modulus 400 GPa and the Poisson's ratio 0.2. The aluminum matrix is modeled by rate-independent von Mises plasticity with linear isotropic hardening, which can be implemented by the radial return scheme explained in Appendix B.1. The linear hardening modulus and initial yield stress are set to the values 500 MPa and 100 MPa, respectively, and the isotropic linear elastic parameters of the matrix material are specified as the Young's modulus 75 GPa and the Poisson's ratio 0.3.

Under the assumption of plane strain, three load paths are simulated, which all have the same final effective strain

$$\bar{\varepsilon}_{\mathrm{f}} = \bar{\varepsilon}_{\mathrm{s}} + \bar{\varepsilon}_{\mathrm{t}} \tag{6.71}$$

with

$$\bar{\varepsilon}_{\mathrm{s}} = \frac{\sqrt{2}}{200} \left(e_1 \otimes e_2 + e_2 \otimes e_1 \right), \qquad \bar{\varepsilon}_{\mathrm{t}} = \frac{\sqrt{2}}{200} \left(e_1 \otimes e_1 - e_2 \otimes e_2 \right). \tag{6.72}$$

In detail, the load cases are specified as follows:

[L1] proportional loading to the final effective strain $\bar{\varepsilon}_{\mathrm{f}}$ defined in (6.71);

[L2] two-step loading with proportional shear loading to $\bar{\varepsilon}_{\mathrm{s}}$ and subsequent additional proportional loading to the final effective strain $\bar{\varepsilon}_{\mathrm{f}}$;

[L3] two-step loading with proportional isochoric tension up to $\bar{\varepsilon}_{\mathrm{t}}$ and subsequent additional proportional loading to the final effective strain $\bar{\varepsilon}_{\mathrm{f}}$.

Figure 6.15 shows two components of the effective stress response computed with CG-FANS. The apparent dissimilarity of the final effective stress states highlights the path-dependence of the composite material. For the final state at the end of the three loadings,
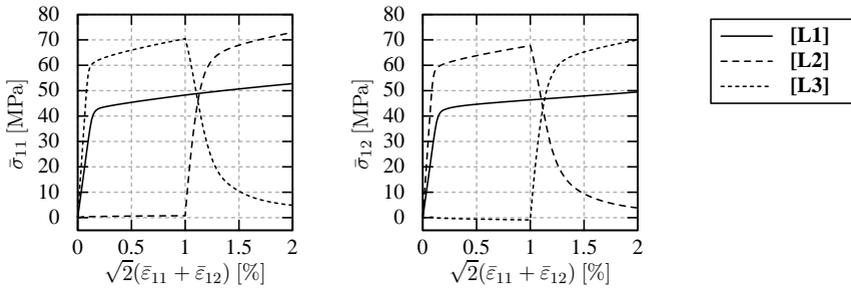
Figure 6.15: Effective stress response of a particle reinforced composite with von Mises plasticity in the matrix material for three load paths with equal terminus.
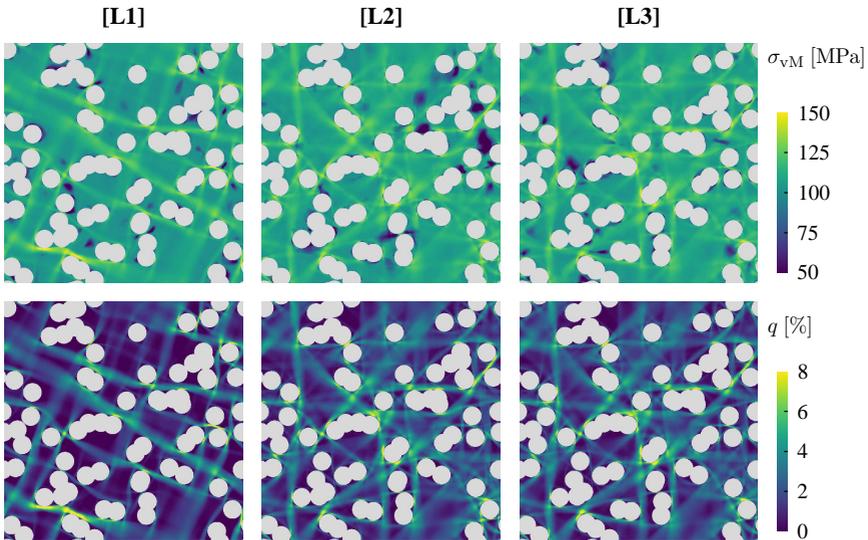

Figure 6.16: Local von Mises stress fields in the matrix *(top)* and local fields of the accumulated plastic strain *(bottom)* at the end of three different load paths with the same final effective strain $\bar{\varepsilon}_{\mathrm{f}}$.

the von Mises stress fields in the matrix material and the accumulated plastic strain fields are shown in Figure 6.16. Path-dependence is also visible here: the shear bands developed during the single-step loading **[L1]** differ significantly from those of the other load cases. However, the accumulated plastic strain fields at the final stages are quite similar for the loadings **[L2]** and **[L3]** (although the effective stresses differ completely, cf. Figure 6.15). This finding is in line with results presented for the benchmark problem with a single square inclusion in Leuschner & Fritzen [2018].

6.6   Discussion and perspectives

FANS has been developed with the intention to provide a numerically efficient full-field homogenization scheme that provides local fields without spurious artifacts for microstructures represented by pixel or voxel data. In fact, spurious oscillations were found neither in FANS solutions for thermal problems nor for mechanical problems. Moreover, for the benchmark problem presented in Section 6.5.1, the FANS result showed (slightly) better accordance with the closed-form solution than the one obtained with the rotated grid MGO scheme. Smoothness of the local fields is attained via FE shape functions, and the same would be possible with direct FE solvers in theory. However, with increasing model size, both computational effort and memory demand of direct solvers grow faster than for iterative solvers, which are usually favorable for large real-world homogenization problems [cf. Leuschner & Fritzen, 2018]. It is worth mentioning that all presented FANS results have been obtained with full integration. Unless suitable hourglass control is incorporated, reduced integration leads to pronounced checkerboards, as demonstrated in Leuschner & Fritzen [2018]. Note that computing the fundamental solution with full integration is not sufficient to suppress hourglassing.

Regarding numerical efficiency, the first aspect to be considered in a comparison of FANS with competing Fourier-based schemes is the convergence behavior. It is recalled that a direct comparison of convergence rates in terms of one of the respective error measures is unreasonable. A comparison on the basis of the convergence indicator $\mathcal{C}_{Q_1}$ defined in (6.56) showed rather similar convergence rates for FANS and for the rotated grid approach with a small advantage of FANS in the case of the square inclusion benchmark problem. The second aspect concerns the numerical cost per iteration. Table 6.2 specifies the numbers of relevant operations during fixed-point iterations of FANS, of FFT-Q_1Quad/Hex, and of conventional Fourier-based schemes following the run of Algorithm 6.3. An apparent issue with FFT-Q_1Quad/Hex is that its numerical cost scales almost linearly with the number P of integration points per element, such that FFT-Q_1Quad/Hex is competitive performance-wise with reduced integration only. This is in contrast to FANS, where the quadrature rule affects the effort for the assembly of the conductance/stiffness matrix only. The conductance/stiffness matrix also allows to avoid repeated evaluations of constitutive laws in the iterations. Admittedly, the numerical cost to evaluate Fourier's law or Hooke's law is almost negligible, but constitutive subroutines for complex nonlinear models can massively contribute to the total cost. Overall, it is fair to say that the periodized conductance/stiffness matrix requires a considerable amount of memory, and its assembly causes substantial one-time[27] cost, but it allows for fast iterations. Therefore, FANS are advantageous especially for problems that require many iterations. The break-even point, where the numerical effort for FANS corresponds to the one of the rotated grid scheme (or of other schemes in accordance with Algorithm 6.3), was in the range of nine to 15 iterations with a MATLAB implementation for thermal

---

[27]For linear problems, "one-time" refers to the entire homogenization problem including different loading conditions; for nonlinear problems, "one-time" means once per global Newton–Raphson iteration.

operations per FP iteration	conventional		FFT-Q_1 Quad/Hex		FP-FANS	
	T	M	T	M	T	M
forward/backward DFTs	d	$\frac{d}{2}(d+1)$	dP	$\frac{d}{2}(d+1)P$	1	d
eval. of constitutive law ($\times N$)	1	1	P	P	–	–
multipl. in real space ($\times N$)	–	–	–	–	3^d	$3^d d$
multipl. in Fourier space ($\times N$)	d^2	$\left(\frac{d}{2}(d+1)\right)^2$	$2dP+1$	$d^2(2P+1)$	1	d^2

Table 6.2: Comparison of numerical operations per iteration for different fixed-point schemes for thermal ("T") and mechanical ("M") problems. Multiplications arising during the evaluation of constitutive laws are not included in the second last row.

2D problems [considering different mesh sizes, cf. Leuschner & Fritzen, 2018]. Further preliminary computing times are presented in Leuschner & Fritzen [2018]. However, dedicated benchmark tests are outstanding and should be addressed in future studies with sophisticated implementations for 3D problems.

Meanwhile, it is pointed out that the computational complexity of FFT algorithms is $\mathcal{O}(N \log(N))$, while the remaining operations of Fourier-based schemes have the complexity $\mathcal{O}(N)$ only. Thus, for increasing numbers N of pixels/voxels, the number of forward and backward FFTs per iteration become more and more critical with regard to the overall numerical cost. With its lower number of FFTs compared to FFT-Q_1Quad/Hex and conventional Fourier-based schemes (cf. Table 6.2), FANS are favored in terms of computing times for large problems. The lower number of forward and backward FFTs results from the fact that the principal field of unknowns (temperature/displacement) and the divergence of the flux field (heat flux/Cauchy stress) are transformed in the FANS scheme, while the higher-dimensional gradient field (temperature gradient/strain) and flux field are transformed by conventional Fourier-based methods. The idea to perform the FFT on the lower-dimensional temperature/displacement field and on the divergence of the flux field has been first exploited in the *reduced scheme* of Willot et al. [2014] [see also Schneider et al., 2016] and necessitates the evaluation of the gradient and divergence fields in real space. While these differential operations are explicitly conducted in the reduced scheme of Willot et al. [2014], they are implicitly and efficiently performed via sparse multiplication with the periodized conductance/stiffness matrix in FANS. Figure 6.17 gives an overview of the main steps conducted in real space and in Fourier space for the Fourier-based methods discussion above. It is noted that a matrix-free version of FANS can be realized which somewhat corresponds to the reduced scheme shown in Figure 6.17. This approach is useful when the memory resources do not allow to store the periodized conductance/stiffness matrix but is not as fast as matrix-based FANS. However, the computing times of matrix-free and matrix-based FANS are near identical for linear constitutive models.

conventional [cf. Moulinec & Suquet, 1994]

g — evaluate constitutive law

apply (modified) Green's op. — q
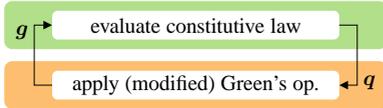
u : principal field (temperature/displacement)
g : gradient field (temperature gradient/strain)
q : flux field (heat flux/Cauchy stress)
r : divergence of flux field
● : real space
● : Fourier space

FANS

u — multiply with periodized matrix

apply fundamental solution — r
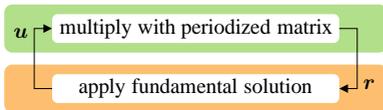
reduced scheme [cf. Willot et al., 2014]

u — compute gradient field

evaluate constitutive law — g

q — compute divergence field

apply fundamental solution — r
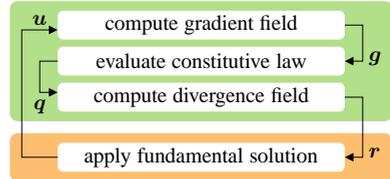
FFT-Q_1Quad/Hex [Schneider et al., 2016]

g — evaluate constitutive law

compute divergence field — q

r — apply fundamental solution

compute gradient field — u
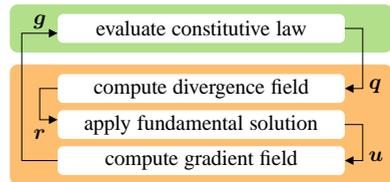
Figure 6.17: Real space operations (green) and Fourier space operations (orange) of different Fourier-based homogenization schemes.

Chapter 7:
Potential-based reduced basis homogenization

7.1 Introduction

As already mentioned in Section 5.1, the high numerical effort related to computational full-field homogenization schemes has motivated the development of various alternative, more efficient methods. One widely recognized example which is still subject of current research [see, e.g., Covezzi et al., 2017] is the *transformation field analysis* (TFA) originally proposed by Dvorak [1992] and Dvorak & Benveniste [1992]. The fundamental concept of the TFA is to divide inelastic phases of an RVE into subdomains in which the inelastic strain is assumed to be constant. Based on the TFA, Michel et al. [2000] proposed the *nonuniform transformation field analysis* (NTFA) for (visco-) plastic GSMs, which takes up several ideas of the TFA but introduces a nonuniform reduced basis (RB) for the inelastic strain, replacing the piecewise constant ansatz [see also Michel & Suquet, 2003, 2004, for early contributions to the NTFA]. Although other strategies are possible, appropriate RBs are in practice often identified by means of a proper orthogonal decomposition (POD) from a set of training solutions computed with a full-field method. Thus, although emerged from micro-mechanical considerations and initially not recognized as an MOR technique, the NTFA exhibits the relevant characteristics of reduced basis model order reduction (RBMOR) methods. However, it is pointed out that making an RB ansatz for the inelastic strain field, i.e., for internal state variables, is in contrast to many other RBMOR schemes which introduce RBs for the fields of principal unknowns (e.g., for the displacement field). Note that homogenization problems are well suited for MOR approaches because of two reasons: firstly, they are frequently applied in many query contexts such as two-scale simulations or parameter identification procedures, and secondly, the specific types of boundary conditions used for computational homogenization allow for neat parameterizations of the loading cases to be considered online and in the training.

Besides the RB approach, the postulation of semi-phenomenological macroscopic evolution laws is a key ingredient in the original formulation of the NTFA. Thereby, computational operations at the micro level are avoided and exceptional computational efficiency is attained. This advantage comes at the expense of fixedness with respect to the underlying constitutive models assumed at the small scale. For materials with viscoelastic constituents, a modified version of the NTFA with a macroscopic evolution law rigorously derived from a global dissipation potential was presented by Fritzen & Böhlke [2013]. This modification can be seen as an intermediate step towards the

potential-based RBMOR (pRBMOR) homogenization scheme proposed by Fritzen & Leuschner [2013] in order to cover a more comprehensive class of GSMs. The pRBMOR technique is a hybrid approach combining the RB ansatz of the NTFA with an alternative rigorous derivation of the macroscopic evolution law from the constitutive potentials given at the microscale. The versatility of this more general evolution law is enabled by local operations, which make for the crucial part of the overall computational cost in the online phase and prevent to keep up with the numerical efficiency of the NTFA. However, compared to full-field methods, significant savings in terms of computing time and memory requirement are still achieved with the pRBMOR homogenization scheme. It is also emphasized that the local online operations are small-sized and independent and thus perfectly suited for parallelization on graphics processing units (GPUs). Details concerning highly efficient implementations of the pRBMOR homogenization method on GPUs have been elucidated by Fritzen et al. [2014]. Fritzen & Hodapp [2016] have presented an application of such a GPU-accelerated implementation in a macroscopic FE simulation, referred to as FE[2R] ("FE square reduced"), and the FE[2R] scheme has been successfully applied in the context of topology optimization by Fritzen et al. [2016]. In order to obtain a purely global, more efficient model instead of a hybrid model with explicit incorporation of local information, Michel & Suquet [2016a,b] have recently proposed a modified version of the NTFA for moderately nonlinear materials. Here, the exact evaluations of the gradients of the local potentials considered in the pRBMOR scheme are replaced by tangent second order (TSO) approximations, and the approach is therefore called NTFA-TSO.

Both the NTFA and the pRBMOR scheme were originally proposed for microstructures with viscoplastic[28] constituents and without imperfect interfaces. The scalar hardening variable related to isotropic hardening was assumed to be phase-wise constant. An additional RB allowing to represent heterogeneous hardening states was introduced in Fritzen et al. [2014]. A further generalization of the pRBMOR concept to microstructures with imperfect interfaces is associated with incisive theoretical and practical modifications and was first addressed in Fritzen & Leuschner [2015]. Here, basic mechanisms related to reduced basis representations of displacement jump fields have been studied at the example of regularized unilateral contact without friction as defined in (4.19) at the boundary between two elastic phases. An extension towards dissipative imperfect interfaces in viscoplastic microstructures was eventually presented by Leuschner & Fritzen [2017]. In the present work, another two novel aspects are considered within the pRBMOR method for the first time:

- incorporation of more than one RB for hardening variables in the bulk, which allows to choose separate parameterizations for isotropic hardening variables and for NLKH internal state variables, and

- homogenization of thin layers via hybrid uniform–periodic boundary conditions.

---

[28]The NTFA has been proposed for rate-independent plasticity as well.

7.2   Constitutive assumptions

In addition to the hypotheses **[H1]**–**[H4]** and **[HM1]**–**[HM4]** from Section 5.3, the pRBMOR technique crucially exploits the assumption that all constitutive models given at the microscale are potential-based, which is also reflected in the method's name. More precisely, the bulk behavior of the microstructure is described by GSM models (cf. Chapter 3), while the imperfect interface is modeled within the SDCZ framework (cf. Section 4.6). Both, the GSM and the SDCZ models, are assumed to be rate-sensitive[29], and the local evolution laws are explicitly given in terms of dual dissipation potentials in accordance with (3.5) and (4.14). These preconditions allow to formulate an incremental variational principle from which the effective evolution law will be derived in Section 7.5. Furthermore, it is assumed that the internal variables of the GSM are separated into the inelastic strain $\boldsymbol{\varepsilon}_{\mathrm{p}}$ and into $N_{\mathrm{q}} \in \mathbb{N}_{>0}$ (formal) hardening variables[30] according to

$$\boldsymbol{\mathcal{I}} = \left(\boldsymbol{\varepsilon}_{\mathrm{p}}, \boldsymbol{q}_{[1]}, \ldots, \boldsymbol{q}_{[N_{\mathrm{q}}]} \right) \tag{7.1}$$

such that the Helmholtz free energy density can be expressed in the form

$$\psi(\boldsymbol{\varepsilon}, \boldsymbol{\mathcal{I}}) = \frac{1}{2} \left(\boldsymbol{\varepsilon} - \boldsymbol{\varepsilon}_{\mathrm{p}} \right) : \mathbb{C} : \left(\boldsymbol{\varepsilon} - \boldsymbol{\varepsilon}_{\mathrm{p}} \right) + \frac{1}{2} \boldsymbol{\varepsilon}_{\mathrm{p}} : \mathbb{K}_{\mathrm{l}} : \boldsymbol{\varepsilon}_{\mathrm{p}} + \sum_{i=1}^{N_{\mathrm{q}}} \psi_{[i]} \left(\boldsymbol{q}_{[i]} \right) \tag{7.2}$$

with a stiffness tensor $\mathbb{C}$ that is positive definite on the space of symmetric second order tensors (cf. Appendix A.1.2), an isotropic stiffness tensor $\mathbb{K}_{\mathrm{l}}$ in accordance with (3.16), and strongly convex hardening potentials $\psi_{[1]}, \ldots, \psi_{[N_{\mathrm{q}}]}$. This assumption is consistent with the general formulation for the free energy density previously adopted in (3.14) and (3.15), hence all GSM models from Chapter 3 are covered. The reason for the separated representation of the internal state variables is that each component on the right-hand side of (7.1) will be equipped with its own RB in Section 7.3.1. Note that (7.2) implies that all components of the separated representation are decoupled from each other, i.e., any gradient of ψ with respect to one component of $\boldsymbol{\mathcal{I}}$ is independent of all other components on the right-hand side of (7.1). The inelastic strain $\boldsymbol{\varepsilon}_{\mathrm{p}}$ is distinguished from the other internal state variables $\boldsymbol{q}_{[i]}$ in the bulk because it is the only one coupled to the strain $\boldsymbol{\varepsilon}$, and because it appears only in quadratic terms of the free energy density. Note that the generalized Hooke's law (3.9) induced by the first quadric term in (7.2) allows for the auxiliary elastic analyses in Section 7.4.

---

[29]The rate-sensitivity may result from viscous regularizations of rate-independent constitutive models.

[30]It is not required that one formal hardening variable represents one physical hardening variable, i.e., multiple physical hardening variables can be gathered in one formal hardening variable, or a non-scalar physical hardening variable might be split into several formal hardening variables such that different components of a vector or tensor are treated individually. In the latter case, deviatoric internal state variables $\boldsymbol{\alpha}^{(i)}$ for modeling NLKH as introduced in (3.13) must be represented by five-dimensional vectors.

Concerning the internal state variables at the imperfect interface, attention is limited to the ansatz $\breve{\mathcal{I}} = \boldsymbol{y}$ in this work, but extensions to separated representations like (7.1) are straightforward. No particular assumptions are made regarding the Helmholtz free energy $\breve{\psi} \equiv \breve{\psi}(\boldsymbol{\delta}, \boldsymbol{y})$ of the SDCZ except for strong convexity. The requirement that $\breve{\psi}$ and the (bulk) hardening potentials are strongly convex is necessary for technical reasons (see Appendix B.3) but reflects also the theoretical limitations of first order homogenization schemes.

The Helmholtz free energy densities ψ and $\breve{\psi}$ are functions of the primal local states

$$\boldsymbol{\mathcal{S}} = (\boldsymbol{\varepsilon}, \boldsymbol{\mathcal{I}}) \qquad \text{in } \Omega, \qquad\qquad \breve{\boldsymbol{\mathcal{S}}} = \left(\boldsymbol{\delta}, \breve{\boldsymbol{\mathcal{I}}}\right) \qquad \text{on } \mathscr{I} \qquad (7.3)$$

and define the corresponding dual local states

$$\boldsymbol{\mathcal{S}}^* = (\boldsymbol{\sigma}, \boldsymbol{\mathcal{F}}) \qquad \text{in } \Omega, \qquad\qquad \breve{\boldsymbol{\mathcal{S}}}^* = \left(\breve{\boldsymbol{t}}, \breve{\boldsymbol{\mathcal{F}}}\right) \qquad \text{on } \mathscr{I} \qquad (7.4)$$

via the constitutive relations (3.1) and (4.14), respectively. In particular, the driving forces conjugate to the internal state variables are defined and denoted according to

$$\boldsymbol{\mathcal{F}} = -\frac{\partial \psi}{\partial \boldsymbol{\mathcal{I}}} = \left(\boldsymbol{\sigma}_{\mathbf{p}}, \boldsymbol{r}_{[1]}, \dots, \boldsymbol{r}_{[N_q]}\right), \qquad\qquad \breve{\boldsymbol{\mathcal{F}}} = -\frac{\partial \breve{\psi}}{\partial \breve{\boldsymbol{\mathcal{I}}}} = \boldsymbol{z}. \qquad (7.5)$$

7.3 Reduced basis ansatz

7.3.1 Reduced basis parameterizations

An essential task in the development of homogenization schemes is to define suitable finite parameterizations of the fields of kinematic and internal state variables. Any possible kinematic state of an RVE is characterized by the global displacement gradient $\bar{\boldsymbol{H}}$ and by the displacement fluctuation field. The set $\mathcal{U}$ of all admissible displacement fluctuation fields $\tilde{\boldsymbol{u}}(\boldsymbol{x})$ is infinite dimensional in general. Further, the sets $\mathcal{Y}$ and $\breve{\mathcal{Y}}$ comprising all possible fields $\boldsymbol{\mathcal{I}}(\boldsymbol{x})$ and $\breve{\boldsymbol{\mathcal{I}}}(\breve{\boldsymbol{x}})$ of internal state variables in the bulk and on the interface, respectively, are infinite dimensional as well. The introduction of a finite parameterization of the (primal) RVE state necessitates the replacement of the infinite dimensional sets $\mathcal{U}$, $\mathcal{Y}$, and $\breve{\mathcal{Y}}$ by finite dimensional subsets (unless the overall behavior is linear elastic). Linear elastic two-scale materials represent a special case where $\mathcal{Y}$ and $\breve{\mathcal{Y}}$ are empty and the displacement fluctuation field is uniquely determined by $\bar{\boldsymbol{H}}$ already, as will be seen in Section 7.4. However, nontrivial finite parameterizations of the RVE state are required in the presence of nonlinearities. In this work, such nonlinearities are due to internal state variables and/or due to nonlinear interfaces[31].

Standard discretizations of RVEs yield finite parameterizations, but the number of independent variables to be stored is typically enormous such that even saving the

---

[31]Nonlinear elastic materials (typically adopted in finite strain settings) contradict the constitutive assumption (7.2) and are thus not taken into account; such materials necessitate nontrivial parameterizations of the RVE state as well.

current state of a realistic two-scale simulation is a challenge (not to mention the time history). Such discretizations are therefore not suitable in many situations. Piecewise constant representations, as chosen for the TFA, do not suffer from the above-mentioned difficulty if the number of subdomains is moderate. However, the constitutive response predicted by the TFA with relatively few subdomains is in general too stiff, and quite a lot subdomains can be necessary in order to capture micro-fluctuations, which can have a considerable influence on the overall material behavior, sufficiently well. In response to this issue, the eponymous concept of the NTFA is to utilize nonuniform transformation fields $\boldsymbol{\mu}^{(1)}(\boldsymbol{x}), \dots, \boldsymbol{\mu}^{(N_\xi)}(\boldsymbol{x})$ which provide low-dimensional parameterizations while capturing the most relevant characteristics of the microscopic fields. Typically, the dimension N_ξ of the parameterizations is in the range of one-digit or small two-digit integers. Mathematically speaking, the nonuniform transformation fields are time-independent reduced basis vector fields with global support (in contrast to finite element shape functions with local support). Following Michel & Suquet [2003], the plastic strain is approximated via the space–time decomposition

$$\boldsymbol{\varepsilon}_{\mathrm{p}}(\boldsymbol{x}, t) = \sum_{j=1}^{N_\xi} \xi_j(t)\, \boldsymbol{\mu}^{(j)}(\boldsymbol{x}) \qquad \Leftrightarrow \qquad \underline{\varepsilon}_{\mathrm{p}}(\boldsymbol{x}, t) = \underline{\underline{P}}(\boldsymbol{x})\, \underline{\xi}(t) \qquad (\boldsymbol{x} \in \Omega) \qquad (7.6)$$

with the time-dependent coefficients collected in the vector $\underline{\xi}(t)$, which can be understood as a vector of global internal variables. The matrix–vector notation of the linear combination is introduced to simplify subsequent technical descriptions and is based on a columnwise assembly of the reduced basis according to

$$\underline{\underline{P}} \colon \Omega \to \mathbb{R}^{6 \times N_\xi}$$
$$\boldsymbol{x} \mapsto \left[\underline{\mu}^{(1)}(\boldsymbol{x}) \quad \cdots \quad \underline{\mu}^{(N_\xi)}(\boldsymbol{x}) \right]. \qquad (7.7)$$

Since it allows to recover the local plastic strain from the global vector $\underline{\xi}$, $\underline{\underline{P}}$ is referred to as plastic *localization operator*. One proceeds similarly with the remaining internal state variables. For the ith bulk hardening variable ($i \in \{1, \dots, N_{\mathrm{q}}\}$), the representation

$$\boldsymbol{q}_{[i]}(\boldsymbol{x}, t) = \sum_{j=1}^{N_\lambda^{[i]}} \lambda_j^{[i]}(t)\, \boldsymbol{q}_{[i]}^{(j)}(\boldsymbol{x}) \quad \Leftrightarrow \quad \underline{q}_{[i]}(\boldsymbol{x}, t) = \underline{\underline{Q}}^{[i]}(\boldsymbol{x})\, \underline{\lambda}^{[i]}(t) \qquad (\boldsymbol{x} \in \Omega) \quad (7.8)$$

is adopted with a hardening localization operator $\underline{\underline{Q}}^{[i]}$ defined columnwise analogous to (7.7). A reduced basis for internal state variables $\overline{\boldsymbol{y}}$ at the imperfect interface [first considered by Leuschner & Fritzen, 2017] is incorporated via

$$\boldsymbol{y}(\check{\boldsymbol{x}}, t) = \sum_{j=1}^{N_\nu} \nu_j(t)\, \boldsymbol{y}^{(j)}(\check{\boldsymbol{x}}) \qquad \Leftrightarrow \qquad \underline{y}(\check{\boldsymbol{x}}, t) = \underline{\underline{Y}}(\check{\boldsymbol{x}})\, \underline{\nu}(t) \qquad (\check{\boldsymbol{x}} \in \mathscr{I}). \qquad (7.9)$$

For notational brevity, the coefficient vectors from (7.6), (7.8), and (7.9), corresponding to the global internal state variables, are concatenated according to

$$\bar{\underline{\mathcal{I}}} = \begin{bmatrix} \underline{\xi}^{\mathsf{T}} & \underline{\lambda}^{\mathsf{T}} & \underline{\nu}^{\mathsf{T}} \end{bmatrix}^{\mathsf{T}} \in \mathbb{R}^{N_{\mathcal{I}}} \qquad \text{with } \underline{\lambda} = \begin{bmatrix} \underline{\lambda}^{[1]\mathsf{T}} & \cdots & \underline{\lambda}^{[N_{\mathrm{q}}]\mathsf{T}} \end{bmatrix}^{\mathsf{T}} \in \mathbb{R}^{N_{\lambda}}, \quad (7.10)$$

where the abbreviations

$$N_{\mathcal{I}} = N_{\xi} + N_{\lambda} + N_{\nu}, \qquad\qquad N_{\lambda} = \sum_{i=1}^{N_{\mathrm{q}}} N_{\lambda}^{[i]} \qquad\qquad (7.11)$$

have been used. The sets of all fields of internal state variables covered by the reduced basis representation are denoted $\mathcal{Y}_{\mathrm{RB}} \subset \mathcal{Y}$ for the bulk and $\check{\mathcal{Y}}_{\mathrm{RB}} \subset \check{\mathcal{Y}}$ for the interface. It is concluded that the local internal state variables of the microstructure are directly parameterized by the reduced global internal state $\bar{\underline{\mathcal{I}}}$. In contrast, the local kinematic state is represented by the strain field $\boldsymbol{\varepsilon}(\boldsymbol{x})$ in the bulk and by the displacement jump field $\boldsymbol{\delta}(\check{\boldsymbol{x}})$ at the imperfect interface and is not fully defined by the global kinematic loading $\bar{\boldsymbol{H}}$, which is specified either by the prescribed global strain $\bar{\boldsymbol{\varepsilon}}$ for HBM or by the prescribed global displacement $\bar{\boldsymbol{\delta}}$ for HTL (cf. Section 5.4). An additional reduced basis is introduced as a reasonable parameterization of the displacement jump field [first proposed by Fritzen & Leuschner, 2015]

$$\boldsymbol{\delta}(\check{\boldsymbol{x}}, t) = \sum_{j=1}^{N_{\zeta}} \zeta_j(t)\, \boldsymbol{\delta}^{(j)}(\check{\boldsymbol{x}}) \qquad \Leftrightarrow \qquad \underline{\delta}(\check{\boldsymbol{x}}, t) = \underline{\underline{\Delta}}(\check{\boldsymbol{x}})\, \underline{\zeta}(t) \qquad (\check{\boldsymbol{x}} \in \mathscr{I}). \quad (7.12)$$

The coefficient vector $\underline{\zeta}$ is a reduced global kinematic state variable. At the same time, it is an intrinsic variable since it is not prescribed at the macroscopic level ("from outside") as opposed to the global displacement gradient $\bar{\boldsymbol{H}}$. Therefore, it can be considered a *kinematic* internal state variable, while $\bar{\underline{\mathcal{I}}}$ describes the *constitutive* internal state. In contrast to the kinematic state at the interface, the kinematic state in the bulk is not equipped with a dedicated reduced basis. This saving of yet another reduced basis[32] is made possible by the assumption of the generalized Hooke's law (3.9) through the specific structure of the Helmholtz free energy density in the bulk in (7.2). It will be shown in Section 7.4 that all physically admissible local strain fields are uniquely determined for a given (primal) global state

$$\bar{\underline{\mathcal{S}}} = \begin{cases} (\bar{\varepsilon}, \bar{\underline{\mathcal{I}}}, \underline{\zeta}) & \text{for HBM;} \\ (\bar{\underline{\delta}}, \bar{\underline{\mathcal{I}}}, \underline{\zeta}) & \text{for HTL} \end{cases} \qquad\qquad (7.13)$$

and can be obtained by a superposition principle. With the reduced basis representation given in terms of $\bar{\underline{\mathcal{S}}}$, the set of all admissible displacement fluctuation fields $\mathcal{U}$ is replaced by the subset $\mathcal{U}_{\mathrm{RB}} \subset \mathcal{U}$. It is recalled that the constitutive relations (3.1) and (4.14) define the conjugate dual state for any primal state of the RVE. The sets $\mathcal{Z}$ and $\check{\mathcal{Z}}$ of all fields

---

[32]In contrast, an additional reduced basis for the kinematic state in the bulk would be required in the geometrically nonlinear setting. The extension of pRBMOR to large deformations is subject of ongoing research.

of driving forces $\mathcal{F}(\boldsymbol{x})$ and $\breve{\mathcal{F}}(\breve{\boldsymbol{x}})$ are thus implicitly defined by $\mathcal{U}$, $\mathcal{Y}$, and $\breve{\mathcal{Y}}$. Similarly, the subsets $\mathcal{Z}_{\mathrm{RB}} \subset \mathcal{Z}$ and $\breve{\mathcal{Z}}_{\mathrm{RB}} \subset \breve{\mathcal{Z}}$ are obtained from $\mathcal{U}_{\mathrm{RB}}$, $\mathcal{Y}_{\mathrm{RB}}$, and $\breve{\mathcal{Y}}_{\mathrm{RB}}$ via (3.1) and (4.14). In other words, no distinct parameterization is introduced for the dual state of the RVE, but the one naturally induced by the reduced basis parameterization of the primal RVE state is assumed.

7.3.2 Reduced basis identification

The time-independent reduced bases are computed once in advance in the offline phase, and the online algorithm of the pRBMOR homogenization scheme is derived without further assumptions concerning their identification. Readers familiar with reduced basis identification by the POD approach are encouraged to skip to Section 7.4.

It is self-evident that the attainable accuracy of reduced basis homogenization methods depends crucially on their capability to capture relevant microscopic fields. In reduced order modeling, the POD[33] is established as a powerful tool to identify appropriate reduced bases, and, for completeness, its basics are briefly summarized below [roughly following Fritzen, 2017]. The point of departure is to collect data from (full-field) training simulations which are given in the form of $n \in \mathbb{N}_{>0}$ snapshots $\boldsymbol{s}^{(1)}, \dots, \boldsymbol{s}^{(n)}$ from a high fidelity solution space

$$\mathcal{V} = \mathrm{span}\left\{\boldsymbol{\varphi}^{(1)}, \dots, \boldsymbol{\varphi}^{(N)}\right\} \tag{7.14}$$

with the finite dimension $N \geq n$. It is assumed that $\mathcal{V}$ is a Hilbert space with an inner product denoted $(\bullet, \bullet)_{\mathcal{V}}$. The goal is to find an orthonormal reduced basis $\left\{\boldsymbol{b}_*^{(j)} : 1 \leq j \leq p\right\}$ of the p-dimensional subspace $(p < n)$

$$\mathcal{V}_{\mathrm{RB}} = \mathrm{span}\left\{\boldsymbol{b}_*^{(1)}, \dots, \boldsymbol{b}_*^{(p)}\right\} \subset \mathcal{V} \tag{7.15}$$

which allows for the best possible approximations of the snapshots. Mathematically speaking, the task is to solve the minimization problem

$$\left(\boldsymbol{b}_*^{(1)}, \dots, \boldsymbol{b}_*^{(p)}\right) = \underset{\substack{\boldsymbol{b}^{(1)}, \dots, \boldsymbol{b}^{(p)} \\ \text{with } \left(\boldsymbol{b}^{(i)}, \boldsymbol{b}^{(j)}\right)_{\mathcal{V}} = \delta_{ij}}}{\mathrm{argmin}} \sum_{i=1}^{n} \min_{\xi \in \mathbb{R}^p} \left\| \boldsymbol{s}^{(i)} - \sum_{j=1}^{p} \xi_j \, \boldsymbol{b}^{(j)} \right\|_{\mathcal{V}}^2 \tag{7.16}$$

where $\|\bullet\|_{\mathcal{V}}$ denotes the norm induced by $(\bullet, \bullet)_{\mathcal{V}}$. The basis functions $\boldsymbol{\varphi}^{(i)}$ corresponding to the full-field discretization are used to define the symmetric and positive definite matrix

$$\underline{M} \in \mathbb{R}^{N \times N} \qquad \text{with } M_{ij} = \left(\boldsymbol{\varphi}^{(i)}, \boldsymbol{\varphi}^{(j)}\right)_{\mathcal{V}}. \tag{7.17}$$

---

[33]The POD is also known as *principal component analysis* (PCA) or as *Karhunen–Loève transform* in other fields of applications.

Any $\boldsymbol{f} \in \mathcal{V}$ has a unique vector representation $\underline{f} \in \mathbb{R}^N$ in terms of the basis functions $\boldsymbol{\varphi}^{(i)}$

$$\boldsymbol{f} = \sum_{i=1}^{N} f_i \, \boldsymbol{\varphi}^{(i)} \qquad \text{with } \left(\underline{f}\right)_i = f_i = \sum_{j=1}^{N} \left(\underline{\underline{M}}^{-1}\right)_{ij} \left(\boldsymbol{f}, \boldsymbol{\varphi}^{(j)}\right)_{\mathcal{V}}, \tag{7.18}$$

and the inner product of $\boldsymbol{f}, \boldsymbol{g} \in \mathcal{V}$ can be expressed by

$$(\boldsymbol{f}, \boldsymbol{g})_{\mathcal{V}} = \underline{f}^{\mathsf{T}} \underline{\underline{M}} \, \underline{g}. \tag{7.19}$$

Making use of the above introduced vector notation, the snapshots and the reduced basis functions are wrapped into the matrices

$$\underline{\underline{S}} = \begin{bmatrix} \underline{s}^{(1)} & \cdots & \underline{s}^{(n)} \end{bmatrix} \in \mathbb{R}^{N \times n}, \qquad \underline{\underline{B}} = \begin{bmatrix} \underline{b}^{(1)} & \cdots & \underline{b}^{(p)} \end{bmatrix} \in \mathbb{R}^{N \times p}, \tag{7.20}$$

respectively. The orthonormality of the reduced basis functions can be characterized by

$$\underline{\underline{B}}^{\mathsf{T}} \underline{\underline{M}} \, \underline{\underline{B}} = \underline{\underline{I}} \in \mathbb{R}^{p \times p}. \tag{7.21}$$

For a fixed $\underline{\underline{B}} \in \mathbb{R}^{N \times p}$ satisfying (7.21), a straightforward calculation yields

$$\min_{\underline{\xi} \in \mathbb{R}^p} \left\| \boldsymbol{s}^{(i)} - \sum_{j=1}^{p} \xi_j \, \boldsymbol{b}^{(j)} \right\|_{\mathcal{V}}^2 = \left(\underline{s}^{(i)}\right)^{\mathsf{T}} \left(\underline{\underline{M}} - \underline{\underline{M}} \, \underline{\underline{B}} \, \underline{\underline{B}}^{\mathsf{T}} \underline{\underline{M}}\right) \underline{s}^{(i)} \qquad (i = 1, \dots, n). \tag{7.22}$$

Thereby, the minimization problem (7.16) can be reformulated as

$$\underline{\underline{B}}_* = \underset{\substack{\underline{\underline{B}} \in \mathbb{R}^{N \times p} \\ \text{with } \underline{\underline{B}}^{\mathsf{T}} \underline{\underline{M}} \, \underline{\underline{B}} = \underline{\underline{I}}}}{\operatorname{argmin}} \; \operatorname{tr} \left(\underline{\underline{S}}^{\mathsf{T}} \left(\underline{\underline{M}} - \underline{\underline{M}} \, \underline{\underline{B}} \, \underline{\underline{B}}^{\mathsf{T}} \underline{\underline{M}} \right) \underline{\underline{S}} \right) \tag{7.23}$$

$$= \underset{\substack{\underline{\underline{B}} \in \mathbb{R}^{N \times p} \\ \text{with } \underline{\underline{B}}^{\mathsf{T}} \underline{\underline{M}} \, \underline{\underline{B}} = \underline{\underline{I}}}}{\operatorname{argmax}} \; \operatorname{tr} \left(\underline{\underline{S}}^{\mathsf{T}} \underline{\underline{M}} \, \underline{\underline{B}} \, \underline{\underline{B}}^{\mathsf{T}} \underline{\underline{M}} \, \underline{\underline{S}} \right). \tag{7.24}$$

The closed-form solution maximizing (7.24) is obtained from a truncated singular value decomposition (SVD) of $\underline{\underline{\tilde{S}}} = \sqrt{\underline{\underline{M}}} \, \underline{\underline{S}}$, which can be computed via the eigendecomposition of the correlation matrix $\underline{\underline{\tilde{C}}} = \underline{\underline{\tilde{S}}}^{\mathsf{T}} \underline{\underline{\tilde{S}}} \in \mathbb{R}^{n \times n}$

$$\underline{\underline{\tilde{C}}} \, \underline{\underline{E}} = \underline{\underline{E}} \, \underline{\underline{\Lambda}} \qquad \text{with } \underline{\underline{E}}^{\mathsf{T}} \underline{\underline{E}} = \underline{\underline{E}} \, \underline{\underline{E}}^{\mathsf{T}} = \underline{\underline{I}} \in \mathbb{R}^{n \times n}, \quad \underline{\underline{\Lambda}} = \underline{\underline{\Sigma}} \, \underline{\underline{\Sigma}} \in \mathbb{R}^{n \times n}, \tag{7.25}$$

$$\underline{\underline{\Sigma}} = \operatorname{diag}\left(s_1, \dots, s_n\right), \quad s_1 \geq \cdots \geq s_n \geq 0. \tag{7.26}$$

The SVD of $\underline{\underline{\tilde{S}}}$ reads

$$\underline{\underline{\tilde{S}}} = \underline{\underline{\tilde{A}}} \, \underline{\underline{\Sigma}} \, \underline{\underline{E}}^{\mathsf{T}} \qquad \text{with } \underline{\underline{\tilde{A}}} = \sqrt{\underline{\underline{M}}} \, \underline{\underline{A}} \in \mathbb{R}^{N \times n}, \quad \underline{\underline{A}} = \underline{\underline{S}} \, \underline{\underline{E}} \, \underline{\underline{\Sigma}}^{-1} \in \mathbb{R}^{N \times n}, \tag{7.27}$$

and the desired reduced basis matrix $\underline{\underline{B}}_*$ is given by the first p columns of $\underline{\underline{A}}$.

Basis functions computed via a POD are commonly referred to as *modes*. In contrast to the original NTFA, the pRBMOR scheme is invariant to scaling of the modes. For convenience, the modes used for pRBMOR are normalized according to

$$\left\langle \underline{\underline{P}}^{\mathsf{T}} \underline{\underline{P}} \right\rangle_{\Omega} = \underline{\underline{I}} \in \mathbb{R}^{N_\xi \times N_\xi}, \quad \left\langle \left(\underline{\underline{Q}}^{[i]}\right)^{\mathsf{T}} \underline{\underline{Q}}^{[i]} \right\rangle_{\Omega} = \underline{\underline{I}} \in \mathbb{R}^{N_\lambda^{[i]} \times N_\lambda^{[i]}} \quad (i = 1, \dots, N_{\mathrm{q}}),$$
(7.28)

$$\left\langle \underline{\underline{Y}}^{\mathsf{T}} \underline{\underline{Y}} \right\rangle_{\mathscr{I}} = \underline{\underline{I}} \in \mathbb{R}^{N_\nu \times N_\nu}, \qquad \left\langle \underline{\underline{\Delta}}^{\mathsf{T}} \underline{\underline{\Delta}} \right\rangle_{\mathscr{I}} = \underline{\underline{I}} \in \mathbb{R}^{N_\zeta \times N_\zeta}.$$
(7.29)

For the identification of the displacement jump modes, multiple snapshots of displacement jump fields at different time steps are usually collected from each training simulation. This strategy can also be used to identify the modes for internal state variables, but experience shows that training with snapshots of time-weighted rates (corresponding to increments) of internal variables gives better results. Attention is required for (local) internal state variables which are subject to constraints. For instance, non-negativity of an isotropic hardening variable cannot be guaranteed with the linear combination in (7.9) without further ado. In practice, this has not caused trouble thus far, and it was always sufficient to just set occasional negative values to zero. Still, a more rigorous approach with a non-negative reduced basis is possible. With the additional requirement that the matrix $\underline{\underline{B}}$ must be componentwise non-negative, the maximization of (7.24) does no longer have a closed-form solution. However, several iterative non-negative matrix factorization (NMF) algorithms exist [see, e.g., Lee & Seung, 2000] to solve problems of that kind. Additional non-negativity constraints imposed on the corresponding global internal variables will ensure the required local non-negativity. Due to missing need, this NMF-based approach has not yet been implemented for the pRBMOR framework and is left to future work.

7.4 Auxiliary elastic analyses

The generalized Hooke's law (3.9) adopted through the constitutive assumption (7.2) implies that the nonlinearity of the overall stress response is either due to plastic yielding or due to an opening of the imperfect interface. Consequently, if a fixed plastic strain field $\varepsilon_{\mathrm{p}}^{!}(\boldsymbol{x})$ and a fixed interface opening field $\boldsymbol{\delta}^{!}(\breve{\boldsymbol{x}})$ are prescribed, a linear boundary value problem is obtained, which is defined by the equations

$$\operatorname{div}(\boldsymbol{\sigma}) = \boldsymbol{0}, \qquad \boldsymbol{\sigma} = \mathbb{C} : \left(\operatorname{sym}\left(\bar{\boldsymbol{H}} + \operatorname{grad}\left(\tilde{\boldsymbol{u}} \right) \right) - \varepsilon_{\mathrm{p}}^{!} \right) \qquad \text{in } \Omega, \qquad (7.30)$$

$$[\![\boldsymbol{\sigma}]\!] \, \breve{\boldsymbol{n}} = \boldsymbol{0}, \qquad [\![\tilde{\boldsymbol{u}}]\!] = \boldsymbol{\delta}^{!} \qquad \qquad \text{at } \mathscr{I} \qquad (7.31)$$

combined with periodic boundary conditions (cf. Figure 5.2) or hybrid uniform–periodic boundary conditions (cf. Figure 5.4) imposed on the displacement fluctuations $\tilde{\boldsymbol{u}}$. Clearly, the reduced basis setting requires that the fixed fields $\varepsilon_{\mathrm{p}}^{!}(\boldsymbol{x})$ and $\boldsymbol{\delta}^{!}(\breve{\boldsymbol{x}})$ can be described by the space–time representations (7.6) and (7.12), respectively. Thus, as a consequence of the superposition principle, the solution space of the above linear

	Request ("Input")			Solution ("Output")			Index range
	$\bar{H}$	$\varepsilon_{\mathrm{p}}^{!}(\boldsymbol{x})$	$\boldsymbol{\delta}^{!}(\check{\boldsymbol{x}})$	$\boldsymbol{u}(\boldsymbol{x})$	$\varepsilon(\boldsymbol{x})$	$\sigma(\boldsymbol{x})$	i
[E1-HBM]	$\boldsymbol{B}^{(i)}$	$\boldsymbol{0}$	$\boldsymbol{0}$	$\boldsymbol{u}_{\bar{\varepsilon}}^{(i)}(\boldsymbol{x})$	$\varepsilon_{\bar{\varepsilon}}^{(i)}(\boldsymbol{x})$	$\sigma_{\bar{\varepsilon}}^{(i)}(\boldsymbol{x})$	$1,\ldots,6$
[E1-HTL]	$\boldsymbol{e}_i \otimes \bar{\boldsymbol{n}}$	$\boldsymbol{0}$	$\boldsymbol{0}$	$\boldsymbol{u}_{\bar{\delta}}^{(i)}(\boldsymbol{x})$	$\varepsilon_{\bar{\delta}}^{(i)}(\boldsymbol{x})$	$\sigma_{\bar{\delta}}^{(i)}(\boldsymbol{x})$	$1,\ldots,3$
[E2]	$\boldsymbol{0}$	$\boldsymbol{\mu}^{(i)}(\boldsymbol{x})$	$\boldsymbol{0}$	$\boldsymbol{u}_{\xi}^{(i)}(\boldsymbol{x})$	$\varepsilon_{\xi}^{(i)}(\boldsymbol{x})$	$\sigma_{\xi}^{(i)}(\boldsymbol{x})$	$1,\ldots,N_\xi$
[E3]	$\boldsymbol{0}$	$\boldsymbol{0}$	$\boldsymbol{\delta}^{(i)}(\check{\boldsymbol{x}})$	$\boldsymbol{u}_{\zeta}^{(i)}(\boldsymbol{x})$	$\varepsilon_{\zeta}^{(i)}(\boldsymbol{x})$	$\sigma_{\zeta}^{(i)}(\boldsymbol{x})$	$1,\ldots,N_\zeta$

Table 7.1: Summary of the auxiliary elastic analyses described in Section 7.4.

boundary value problem has a finite dimensional parameterization in terms of the global state variables $\bar{\varepsilon}$, ξ, and ζ. This parameterization is developed through auxiliary elastic analyses, in which the linear problem is solved for several distinct choices of the global displacement gradient $\bar{H}$ and of the fixed fields $\varepsilon_{\mathrm{p}}^{!}(\boldsymbol{x})$ and $\boldsymbol{\delta}^{!}(\check{\boldsymbol{x}})$. In detail, the linear problem is solved consecutively with the following presets:

[E1] the fields $\varepsilon_{\mathrm{p}}^{!}(\boldsymbol{x})$ and $\boldsymbol{\delta}^{!}(\check{\boldsymbol{x}})$ are set to zero, while $\bar{H}$ is defined as

> **[E1-HBM]** $\boldsymbol{B}^{(i)}$ $(i=1,\ldots,6)$ for HBM[34] according to Section 5.4.1, or as
> **[E1-HTL]** $\boldsymbol{e}_i \otimes \bar{\boldsymbol{n}}$ $(i=1,\ldots,3)$ for HTL following Section 5.4.2;

[E2] with $\bar{H}$ and $\boldsymbol{\delta}^{!}(\check{\boldsymbol{x}})$ set to zero, the ith plastic mode $\boldsymbol{\mu}^{(i)}(\boldsymbol{x})$ $(i=1,\ldots,N_\xi)$ is prescribed as $\varepsilon_{\mathrm{p}}^{!}(\boldsymbol{x})$;

[E3] while $\bar{H}$ and $\varepsilon_{\mathrm{p}}^{!}(\boldsymbol{x})$ are assumed to vanish, $\boldsymbol{\delta}^{!}(\check{\boldsymbol{x}})$ is defined as the ith displacement jump mode $\boldsymbol{\delta}^{(i)}(\check{\boldsymbol{x}})$ $(i=1,\ldots,N_\zeta)$.

The displacement, strain, and stress fields of the respective solutions are denoted as summarized in Table 7.1. The strain localization operators

$$\underline{\underline{E}}_{\bar{\varepsilon}}(\boldsymbol{x}) = \begin{bmatrix} \underline{\varepsilon}_{\bar{\varepsilon}}^{(1)}(\boldsymbol{x}) & \cdots & \underline{\varepsilon}_{\bar{\varepsilon}}^{(6)}(\boldsymbol{x}) \end{bmatrix} \quad \text{or} \quad \underline{\underline{E}}_{\bar{\delta}}(\boldsymbol{x}) = \begin{bmatrix} \underline{\varepsilon}_{\bar{\delta}}^{(1)}(\boldsymbol{x}) & \cdots & \underline{\varepsilon}_{\bar{\delta}}^{(3)}(\boldsymbol{x}) \end{bmatrix}, \quad (7.32)$$

$$\underline{\underline{E}}_{\xi}(\boldsymbol{x}) = \begin{bmatrix} \underline{\varepsilon}_{\xi}^{(1)}(\boldsymbol{x}) & \cdots & \underline{\varepsilon}_{\xi}^{(N_\xi)}(\boldsymbol{x}) \end{bmatrix}, \qquad \underline{\underline{E}}_{\zeta}(\boldsymbol{x}) = \begin{bmatrix} \underline{\varepsilon}_{\zeta}^{(1)}(\boldsymbol{x}) & \cdots & \underline{\varepsilon}_{\zeta}^{(N_\zeta)}(\boldsymbol{x}) \end{bmatrix} \quad (7.33)$$

are defined as columnwise arrangements of the vector representations of the strain solution fields, similar to the definitions of the reduced basis localization operators in

---

[34]Here, $\boldsymbol{B}^{(1)},\ldots,\boldsymbol{B}^{(6)}$ denotes the basis of symmetric second order tensors specified in Appendix A.2.
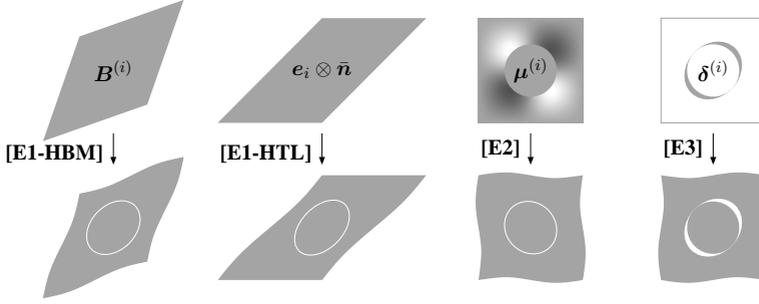
Figure 7.1: Illustration of the auxiliary elastic analyses described in Section 7.4.

Section 7.3.1. The stress localization operators can be defined analogously, or can be expressed by

$$\underline{\underline{S}}_{\bar{\varepsilon}}(\boldsymbol{x}) = \underline{\underline{C}}(\boldsymbol{x})\,\underline{\underline{E}}_{\bar{\varepsilon}}(\boldsymbol{x}) \qquad \text{or} \qquad \underline{\underline{S}}_{\bar{\delta}}(\boldsymbol{x}) = \underline{\underline{C}}(\boldsymbol{x})\,\underline{\underline{E}}_{\bar{\delta}}(\boldsymbol{x}), \qquad (7.34)$$

$$\underline{\underline{S}}_{\xi}(\boldsymbol{x}) = \underline{\underline{C}}(\boldsymbol{x})\left(\underline{\underline{E}}_{\xi}(\boldsymbol{x}) - \underline{\underline{P}}(\boldsymbol{x})\right), \qquad \underline{\underline{S}}_{\zeta}(\boldsymbol{x}) = \underline{\underline{C}}(\boldsymbol{x})\,\underline{\underline{E}}_{\zeta}(\boldsymbol{x}) \qquad (7.35)$$

via the stiffness tensor $\mathbb{C}$. The local strain and stress fields are obtained as

$$\underline{\varepsilon}(\boldsymbol{x}) = \underline{\underline{E}}_{\xi}(\boldsymbol{x})\,\underline{\xi} + \underline{\underline{E}}_{\zeta}(\boldsymbol{x})\,\underline{\zeta} + \begin{cases} \underline{\underline{E}}_{\bar{\varepsilon}}(\boldsymbol{x})\,\bar{\underline{\varepsilon}} & \text{for HBM;} \\ \frac{1}{L}\underline{\underline{E}}_{\bar{\delta}}(\boldsymbol{x})\,\underline{\bar{\delta}} & \text{for HTL,} \end{cases} \qquad (7.36)$$

$$\underline{\sigma}(\boldsymbol{x}) = \underline{\underline{S}}_{\xi}(\boldsymbol{x})\,\underline{\xi} + \underline{\underline{S}}_{\zeta}(\boldsymbol{x})\,\underline{\zeta} + \begin{cases} \underline{\underline{S}}_{\bar{\varepsilon}}(\boldsymbol{x})\,\bar{\underline{\varepsilon}} & \text{for HBM;} \\ \frac{1}{L}\underline{\underline{S}}_{\bar{\delta}}(\boldsymbol{x})\,\underline{\bar{\delta}} & \text{for HTL,} \end{cases} \qquad (7.37)$$

where $\underline{\bar{\delta}}$ denotes the vector representation of the effective displacement jump $\bar{\boldsymbol{\delta}}$ with respect to the orthonormal basis $\{\boldsymbol{e}_1, \boldsymbol{e}_2, \boldsymbol{e}_3\}$ assumed in **[E1-HTL]**. It is worth noting that the construction of the strain localization operators directly yields

$$\left\langle \underline{\underline{E}}_{\bar{\varepsilon}} \right\rangle_{\Omega} = \underline{\underline{I}} \in \mathbb{R}^{6\times 6} \quad \text{or} \quad \left\langle \underline{\underline{E}}_{\bar{\delta}} \right\rangle_{\Omega} = \underline{\underline{\bar{E}}}_{\bar{\delta}} \in \mathbb{R}^{6\times 3}, \quad \left\langle \underline{\underline{E}}_{\xi} \right\rangle_{\Omega} = \underline{\underline{0}} \in \mathbb{R}^{6\times N_{\xi}}, \quad (7.38)$$

where the specific form of $\underline{\underline{\bar{E}}}_{\bar{\delta}}$ depends on the orientation of the RVE with respect to the basis $\{\boldsymbol{e}_1, \boldsymbol{e}_2, \boldsymbol{e}_3\}$ and is exemplified by

$$\underline{\underline{\bar{E}}}_{\bar{\delta}} = \begin{bmatrix} 0 & 0 & 0 & 0 & \frac{\sqrt{2}}{2} & 0 \\ 0 & 0 & 0 & 0 & 0 & \frac{\sqrt{2}}{2} \\ 0 & 0 & 1 & 0 & 0 & 0 \end{bmatrix}^{\mathsf{T}} \qquad \text{for the special case}^{35}\ \bar{\boldsymbol{n}} = \boldsymbol{e}_3. \qquad (7.39)$$

---

[35]In the context of multiscale simulations, it is sufficient to consider this special case when introducing a corotational coordinate system at the thin layer treated as an imperfect interface.

The step **[E1-HBM]** in which six linear elastic boundary value problems are solved serves to determine the effective stiffness tensor $\bar{\mathbb{C}}$, whose matrix representation is

$$\underline{\underline{\bar{C}}} = \left\langle \underline{\underline{E_{\bar{\varepsilon}}}}^{\mathsf{T}} \, \underline{\underline{C}} \, \underline{\underline{E_{\bar{\varepsilon}}}} \right\rangle_{\Omega} = \left\langle \underline{\underline{S_{\bar{\varepsilon}}}}^{\mathsf{T}} \, \underline{\underline{C}}^{-1} \, \underline{\underline{S_{\bar{\varepsilon}}}} \right\rangle_{\Omega} = \left\langle \underline{\underline{S_{\bar{\varepsilon}}}} \right\rangle_{\Omega} \in \mathbb{R}^{6 \times 6}. \tag{7.40}$$

This course of action is sufficient to characterize the effective behavior of linear elastic heterogeneous (bulk) materials without imperfect interfaces and is therefore known as *linear elastic computational homogenization*. Similarly, by solving three linear elastic problems in **[E1-HTL]**, the effective normalized[36] interface stiffness

$$\underline{\underline{\bar{C}_{\bar{\delta}}}} = \left\langle \underline{\underline{E_{\bar{\delta}}}}^{\mathsf{T}} \, \underline{\underline{C}} \, \underline{\underline{E_{\bar{\delta}}}} \right\rangle_{\Omega} = \left\langle \underline{\underline{S_{\bar{\delta}}}}^{\mathsf{T}} \, \underline{\underline{C}}^{-1} \, \underline{\underline{S_{\bar{\delta}}}} \right\rangle_{\Omega} = \underline{\underline{\bar{E}_{\bar{\delta}}}}^{\mathsf{T}} \left\langle \underline{\underline{S_{\bar{\delta}}}} \right\rangle_{\Omega} \in \mathbb{R}^{3 \times 3} \tag{7.41}$$

is obtained for HTL. The step **[E2]** corresponds to N_{ξ} linear problems with different prescribed eigenstrains given by the plastic modes (at closed interfaces and vanishing global displacement gradient $\bar{\boldsymbol{H}}$). Finally, **[E3]** can be understood as collection of N_{ζ} linear problems with different rigid insertions at the imperfect interface, whose shapes are specified by the displacement jump modes, respectively. An illustration of the steps conducted in the auxiliary elastic analyses is depicted in Figure 7.1.

Overall, $6 + N_{\xi} + N_{\zeta}$ (for HBM) or $3 + N_{\xi} + N_{\zeta}$ (for HTL) linear elastic boundary value problems are solved during the auxiliary elastic analyses. This is done at the end of the offline phase, i.e., no adaptive reduced bases with modifications during the online stage are considered. When using a finite element solver, it suffices to assemble the stiffness matrix once in advance in order to solve **[E1–3]** because all linear problems of the auxiliary elastic analyses differ only by the right-hand side vectors. However, even without the numerical savings enabled thereby, the auxiliary elastic analyses make for a rather small part of the total numerical cost of a typical offline phase[37]. The final step of the auxiliary analyses is to compute the effective stiffness matrix according to (7.40) or (7.41) as well as additional system matrices, which are introduced in Section 7.7.1.

7.5   Incremental variational principles

The crucial difference between the NTFA [originating from the works of Michel et al., 2000, Michel & Suquet, 2003, 2004] and the hybrid pRBMOR scheme lies in the determination of effective evolution laws for the global internal variables. Michel & Suquet [2016b] refer to this issue as "reduced kinetics" and call it "a hard problem" since it embodies a major challenge in the development of reduced order homogenization methods. The key contribution of the hybrid scheme proposed

---

[36]A normalization with respect to the interface thickness L is used such that $\underline{\underline{\bar{C}_{\bar{\delta}}}}$ has the same physical dimension as $\underline{\underline{\bar{C}}}$. This normalized form of the effective stiffness matrix must be used together with a normalized effective displacement jump vector $\frac{1}{L}\bar{\boldsymbol{\delta}}$. E.g., for linear elastic overall behavior, the effective traction is obtained by $\bar{\boldsymbol{t}} = \frac{1}{L}\bar{\boldsymbol{C}}_{\bar{\delta}}\,\bar{\boldsymbol{\delta}}$.

[37]The special case of linear elastic materials without imperfect interfaces represents an exception for which the entire homogenization problem reduces to the step **[E1]**.

in Fritzen & Leuschner [2013] was to address the reduced kinetics problem with a global incremental variational principle in the fashion of the (local) formulation from Section 3.5. An extended variational principle accounting for multiple bulk hardening variables as well as for dissipative imperfect interfaces is presented in Section 7.5.1, loosely following Leuschner & Fritzen [2017].

7.5.1 Homogenization of bulk materials

The following explication presupposes a time-discrete setting and refers to one single time increment in which the rates of internal state variables are assumed to be constant, which is in line with the backward Euler scheme. Based on the local incremental stress potentials W and $\breve{W}$ defined in (3.56) and in (4.15), a global incremental stress potential is defined as

$$\bar{W}(\bar{\boldsymbol{\varepsilon}}) = \inf_{\tilde{\boldsymbol{u}}(\boldsymbol{x}) \in \mathcal{U}} \left(\langle W \rangle_{\Omega} + \left\langle \breve{W} \right\rangle_{\mathscr{I}} \right), \tag{7.42}$$

extending a formulation of Miehe [2002] to microstructures with imperfect interfaces. The effective stress at the end of the increment is thereby determined according to

$$\bar{\boldsymbol{\sigma}} = \partial_{\bar{\boldsymbol{\varepsilon}}} \bar{W}(\bar{\boldsymbol{\varepsilon}}). \tag{7.43}$$

With the local incremental work potentials Π and $\breve{\Pi}$ given in (3.55) and (4.16) and with the definitions of the local mixed incremental potentials Π^* and $\breve{\Pi}^*$ from (3.57) and (4.17), the global incremental stress potential is rewritten

$$\bar{W}(\bar{\boldsymbol{\varepsilon}}) = \inf_{\tilde{\boldsymbol{u}}(\boldsymbol{x}) \in \mathcal{U}} \inf_{\substack{\Delta \boldsymbol{\mathcal{I}}(\boldsymbol{x}) \in \mathcal{Y} \\ \Delta \breve{\boldsymbol{\mathcal{I}}}(\breve{\boldsymbol{x}}) \in \breve{\mathcal{Y}}}} \left(\langle \Pi \rangle_{\Omega} + \left\langle \breve{\Pi} \right\rangle_{\mathscr{I}} \right) \tag{7.44}$$

$$= \inf_{\tilde{\boldsymbol{u}}(\boldsymbol{x}) \in \mathcal{U}} \inf_{\substack{\Delta \boldsymbol{\mathcal{I}}(\boldsymbol{x}) \in \mathcal{Y} \\ \Delta \breve{\boldsymbol{\mathcal{I}}}(\breve{\boldsymbol{x}}) \in \breve{\mathcal{Y}}}} \sup_{\substack{\boldsymbol{\mathcal{F}}(\boldsymbol{x}) \in \mathcal{Z} \\ \breve{\boldsymbol{\mathcal{F}}}(\breve{\boldsymbol{x}}) \in \breve{\mathcal{Z}}}} \left(\langle \Pi^* \rangle_{\Omega} + \left\langle \breve{\Pi}^* \right\rangle_{\mathscr{I}} \right). \tag{7.45}$$

It is emphasized that these infima and suprema are not evaluated pointwise but with respect to fields, which is indicated by the spatial arguments $\boldsymbol{x}$ and $\breve{\boldsymbol{x}}$. Note that the above representations of $\bar{W}$ are exact, spatially continuous formulations.

First-level approximation based on a primal formulation. Bringing the reduced basis approach from Section 7.3.1 into play, the infima in (7.44) are evaluated over the subsets $\mathcal{U}_{\mathrm{RB}}$, $\mathcal{Y}_{\mathrm{RB}}$, and $\breve{\mathcal{Y}}_{\mathrm{RB}}$ which are covered by the reduced basis parameterization in terms of the global state $\underline{\bar{S}}$. This leads to the approximated incremental stress potential

$$\bar{\mathcal{W}}_{\mathrm{I}}(\bar{\boldsymbol{\varepsilon}}) = \inf_{\tilde{\boldsymbol{u}}(\boldsymbol{x}) \in \mathcal{U}_{\mathrm{RB}}} \inf_{\substack{\Delta \boldsymbol{\mathcal{I}}(\boldsymbol{x}) \in \mathcal{Y}_{\mathrm{RB}} \\ \Delta \breve{\boldsymbol{\mathcal{I}}}(\breve{\boldsymbol{x}}) \in \breve{\mathcal{Y}}_{\mathrm{RB}}}} \left(\langle \Pi \rangle_{\Omega} + \left\langle \breve{\Pi} \right\rangle_{\mathscr{I}} \right) = \inf_{\underline{\varsigma}} \inf_{\underline{\Delta \bar{\mathcal{I}}} \in \bar{\mathcal{Y}}} \bar{\Pi}(\underline{\bar{S}}) \geq \bar{W}(\bar{\boldsymbol{\varepsilon}}),$$

$$\tag{7.46}$$

which is expressed in terms of the incremental work potential

$$\bar{\Pi}(\underline{\bar{S}}) = \langle \Pi \rangle_\Omega + \left\langle \breve{\Pi} \right\rangle_\mathscr{I} = \Delta\bar{\psi}(\underline{\bar{S}}) + \Delta t \, \bar{\phi}_\mathrm{I}\left(\underline{\dot{\bar{\mathcal{I}}}}\right) \tag{7.47}$$

on the global scale. The global Helmholtz free energy density $\bar{\psi}$ and the global (primal) dissipation potential $\bar{\phi}_\mathrm{I}$ defined as

$$\bar{\psi}(\underline{\bar{S}}) = \langle \psi \rangle_\Omega + \left\langle \breve{\psi} \right\rangle_\mathscr{I}, \qquad\qquad \bar{\phi}_\mathrm{I}\left(\underline{\dot{\bar{\mathcal{I}}}}\right) = \langle \phi \rangle_\Omega + \left\langle \breve{\phi} \right\rangle_\mathscr{I} \tag{7.48}$$

describe a global GSM which incorporates a non-standard condition expressed by the infimum with respect to the displacement jump mode coefficients $\underline{\zeta}$ in (7.46). The global driving forces conjugate to the global internal state variables $\underline{\bar{\mathcal{I}}}$ are defined and decomposed according to

$$\underline{\bar{\mathcal{F}}} = -\frac{\partial\bar{\psi}}{\partial\underline{\bar{\mathcal{I}}}} = \left[\begin{array}{c} \underline{\tau} \\ \underline{R} \\ \underline{Z} \end{array} \right] \in \mathbb{R}^{N_\mathcal{I}} \qquad \text{with } \underline{R} = \left[\begin{array}{c} \underline{R}^{[1]} \\ \vdots \\ \underline{R}^{[N_\mathrm{q}]} \end{array} \right] \in \mathbb{R}^{N_\lambda}. \tag{7.49}$$

In (7.46), $\bar{\mathcal{Y}}$ denotes the set of all admissible increments of internal state variables, which is assumed to be $\mathbb{R}^{N_\mathcal{I}}$ throughout this work; other choices of $\bar{\mathcal{Y}}$ are possible in order to consider restrictions imposed on $\underline{\Delta\bar{\mathcal{I}}}$ when adopting an NMF-based approach (cf. Section 7.3.2).

If closed-form expressions of the local primal dissipation potentials ϕ and $\breve{\phi}$ are given, one can directly work with the approximated potential $\bar{\mathcal{W}}_\mathrm{I}$, which poses a minimization problem. This is desirable not only because the approximation $\bar{\mathcal{W}}_\mathrm{I}$ is known to be an upper estimation of the exact incremental potential $\bar{W}$ but also because of numerical simplicity. However, for many GSM and SDCZ models, such closed-form primal dissipation potentials are unknown. A formulation based on the local dual dissipation potentials ϕ^* and $\breve{\phi}^*$, as presented in the next paragraph, is then required.

Second-level approximation based on a mixed formulation. The representation of $\bar{W}$ based on mixed incremental potentials in (7.45) leads to the second-level approximation

$$\bar{\mathcal{W}}_\mathrm{II}(\bar{\boldsymbol{\varepsilon}}) = \inf_{\underline{\zeta}} \inf_{\underline{\Delta\bar{\mathcal{I}}}} \sup_{\substack{\boldsymbol{\mathcal{F}}(\boldsymbol{x})\in\mathcal{Z}_\mathrm{RB}|_{\bar{\boldsymbol{\varepsilon}},\underline{\zeta}} \\ \breve{\boldsymbol{\mathcal{F}}}(\breve{\boldsymbol{x}})\in\breve{\mathcal{Z}}_\mathrm{RB}|_{\underline{\zeta}}}} \left(\langle \Pi^* \rangle_\Omega + \left\langle \breve{\Pi}^* \right\rangle_\mathscr{I} \right) \tag{7.50}$$

$$= \inf_{\underline{\zeta}} \inf_{\underline{\Delta\bar{\mathcal{I}}}} \sup_{\underline{\bar{\mathcal{F}}}\in\bar{\mathcal{Z}}|_{\bar{\boldsymbol{\varepsilon}},\underline{\zeta}}} \bar{\Pi}^*(\underline{\bar{S}},\underline{\bar{\mathcal{F}}}) \leq \bar{\mathcal{W}}_\mathrm{I}(\bar{\boldsymbol{\varepsilon}}) \tag{7.51}$$

based on the global dual dissipation potential

$$\bar{\phi}_\mathrm{II}^*(\underline{\bar{\mathcal{F}}}) = \langle \phi^* \rangle_\Omega + \left\langle \breve{\phi}^* \right\rangle_\mathscr{I} \tag{7.52}$$

via the global mixed incremental potential

$$\bar{\Pi}^*\big(\underline{\bar{\mathcal{S}}}, \underline{\bar{\mathcal{F}}}\big) = \big\langle \Pi^* \big\rangle_\Omega + \big\langle \breve{\Pi}^* \big\rangle_{\mathscr{I}} = \Delta\bar{\psi}(\underline{\bar{\mathcal{S}}}) + \underline{\Delta\bar{\mathcal{I}}} \cdot \underline{\bar{\mathcal{F}}} - \Delta t\, \bar{\phi}_{\mathrm{II}}^*\big(\underline{\bar{\mathcal{F}}}\big). \tag{7.53}$$

The approximation $\bar{\mathcal{W}}_{\mathrm{II}}$ differs from $\bar{\mathcal{W}}_{\mathrm{I}}$ as a result of the supremum being evaluated not over $\mathcal{Z}$ and $\breve{\mathcal{Z}}$ but over the subsets

$$\mathcal{Z}_{\mathrm{RB}}\big|_{\bar{\varepsilon},\varsigma} \subset \mathcal{Z}_{\mathrm{RB}} \subset \mathcal{Z}, \qquad\qquad \breve{\mathcal{Z}}_{\mathrm{RB}}\big|_\varsigma \subset \breve{\mathcal{Z}}_{\mathrm{RB}} \subset \breve{\mathcal{Z}}. \tag{7.54}$$

Consequently, the global free energy density $\bar{\psi}$ from (7.48) and the global dual dissipation potential $\bar{\phi}_{\mathrm{II}}^*$ define an effective GSM slightly different[38] from the previous one defined via the primal potential $\bar{\phi}_{\mathrm{I}}$.

Analyzing the global free energy density $\bar{\psi}$ shows that the fields of local driving forces $\boldsymbol{\mathcal{F}}(\boldsymbol{x}) \in \mathcal{Z}_{\mathrm{RB}}\big|_{\bar{\varepsilon},\varsigma}$ and $\breve{\boldsymbol{\mathcal{F}}}(\breve{\boldsymbol{x}}) \in \breve{\mathcal{Z}}_{\mathrm{RB}}\big|_\varsigma$ determine the global driving forces $\underline{\bar{\mathcal{F}}}$ via

$$\underline{\bar{\mathcal{T}}} = \big\langle \underline{\underline{P}}^\mathsf{T} \underline{\sigma}_{\mathrm{P}} \big\rangle_\Omega, \quad \underline{R}_{[i]} = \big\langle \underline{\underline{Q}}^{[i]\mathsf{T}} \underline{r}_{[i]} \big\rangle_\Omega \quad (i = 1, \dots, N_{\mathrm{q}}), \quad \underline{Z} = \big\langle \underline{\underline{Y}}^\mathsf{T} \underline{z} \big\rangle_{\mathscr{I}}. \tag{7.55}$$

These relations define a surjective function

$$\mathfrak{F}\colon \mathcal{Z}_{\mathrm{RB}}\big|_{\bar{\varepsilon},\varsigma} \times \breve{\mathcal{Z}}_{\mathrm{RB}}\big|_\varsigma \to \bar{\mathcal{Z}}\big|_{\bar{\varepsilon},\varsigma} \qquad\qquad \text{with } \underline{\bar{\mathcal{Z}}}\big|_{\bar{\varepsilon},\varsigma} = -\partial_{\underline{\bar{\mathcal{I}}}}\bar{\psi}(\bar{\varepsilon}, \underline{\bar{\mathcal{Y}}}, \varsigma). \tag{7.56}$$

The surjectivity has been exploited for the transition from (7.50) to (7.51). It is important to note that the definitions (7.52) and (7.53) are only reasonable if any global vector $\underline{\bar{\mathcal{F}}} \in \bar{\mathcal{Z}}\big|_{\bar{\varepsilon},\varsigma}$ determines the associated fields of local driving forces $\boldsymbol{\mathcal{F}}(\boldsymbol{x}) \in \mathcal{Z}_{\mathrm{RB}}\big|_{\bar{\varepsilon},\varsigma}$ and $\breve{\boldsymbol{\mathcal{F}}}(\breve{\boldsymbol{x}}) \in \breve{\mathcal{Z}}_{\mathrm{RB}}\big|_\varsigma$ in a well-defined manner, i.e., the function $\mathfrak{F}$ must be also bijective. Its injectivity is proven as follows: by definition, $\mathcal{Z}_{\mathrm{RB}}$ and $\breve{\mathcal{Z}}_{\mathrm{RB}}$ are parameterized by the (primal) global state $\underline{\bar{\mathcal{S}}}$. Hence, with the global kinematic state variables $\bar{\varepsilon}$ and ς fixed, $\mathcal{Z}_{\mathrm{RB}}\big|_{\bar{\varepsilon},\varsigma}$ and $\breve{\mathcal{Z}}_{\mathrm{RB}}\big|_\varsigma$ are parameterized by the global internal state variables $\underline{\bar{\mathcal{I}}}$. Therefore it suffices to show that the mapping

$$\begin{aligned} \mathfrak{M}\colon\ &\underline{\bar{\mathcal{Y}}} \to \bar{\mathcal{Z}}\big|_{\bar{\varepsilon},\varsigma} \\ &\underline{\bar{\mathcal{I}}} \mapsto \underline{\bar{\mathcal{F}}} \end{aligned} \tag{7.57}$$

is invertible. The proof of the invertibility exploits the strong convexity of the local Helmholtz free energy densities ψ and $\breve{\psi}$ assumed in Section 7.2. It was previously conducted in Leuschner & Fritzen [2017] and is presented in Appendix B.3 for completeness.

In contrast to $\bar{\mathcal{W}}_{\mathrm{I}}$, the second-level approximation $\bar{\mathcal{W}}_{\mathrm{II}}$ does not provide an upper or lower estimation of the exact incremental stress potential $\bar{W}$, and it poses a saddle-point problem instead of a minimization problem. In the following, attention is restricted to the saddle-point formulation, and the shortened notation $\bar{\phi}^* = \bar{\phi}_{\mathrm{II}}^*$ is used.

---

[38]In fact, $\bar{\phi}_{\mathrm{II}}^*$ is only approximately equal to $\bar{\phi}_{\mathrm{I}}^*$, which is defined as the Legendre–Fenchel transform of $\bar{\phi}_{\mathrm{I}}$. Likewise, $\bar{\phi}_{\mathrm{I}}$ is only approximately equal to $\bar{\phi}_{\mathrm{II}}$, which is defined as the Legendre–Fenchel transform of $\bar{\phi}_{\mathrm{II}}^*$.

7.5.2 Homogenization of thin layers

A mixed primal–dual incremental formulation for HTL is obtained similarly as described for HBM in Section 7.5.1. Without declaring details regarding the derivation, the approximated incremental quasi-hyperelastic potential[39]

$$\mathscr{W}\big(\bar{\boldsymbol{\delta}}\big) = L \inf_{\underline{\varsigma}} \ \inf_{\Delta\bar{\mathcal{I}}\in\bar{\mathcal{Y}}} \ \sup_{\bar{\mathcal{F}}\in\bar{\mathcal{Z}}|_{\bar{\boldsymbol{\delta}},\underline{\varsigma}}} \ \bar{\Pi}^*\big(\underline{\bar{\mathcal{S}}},\bar{\mathcal{F}}\big) \tag{7.58}$$

is specified based on a mixed incremental potential $\bar{\Pi}^*$ defined as in (7.53). Thereby, the effective cohesive traction is determined via

$$\bar{\boldsymbol{t}} = \partial_{\bar{\boldsymbol{\delta}}}\mathscr{W}\big(\bar{\boldsymbol{\delta}}\big). \tag{7.59}$$

The homogenized behavior of the thin layer is captured by an effective SDCZ model described by the global Helmholtz free energy density $\breve{\bar{\psi}} = L\bar{\psi}$ and by the global dual dissipation potential $\breve{\bar{\phi}}^* = L\bar{\phi}^*$. Like the effective GSM in Section 7.5.1, the effective SDCZ has the internal state variables $\bar{\mathcal{I}}$, whose conjugate driving forces are $\breve{\bar{\mathcal{F}}} = L\bar{\mathcal{F}}$ now. The global kinematic state is represented by the effective displacement jump $\bar{\boldsymbol{\delta}}$ supplemented with the displacement jump modes coefficient vector $\underline{\varsigma}$.

7.6 Stationarity conditions

The reduced basis homogenization schemes for HBM and for HTL are based on the mixed incremental formulations (7.51) and (7.58), which pose two structurally equivalent saddle-point problems. For both types of homogenization, the stationarity conditions induced by the saddle-point problem are [cf. Leuschner & Fritzen, 2017]

$$0 \overset{!}{=} \delta_{\underline{\varsigma}}\bar{\Pi}^* = \frac{\partial\bar{\Pi}^*}{\partial\underline{\varsigma}} \cdot \delta\underline{\varsigma} = \frac{\partial\bar{\psi}}{\partial\underline{\varsigma}} \cdot \delta\underline{\varsigma} \qquad\qquad \text{for all } \delta\underline{\varsigma}, \tag{7.60}$$

$$0 \overset{!}{=} \delta_{\bar{\mathcal{I}}}\bar{\Pi}^* = \frac{\partial\bar{\Pi}^*}{\partial\bar{\mathcal{I}}} \cdot \delta\bar{\mathcal{I}} = \left(\frac{\partial\bar{\psi}}{\partial\bar{\mathcal{I}}} + \bar{\mathcal{F}}\right) \cdot \delta\bar{\mathcal{I}} \qquad\qquad \text{for all } \delta\bar{\mathcal{I}}, \tag{7.61}$$

$$0 \overset{!}{=} \delta_{\bar{\mathcal{F}}}\bar{\Pi}^* = \frac{\partial\bar{\Pi}^*}{\partial\bar{\mathcal{F}}} \cdot \delta\bar{\mathcal{F}} = \left(\Delta\bar{\mathcal{I}} - \Delta t\,\frac{\partial\bar{\phi}^*}{\partial\bar{\mathcal{F}}}\right) \cdot \delta\bar{\mathcal{F}} \qquad\qquad \text{for all } \delta\bar{\mathcal{F}}. \tag{7.62}$$

The arbitrariness of the variations $\delta\underline{\varsigma}$, $\delta\bar{\mathcal{I}}$, and $\delta\bar{\mathcal{F}}$ yields

$$\frac{\partial\bar{\psi}}{\partial\underline{\varsigma}} \overset{!}{=} 0, \qquad\qquad \frac{\partial\bar{\psi}}{\partial\bar{\mathcal{I}}} + \bar{\mathcal{F}} \overset{!}{=} 0, \qquad\qquad \Delta\bar{\mathcal{I}} - \Delta t\,\frac{\partial\bar{\phi}^*}{\partial\bar{\mathcal{F}}} \overset{!}{=} 0. \tag{7.63}$$

Here, the second and third equation represent constitutive conditions which are characteristic of GSMs and SDCZs. Meanwhile, the first equation in (7.63) is an additional, non-standard constraint which amounts to a weak form of Cauchy's fundamen-

---

[39]It is recalled from Section 5.4 that L denotes the thickness of the thin layer.

tal lemma (2.37) at the imperfect interface with the displacement jump modes acting as test functions, as was shown in Fritzen & Leuschner [2015] (see Appendix B.4 for details). The stationarity conditions from (7.63) provide the theoretical foundation for the implementation of the pRBMOR online algorithm, which is presented in Section 7.8. It is pointed out that the nonlinear problem to be solved online is an initial value problem defined at the global level. Due to the auxiliary elastic analyses, the local stress field is a priori divergence-free at all stages of the online algorithm, thus no partial differential equation (PDE) within the bulk is solved online.

7.7 Analysis of the global potentials

In order to prepare a sleek algorithmic description in Section 7.8, a rather technical analysis of the global potentials $\bar{\psi}$ and $\bar{\phi}^*$ is presented next. Wide parts of Section 7.7 are taken from Leuschner & Fritzen [2017] with minor modifications and extensions.

7.7.1 Gradients of the global Helmholtz free energy density

Second order gradients. Due to the constitutive assumption (7.2), some of the second order gradients of the global free energy density $\bar{\psi}$ defined in (7.48) are constant. E.g., the effective stiffnesses for HBM and for HTL

$$\underline{\underline{\bar{C}}} = \frac{\partial^2 \bar{\psi}}{\partial \bar{\xi}^2} = \left\langle \underline{\underline{S_{\bar{\varepsilon}}}} \right\rangle_\Omega, \qquad\qquad \underline{\underline{\bar{C}_{\bar{\delta}}}} = L^2 \frac{\partial^2 \bar{\psi}}{\partial \bar{\delta}^2} = \underline{\underline{\bar{E}_{\bar{\delta}}}}^{\mathsf{T}} \left\langle \underline{\underline{S_{\bar{\delta}}}} \right\rangle_\Omega \qquad (7.64)$$

have been already introduced in (7.40) and (7.41). The other two symmetric and constant system matrices are

$$\underline{\underline{D_\xi}} = -\frac{\partial^2 \bar{\psi}}{\partial \underline{\xi}^2} = -\left\langle \underline{\underline{P}}^{\mathsf{T}} \left(\underline{\underline{C}} + \underline{\underline{K_1}} \right) \underline{\underline{P}} \right\rangle_\Omega, \qquad \underline{\underline{D_\zeta}} = -\left\langle \underline{\underline{E_\zeta}}^{\mathsf{T}} \underline{\underline{C}} \, \underline{\underline{E_\zeta}} \right\rangle_\Omega. \qquad (7.65)$$

As far as non-symmetric but constant system matrices are concerned,

$$\underline{\underline{A_\xi^{\bar{\varepsilon}}}} = -\frac{\partial^2 \bar{\psi}}{\partial \underline{\xi} \, \partial \bar{\varepsilon}} = -\left\langle \underline{\underline{S_\xi}}^{\mathsf{T}} \right\rangle_\Omega = \left\langle \underline{\underline{P}}^{\mathsf{T}} \underline{\underline{S_{\bar{\varepsilon}}}} \right\rangle_\Omega, \qquad \underline{\underline{A_\zeta^{\bar{\varepsilon}}}} = -\frac{\partial^2 \bar{\psi}}{\partial \underline{\zeta} \, \partial \bar{\varepsilon}} = -\left\langle \underline{\underline{S_\zeta}}^{\mathsf{T}} \right\rangle_\Omega, \quad (7.66)$$

describe the coupling of $\bar{\varepsilon}$ to $\underline{\xi}$ and to $\underline{\zeta}$ for HBM, while

$$\underline{\underline{A_\xi^{\bar{\delta}}}} = -L \frac{\partial^2 \bar{\psi}}{\partial \underline{\xi} \, \partial \bar{\delta}} = -\left\langle \underline{\underline{S_\xi}}^{\mathsf{T}} \right\rangle_\Omega \underline{\underline{\bar{E}_{\bar{\delta}}}} = \left\langle \underline{\underline{P}}^{\mathsf{T}} \underline{\underline{S_{\bar{\delta}}}} \right\rangle_\Omega, \qquad (7.67)$$

$$\underline{\underline{A_\zeta^{\bar{\delta}}}} = -L \frac{\partial^2 \bar{\psi}}{\partial \underline{\zeta} \, \partial \bar{\delta}} = -\left\langle \underline{\underline{S_\zeta}}^{\mathsf{T}} \right\rangle_\Omega \underline{\underline{\bar{E}_{\bar{\delta}}}} \qquad (7.68)$$

describe the coupling of $\underline{\bar{\delta}}$ to $\underline{\xi}$ and to $\underline{\zeta}$ for HTL. For both types of homogenization, the coupling between plasticity in the bulk and displacement jump fields at the imperfect interface is described by

$$\underline{\underline{A_\zeta^\xi}} = -\frac{\partial^2 \bar{\psi}}{\partial\underline{\zeta}\,\partial\underline{\xi}} = -\left\langle \underline{\underline{E_\zeta}}^{\mathsf{T}} \underline{\underline{S_\xi}} \right\rangle_\Omega = \left\langle \underline{\underline{S_\zeta}}^{\mathsf{T}} \underline{\underline{P}} \right\rangle_\Omega. \tag{7.69}$$

The constant system matrices are computed at the end of the offline phase, i.e., as the last step of the auxiliary elastic analyses. The remaining non-vanishing contributions to the second order gradient of $\bar{\psi}$ are non-constant. They are denoted

$$\underline{\underline{\mathcal{D}}} = -\left\langle \underline{\underline{\Delta}}^{\mathsf{T}} \frac{\partial^2 \breve{\psi}}{\partial\underline{\delta}^2} \underline{\underline{\Delta}} \right\rangle_{\mathscr{I}}, \qquad\qquad \underline{\underline{\mathcal{E}}} = -\frac{\partial^2 \bar{\psi}}{\partial\underline{\zeta}\,\partial\underline{\nu}} = -\left\langle \underline{\underline{\Delta}}^{\mathsf{T}} \frac{\partial^2 \breve{\psi}}{\partial\underline{\delta}\,\partial\underline{y}} \underline{\underline{Y}} \right\rangle_{\mathscr{I}}, \tag{7.70}$$

$$\underline{\underline{\mathcal{G}}} = -\frac{\partial^2 \bar{\psi}}{\partial\underline{\nu}^2} = -\left\langle \underline{\underline{Y}}^{\mathsf{T}} \frac{\partial^2 \breve{\psi}}{\partial\underline{y}^2} \underline{\underline{Y}} \right\rangle_{\mathscr{I}}, \qquad \underline{\underline{\mathcal{H}}} = -\frac{\partial^2 \bar{\psi}}{\partial\underline{\lambda}^2}, \tag{7.71}$$

where $\underline{\underline{\mathcal{H}}}$ is a block diagonal matrix with the main diagonal blocks

$$\underline{\underline{\mathcal{H}}}^{[i]} = -\frac{\partial^2 \bar{\psi}}{\partial\left(\underline{\lambda}^{[i]}\right)^2} = -\left\langle \left(\underline{\underline{Q}}^{[i]}\right)^{\mathsf{T}} \frac{\partial^2 \psi_{[i]}}{\partial q_{[i]}^2} \underline{\underline{Q}}^{[i]} \right\rangle_\Omega \qquad (i = 1, \dots, N_{\mathrm{q}}). \tag{7.72}$$

The second order gradient of $\bar{\psi}$ with respect to $\underline{\bar{\mathcal{I}}}$ plays an important role in the pRBMOR scheme, hence the additional abbreviation

$$\underline{\underline{\mathcal{M}}} = -\frac{\partial^2 \bar{\psi}}{\partial\underline{\bar{\mathcal{I}}}^2} = \begin{bmatrix} \underline{\underline{D_\xi}} & \underline{\underline{0}} & \underline{\underline{0}} \\ & \underline{\underline{\mathcal{H}}} & \underline{\underline{0}} \\ \text{sym.} & & \underline{\underline{\mathcal{G}}} \end{bmatrix} \tag{7.73}$$

is introduced. Because of the strong convexity of the local free energy densities assumed in Section 7.2, $\underline{\underline{\mathcal{M}}}$ is negative definite (see Appendix B.3 for the proof). For completeness it is mentioned that the second order gradient of $\bar{\psi}$ with respect to $\underline{\zeta}$ is composed of a constant and a non-constant part according to

$$-\frac{\partial^2 \bar{\psi}}{\partial\underline{\zeta}^2} = \underline{\underline{D_\zeta}} + \underline{\underline{\mathcal{D}}} \tag{7.74}$$

with $\underline{\underline{D_\zeta}}$ reflecting a coupling of the displacement jump field and the bulk and $\underline{\underline{\mathcal{D}}}$ stemming from the SDCZ model alone.

First order gradients.   The first order gradients of $\bar{\psi}$ are summarized as

$$\frac{\partial\bar{\psi}}{\partial\underline{\bar{S}}} = \begin{bmatrix} \underline{s} \\ -\underline{m} \\ \underline{f_\zeta} \end{bmatrix} \qquad \text{with } \underline{s} = \begin{cases} \underline{\bar{\sigma}} & \text{for HBM;} \\ \underline{\bar{t}}/L & \text{for HTL.} \end{cases} \tag{7.75}$$

Here, the residual corresponding to the first stationarity condition in (7.63) is given by

$$
\underline{f_\zeta} = \left\langle \underline{\underline{\Delta}}^\mathsf{T} \frac{\partial \breve{\psi}}{\partial \underline{\breve{\delta}}} \right\rangle_{\mathscr{I}} - \underline{\underline{A_\zeta^\xi}} \, \underline{\xi} - \underline{\underline{D_\zeta}} \, \underline{\zeta} - \begin{cases} \underline{\underline{A_\zeta^{\bar{\bar{\varepsilon}}}}} \, \underline{\bar{\bar{\varepsilon}}} & \text{for HBM;} \\ \frac{1}{L} \underline{\underline{A_\zeta^{\bar{\delta}}}} \, \underline{\bar{\delta}} & \text{for HTL.} \end{cases} \tag{7.76}
$$

The vector $\underline{m}$ is defined by and assembled according to

$$
\underline{m} = -\frac{\partial \bar{\psi}}{\partial \underline{\bar{\mathcal{I}}}} = \begin{bmatrix} \underline{m_\xi} \\ \underline{m_\lambda} \\ \underline{m_\nu} \end{bmatrix} \in \mathbb{R}^{N_\mathcal{I}} \qquad \text{with } \underline{m_\lambda} = \begin{bmatrix} \underline{m_\lambda^{[1]}} \\ \vdots \\ \underline{m_\lambda^{[N_q]}} \end{bmatrix} \in \mathbb{R}^{N_\lambda} \tag{7.77}
$$

from the components

$$
\underline{m_\xi} = \underline{\underline{D_\xi}} \, \underline{\xi} + \left(\underline{\underline{A_\zeta^\xi}} \right)^\mathsf{T} \underline{\zeta} + \begin{cases} \underline{\underline{A_\xi^{\bar{\bar{\varepsilon}}}}} \, \underline{\bar{\bar{\varepsilon}}} & \text{for HBM;} \\ \frac{1}{L} \underline{\underline{A_\xi^{\bar{\delta}}}} \, \underline{\bar{\delta}} & \text{for HTL,} \end{cases} \tag{7.78}
$$

$$
\underline{m_\nu} = -\left\langle \underline{\underline{Y}}^\mathsf{T} \frac{\partial \breve{\psi}}{\partial \underline{y}} \right\rangle_{\mathscr{I}}, \qquad \underline{m_\lambda^{[i]}} = -\left\langle \left(\underline{\underline{Q^{[i]}}} \right)^\mathsf{T} \frac{\partial \psi_{[i]}}{\partial \underline{q_{[i]}}} \right\rangle_\Omega \qquad (i = 1, \dots, N_q). \tag{7.79}
$$

Note that $\underline{m}$ coincides with $\underline{\bar{\mathcal{F}}}$ at the stationary point.

7.7.2 Gradients of the global dual dissipation potential

By virtue of straightforward calculations [cf. Fritzen & Leuschner, 2013, Fritzen et al., 2014], the first order gradient of the global dual dissipation potential has the representation

$$
\frac{\partial \bar{\phi}^*}{\partial \underline{\bar{\mathcal{F}}}} = \underline{\underline{\mathcal{M}}}^{-1} \underline{l} \qquad \text{with } \underline{l} = \begin{bmatrix} \underline{l_\xi} \\ \underline{l_\lambda} \\ \underline{l_\nu} \end{bmatrix}, \quad \underline{l_\lambda} = \begin{bmatrix} \underline{l_\lambda^{[1]}} \\ \vdots \\ \underline{l_\lambda^{[N_q]}} \end{bmatrix}, \tag{7.80}
$$

and

$$
\underline{l_\lambda^{[i]}} = -\left\langle \left(\underline{\underline{Q^{[i]}}} \right)^\mathsf{T} \frac{\partial^2 \psi_{[i]}}{\partial \underline{q_{[i]}}^2} \frac{\partial \phi^*}{\partial \underline{r_{[i]}}} \right\rangle_\Omega \qquad (i = 1, \dots, N_q), \tag{7.81}
$$

$$
\underline{l_\xi} = \left\langle \underline{\underline{T_\xi}}^\mathsf{T} \frac{\partial \phi^*}{\partial \underline{\sigma_\mathrm{P}}} \right\rangle_\Omega, \qquad \underline{l_\nu} = -\left\langle \underline{\underline{Y}}^\mathsf{T} \frac{\partial^2 \breve{\psi}}{\partial \underline{y}^2} \frac{\partial \breve{\phi}^*}{\partial \underline{z}} \right\rangle_{\mathscr{I}}. \tag{7.82}
$$

The localization operator

$$
\underline{\underline{T_\xi}}(\boldsymbol{x}) = \underline{\underline{S_\xi}}(\boldsymbol{x}) - \underline{\underline{K_1}}(\boldsymbol{x}) \underline{\underline{P}}(\boldsymbol{x}) \tag{7.83}
$$

has been employed here, which allows to write

$$\underline{\sigma}_{\mathrm{p}}(\boldsymbol{x}) = \underline{\underline{T}}_{\xi}(\boldsymbol{x})\underline{\xi} + \underline{\underline{S}}_{\zeta}(\boldsymbol{x})\underline{\zeta} + \begin{cases} \underline{\underline{S}}_{\bar{\varepsilon}}(\boldsymbol{x})\underline{\bar{\varepsilon}} & \text{for HBM;} \\ \frac{1}{L}\underline{\underline{S}}_{\bar{\delta}}(\boldsymbol{x})\underline{\bar{\delta}} & \text{for HTL.} \end{cases} \tag{7.84}$$

Furthermore, the second order gradient has the form

$$\frac{\partial^2 \bar{\phi}^*}{\partial \underline{\bar{\mathcal{F}}}^2} = \underline{\underline{\mathcal{M}}}^{-1}\underline{\underline{\mathcal{L}}}\,\underline{\underline{\mathcal{M}}}^{-1} \qquad \text{with } \underline{\underline{\mathcal{L}}} = \begin{bmatrix} \underline{\underline{\mathcal{L}}}_{\xi\xi} & \underline{\underline{\mathcal{L}}}_{\xi\lambda}^{[1]} & \cdots & \underline{\underline{\mathcal{L}}}_{\xi\lambda}^{[N_{\mathrm{q}}]} & \underline{\underline{0}} \\ & \underline{\underline{\mathcal{L}}}_{\lambda\lambda}^{[1,1]} & \cdots & \underline{\underline{\mathcal{L}}}_{\lambda\lambda}^{[1,N_{\mathrm{q}}]} & \underline{\underline{0}} \\ & & \ddots & \vdots & \vdots \\ & \text{sym.} & & \underline{\underline{\mathcal{L}}}_{\lambda\lambda}^{[N_{\mathrm{q}},N_{\mathrm{q}}]} & \underline{\underline{0}} \\ & & & & \underline{\underline{\mathcal{L}}}_{\nu\nu} \end{bmatrix}, \tag{7.85}$$

where the abbreviations

$$\underline{\underline{\mathcal{L}}}_{\xi\xi} = \left\langle \underline{\underline{T}}_{\xi}^{\mathsf{T}} \frac{\partial^2 \phi^*}{\partial \underline{\sigma}_{\mathrm{p}}^2} \underline{\underline{T}}_{\xi} \right\rangle_{\Omega}, \quad \underline{\underline{\mathcal{L}}}_{\lambda\lambda}^{[i,j]} = \left\langle \left(\underline{\underline{Q}}^{[i]}\right)^{\mathsf{T}} \frac{\partial^2 \psi_{[i]}}{\partial \underline{q}_{[i]}^2} \frac{\partial^2 \phi^*}{\partial \underline{r}_{[i]} \partial \underline{r}_{[j]}} \frac{\partial^2 \psi_{[j]}}{\partial \underline{q}_{[j]}^2} \underline{\underline{Q}}^{[j]} \right\rangle_{\Omega}, \tag{7.86}$$

$$\underline{\underline{\mathcal{L}}}_{\xi\lambda}^{[i]} = -\left\langle \underline{\underline{T}}_{\xi}^{\mathsf{T}} \frac{\partial^2 \phi^*}{\partial \underline{\sigma}_{\mathrm{p}} \partial \underline{r}_{[i]}} \frac{\partial^2 \psi_{[i]}}{\partial \underline{q}_{[i]}^2} \underline{\underline{Q}}^{[i]} \right\rangle_{\Omega}, \qquad \underline{\underline{\mathcal{L}}}_{\nu\nu} = \left\langle \underline{\underline{Y}}^{\mathsf{T}} \frac{\partial^2 \breve{\psi}}{\partial \underline{y}^2} \frac{\partial^2 \breve{\phi}^*}{\partial \underline{z}^2} \frac{\partial^2 \breve{\psi}}{\partial \underline{y}^2} \underline{\underline{Y}} \right\rangle_{\mathscr{I}} \tag{7.87}$$

have been used $(i, j = 1, \ldots, N_{\mathrm{q}})$. Due to the convexity of the underlying local potentials ϕ^* and $\breve{\phi}^*$, $\underline{\underline{\mathcal{L}}}$ is positive semi-definite.

7.8 Algorithmic treatment

The nonlinear problem posed by the stationarity conditions (7.63) is solved with a monolithic Newton–Raphson scheme. The residual function and the associated Jacobian are described in terms of the abbreviations introduced in Section 7.7 according to

$$\underline{f}\big(\Delta\underline{\bar{\mathcal{I}}}, \underline{\bar{\mathcal{F}}}, \underline{\zeta}\big) = \begin{bmatrix} \underline{f}_{\mathcal{I}} \\ \underline{f}_{\mathcal{F}} \\ \underline{f}_{\zeta} \end{bmatrix} \qquad \text{with} \quad \underline{f}_{\mathcal{I}} = \underline{\bar{\mathcal{F}}} - \underline{m}, \quad \underline{f}_{\mathcal{F}} = \Delta\underline{\bar{\mathcal{I}}} - \Delta t\,\underline{\underline{\mathcal{M}}}^{-1}\underline{l}, \tag{7.88}$$

$$\underline{\underline{J}}\big(\Delta\underline{\bar{\mathcal{I}}}, \underline{\bar{\mathcal{F}}}, \underline{\zeta}\big) = \begin{bmatrix} -\underline{\underline{\mathcal{M}}} & & \text{sym.} \\ \hline \underline{\underline{I}} & -\Delta t\,\underline{\underline{\mathcal{M}}}^{-1}\underline{\underline{\mathcal{L}}}\,\underline{\underline{\mathcal{M}}}^{-1} & \\ \hline \begin{bmatrix} -\underline{\underline{A}}_{\zeta}^{\xi} & \underline{\underline{0}} & -\underline{\underline{\mathcal{E}}} \end{bmatrix} & \underline{\underline{0}} & -\underline{\underline{D}}_{\zeta} - \underline{\underline{\mathcal{D}}} \end{bmatrix}. \tag{7.89}$$

When the iterative scheme has converged, the effective stress

$$\underline{\bar{\sigma}} = \underline{\underline{\bar{C}}}\,\underline{\bar{\varepsilon}} - \left(\underline{\underline{A_\xi^{\bar{\varepsilon}}}}\right)^{\mathsf{T}}\underline{\xi} - \left(\underline{\underline{A_\zeta^{\bar{\varepsilon}}}}\right)^{\mathsf{T}}\underline{\zeta} \tag{7.90}$$

is computed for HBM, or the effective traction

$$\underline{\bar{t}} = \underline{\underline{\bar{E}_{\bar{\delta}}}}^{\mathsf{T}}\underline{\bar{\sigma}} = \frac{1}{L}\underline{\underline{\bar{C}_{\bar{\delta}}}}\,\underline{\bar{\delta}} - \left(\underline{\underline{A_\xi^{\bar{\delta}}}}\right)^{\mathsf{T}}\underline{\xi} - \left(\underline{\underline{A_\zeta^{\bar{\delta}}}}\right)^{\mathsf{T}}\underline{\zeta} \tag{7.91}$$

is calculated for HTL. If needed, the algorithmic stiffness can be obtained following a similar strategy as for ordinary GSMs (cf. Section 3.6). For an effective GSM, it is given by

$$\underline{\underline{\bar{C}^{\mathrm{a}}}} = \frac{\mathrm{d}\underline{\bar{\sigma}}}{\mathrm{d}\underline{\bar{\varepsilon}}} = \underline{\underline{\bar{C}}} - \left(\underline{\underline{A_\xi^{\bar{\varepsilon}}}}\right)^{\mathsf{T}}\frac{\partial\underline{\xi}}{\partial\underline{\bar{\varepsilon}}} - \left(\underline{\underline{A_\zeta^{\bar{\varepsilon}}}}\right)^{\mathsf{T}}\frac{\partial\underline{\zeta}}{\partial\underline{\bar{\varepsilon}}}, \tag{7.92}$$

where $\partial\underline{\xi}/\partial\underline{\bar{\varepsilon}}$ and $\partial\underline{\zeta}/\partial\underline{\bar{\varepsilon}}$ are determined via the linearization of the residual vector

$$0 \stackrel{!}{=} \frac{\mathrm{d}\underline{f}}{\mathrm{d}\underline{\bar{\varepsilon}}} = \frac{\partial\underline{f}}{\partial\underline{\bar{\varepsilon}}} + \underline{\underline{J}}\,\frac{\partial}{\partial\underline{\bar{\varepsilon}}}\begin{bmatrix}\underline{\underline{\bar{\mathcal{I}}}}\\\underline{\underline{\bar{\mathcal{F}}}}\\\underline{\zeta}\end{bmatrix} \qquad \text{with } \frac{\partial\underline{f}}{\partial\underline{\bar{\varepsilon}}} = \begin{bmatrix}-\underline{\underline{A_\xi^{\bar{\varepsilon}}}}\\\underline{\underline{0}}\\-\underline{\underline{A_\zeta^{\bar{\varepsilon}}}}\end{bmatrix}. \tag{7.93}$$

Similarly, the (normalized) algorithmic stiffness of an effective SDCZ is obtained as

$$\underline{\underline{\bar{C}_{\bar{\delta}}^{\mathrm{a}}}} = L\frac{\mathrm{d}\underline{\bar{t}}}{\mathrm{d}\underline{\bar{\delta}}} = \underline{\underline{\bar{C}_{\bar{\delta}}}} - L\left(\underline{\underline{A_\xi^{\bar{\delta}}}}\right)^{\mathsf{T}}\frac{\partial\underline{\xi}}{\partial\underline{\bar{\delta}}} - L\left(\underline{\underline{A_\zeta^{\bar{\delta}}}}\right)^{\mathsf{T}}\frac{\partial\underline{\zeta}}{\partial\underline{\bar{\delta}}} \tag{7.94}$$

with $\partial\underline{\xi}/\partial\underline{\bar{\delta}}$ and $\partial\underline{\zeta}/\partial\underline{\bar{\delta}}$ computed via

$$0 \stackrel{!}{=} \frac{\mathrm{d}\underline{f}}{\mathrm{d}\underline{\bar{\delta}}} = \frac{\partial\underline{f}}{\partial\underline{\bar{\delta}}} + \underline{\underline{J}}\,\frac{\partial}{\partial\underline{\bar{\delta}}}\begin{bmatrix}\underline{\underline{\bar{\mathcal{I}}}}\\\underline{\underline{\bar{\mathcal{F}}}}\\\underline{\zeta}\end{bmatrix} \qquad \text{with } \frac{\partial\underline{f}}{\partial\underline{\bar{\delta}}} = \frac{1}{L}\begin{bmatrix}-\underline{\underline{A_\xi^{\bar{\delta}}}}\\\underline{\underline{0}}\\-\underline{\underline{A_\zeta^{\bar{\delta}}}}\end{bmatrix}. \tag{7.95}$$

Utilizing (7.93) or (7.95), the algorithmic stiffness can be computed by solving systems of linear equations with the matrix of coefficients given by the Jacobian $\underline{\underline{J}}$ evaluated at the stationarity point. In practice, the Jacobian from the last Newton–Raphson iteration is used such that the additional numerical effort to compute the algorithmic stiffness is negligible compared to that of the preceding steps of the pRBMOR online algorithm. Algorithm 7.1 summarizes the steps conducted during a simple Newton–Raphson procedure (possibly involving quasi-Newton iterations in order to reduce computational cost), which was found to be quite robust even when applied to complex material models. Nevertheless, numerical tweaks such as sub-stepping or line search are advisable and may further improve robustness or convergence. Note that the local strain and plastic strain fields[40] are not computed during the online scheme but could

---

[40]Also, only $\boldsymbol{\sigma}_{\mathrm{p}}$ is computed online via (7.84) but not the Cauchy stress $\boldsymbol{\sigma}$. However, both quantities coincide in the absence of LKH.

Algorithm 7.1: pRBMOR online algorithm (one time increment).

---

1 initialize global state variables $\bar{\mathcal{I}}$, $\bar{\mathcal{F}}$, and $\underline{\zeta}$

2 **while** *Newton–Raphson scheme has not converged* **do**

3   compute local fields $\boldsymbol{q}_{[1]}(\boldsymbol{x}), \ldots, \boldsymbol{q}_{[N_{\mathrm{q}}]}(\boldsymbol{x})$, $\boldsymbol{\sigma}_{\mathrm{P}}(\boldsymbol{x})$, $\boldsymbol{y}(\check{\boldsymbol{x}})$, $\boldsymbol{\delta}(\check{\boldsymbol{x}})$

4   evaluate gradients of local Helmholtz free energy densities ψ and $\check{\psi}$

5   evaluate gradients of local dual dissipation potentials ϕ^* and $\check{\phi}^*$

6   compute vectors $\underline{l}$ and $\underline{m}$ and matrices $\underline{\mathcal{G}}$ and $\underline{\mathcal{H}}$

7   assemble residual $\underline{f}$ and quit loop if scheme has converged

8   **if** *the current iteration is not a quasi-Newton iteration* **then**

9   compute matrices $\underline{\mathcal{D}}$, $\underline{\mathcal{E}}$, and $\underline{\mathcal{L}}$

10   assemble Jacobian $\underline{\underline{J}}$

11   **end**

12   solve global system of linear equations

13   update global state variables $\bar{\mathcal{I}}$, $\bar{\mathcal{F}}$, and $\underline{\zeta}$

14 **end**

15 compute effective stress $\bar{\boldsymbol{\sigma}}$ or effective traction $\bar{\boldsymbol{t}}$

16 compute algorithmic stiffness $\bar{\mathbb{C}}^{\mathrm{a}}$ or $\bar{\boldsymbol{C}}^{\mathrm{a}}_{\bar{\delta}}$ if required

---

be evaluated in a post-processing step. It is pointed out that the online pRBMOR scheme does *not* involve local iterative schemes to compute the constitutive behavior at the microscopic evaluation points in the bulk or at the interface. This is in contrast to most full-field methods, although there are exceptions like the augmented FE approach proposed by Rempler et al. [2011]. For completeness, an overview of the pRBMOR offline procedure is given in Figure 7.2.
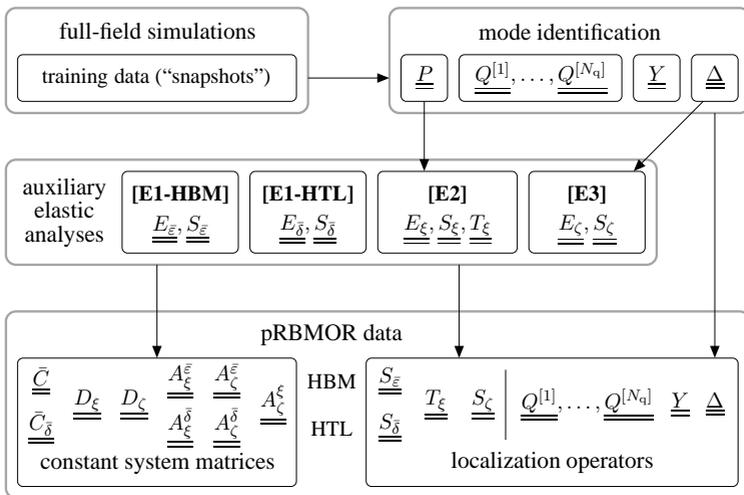
Figure 7.2: Overview of the pRBMOR offline stage. The "pRBMOR data" frame comprises all pre-computable system matrices and localization operators that are required for the online algorithm.
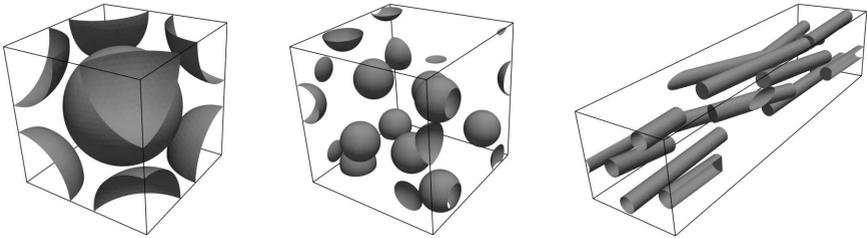
Figure 7.3: Microstructures considered in Section 7.9.1: artificial unit cell with a high volume fraction (53.6%) of spherical inclusions *(left)*, quasi-isotropic RVE with 10% spherical inclusions (middle), and RVE with 10% short fiber reinforcement *(right)*.

7.9   Numerical examples

7.9.1   Unilateral contact at the phase boundaries of elastic composites

All examples presented in Section 7.9.1 are taken from Fritzen & Leuschner [2015] and are concerned with composite bulk materials whose phases are isotropic linear elastic. Three different RVEs with the volume $1\,\text{mm}^3$ are considered, which are depicted in Figure 7.3. The Young's moduli of the matrix materials and of the inclusions are 75 GPa and 400 GPa and the Poisson's ratios are 0.3 and 0.2, respectively. At the phase boundaries, unilateral contact without friction is assumed, which is modeled via the regularized penalty formulation (4.19) with the characteristic length $\delta^{\text{c}} = 0.2\,\mu\text{m}$ and with the normalized penalty stiffness $c_{\text{p}} = 20\,\text{GPa}$. The overall behavior of such materials can be described as almost[41] bilinear elastic with tension–compression asymmetry, as illustrated by the example in Figure 7.4. More precisely, the effective stress response depends nonlinearly on the direction of the applied effective strain $\bar{\varepsilon}$ in general (corresponding to anisotropy) but is (almost) linearly dependent on the amplitude $\|\bar{\varepsilon}\|_2$.

Since no constitutive internal state variables are involved, the saddle-point problem (7.51) reduces to a minimization problem which provides upper-bound estimates of the exact solutions. The class of rather simple materials is investigated for two reasons: firstly, because the absence of path-dependency allows to systematically assess the capabilities of the (isolated) reduced basis approach for displacement jump fields according to (7.12), and secondly, because such homogenization problems can be straightforwardly handled with kernel-based interpolation schemes. A comparison between pRBMOR and interpolation with Gaussian kernels is presented. The kernel method is briefly described in Appendix B.5, and the reader is referred to Wirtz

---

[41]The overall response is only *almost* bilinear due to the regularization of the penalized contact formulation.
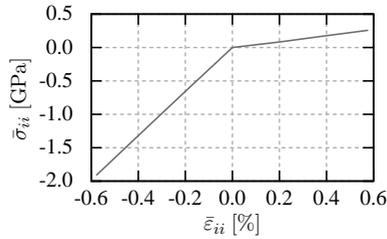
Figure 7.4: Effective stress–strain response of the artificial microstructure depicted on the left-hand side of Figure 7.3 under hydrostatic load (full-field FEM result, $i = 1, \ldots, 3$).

et al. [2015] for further information on reduced order multiscale modeling with kernel methods.

Training and validation strategy. When dealing with reduced basis methods, appropriate approaches for the training and for the validation are of utmost importance. The relevance of properly selected training data is highlighted by the fact that the accuracy of ROM schemes is in general governed by the suitability of the reduced bases for the problems of interest and by the circumstance that the reduced bases are obtained from the training data via fixed, deterministic identification procedures (cf. Section 7.3.2). The accuracy of pRBMOR results (compared to full-field reference solutions) actually depends on the quality of the reduced bases only. Unfortunately, the construction of reduced bases that are optimal in a strict sense is generally not viable in practice. Heuristic approaches based on greedy algorithms are widely used to systematically address this issue [e.g., Veroy et al., 2003, Haasdonk, 2013]. Greedy procedures make use of error indicators; since the development of error indicators for pRBMOR is an open issue, another training strategy is used here, which is presented below.

Let N_t denote the number of training directions. Due to simple geometric considerations, not taking into account given information about the microstructure, a uniform distribution of N_t points on the unit sphere in $\mathbb{R}^6$ is intended as a representation of the training directions. Except for special cases (such as $N_t = 16$, for instance), exact uniform patterns do not exist. However, approximations can be easily computed, e.g., by electron repulsion simulations, and this method has been used for the examples presented in Sections 7.9.1 and 7.9.2. Note that one point on the unit sphere can be fixed during the simulation without biasing the pattern of the distributed points. For instance, hydrostatic tension has been prescribed for all HBM examples in this work.

Once the training directions have been determined, N_v appropriate validation directions are searched after. Validation load cases are necessary in order to demonstrate the predictive capabilities of pRBMOR, which must justify the numerical effort of the offline phase. Reproduction of training cases is of course not enough to highlight the usefulness

of a reduced order model. Based on geometrical considerations, it is argued that the validation directions should be "as far away as possible" from the training directions (e.g., in terms of angles between the directions). Validation directions which approximately satisfy this requirement can be found by additional electron repulsion simulations where the training directions are kept fixed while one new point with a random initialization is allowed to move. The procedure is repeated until N_v directions have been found. At the end of each repetition the current point is rejected if the minimum distance to the previous validation directions is below a certain threshold. The number of validation directions N_v attainable with this procedure is clearly limited and the limit depends on N_t.

Accuracy of the effective stress predictions. To begin with, the artificial microstructure with a high volume fraction of spherical inclusions depicted on the left-hand side of Figure 7.3 is considered. Four sets of training data with 24, 32, 64, and 128 training directions, respectively, are taken into account. The accuracy of the pRBMOR results is specified in terms of the relative stress error

$$\hat{\mathcal{E}} = \frac{\|\bar{\boldsymbol{\sigma}}_\mathrm{ROM} - \bar{\boldsymbol{\sigma}}_\mathrm{FF}\|_2}{\|\bar{\boldsymbol{\sigma}}_\mathrm{FF}\|_2} \tag{7.96}$$

with respect to FEM reference solutions, where $\bar{\boldsymbol{\sigma}}_\mathrm{ROM}$ and $\bar{\boldsymbol{\sigma}}_\mathrm{FF}$ denote the effective stresses obtained with pRBMOR and with a full-field FEM solver, respectively. The error is evaluated at the end of proportional loadings with 1% amplitude (in terms of the norm of the effective strain). Statistical information on the relative errors for the training and for the validation directions at varying numbers of modes is shown in Figure 7.5. Aside from minor exceptions, the following observations are made regarding the accuracy of the pRBMOR results:

- The relative errors decrease monotonically as the number of modes N_ζ increases for all sets of training and validation directions.

- For validation directions, the relative errors at fixed mode numbers decreases when the number N_t of directions considered in the training is increased.

- With identical numbers of training directions and displacement jump modes, the training cases are approximated better than the validation directions.

- The relative errors for training directions are almost decreased to zero for $N_\zeta \geq N_\mathrm{t}$.

Out of these findings, the first three correspond to expected behavior which is typical of reduced basis methods in general. In contrast, the fourth observation is expected to be less pronounced when more complex types of nonlinearities are involved. Note that the finding that N_t training directions can be recovered with the same number of modes does not imply that each training direction contributes only one relevant displacement jump mode, since the accuracy for validation directions is further improved when N_ζ is increased to values greater than N_t.
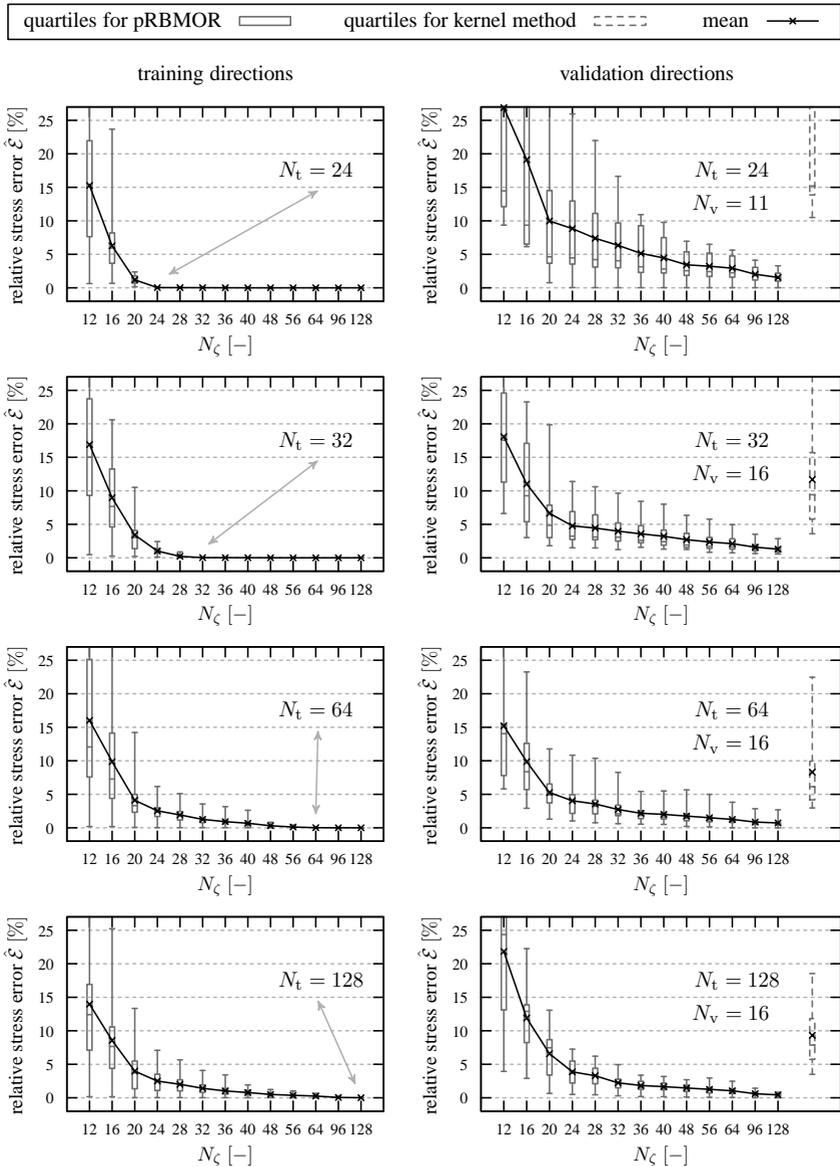
Figure 7.5: Relative errors of the effective stresses with respect to full-field FEM reference solutions for the unit cell depicted on the left-hand side of Figure 7.3 at varying numbers N_ζ of displacement jump modes and at different numbers N_t of training directions.
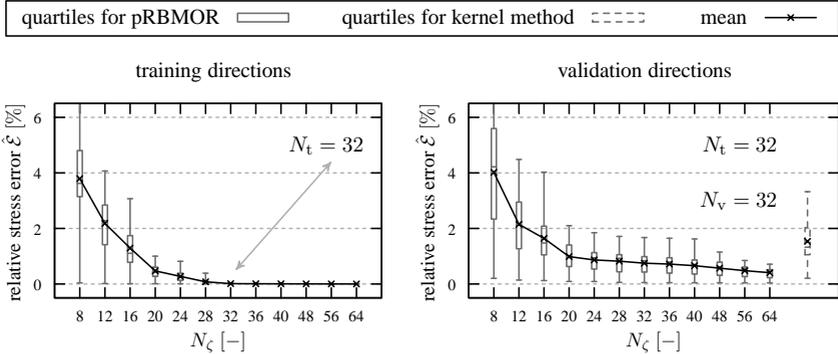
Figure 7.6: Relative errors of the effective stresses with respect to full-field FEM reference solutions for the quasi-isotropic RVE with spherical inclusions (depicted in the middle of Figure 7.3) at varying numbers N_ζ of displacement jump modes.
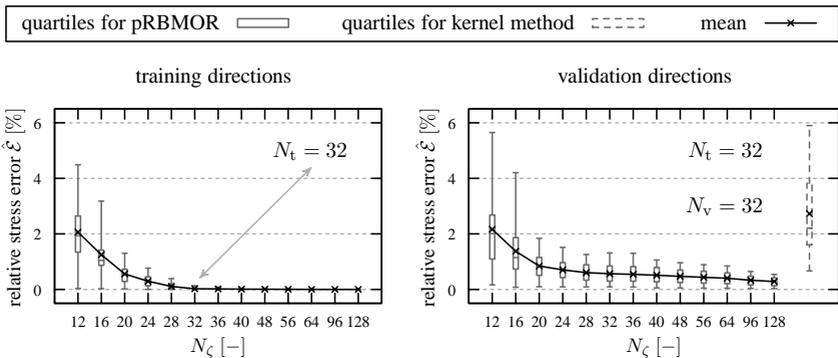
Figure 7.7: Relative errors of the effective stresses with respect to full-field FEM reference solutions for the short fiber RVE (shown on the right-hand side of Figure 7.3) at varying numbers N_ζ of displacement jump modes.

For the comparison between pRBMOR and interpolation based on Gaussian kernels according to Appendix B.5, the relative errors of the interpolated effective stresses are defined analogously to $\hat{\mathcal{E}}$. Since kernel interpolation recovers training data exactly, results of the kernel method are only depicted for validation loadings in Figure 7.5. In principle, the accuracy of the interpolation scheme is improved when the number of training directions is increased. However, the minimum and the mean of the relative errors are not reduced by using 128 instead of 64 training directions, and the relative error does not come below a level of approximately 3% for any validation case. For all sets of training data, pRBMOR with a sufficient number of modes easily outperforms the kernel-based interpolation scheme accuracy-wise.

In order to investigate the influence of different microstructures, the two RVEs with 10% inclusions depicted in the middle and on the right-hand side of Figure 7.3 are considered next. For both microstructures, training data were computed with the set of 32 training directions utilized before[42]. Figures 7.6 and 7.7 show statistical information about the relative stress errors for the quasi-isotropic RVE and for the anisotropic fiber-reinforced material. The findings are in line with the previous ones for the artificial unit cell, but the general magnitude of the errors is lower due to the smaller interface-area-to-volume ratios. Interestingly, pRBMOR performs better for the anisotropic RVE than for the quasi-isotropic RVE, while the opposite is observed for the kernel-based method. It is emphasized that both methods have been trained with the same sets of training data, but additional full-field training solutions have been used to calibrate the free parameter of the radial basis function kernel (cf. Appendix B.5), i.e., the interpolation scheme benefits from additional empirical information. Still, for both RVEs, the accuracy obtained with pRBMOR is better than that of the kernel method if enough modes are used. Thus, the numerical results showcase the advantage of the energy-based reduced basis approach over the purely empirical kernel interpolation scheme, which does not incorporate any given information about the physics at the microscale. However, it should not go unmentioned that the evaluation of the kernel interpolation is much faster than the pRBMOR online algorithm.

7.9.2 Unidirectional fibrous composite with viscoelastic interface

Following the work of Gosz et al. [1991], a fiber-reinforced composite with a viscoelastic interface is investigated. A unidirectional, hexagonal arrangement of graphite fibers inside an epoxy resin matrix is considered. The microstructure is represented by a unit cell with the discretization depicted in Figure 7.8. As in Gosz et al. [1991], the elastic parameters of the transversely isotropic fibers identified by Kriz & Stinchcomb [1979] are assumed, which are summarized in Table 7.2. In Leuschner & Fritzen [2017], the pRBMOR scheme has been applied to this kind of homogenization problem with the epoxy resin model with Voce-type isotropic hardening from Section 3.7.1. In the following, the epoxy resin model with LKH and NLKH from Section 3.7.2 is incorporated instead in order to allow for physically meaningful descriptions of loading–unloading behavior. This (visco-) plastic GSM has the hardening variables $\boldsymbol{\alpha} = \boldsymbol{\alpha}^{(1)}$ and q, which can be equipped either with joint modes or with separate modes according to Sections 7.2 and 7.3.1; both cases are formally distinguished via

[Q1] $\boldsymbol{q}_{[1]} = (\boldsymbol{\alpha}, q)$ $(N_{\mathrm{q}} = 1)$,

[Q2] $\boldsymbol{q}_{[1]} = \boldsymbol{\alpha}$, $\boldsymbol{q}_{[2]} = q$ $(N_{\mathrm{q}} = 2)$.

---

[42]The training directions and the corresponding validation directions are specified in Table C.4 and in Table C.5 in Appendix C.2, respectively.

E_l	E_t	G_l	G_t	ν_{lt}
232 GPa	15 GPa	24 GPa	5.03 GPa	0.279

Table 7.2: Elastic parameters of transversely isotropic graphite fibers according to Kriz & Stinchcomb [1979]. The meaning of the parameters is specified in Appendix A.3.2.


$$l_1 = \sqrt{\pi\sqrt{3}}d$$
$$l_2 = \frac{\sqrt{3}}{3}l_1$$
$$l_3 = \frac{1}{10}l_1$$
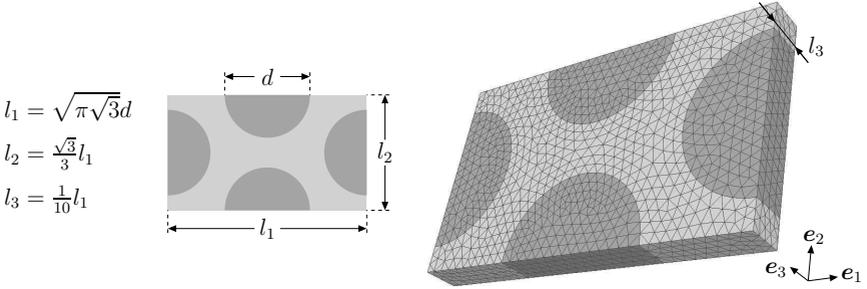
Figure 7.8: Unit cell representing a unidirectional, hexagonal arrangement of fibers with 50% volume fraction [previously used in Leuschner & Fritzen, 2017]. The finite element discretization contains 8116 second order tetrahedra, 664 interface elements, and 16,425 nodes (including duplicated nodes at the interface).

While the second representation is more reasonable from the theoretical perspective, it is left to clarify if it is also advantageous in practice. The viscoelastic interface is modeled as an SLI defined by (4.20) and (4.21) with isotropic interface stiffness tensors

$$\boldsymbol{K} = k\,\boldsymbol{I}, \qquad\qquad \boldsymbol{K}_v = k_v\,\boldsymbol{I}. \qquad\qquad (7.97)$$

As in Leuschner & Fritzen [2017], the following fixed relations between the viscosity η and the stiffnesses k, k_v, and k_p are assumed:

$$k_v = 9\,k, \qquad\qquad k_p = 1000\,k, \qquad\qquad \eta = k_v\,(1\,\text{s})\,. \qquad (7.98)$$

Under these assumptions, the behavior of the SLI can be characterized by one free parameter such as the normalized interface stiffness

$$c = \frac{d}{2G_m}\,(k + k_v) = 5\frac{dk_v}{G_m}, \qquad\qquad (7.99)$$

where G_m denotes the shear modulus of the matrix material and d is the fiber diameter. Note that a change of the normalized stiffness c can be understood as an alteration of the interfacial properties at a constant fiber diameter or, alternatively, as a scaling of the geometric dimensions at fixed constitutive properties. Thus, the size effect induced by the imperfect interface can be studied by simply changing the normalized stiffness c, as illustrated in Figure 7.9.
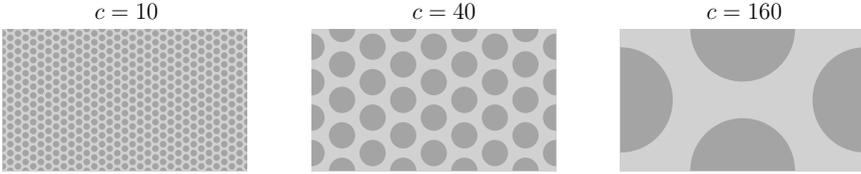
Figure 7.9: For fixed interfacial constitutive properties, an alteration of the normalized interface stiffness c defined in (7.99) corresponds to scaling of the microstructure.
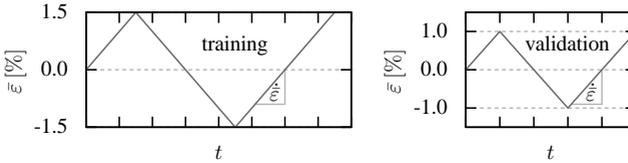

Figure 7.10: Cyclic loading for training and for validation.

Training and validation strategy. In the following, attention is directed at cyclic loadings characterized by

$$\bar{\boldsymbol{\varepsilon}}(t) = \bar{\varepsilon}(t)\,\boldsymbol{D}, \qquad\qquad |\dot{\bar{\varepsilon}}| = \text{const.}, \qquad\qquad \|\boldsymbol{D}\|_2 = 1 \qquad (7.100)$$

and by $\bar{\varepsilon}(t)$ varying as shown in Figure 7.10. It has been observed for several examples that the accuracy at the end of a loading can be improved considerably by using higher amplitudes in the training than intended later on. Hence, for validation load amplitudes of 1%, the training data were computed with 1.5% load amplitude. The same 32 training directions previously used for the example in Section 7.9.1 (cf. Table C.4) are utilized. By consideration of the associated 32 validation directions (cf. Table C.5), the predictivity with respect to untrained load paths is investigated, which corresponds to the principal concern of ROMs for nonlinear homogenization. In addition, for the present example, the predictive capabilities of the ROM with respect to both the load rate $\dot{\bar{\varepsilon}}$ and the normalized stiffness c are also of great interest in view of the size effect and the pronounced rate-dependence induced by the viscoelastic interface. Thus, the values

$$c = \begin{cases} 10 \\ 40 \\ 160 \end{cases} \qquad \text{and} \qquad |\dot{\bar{\varepsilon}}| = \begin{cases} 10^{-5}\ \text{s}^{-1} \\ 10^{-3}\ \text{s}^{-1} \\ 10^{-1}\ \text{s}^{-1} \end{cases} \qquad (7.101)$$

are considered in different combinations. Two training setups are considered, for which two separate sets of modes are identified:

[T1] All 32 training full-field solutions are computed with $c = 40$ and $\left|\dot{\bar{\varepsilon}}\right| = 10^{-3}\ \text{s}^{-1}$.

[T2] The training simulations are assembled from four blocks:
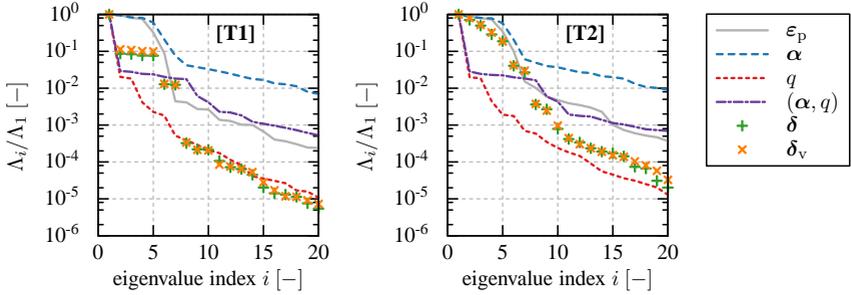
Figure 7.11: Eigenvalue decays for the modes obtained from the training data sets **[T1]** and **[T2]**.

[T2a] directions 1–8 are computed with $c = 160$ and $\left|\dot{\bar{\varepsilon}}\right| = 10^{-5}\ \mathrm{s}^{-1}$;

[T2b] directions 9–16 are computed with $c = 10$ and $\left|\dot{\bar{\varepsilon}}\right| = 10^{-1}\ \mathrm{s}^{-1}$;

[T2c] directions 17–24 are computed with $c = 10$ and $\left|\dot{\bar{\varepsilon}}\right| = 10^{-5}\ \mathrm{s}^{-1}$;

[T2d] directions 25–32 are computed with $c = 160$ and $\left|\dot{\bar{\varepsilon}}\right| = 10^{-1}\ \mathrm{s}^{-1}$.

With the modes obtained therefrom, the following two-step validation scheme is conducted:

[V1] For $c = 40$ and $\left|\dot{\bar{\varepsilon}}\right| = 10^{-3}\ \mathrm{s}^{-1}$, the ROM results are compared to full-field FEM reference solutions at all 32 validation directions.

[V2] The three validation directions for which the most inaccurate approximations are identified in **[V1]** are used to study the accuracy at $c = 10$ and at $c = 160$. For either of the two normalized stiffnesses, the three load rates specified in (7.101) are considered.

It is emphasized that both training procedures are equivalent with regard to numerical effort up to differing numbers of iterations due to different convergence properties. Clearly, the reduced bases from **[T1]** are expected to yield better approximations in **[V1]**. On the other hand, **[T2]** is taken into account with the intention to enable better performance in **[V2]** although there is no compelling reason for that to be expected. The eigenvalue decays for the reduced bases, which comprise information on the compressibility of the training data sets, are depicted in Figure 7.11.
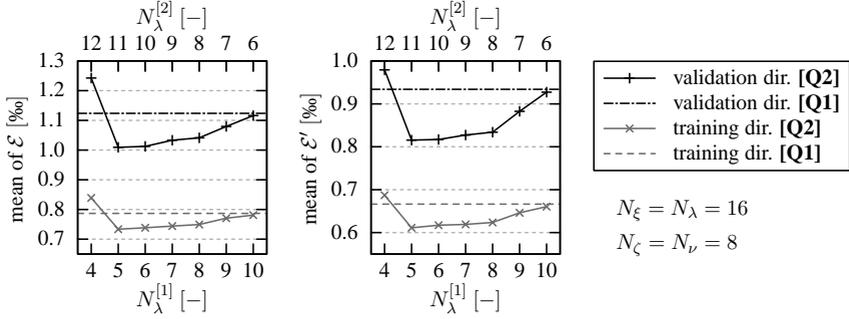
Figure 7.12: Comparison of the pRBMOR accuracy for different but equal sized systems of hardening modes. For 32 training directions and for 32 validation directions with $c = 40$ and $\left|\dot{\bar{\varepsilon}}\right| = 10^{-3}\ \mathrm{s}^{-1}$, the means of the errors $\mathcal{E}$ and $\mathcal{E}'$ were computed using reduced bases gained from the training data set **[T1]**.

Accuracy of the effective stress predictions.   The two error measures used to assess the accuracy of the ROM results are

$$
\mathcal{E} = \frac{\sqrt{\dfrac{1}{N}\sum_{n=1}^{N}\left\|\bar{\boldsymbol{\sigma}}_{\mathrm{ROM}}(t_n) - \bar{\boldsymbol{\sigma}}_{\mathrm{FF}}(t_n)\right\|_2^2}}{\max_{1\leq n\leq N}\left\|\bar{\boldsymbol{\sigma}}_{\mathrm{FF}}(t_n)\right\|_2}, \quad
\mathcal{E}' = \frac{\sqrt{\dfrac{1}{N}\sum_{n=1}^{N}\left\|\bar{\boldsymbol{\sigma}}'_{\mathrm{ROM}}(t_n) - \bar{\boldsymbol{\sigma}}'_{\mathrm{FF}}(t_n)\right\|_2^2}}{\max_{1\leq n\leq N}\left\|\bar{\boldsymbol{\sigma}}_{\mathrm{FF}}(t_n)\right\|_2},
$$

$$(7.102)$$

where $t_1, \ldots, t_N$ denote the (adaptive) time steps of the full-field FEM simulation which have been also prescribed for the ROM calculations. In a first step, the best configuration of hardening modes is searched-for. Attention is restricted to mode systems with

$$
N_\xi = N_\lambda = 16, \qquad\qquad N_\zeta = N_\nu = 8, \qquad\qquad (7.103)
$$

which is assumed to be a reasonable choice in view of Figure 7.11. In the case **[Q1]**, this means that 16 joint hardening modes are considered, while different splittings into kinematic and isotropic hardening modes are possible for **[Q2]** without altering the overall number of reduced degrees of freedom. Using the modes obtained from **[T1]**, the validation step **[V1]** has been performed with different mode configurations. In addition, the 32 training solutions of **[T1]** have been recalculated with pRBMOR, and the means of the errors $\mathcal{E}$ and $\mathcal{E}'$ over the 32 directions are comprised in Figure 7.12. Three observation are made: firstly, both error measures provide quantitatively different but qualitatively similar results. Secondly, if a favorable split between kinematic and isotropic hardening modes is chosen, the **[Q2]** approach provides better (mean) accuracy than **[Q1]**; this result is expected since the kinematic hardening variable $\boldsymbol{\alpha}$ and the isotropic hardening variable q evolve differently during cyclic loadings. Thirdly, although the training cases are recovered with much better accuracy than the validation cases (as expected), a qualitatively similar dependence of the accuracies on the mode setup is observed for
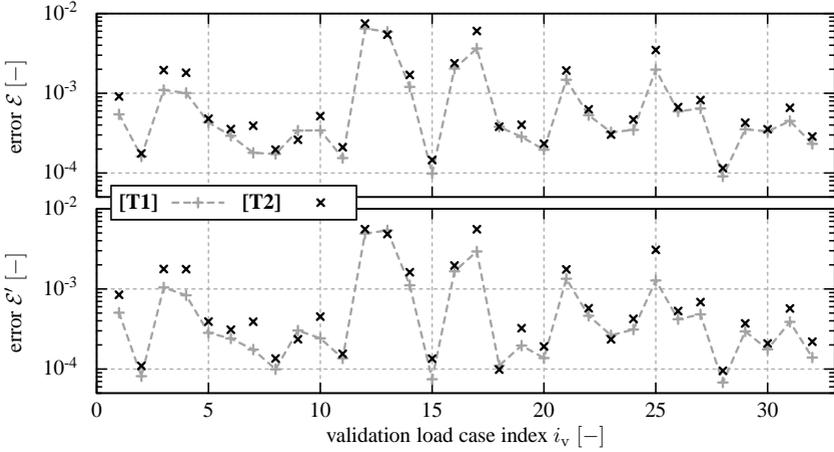
Figure 7.13: Overview of the errors $\mathcal{E}$ and $\mathcal{E}'$ obtained in the validation step **[V1]**.

training cases and for validation cases. This last finding is due to the fact that the training and validation loadings are of the same kind and needs to be confirmed for other examples. Such a correlation has practical relevance since it allows to determine the best setup of hardening modes without the need for additional (validation) full-field simulations.

The results presented in the following are computed with the hardening mode configuration which is optimal according to Figure 7.12, i.e., with $N_\lambda^{[1]} = 5$ and $N_\lambda^{[2]} = 11$. With these mode numbers, the validation step **[V1]** has been also conducted with the modes derived from **[T2]**, and the resultant errors $\mathcal{E}$ and $\mathcal{E}'$ are given for all 32 validation directions in Figure 7.13. Again, both error measures yield qualitatively similar results. As expected, the training strategy **[T1]** gives slightly better results than **[T2]** all in all. The validation directions $i_\mathrm{v} = 12$, $i_\mathrm{v} = 13$, and $i_\mathrm{v} = 17$ are clearly identified as those with the highest aberrations from the full-field reference and are selected for the second validation step **[V2]**. The effective stress response for these worst case directions is shown in Figure 7.14. Some small deviations from the reference solutions are found, e.g., for the normal stresses of validation direction 12 (especially in the compressive regime), for the dominant shear stresses of the directions 12 and 17, and for the three shear stress components of validation direction 13. Overall, the accuracy of the pRBMOR predictions is quite satisfactory with the reduced bases from **[T1]** as well as with those from **[T2]**. Figures 7.15 and 7.16 show selected components of the effective stresses obtained for the worst case directions in the second validation step **[V2]**. These results highlight the considerable rate-dependence of the effective behavior and its dependence on the normalized interface stiffness c (or, equivalently, its size-dependence). A decrease of the normalized stiffness c and a decrease of the load rate $|\dot{\bar{\varepsilon}}|$ both lead to a softer overall response of the microstructure. The combination of both effects $\left(c = 10 \text{ and } |\dot{\bar{\varepsilon}}| = 10^{-5} \text{ s}^{-1}\right)$ is too
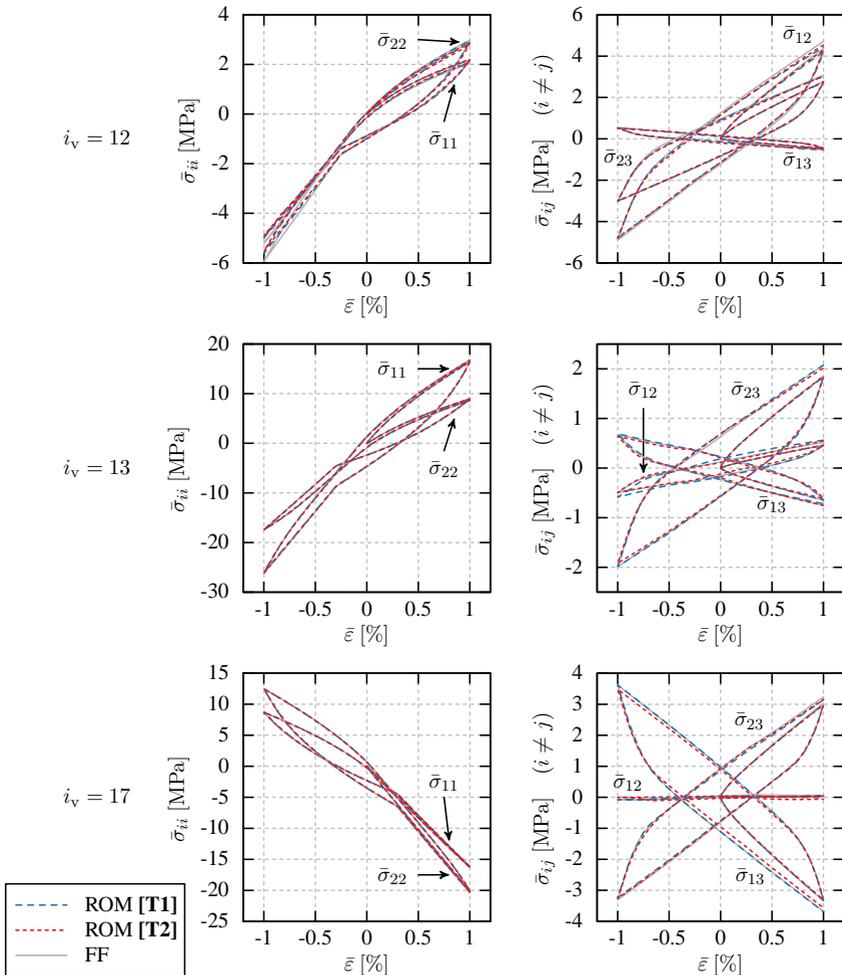
Figure 7.14: Effective stresses for the worst case validation directions at $c = 40$ and $\left|\bar{\dot{\varepsilon}}\right| = 10^{-3}\,\mathrm{s}^{-1}$. The normal stress component $\bar{\sigma}_{33}$ corresponding to the fiber direction is virtually linear (not shown).

strong to be captured by the modes obtained from **[T1]** such that the Newton–Raphson procedure does not converge. In contrast, despite the fact that only one quarter of the training data **[T2]** has been computed at the respective normalized interface stiffnesses and load rate, the reduced bases derived from **[T2]** make for convergence at all considered validation cases. The accuracy of all effective stress predictions within the validation step **[V2]** is specified in terms of the errors $\mathcal{E}$ and $\mathcal{E}'$ in Figure 7.17.
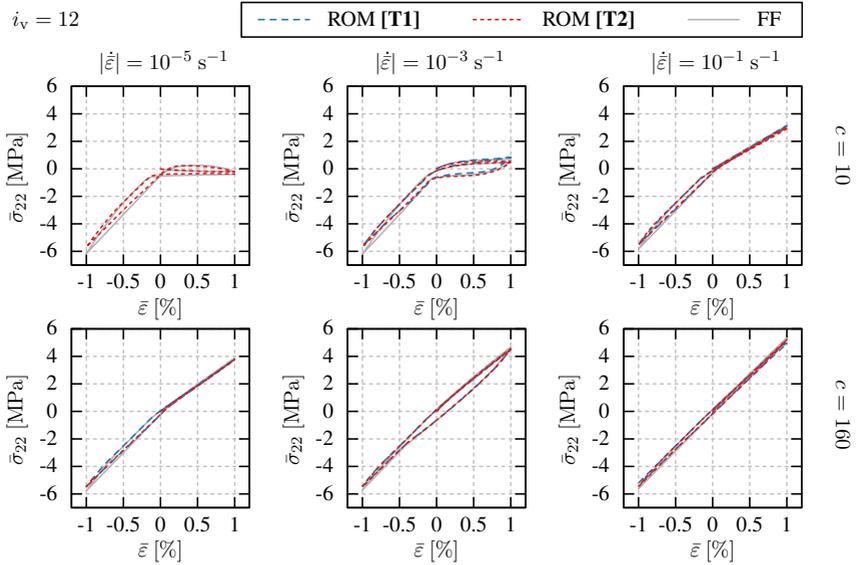
Figure 7.15: Full-field solutions and ROM predictions of the effective normal stress $\bar{\sigma}_{22}$ for validation direction 12 at varying load rate and varying normalized interface stiffness.
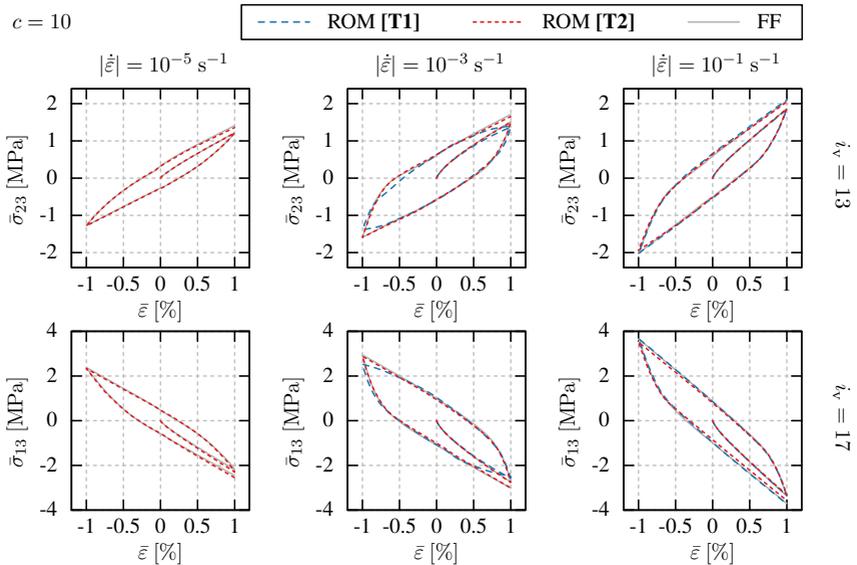

Figure 7.16: Full-field solutions and ROM predictions of the dominant effective shear stress components of the validation directions 13 and 17 at $c = 10$ and at varying load rate.
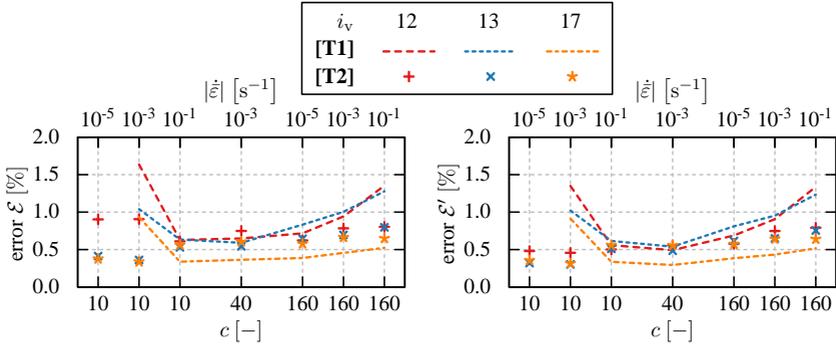
Figure 7.17: Errors $\mathcal{E}$ and $\mathcal{E}'$ for the validation step **[V2]**.

Predictions of local fields.   One advantage of the reduced basis approach over many other homogenization schemes is its ability to predict not only the effective constitutive behavior but also all involved microscopic fields. For instance, statistical information on the interface opening has been looked at in Fritzen & Leuschner [2015], and the partition of the mechanical energy into elastic and inelastic parts in the bulk and at the interface has been examined in Leuschner & Fritzen [2017]. ROM predictions of local fields can be exploited for various kinds of analyses in the context of developing high performance materials or designing structures made from them. Here, without going into details regarding the predictive capabilities of pRBMOR at the microscopic level, an impression is given in terms of the fields of the von Mises equivalent stress. Figures 7.18 and 7.19 show the ROM results based on the **[T1]** and **[T2]** trainings along with finite element references for the validation load cases $i_{\mathrm{v}} = 12$ and $i_{\mathrm{v}} = 13$. For the (intermediate) load rate $\left| \dot{\bar{\varepsilon}} \right| = 10^{-3}\,\mathrm{s}^{-1}$, a variation of the normalized interface stiffness c is considered in order to illustrate the interface-induced size effect. Despite significant differences between the two considered validation loadings, it is found that the main characteristics of the von Mises stress fields are captured quite well in each case. However, at $c = 10$, the FE reference is underestimated by pRBMOR, especially with the modes obtained from **[T1]**. This finding is in agreement with Figure 7.17, where the errors for the corresponding validation scenario are considerably higher for **[T1]** than for **[T2]**. Further, the peak values near the phase boundaries at $c = 160$ are slightly underestimated for both load directions and with both sets of training data. In spite of quantitative deviations from the FE references, it is concluded that pRBMOR is able to qualitatively predict local effects even for cases which differ significantly from those considered in the training.

In view of the results in Section 7.9.1, an improvement not only of the global but also of the local predictions is anticipated when using more comprehensive sets of training data. This strategy has been previously investigated in Leuschner & Fritzen [2017], where it was found that, in addition, the numbers of modes must be increased in order to improve the accuracy of the local predictions. In practice, rather low numbers of modes may suffice for the effective stress prediction, but more global degrees of freedom may be
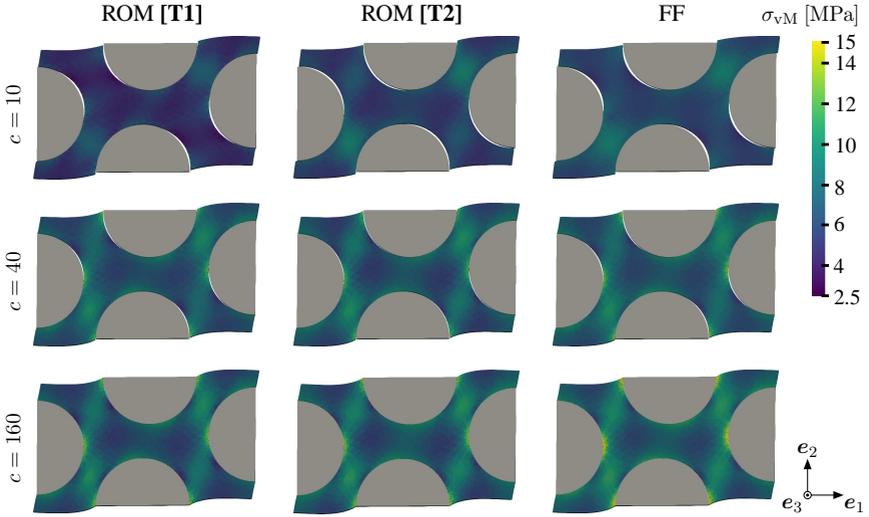
Figure 7.18: Von Mises equivalent stress fields in the viscoplastic matrix at the end of validation load case 12: comparison between pRBMOR results and FE reference solutions for different normalized interface stiffnesses c at $\left|\dot{\bar{\varepsilon}}\right| = 10^{-3}\,\mathrm{s}^{-1}$. Deformations are displayed with scale factor 10.
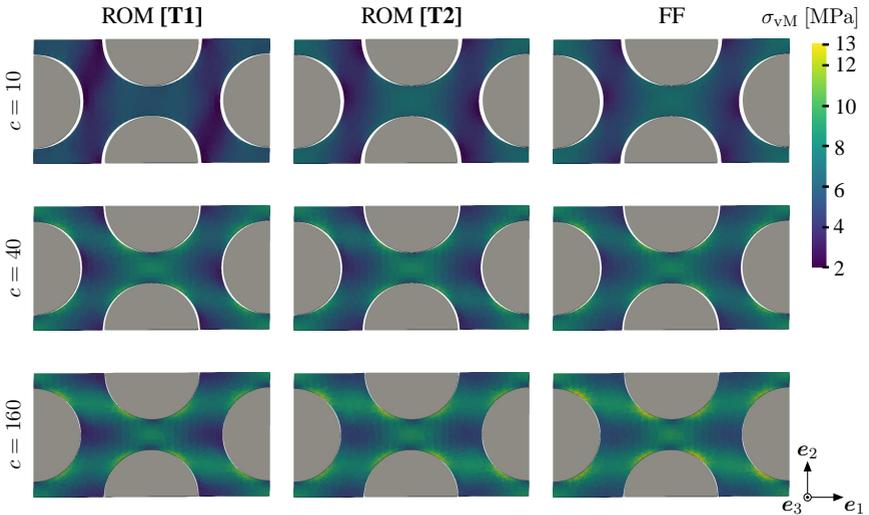
Figure 7.19: Von Mises equivalent stress fields in the viscoplastic matrix at the end of validation load case $i_{\mathrm{v}} = 13$: comparison between pRBMOR results and FE reference solutions for different normalized stiffnesses c at $\left|\dot{\bar{\varepsilon}}\right| = 10^{-3}\,\mathrm{s}^{-1}$. Deformations are displayed with scale factor 10.
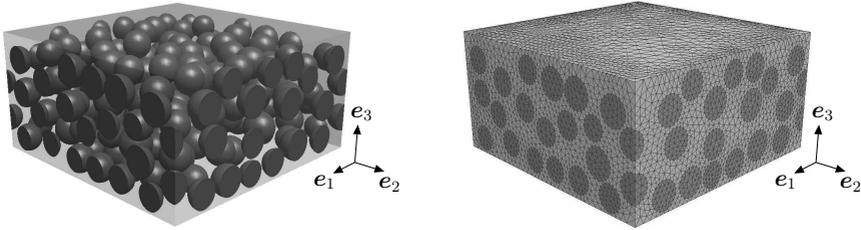
Figure 7.20: Periodic RVE representing an adhesive layer with 176 spherical inclusions (30% volume fraction). The in-plane edge lengths are twice as long as the layer thickness $L = l_3 = 750$ μm, and the particle diameters are distributed randomly between 150 μm and 200 μm (cf. Figure 7.21). The FE mesh has 334,670 nodes and 240,661 tetrahedral second order elements.

necessary for adequate local predictions. For numerical efficiency, two-scale simulations should be performed with not too many modes. In order to still obtain precise local predictions, one can identify the load paths of selected post-processing points during two-scale simulations with few modes and re-calculate the behavior of the RVE with more modes afterwards. If regions of interest are known a priori such that the post-processing points can be selected in advance, the two-scale simulation can already be conducted with more modes at these points.

7.9.3 Particle-reinforced adhesive

Apart from its common use as a matrix material in composites for lightweight construction, epoxy is frequently used for structural adhesives in many engineering applications. In order to improve certain mechanical properties, epoxy adhesives can be equipped with different types of fillers. E.g., Kim et al. [2008] and Budzik et al. [2009] have investigated the effect of nanoparticle fillers on the fracture toughness and on the crack growth rate of epoxy adhesives. Since the layer thickness of nanocomposite adhesives is usually much above the size of the particles, separation of length scales is satisfied and standard HBM homogenization principles can be applied. In contrast, adhesives with particles sizes not clearly separated from the length scale of the layer thickness must be treated with HTL approaches. That situation is found, e.g., in the experimental study of Khalili et al. [2008], who investigated adhesive joints where the adhesive layer of 750 μm thickness consisted of epoxy reinforced by glass powder with 150–200 μm particle size. A similar problem has been investigated numerically by Reina-Romo & Sanz-Herrera [2011]. These two papers have inspired the following numerical example of pRBMOR applied to HTL.

A periodic RVE has been generated in which the glass powder is represented by non-intersecting spheres (see Figure 7.20). The volume fraction of the spherical inclusions was set to 30%, corresponding to the microstructure for which the best mechanical properties have been measured by Khalili et al. [2008], and the radii of the inclusions have
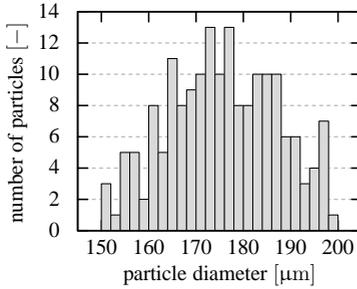
Figure 7.21: Distribution of inclusion diameters for the RVE shown in Figure 7.20.
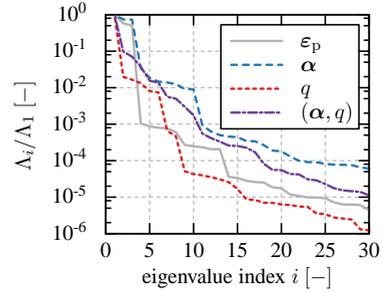

Figure 7.22: Eigenvalue decays for the HTL example with a particle-reinforced adhesive.

	training							validation					
	1	2	3	4	5	6	7	1	2	3	4	5	6
d_3	1	0	0	$\frac{\sqrt{3}}{3}$	$-\frac{\sqrt{3}}{3}$	$\frac{\sqrt{3}}{3}$	$-\frac{\sqrt{3}}{3}$	$\frac{\sqrt{2}}{2}$	$-\frac{\sqrt{2}}{2}$	$\frac{\sqrt{2}}{2}$	$-\frac{\sqrt{2}}{2}$	0	0
d_1	0	1	0	$\frac{\sqrt{3}}{3}$	$\frac{\sqrt{3}}{3}$	$-\frac{\sqrt{3}}{3}$	$-\frac{\sqrt{3}}{3}$	$\frac{\sqrt{2}}{2}$	$\frac{\sqrt{2}}{2}$	0	0	$\frac{\sqrt{2}}{2}$	$-\frac{\sqrt{2}}{2}$
d_2	0	0	1	$\frac{\sqrt{3}}{3}$	$\frac{\sqrt{3}}{3}$	$\frac{\sqrt{3}}{3}$	$\frac{\sqrt{3}}{3}$	0	0	$\frac{\sqrt{2}}{2}$	$\frac{\sqrt{2}}{2}$	$\frac{\sqrt{2}}{2}$	$\frac{\sqrt{2}}{2}$

Table 7.3: Training and validation load directions for HTL in Section 7.9.3.

been sampled from a random distribution (cf. Figure 7.21). As in the previous example presented in Section 7.9.2, the epoxy matrix material is modeled with the viscoplastic GSM with linear and nonlinear kinematic hardening from Section 3.7.2. Following Reina-Romo & Sanz-Herrera [2011], the glass powder is assumed to be isotropically elastic with Young's modulus 6 GPa and Poisson's ratio 0.235 and perfect bonding at the phase boundaries is taken as granted, i.e., perfect interfaces are assumed. Thus, the effective response of the microstructure has no tension–compression asymmetry.

Training and validation strategy. The load directions for training and for validation, represented by unit vectors denoted d, are chosen by similar considerations as in the previous examples. However, the directions are represented by points on the three-dimensional unit sphere for HTL (instead of the six-dimensional unit sphere for HBM), which allows for intuitive geometric understanding. A perfectly uniform distribution of 14 points can be directly constructed, which consists of seven pairs of (exact) antipodes. Similarly, the candidate points for the validation directions are represented by six pairs of antipodes. Because of missing tension–compression asymmetry, it is sufficient to choose only one point of each pair. According to this, the training and validation directions are defined as specified in Table 7.3 and illustrated in Figure 7.23.
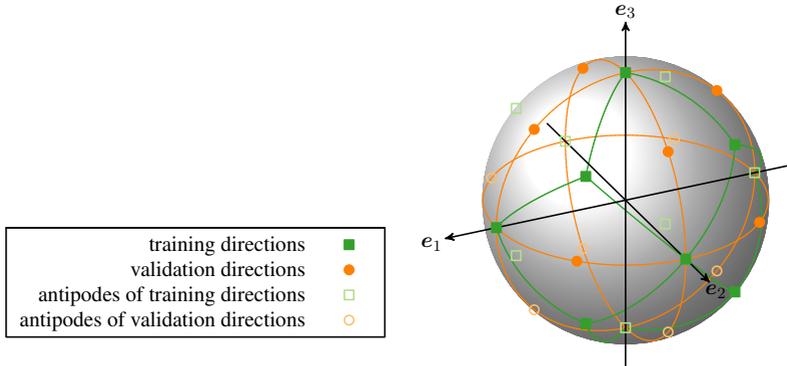
Figure 7.23: Illustration of the training and validation directions for HTL (cf. Table 7.3).
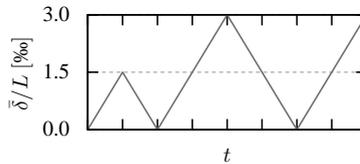

Figure 7.24: Cyclic loading for validation.

The ROM is validated for cyclic loadings described by

$$\bar{\boldsymbol{\delta}}(t) = \bar{\delta}(t)\,\boldsymbol{d}, \qquad\qquad \left|\dot{\bar{\delta}}\right| = \text{const.}, \qquad\qquad \|\boldsymbol{d}\|_2 = 1, \qquad (7.104)$$

where $\bar{\delta}(t)$ varies according to Figure 7.24. However, only proportional loadings with the final amplitude $\left\|\bar{\boldsymbol{\delta}}\right\|_2 = 0.0045L$ are considered for training in order to investigate the predictive capabilities with respect to the complexity of loadings. Attention is limited to training and validation loadings with the load rate $\left|\dot{\bar{\delta}}\right| = 10^{-3}L\,\mathrm{s}^{-1}$ which is not varied since the GSM model of epoxy exhibits only a very weak rate-dependence. The eigenvalue decays associated with the reduced bases obtained from the proportional training loadings are shown in Figure 7.22. Both joint and split hardening modes, labeled **[Q1]** and **[Q2]** as in Section 7.9.2, will be considered.

Accuracy of the effective cohesive tractions. To begin with, reasonable numbers of modes shall be determined. Since the plastic modes affect the approximation of the local stress field (and thus, the accuracy of the effective traction vector) in a more direct way than the hardening modes, the number N_ξ of plastic modes should be chosen relatively generous; this suggestion is supported by practical experience from previous numerical examples. Also, the example from Section 7.9.2 indicates that the number of modes for the nonlinear kinematic hardening variable $\boldsymbol{\alpha}$ can be chosen rather low
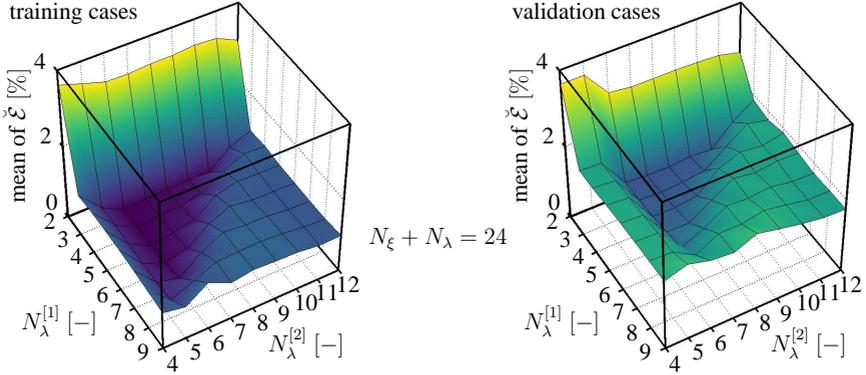
Figure 7.25: Mean of the error $\breve{\mathcal{E}}$ for 7 training cases and for 6 validation cases for different but equal sized **[Q2]** mode systems.

compared to the one for isotropic hardening. For a good trade-off between accuracy and numerical efficiency, it is advisable to select numbers of modes that are directly ahead of rapid declines in the respective eigenvalue decays. Thus, in view of Figure 7.22,

$$N_\xi = 13, \qquad\qquad N_\lambda^{[1]} = 3, \qquad\qquad N_\lambda^{[2]} = 8 \qquad\qquad (7.105)$$

are guessed to be reasonable numbers of modes. In order to assess the validity of this assumption, a systematic study of different mode systems with the total number of modes $N_\xi + N_\lambda = 24$ was conducted. The error measure

$$\breve{\mathcal{E}} = \frac{\sqrt{\dfrac{1}{N} \sum_{n=1}^{N} \|\bar{\boldsymbol{t}}_{\mathrm{ROM}}(t_n) - \bar{\boldsymbol{t}}_{\mathrm{FF}}(t_n)\|_2^2}}{\max\limits_{1 \leq n \leq N} \|\bar{\boldsymbol{t}}_{\mathrm{FF}}(t_n)\|_2} \qquad\qquad (7.106)$$

was evaluated for all training and for all validation simulations, where $\bar{\boldsymbol{t}}_{\mathrm{ROM}}$ and $\bar{\boldsymbol{t}}_{\mathrm{FF}}$ denote the effective cohesive tractions predicted with pRBMOR and obtained from the corresponding full-field FE solution, respectively. Figure 7.25 shows the means of the error $\breve{\mathcal{E}}$ for the seven training cases and for the six validation cases evaluated for 72 different mode systems. As expected, the training cases can be captured with much better accuracy than the validation cases. While the training cases are best recovered with $N_\xi = 15$, $N_\lambda^{[1]} = 3$, and $N_\lambda^{[2]} = 6$, the validation cases are in fact best approximated with the mode numbers in (7.105). However, a striking qualitative agreement between the results for training and for validation cases is found. The observed qualitative similarity affirms the similar finding for the examples from Section 7.9.2 in Figure 7.12 and is quite remarkable since different types of loadings have been considered for training and for validation. A depiction of the three modes used as a reduced basis for the NLKH variable $\boldsymbol{\alpha}$ in the case **[Q2]** is shown in Figure 7.26.
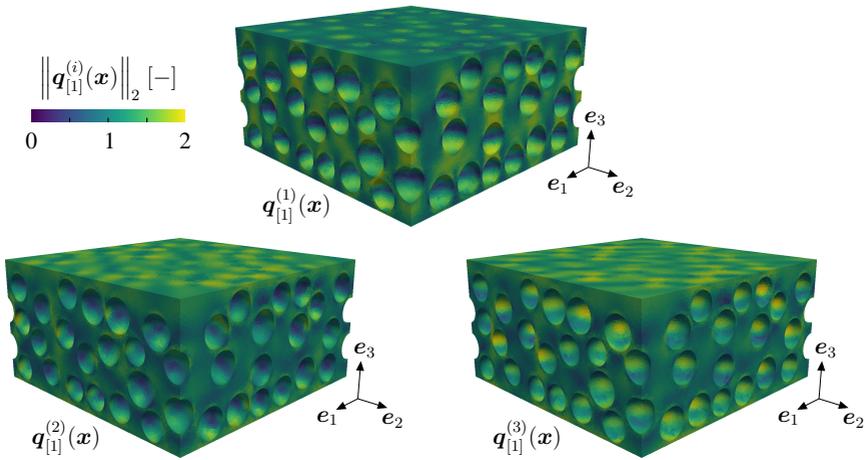
**Figure 7.26:** Depiction of the first three modes for the NLKH internal variable $\boldsymbol{\alpha}$ for **[Q2]**.
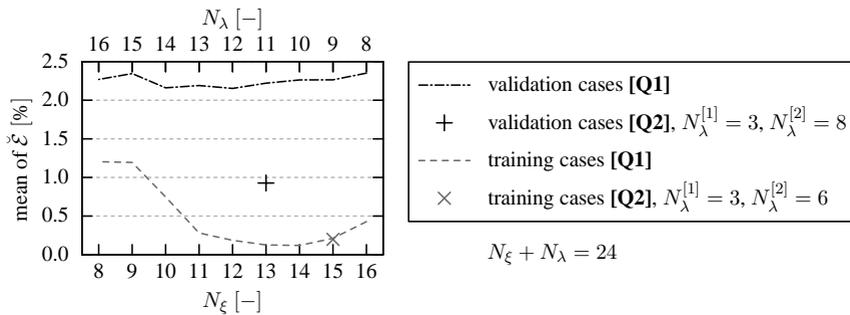
Figure 7.27: Mean of the error $\breve{\mathcal{E}}$ for 7 training cases and for 6 validation cases for different but equal sized **[Q1]** mode systems. For comparison, the optimal **[Q2]** configurations from Figure 7.25 are shown as single data points.

A similar comparison has been conduced also for joint hardening modes in accordance with **[Q1]**, and the results are summarized in Figure 7.27. Other than for the example in Section 7.9.2, the optimal configuration with joint hardening modes provides even better approximations than the best possible setup with split hardening modes for the training cases. This is because there is no real decoupling of the hardening variables $\boldsymbol{\alpha}$ and q during proportional loadings. For the same reason, the joint modes trained with proportional loadings are inappropriate for the prediction of the cyclic validation loadings. While split hardening modes have already been found to be advantageous over joint hardening modes for the cyclic validation cases in Section 7.9.2, where the
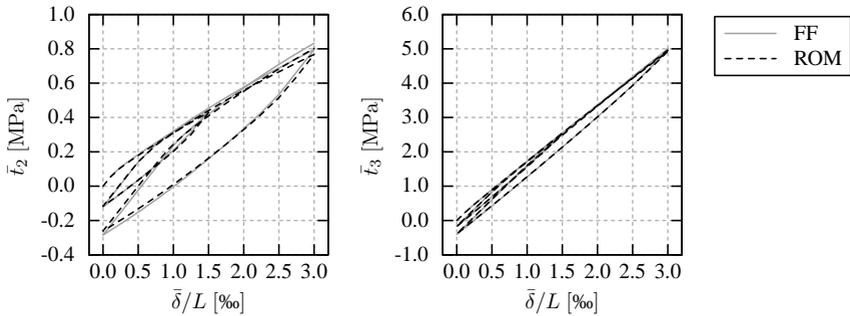
Figure 7.28: Effective cohesive traction for the validation case 3 from Table 7.3.
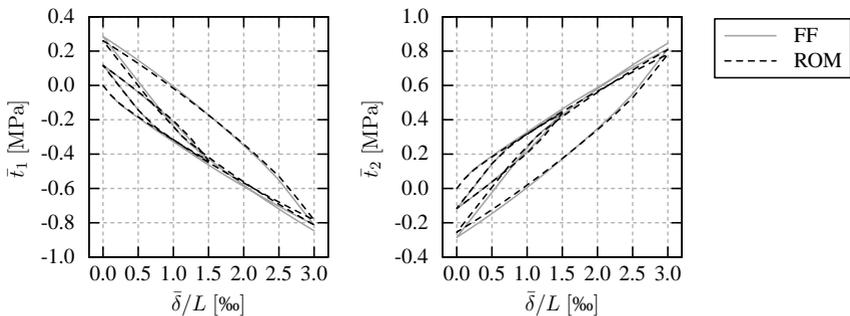

Figure 7.29: Effective cohesive traction for the validation case 6 from Table 7.3.

training data were computed for cyclic loadings, a much more pronounced benefit for split hardening modes is observed in the present example.

The global SDCZ which describes the effective behavior of the adhesive layer is almost transversely isotropic. Therefore, the validation cases 1–4 are almost equivalent to each other as well as the pure shear cases 5 and 6. The worst case representatives of these two groups have been identified (3 and 6) and the relevant components of their effective traction vectors are shown in Figures 7.28 and 7.29, respectively. The displayed results have been computed with the mode numbers from (7.105). It is found that pRBMOR predicts the normal traction for validation case 3 with almost no noticeable deviations from the FE reference. The shear components of both considered worst case loadings are predicted very accurately before the amplitude $\bar{\delta}/L = 1.5‰$ is first exceeded. In the subsequent second hysteresis loops, some noticeable inaccuracy is found. However, the approximation errors are considered still acceptable in view of the fact that relatively few modes have been used, which have been obtained from a rather lean training procedure.

7.10 Discussion and perspectives

The purpose of pRBMOR is to reduce computing times and memory requirement compared to full-field methods for nonlinear homogenization problems. While the storage of the current state of a single RVE is in general not critical on standard hardware, the memory demand of full-field solvers quickly exceeds the available resources when large numbers of RVEs need to be considered simultaneously in two-scale simulations. The capabilities of pRBMOR in such scenarios are obvious: with the reduced global state defined in (7.13), the number of variables required to represent the current state of the RVE is given by the sum of the numbers of modes plus six (for HBM) or plus three (for HTL). This is in contrast to thousands or even millions of state variables for standard FE discretizations or voxel representations. Thus, the one-time storage overhead related to the pRBMOR data (cf. Figure 7.2) already pays off for rather few RVEs that have to be considered simultaneously. Note also that the number of pRBMOR modes is basically independent of the level of detail of the underlying full-field discretization. Therefore, higher memory savings are possible for complex microstructures with many details. For instance, in the example presented in Section 7.9.3, the memory demand is reduced by a factor well above 10^5 with pRBMOR compared to the full-field FEM.

With regard to the numerical effort of pRBMOR, the operations at the global level are negligible, and the computing time increases linearly with the numbers of local evaluation points in the bulk and on the imperfect interface. Moreover, the computational complexity of pRBMOR exhibits a quadratic dependence on the numbers of modes because it is dominated by the assembly of the Jacobian in (7.89). The speedup with respect to full-field simulations is thus strongly dependent on the desired accuracy. Detailed elucidations on computing times can be found in Fritzen & Leuschner [2013] and in particular in Fritzen et al. [2014, including thorough benchmarking]. Typically, the pure methodological speedup of pRBMOR compared to full-field FEM simulations is in the range of one to two orders of magnitude. For the examples in Section 7.9.2 and in Section 7.9.3, the chosen near rate-independent Perzyna-type viscoplastic model of epoxy resin impairs the convergence rate of the pRBMOR online algorithm, and the speedup is suspected to be below the one attainable with more simple (local) constitutive models. However, the observed speedup is still a multiple of ten. When assembling the residual vector and the Jacobian of the global Newton–Raphson procedure, the main computational effort is due to the evaluation of the first and second order gradients of the local GSM and SDCZ potentials and, what is more, due to local matrix–vector and matrix–matrix products, e.g., during the computation of the matrix $\underline{\underline{\mathcal{L}}}$ defined in (7.85). Thus, the crucial part of the overall numerical cost arises in the form of independent, simple, and small-sized operations at the microscopic evaluation points, making pRBMOR perfectly suited for parallelization by general purpose GPU implementations. Note that this is in contrast to full-field solvers, where much larger (though sparse) global systems have to be solved and where the tasks at the local level comprise iterative schemes that cannot be parallelized as efficiently as the above-mentioned local operations. Therefore, GPU acceleration of pRBMOR, which allows

for additional speedups on the order of two magnitudes [cf. Fritzen et al., 2014], can be considered as partially method-enabled speedup.

It is recalled that the pRBMOR variational principle is based on volume and surface averages of the local GSM and SDCZ potentials. In technically straightforward implementations of pRBMOR, the volume and surface averages of the gradients of the local potentials are computed via numerical integration where the integration points are directly inherited from the discretization of the full-field solver used in the offline phase. For the examples presented in Section 7.9, the integration points of the underlying FE discretization have been used as local evaluation points of the pRBMOR scheme. However, from a theoretical point of view, the global quadrature rule can be chosen freely, and practical experience tells that pRBMOR works well with far less integration points than the full-field FEM. For instance, bluntly selecting only every eighth integration point had literally no effect on the pRBMOR accuracy for several considered examples. This observation builds confidence that pRBMOR might successfully operate on reduced integration domains following the example of the *a priori hyperreduction method* [cf. Ryckelynck, 2005, Ryckelynck et al., 2012] or other systematic reduced integration schemes [e.g., in line with Hernández et al., 2014, 2017, Michel & Suquet, 2017]. An additional speedup of at least one order of magnitude is expectable with such approaches.

The assumption that the local constitutive models are potential-based is crucial for the derivation of the pRBMOR scheme but constitutes a limitation since some commonly used models do not meet this requirement. E.g, the evolution law of some material models reads

$$\dot{\boldsymbol{\mathcal{I}}} = \boldsymbol{f}(\boldsymbol{\mathcal{F}}) \tag{7.107}$$

instead of (3.5), where the constitutive function $\boldsymbol{f}$ does not satisfy the Onsager reciprocal relation

$$\left(\frac{\partial \boldsymbol{f}(\boldsymbol{\mathcal{F}})}{\partial \boldsymbol{\mathcal{F}}} \right)^{\top} = \frac{\partial \boldsymbol{f}(\boldsymbol{\mathcal{F}})}{\partial \boldsymbol{\mathcal{F}}}, \tag{7.108}$$

which is a necessary condition for the existence of a dual dissipation potential. In spite of the violation of the theoretical requirements, Michel & Suquet [2016b] have successfully applied the NTFA-TSO—which has the same variational foundation as pRBMOR—to such non-standard models, and the same should be possible with pRBMOR.

Another crucial requirement of the pRBMOR scheme is that the function $\mathfrak{M}$ introduced in (7.57) is invertible. Technically speaking, this means that the matrix $\underline{M}$ defined in (7.73) must be nonsingular, which is directly exploited in the Newton–Raphson procedure defined through (7.88) and (7.89). The requirement corresponds to the global free Helmholtz energy being strongly convex. As shown in Appendix B.3, a sufficient condition for the global strong convexity is that the local free Helmholtz energies are strongly convex, as assumed in Section 7.2. The practical consequence of this assumption is that softening behavior cannot be considered. If desired, one can drop the confinement to strongly convex local free energy densities and abort the pRBMOR online

algorithm when $\underline{\underline{M}}$ becomes singular. However, non-convex global behavior remains unattainable with the present pRBMOR scheme. It is pointed out that this reflects a general theoretical limitation of first order homogenization principles (cf. Section 5.4). Thus, in order to treat non-convex global behavior, pRBMOR ought to be reformulated as a higher order homogenization principle and major adjustments of the variational scheme would be necessary. The parameterization of the local driving forces in terms of global driving forces will be the key issue and might be tackled by introducing additional dual reduced bases.

To conclude with, it is worth mentioning that the pRBMOR principle can be transferred to other applications beyond the context of multiscale material modeling with only minor modifications of the online algorithm. The treatment of the non-classical homogenization scheme for thin layers in this work can be understood as a first step in that direction, and the spots where the HTL version differs from the HBM version essentially indicate where modifications would be necessary for other types of applications. Obviously, the use of other kinds of boundary conditions in full-field training simulations and in the auxiliary elastic analyses is the most important alteration to be made. In principle, pRBMOR (like other reduced basis methods) is suitable for problems where the entirety of all loadings of interest allows to identify an appropriate and manageable set of representative training cases.

Chapter 8:
Summary and conclusions

One main topic of this thesis is the homogenization of the mechanical behavior of heterogeneous materials with imperfect interfaces by means of the potential-based reduced basis model order reduction (pRBMOR) method (see Chapter 7). pRBMOR was first proposed in Fritzen & Leuschner [2013] for materials with perfect interfaces (i.e., continuous displacement fields) taking up ideas of the nonuniform transformation field analysis (NTFA) of Michel et al. [2000], Michel & Suquet [2003, 2004]. The transfer of the pRBMOR concept to microstructures with imperfect interfaces is accompanied with fundamental modifications, such as the introduction of a reduced basis for the displacement jump field, and was first conducted for hyperelastic traction–separation laws in Fritzen & Leuschner [2015]. Section 7.9.1 reproduces numerical examples from Fritzen & Leuschner [2015] which are concerned with the dependence of the approximation accuracy on the numbers of displacement jump modes and on the amount of training data. The examples also highlight the advanced accuracy of pRBMOR compared to interpolation based on Gaussian kernels.

Chapter 7 presents an extended pRBMOR scheme accounting for homogenization problems with coupled dissipative bulk and interface effects [developed in Leuschner & Fritzen, 2017] with two novel aspects: firstly, more than one reduced basis for bulk hardening variables is considered, and secondly, homogenization of thin layers (HTL) is addressed in addition to the "standard" case of homogenization of bulk materials (HBM). The option of multiple sets of hardening modes is geared towards complex material models comprising different types of hardening variables, such as the near rate-independent model of epoxy resin with isotropic and linear as well as nonlinear kinematic hardening from Section 3.7.2. This material model is incorporated in the numerical example of a unidirectional fiber-reinforced composite with a viscoelastic interface exposed to cyclic loadings, which is presented in Section 7.9.2. During loading–unloading cycles, the isotropic hardening variable increases monotonically as opposed to the (nonlinear) kinematic hardening variable. It is therefore suspected that two separate reduced bases for both hardening variables are more adequate than one joint basis. This hypothesis is confirmed by numerical results, which show that better accuracy can be attained with separate bases while the number of reduced DOF remains unaltered.

The adaptation of pRBMOR to HTL aims at heterogeneous thin layers where separation of length scales is not satisfied in the out-of-plane direction such that HBM approaches are not applicable. Viewed from the global perspective, the thin layer is idealized as an imperfect interface, and the HTL procedure yields an effective traction–separation law. As a numerical example, an epoxy-based particle-reinforced adhesive is considered in Section 7.9.3, where the above-mentioned epoxy resin model from Section 3.7.2 is

utilized again. In contrast to the HBM example from Section 7.9.2, the HTL reduced order model is trained with proportional loadings only. It is found that loading–unloading cycles with load directions not considered in the training can still be predicted with satisfactory accuracy when using separate reduced bases for isotropic and kinematic hardening variables.

For all numerical examples in Section 7.9, systematic training–validation concepts have been realized in order to assess the predictive capabilities of the reduced order models as well as realistic numbers of modes, which massively affect the computational effort. Predictions for load directions or load paths not considered in the training are usually the principal purpose of nonlinear homogenization schemes and are examined for all considered examples. In addition, predictive capabilities with respect to the load rate and the normalized interface stiffness are investigated for the unidirectional fiber-reinforced composite with a viscoelastic interface model in Section 7.9.2. The example is designed such that a variation of the normalized interface stiffness can be interpreted both as an alteration of the length scale of the microstructure and as a change of the constitutive properties of the imperfect interface. Thus, the numerical results demonstrate the ability of the reduced order model to investigate the interface-induced size effect and its robustness with respect to modifications of constitutive parameters[43]. The second aspect is of particular relevance because it can be exploited for the application of pRBMOR in inverse parameter identification procedures. The practical relevance of numerically efficient methods for inverse parameter identification is underlined by the fact that interface parameters for phase boundaries in composite materials are often difficult to determine directly.

The rather accurate prediction of scenarios that differ moderately from the training cases is an important advantage of pRBMOR. Even when accuracy wanes, trends and changes caused by the alteration of loadings or constitutive parameters are captured reliably. The reason is that no empirical interpolation is involved, which is in contrast to other MOR techniques such as kernel methods or POD approaches combined with discrete empirical interpolation (DEIM) [see, e.g., Chaturantabut & Sorensen, 2009, Fink & Ehlers, 2015, Radermacher & Reese, 2016]. Instead, pRBMOR is based on an incremental variational principle (see Section 7.5) in which the prescribed local constitutive laws are taken into account. For given reduced bases, either the physically most reasonable solution is found or the Newton–Raphson procedure fails to converge when the modes are unsuitable for the considered problem. In fact, approximation errors versus full-field solutions are solely due to the reduction of the solution space, while the pRBMOR solution scheme could in theory exactly reproduce any full-field solution given reduced bases perfectly matching thereto.

A favorable difference of pRBMOR compared to standard full-field solvers is that no iterative schemes are required at the local level to calculate implicit time increments for

---

[43]Without further ado, modifications of the elastic parameters of the bulk materials cannot be considered because the auxiliary elastic analyses (cf. Section 7.4) are based on the assumption of fixed elastic properties.

path-dependent constitutive models. Only relatively simple, small-sized local operations arise, which dominate the overall cost but can be efficiently parallelized by general purpose GPU implementations [cf. Fritzen et al., 2014]. The avoidance of local constitutive iterations is made possible by the assumptions that the bulk material laws at the microscopic scale belong to the class of generalized standard materials (GSMs, cf. Chapter 3) and that the interface models are defined in a similar framework, referred to as standard dissipative cohesive zones (SDCZs, cf. Section 4.6). Moreover, the local constitutive models are assumed to be viscous or viscously regularized. These assumptions clearly represent limitations[44] regarding practical applicability; a well-known point of criticism of the GSM framework is that it does not include the classical Armstrong–Frederick model for nonlinear kinematic hardening (NLKH). However, a non-classical GSM model with NLKH exists, which is described in Section 3.3.1 and calibrated to experimental results of tensile loading–unloading tests of epoxy resin from da Costa Mattos & Martins [2013] as presented in Section 3.7.2. The calibrated model is employed in numerical examples for pRBMOR in Section 7.9. Virtually rate-independent behavior has been observed by da Costa Mattos & Martins [2013], which is approximated via a Perzyna-type formulation with a high viscosity exponent of 30. It is pointed out that pRBMOR can handle this particular model although viscously regularized approximations of rate-independent models are generally challenging from a numerical point of view. In contrast, Perzyna-type formulations with moderately high viscosity exponents are already beyond the scope of the NTFA-TSO [Michel & Suquet, 2016a,b].

The limitations of potential-based constitutive modeling are even more evident for interface laws than for material models. In fact, most cohesive zone models found in the literature do not belong to the SDCZ class. However, SDCZ damage models, taking into account also mixed mode loadings, have been proposed by Leuschner et al. [2015] and are described in Section 4.7. Numerical examples from Leuschner et al. [2015] including FEM simulations of miniaturized mixed mode bending tests [following Kolluri et al., 2009, 2011] are reproduced in Section 4.8. Softening damage is modeled via non-convex potentials. Unfortunately, incorporation of non-convex local constitutive models in the present pRBMOR scheme is not possible or at least very limited, as elucidated in Section 7.10.

The offline phase of pRBMOR, including the generation of training data and the auxiliary elastic analyses (see Section 7.4), can be implemented with different full-field solvers in general. The consideration of imperfect interfaces at phase boundaries of composite materials—a main goal of this thesis—is rather straightforward with an FEM-based approach, which was therefore used for all presented examples. On the other hand, Fourier-based homogenization methods rely on pixel/voxel discretizations which are less suitable for the representation of imperfect interfaces. One possible workaround

---

[44]On the other hand, the confinement to the GSM and SDCZ frameworks has a practical advantage as well: the implementation of pRBMOR can be realized in a mostly model-independent way. More precisely, the gradients of specific GSM and SDCZ models can be implemented in exchangeable subroutines, while the remainder of the code needs no adjustment towards specific constitutive models.

could be to pick up ideas from the modeling of cracks by phase-field approaches [see, e.g., Miehe et al., 2010, Li et al., 2012], corresponding to regularized descriptions of singular surfaces. Another approach would be to develop an enhanced composite voxel technique, as teased by Kabel et al. [2017]. A drawback of composite voxels is the additional solver time which can become striking when the interface passes through many voxels [cf. Kabel et al., 2015]. With regard to this issue, it can be expected that the Fourier-accelerated nodal solvers (FANS) proposed in Leuschner & Fritzen [2018] and presented in Chapter 6 are favored compared to other FFT-based homogenization schemes. The reason is that with FANS, the additional routines for composite voxels need to be executed only once for each linearized problem in order to determine the tangent stiffnesses, which remain unaltered during the FANS iterations. In contrast, additional cost arises in each iteration when composite voxels are implemented in conventional Fourier-based schemes.

Like the FFT-Q_1Quad/Hex method recently proposed by Schneider et al. [2017], the FANS scheme operates on uniform grids equipped with bi-/trilinear FE shape functions. Other than for FFT-Q_1Quad/Hex, a periodized global conductance/stiffness matrix is assembled, which allows for fast iterative solutions schemes. The relatively high memory requirement for the periodized global matrix is a drawback which can become a limiting factor when large three-dimensional microstructures are considered. However, hardware that allows to handle mechanical homogenization problems at resolutions up to 512^3 voxels with FANS is nowadays available around 10k euros, which is affordable even for small research groups. The FANS concept has been realized as a fixed-point scheme (FP-FANS) and as a preconditioned conjugate gradient scheme (CG-FANS). A key ingredient of both procedures is the discrete periodic convolution of a fundamental solution with the nodal residuals, which can be efficiently accomplished by pointwise multiplication in Fourier space thanks to FFT algorithms. In the case of CG-FANS, the application of the fundamental solution corresponds to the preconditioning step.

FANS schemes are specified for thermal homogenization (see Section 6.3) as well as for mechanical homogenization (see Section 6.4). The numerical examples presented in Section 6.5 start with a method comparison for steady-state heat conduction in Section 6.5.1. A benchmark problem is considered, for which the FANS solution shows better agreement with a closed-form solution than competing FFT-based schemes. Whereas spurious artifacts due to the Gibbs phenomenon are a long recognized issue of Fourier-based homogenization methods, no such artifacts are found in FANS results. For an elastic particle-reinforced composite with two isotropic phases, the influence of the Poisson's ratio associated with the fundamental solution on the convergence of CG-FANS is investigated in Section 6.5.2. It is observed that when assuming the Poisson's ratio of the softer phase for the fundamental solution, the convergence is always at least as good as with the classical proposal of Moulinec & Suquet [1994] geared towards fixed-point schemes, and in many cases it is noticeably better.

A brief example of a particle-reinforced composite with von Mises plasticity in the matrix material is given in Section 6.5.3. Problems involving plasticity exhibit high apparent phase contrasts, for which FFT-based homogenization methods need many iterations in

general. FANS are particularly useful for plasticity problems and in other situations where many iterations are required because the numerical effort per iteration is lower than for competing FFT-based methods, and the one-time cost related to the assembly of the conductance/stiffness matrix pays off after some—usually relatively few—iterations. Another advantage is that FE discretizations are well understood, and extensions of the FANS principle to more complex element types are conceivable. Altogether, the FANS scheme is seen as a highly competitive full-field homogenization approach for heterogeneous materials represented by pixel or voxel data, and it has potential for further development.

Appendix A:
Notation and conventions

A.1   Tensor notation

A.1.1   Basics

The following typesetting is used for tensors: scalar quantities (zeroth order tensors) are denoted by Latin or Greek lowercase letters (e.g., a, α), vectors (first order tensors) are represented by boldface Latin lowercase letters (e.g., $\boldsymbol{a}$), second order tensors are expressed by boldface Latin capital letters or boldface Greek lowercase letters (e.g., $\boldsymbol{A}$, $\boldsymbol{\alpha}$), and fourth order tensors are typeset as blackboard bold Latin capital letters (e.g., $\mathbb{A}$). Let $\mathscr{L}^n$ denote the set of tensors of order $n \in \{0, 1, 2, 3, 4\}$, and let $\{\boldsymbol{e}_1, \boldsymbol{e}_2, \boldsymbol{e}_3\}$ be an orthonormal basis of the three-dimensional Euclidean space $\mathbb{E}^3$. A tensor $\boldsymbol{F} \in \mathscr{L}^m$ ($m \geq 1$) can be expressed in terms of the orthonormal basis according to

$$\boldsymbol{F} = \sum_{i_1, \ldots, i_m = 1}^{3} F_{i_1 \cdots i_m} \boldsymbol{e}_{i_1} \otimes \cdots \otimes \boldsymbol{e}_{i_m}, \tag{A.1}$$

where "$\otimes$" represents the tensor product[45]. An index-free notation without summation convention is used. Single contraction of two tensors $\boldsymbol{F} \in \mathscr{L}^m$ and $\boldsymbol{G} \in \mathscr{L}^n$ with $m, n \geq 1$ is defined by

$$\boldsymbol{F} \cdot \boldsymbol{G} = \sum_{\substack{i_1, \ldots, i_{m-1} = 1 \\ j_2, \ldots, j_n = 1 \\ k = 1}}^{3} F_{i_1 \cdots i_{m-1} k} \, G_{k j_2 \cdots j_n} \, \boldsymbol{e}_{i_1} \otimes \cdots \otimes \boldsymbol{e}_{i_{m-1}} \otimes \boldsymbol{e}_{j_2} \otimes \cdots \otimes \boldsymbol{e}_{j_n}. \tag{A.2}$$

Similarly, double contraction is given by

$$\boldsymbol{F} : \boldsymbol{G} = \sum_{\substack{i_1, \ldots, i_{m-2} = 1 \\ j_3, \ldots, j_n = 1 \\ k, l = 1}}^{3} F_{i_1 \cdots i_{m-2} k l} \, G_{k l j_3 \cdots j_n} \, \boldsymbol{e}_{i_1} \otimes \cdots \otimes \boldsymbol{e}_{i_{m-2}} \otimes \boldsymbol{e}_{j_3} \otimes \cdots \otimes \boldsymbol{e}_{j_n} \tag{A.3}$$

in situations with $m, n \geq 2$. Note that single contraction of two vectors corresponds to the standard scalar product, and double contraction of two second order tensors is a scalar

---

[45]The tensor product of two vectors is widely known as *dyadic product*.

product on $\mathscr{L}^2$. The special case of single contraction where the first operand is a second order tensor is often abbreviated according to

$$\boldsymbol{A} \cdot \boldsymbol{b} = \boldsymbol{A}\boldsymbol{b}, \qquad\qquad\qquad \boldsymbol{A} \cdot \boldsymbol{B} = \boldsymbol{A}\boldsymbol{B}. \tag{A.4}$$

The only third order tensor used in this work is the Levi–Civita symbol for three dimensions

$$\boldsymbol{\epsilon} = \sum_{i_1,i_2,i_3=1}^{3} \left(\prod_{1 \le m < n \le 3} \frac{i_m - i_n}{m - n} \right) \boldsymbol{e}_{i_1} \otimes \boldsymbol{e}_{i_2} \otimes \boldsymbol{e}_{i_3}. \tag{A.5}$$

It defines the cross product of two vectors

$$\boldsymbol{a} \times \boldsymbol{b} = \boldsymbol{\epsilon} : (\boldsymbol{a} \otimes \boldsymbol{b}) \tag{A.6}$$

and, similarly, the cross product of a vector and a second order tensor

$$\boldsymbol{a} \times \boldsymbol{B} = \boldsymbol{\epsilon} : (\boldsymbol{a} \otimes \boldsymbol{B}). \tag{A.7}$$

A.1.2 Identity tensors, symmetries, and positive (semi-) definiteness

A second order tensor $\boldsymbol{A}$ is said to be symmetric if it is equal to its transpose

$$\boldsymbol{A}^{\mathsf{T}} = \sum_{i,j=1}^{3} A_{ji} \boldsymbol{e}_i \otimes \boldsymbol{e}_j. \tag{A.8}$$

Analogously, a fourth order tensor $\mathbb{A}$ has major symmetry if it coincides with its transpose

$$\mathbb{A}^{\mathsf{T}} = \sum_{i,j,k,l=1}^{3} A_{klij} \boldsymbol{e}_i \otimes \boldsymbol{e}_j \otimes \boldsymbol{e}_k \otimes \boldsymbol{e}_l. \tag{A.9}$$

Left and right minor symmetry of $\mathbb{A}$ are characterized by the equalities

$$\sum_{i,j,k,l=1}^{3} A_{jikl} \boldsymbol{e}_i \otimes \boldsymbol{e}_j \otimes \boldsymbol{e}_k \otimes \boldsymbol{e}_l = \sum_{i,j,k,l=1}^{3} A_{ijkl} \boldsymbol{e}_i \otimes \boldsymbol{e}_j \otimes \boldsymbol{e}_k \otimes \boldsymbol{e}_l, \tag{A.10}$$

$$\sum_{i,j,k,l=1}^{3} A_{ijlk} \boldsymbol{e}_i \otimes \boldsymbol{e}_j \otimes \boldsymbol{e}_k \otimes \boldsymbol{e}_l = \sum_{i,j,k,l=1}^{3} A_{ijkl} \boldsymbol{e}_i \otimes \boldsymbol{e}_j \otimes \boldsymbol{e}_k \otimes \boldsymbol{e}_l, \tag{A.11}$$

respectively. The identities on $\mathscr{L}^2$ and on $\mathscr{L}^4$

$$\boldsymbol{I} = \sum_{i,j=1}^{3} \delta_{ij} \boldsymbol{e}_i \otimes \boldsymbol{e}_j, \qquad\qquad \mathbb{I} = \sum_{i,j,k,l=1}^{3} \delta_{ik} \delta_{jl} \boldsymbol{e}_i \otimes \boldsymbol{e}_j \otimes \boldsymbol{e}_k \otimes \boldsymbol{e}_l \tag{A.12}$$

are defined in terms of the Kronecker delta

$$
\delta_{ij} = \begin{cases} 1, & i = j \\ 0, & i \neq j \end{cases}. \tag{A.13}
$$

The identity on symmetric second order tensors

$$
\mathbb{I}^{\mathsf{S}} = \sum_{i,j,k,l=1}^{3} \frac{1}{2} \left(\delta_{ik}\delta_{jl} + \delta_{il}\delta_{jk} \right) \boldsymbol{e}_i \otimes \boldsymbol{e}_j \otimes \boldsymbol{e}_k \otimes \boldsymbol{e}_l \tag{A.14}
$$

maps an arbitrary second order tensor $\boldsymbol{A}$ to its symmetric part

$$
\operatorname{sym}\left(\boldsymbol{A}\right) = \frac{1}{2}\left(\boldsymbol{A} + \boldsymbol{A}^{\mathsf{T}}\right) = \mathbb{I}^{\mathsf{S}} : \boldsymbol{A}. \tag{A.15}
$$

Any second order tensor can be additively decomposed into its symmetric part and its skew-symmetric part

$$
\operatorname{skw}(\boldsymbol{A}) = \frac{1}{2}\left(\boldsymbol{A} - \boldsymbol{A}^{\mathsf{T}}\right) = \left(\mathbb{I} - \mathbb{I}^{\mathsf{S}}\right) : \boldsymbol{A}. \tag{A.16}
$$

With the trace of an arbitrary second order tensor $\boldsymbol{A}$ defined as

$$
\operatorname{tr}(\boldsymbol{A}) = \boldsymbol{A} : \boldsymbol{I}, \tag{A.17}
$$

the spherical part and the deviatoric part are expressed as

$$
\boldsymbol{A}^{\circ} = \frac{\operatorname{tr}(\boldsymbol{A})}{3}\boldsymbol{I} = \mathbb{P}_1^{\text{iso}} : \boldsymbol{A}, \qquad \boldsymbol{A}' = \operatorname{sym}\left(\boldsymbol{A}\right) - \boldsymbol{A}^{\circ} = \mathbb{P}_2^{\text{iso}} : \boldsymbol{A}, \tag{A.18}
$$

where the isotropic projectors are defined by

$$
\mathbb{P}_1^{\text{iso}} = \frac{1}{3}\boldsymbol{I} \otimes \boldsymbol{I}, \qquad\qquad \mathbb{P}_2^{\text{iso}} = \mathbb{I}^{\mathsf{S}} - \mathbb{P}_1^{\text{iso}}. \tag{A.19}
$$

Clearly, $\boldsymbol{A}$ can be additively decomposed into $\boldsymbol{A}^{\circ}$ and $\boldsymbol{A}'$ if it is symmetric. Further, $\boldsymbol{A}$ is said to be positive semi-definite if

$$
\boldsymbol{v} \cdot \boldsymbol{A}\boldsymbol{v} \geq 0 \qquad \text{for all } \boldsymbol{v} \in \mathscr{L}^1. \tag{A.20}
$$

If strict inequality holds for every $\boldsymbol{v} \neq \boldsymbol{0}$ in (A.20), $\boldsymbol{A}$ is called positive definite. Similarly, a fourth order tensor $\mathbb{A}$ is positive semi-definite if

$$
\boldsymbol{B} : \mathbb{A} : \boldsymbol{B} \geq 0 \qquad \text{for all } \boldsymbol{B} \in \mathscr{L}^2 \tag{A.21}
$$

and it is positive definite in the case of strict inequality for all $\boldsymbol{B} \neq \boldsymbol{0}$. Moreover, $\mathbb{A}$ is called positive definite on the space of symmetric second order tensors Sym if

$$
\boldsymbol{B} : \mathbb{A} : \boldsymbol{B} > 0 \qquad \text{for all } \boldsymbol{B} \in Sym \setminus \{\boldsymbol{0}\}. \tag{A.22}
$$

A.2   Matrix–vector notation

Vectors (in the sense of tuples of real or complex numbers) and matrices of arbitrary dimensions are denoted with one or two underlines, respectively. E.g., $\underline{0}$ represents a zero vector and $\underline{\underline{0}}$ denotes a zero matrix. A vector of ones is denoted $\underline{1}$, and identity matrices are written $\underline{\underline{I}}$.

The space of symmetric second order tensors Sym plays an important role for mechanical problems under the assumption of small deformations since it contains the infinitesimal strain tensor $\boldsymbol{\varepsilon}$ and the Cauchy stress $\boldsymbol{\sigma}$. A six-dimensional basis of Sym is given by

$$\boldsymbol{B}^{(i)} = \boldsymbol{e}_i \otimes \boldsymbol{e}_i \qquad (i = 1, \dots, 3), \tag{A.23}$$

$$\boldsymbol{B}^{(i+j)} = \frac{\sqrt{2}}{2} \left(\boldsymbol{e}_i \otimes \boldsymbol{e}_j + \boldsymbol{e}_j \otimes \boldsymbol{e}_i \right) \qquad (i, j = 1, 2, 3, \quad i < j \le 3). \tag{A.24}$$

Thereby, a six-dimensional vector representation $\underline{A}$ of $\boldsymbol{A} \in Sym$ is defined according to

$$(\underline{A})_\alpha = A_\alpha = \boldsymbol{A} : \boldsymbol{B}^{(\alpha)} \qquad (\alpha = 1, \dots, 6) \,. \tag{A.25}$$

Note that the basis $\boldsymbol{B}^{(1)}, \dots, \boldsymbol{B}^{(6)}$ is orthonormal with respect to the scalar product defined by double contraction, whose associated norm is the Frobenius norm

$$\|\boldsymbol{A}\|_{\mathrm{F}} = \sqrt{\boldsymbol{A} : \boldsymbol{A}} = \sqrt{\sum_{i,j=1}^{3} A_{ij}^2} \qquad \left(\boldsymbol{A} \in \mathscr{L}^2 \right). \tag{A.26}$$

For two tensors $\boldsymbol{A}, \boldsymbol{B} \in Sym$ with vector representations $\underline{A}$ and $\underline{B}$, the equality

$$\boldsymbol{A} : \boldsymbol{B} = \underline{A} \cdot \underline{B} = \underline{A}^{\mathsf{T}} \underline{B} = \sum_{\alpha=1}^{6} A_\alpha \, B_\alpha \tag{A.27}$$

is obtained, which yields

$$\|\boldsymbol{A}\|_{\mathrm{F}} = \|\underline{A}\|_2 = \sqrt{\underline{A} \cdot \underline{A}} = \sqrt{\sum_{\alpha=1}^{6} A_\alpha^2}. \tag{A.28}$$

Any fourth order tensor $\mathbb{A}$ with both minor symmetries can be represented by a six-by-six matrix $\underline{\underline{A}}$ via

$$\left(\underline{\underline{A}} \right)_{\alpha\beta} = A_{\alpha\beta} = \boldsymbol{B}^{(\alpha)} : \mathbb{A} : \boldsymbol{B}^{(\beta)} \qquad (\alpha, \beta = 1, \dots, 6) \,. \tag{A.29}$$

The matrix representation is symmetric if and only if $\mathbb{A}$ has major symmetry. Also, $\underline{\underline{A}}$ is a positive semi-definite matrix if and only if $\mathbb{A}$ is positive semi-definite according to (A.21), and $\underline{\underline{A}}$ is positive definite if and only if $\mathbb{A}$ is positive definite on Sym in accordance with (A.22).

A.3 Stiffness tensors

In the geometrically linear setting, the definition of stress–strain relations, e.g., via the generalized Hooke's law (3.9) or the generalized Maxwell model (3.41), usually involves fourth order stiffness tensors. Stiffness tensors are generally assumed to be positive semi-definite and to exhibit major symmetry as well as both minor symmetries.

A.3.1 Isotropy

Isotropic elastic bulk behavior is characterized by two independent material parameters, e.g., by the Young's modulus E and by the Poisson's ratio ν. A useful alternative parameterization is expressed by the Lamé constants

$$\lambda = \frac{E\nu}{(1 - 2\nu)(1 + \nu)}, \qquad\qquad \mu = \frac{E}{2(1 + \nu)}. \tag{A.30}$$

A third parameterization is given in terms of the bulk modulus

$$K = \frac{E}{3(1 - 2\nu)} = \lambda + \frac{2\mu}{3} \tag{A.31}$$

and the shear modulus G, which coincides with the second Lamé constant μ. The stiffness tensor is defined as

$$\mathbb{C} = \lambda\,\boldsymbol{I} \otimes \boldsymbol{I} + 2\mu\,\mathbb{I}^{\mathsf{S}} = 3K\,\mathbb{P}_1^{\mathrm{iso}} + 2G\,\mathbb{P}_2^{\mathrm{iso}} \tag{A.32}$$

and has the matrix representation (cf. Appendix A.2)

$$\underline{\underline{C}} = \begin{bmatrix} 2G + \lambda & \lambda & \lambda & 0 & 0 & 0 \\ & 2G + \lambda & \lambda & 0 & 0 & 0 \\ & & 2G + \lambda & 0 & 0 & 0 \\ & & & 2G & 0 & 0 \\ & \text{sym.} & & & 2G & 0 \\ & & & & & 2G \end{bmatrix}. \tag{A.33}$$

A.3.2 Transverse isotropy

A constitutive model is said to be transversely isotropic if the physical behavior is symmetric about a polar axis. Such models are isotropic in the transverse plane perpendicular to the longitudinal direction defined by the polar axis. Transversely isotropic elastic bulk behavior is characterized by five independent material parameters. The common representation makes use of the following parameters:

E_{l} Young's modulus for loading in longitudinal direction
E_{t} Young's modulus for loading perpendicular to the longitudinal direction
G_{l} shear modulus in planes parallel to the longitudinal axis
G_{t} in-plane shear modulus
ν_{lt} Poisson's ratio for loading in longitudinal direction

Here, the subscripts "l" and "t" refer to the longitudinal direction and to the transverse plane, respectively. Some useful dependent variables are

$$\nu_{tt} = \frac{E_t}{2E_t} - 1, \qquad\qquad \nu_{tl} = \nu_{lt}\frac{E_t}{E_l}, \qquad\qquad \text{(A.34)}$$

$$\alpha = \frac{1}{1 - \nu_{tt} - 2\nu_{lt}\nu_{tl}}, \qquad\qquad \beta = \frac{\nu_{lt}\nu_{tl} + \nu_{tt}}{1 + \nu_{tt}}\alpha E_t. \qquad\qquad \text{(A.35)}$$

The stiffness tensor $\mathbb{C}$ of a transversely isotropic material whose polar axis coincides with the third coordinate axis e_3 has the matrix representation (cf. Appendix A.2)

$$\underline{\underline{C}} = \begin{bmatrix} C_{11} & C_{12} & C_{13} & 0 & 0 & 0 \\ & C_{11} & C_{13} & 0 & 0 & 0 \\ & & C_{33} & 0 & 0 & 0 \\ & & & C_{11}-C_{12} & 0 & 0 \\ & \text{sym.} & & & C_{55} & 0 \\ & & & & & C_{55} \end{bmatrix} \quad \text{with} \quad \begin{aligned} C_{11} &= \beta + 2G_t, \\ C_{12} &= \beta, \\ C_{13} &= 2\nu_{lt}\left(\beta + G_t\right), \\ C_{33} &= (1 - \nu_{tt})\alpha E_l, \\ C_{55} &= 2G_l. \end{aligned}$$

$$\text{(A.36)}$$

A.4 Discrete Fourier transform

An $(N_1 \times N_2 \times N_3)$-array a is considered which represents a scalar field discretized on a regular grid for a three-dimensional problem. The corresponding Fourier representation $\widehat{a}$ is a three-dimensional array of the same size. The relationship between a and $\widehat{a}$ is given by the forward DFT and by the backward DFT defined according to

$$\widehat{a}_{\alpha,\beta,\gamma} = \sum_{i=1}^{N_1}\left(\omega_1^{(\alpha-1)(i-1)}\sum_{j=1}^{N_2}\left(\omega_2^{(\beta-1)(j-1)}\sum_{k=1}^{N_3}\omega_3^{(\gamma-1)(k-1)}a_{i,j,k}\right)\right), \qquad \text{(A.37)}$$

$$a_{i,j,k} = \frac{1}{N}\sum_{\alpha=1}^{N_1}\left(\omega_1^{-(\alpha-1)(i-1)}\sum_{\beta=1}^{N_2}\left(\omega_2^{-(\beta-1)(j-1)}\sum_{\gamma=1}^{N_3}\omega_3^{-(\gamma-1)(k-1)}\widehat{a}_{\alpha,\beta,\gamma}\right)\right)$$

$$\text{(A.38)}$$

with one-based array indices and the N_ith root of unity given by

$$\omega_i = \exp\left(\frac{-\imath 2\pi}{N_i}\right) \qquad (i = 1, 2, 3), \qquad\qquad \text{(A.39)}$$

where $\imath$ denotes the imaginary unit. The two-dimensional DFT is straightforwardly obtained as a shortened version thereof.

A.5   Other

Based on the signum function, the Heaviside step function is defined as

$$\Theta(x) = \frac{1}{2}\left(1 + \mathrm{sgn}(x)\right). \tag{A.40}$$

Macauley brackets $\langle \bullet \rangle_+$ and their negative counterpart $\langle \bullet \rangle_-$ are defined by

$$\langle x \rangle_\pm = \pm \max\left\{0, \pm x\right\}. \tag{A.41}$$

Appendix B:
Supplements

B.1 Radial return scheme for isotropic von Mises plasticity with linear hardening

Isotropic von Mises plasticity with linear isotropic hardening is a special case of plasticity where implicit time increments are possible without the need for an iterative scheme. The trial stress and the corresponding trial value of the yield surface function are defined by

$$\boldsymbol{\sigma}_{\text{tr}} = \boldsymbol{\sigma}_n + \mathbb{C} : \Delta\boldsymbol{\varepsilon}, \qquad\qquad \varphi_{\text{tr}} = \sqrt{\frac{3}{2}} \left\| \boldsymbol{\sigma}'_{\text{tr}} \right\|_2 - \sigma_{\text{y}}(t_n). \tag{B.1}$$

From the fact that the old and the new (current) yield surface are spherical and concentric in the deviatoric stress space it is concluded that the trial stress and the new (current) stress are collinear. For an inelastic increment ($\varphi_{\text{tr}} > 0$) it is therefore possible to express φ_{tr} by

$$\varphi_{\text{tr}} = \sqrt{\frac{3}{2}} \left\| \boldsymbol{\sigma}'_{\text{tr}} \right\|_2 - \left(\sqrt{\frac{3}{2}} \|\boldsymbol{\sigma}'\|_2 - \Delta\sigma_{\text{y}} \right) = \sqrt{\frac{3}{2}} \left\| \boldsymbol{\sigma}'_{\text{tr}} - \boldsymbol{\sigma}' \right\|_2 + \Delta\sigma_{\text{y}}. \tag{B.2}$$

Exploiting the isotropy of the stiffness matrix $\mathbb{C}$ with shear modulus G and the linearity of the isotropic hardening rule with hardening modulus H, the expressions

$$\left\| \boldsymbol{\sigma}'_{\text{tr}} - \boldsymbol{\sigma}' \right\|_2 = 2G\|\Delta\boldsymbol{\varepsilon}_{\text{p}}\|_2 = \sqrt{6}\,G\Delta q, \qquad\qquad \Delta\sigma_{\text{y}} = H\Delta q \tag{B.3}$$

are obtained. Together with (B.2) and with (3.31) it is concluded that an implicit inelastic increment is directly expressed by

$$\Delta\boldsymbol{\varepsilon}_{\text{p}} = \Delta q \sqrt{\frac{3}{2}} \frac{\boldsymbol{\sigma}'_{\text{tr}}}{\left\| \boldsymbol{\sigma}'_{\text{tr}} \right\|_2} \qquad \text{with } \Delta q = \frac{\varphi_{\text{tr}}}{H + 3G}. \tag{B.4}$$

B.2   Definitions of global FANS matrices

The global conductance matrix $\underline{\underline{K}}^{\daleth}$ for FANS is defined in accordance with standard FE conventions as described in the following. The element conductance matrix of the eth element is defined by

$$\underline{\underline{K}}^{\langle e\rangle} = \left(\prod_{i=1}^{d} h_i\right) \sum_{p=1}^{P} w^{(p)} \left(\underline{\underline{B}}\left(\underline{z}^{(p)}\right)\right)^{\mathsf{T}} \underline{\underline{\kappa}}^{\langle e\rangle} \underline{\underline{B}}\left(\underline{z}^{(p)}\right) \qquad (e = 1, \dots, N) \, . \quad (B.5)$$

Here, $\underline{B}$ denotes the FE gradient operator[46] (scaled to the dimensions of the pixels/voxels), and $\underline{\underline{\kappa}}^{\langle e\rangle}$ is the matrix representation of the second order conductivity tensor in the eth element[47]. The global conductance matrix is formally expressed as

$$\underline{\underline{K}}^{\daleth} = \sum_{e=1}^{N} \left(\underline{\underline{L}}^{\langle e\rangle}\right)^{\mathsf{T}} \underline{\underline{K}}^{\langle e\rangle} \underline{\underline{L}}^{\langle e\rangle}. \qquad (B.6)$$

The standard FE gather matrix $\underline{\underline{L}}^{\langle e\rangle} \in \mathbb{R}^{2^d \times N}$ for the eth element is sparse with 2^d non-zero entries (one in each row). When applied to an $N^{\daleth}$-dimensional global vector representing a scalar-valued field defined on the set of all nodes $X^{\daleth}$, it selects the values for the nodes of the eth element ordered in accordance with (6.12).

For mechanical problems, the gradient operator is replaced by a strain operator and $\underline{\underline{\kappa}}$ is substituted by the matrix representation of the (tangent[48]) stiffness tensor in (B.5) to obtain the element stiffness matrices. The assembly of the global stiffness matrix is analogous to (B.6) with $\underline{\underline{L}}^{\langle e\rangle}$ being replaced by the block matrix $\underline{\underline{L_d}}^{\langle e\rangle} \in \mathbb{R}^{d2^d \times dN}$ characterized by d non-zero blocks all equal to $\underline{\underline{L}}^{\langle e\rangle}$ located on the main diagonal. Here it is taken into account that due to technical reasons, FANS uses a numbering of the DOF of vector-valued problems which differs from the standard FE convention (cf. Section 6.4).

B.3   Invertibility proof for the function $\mathfrak{M}$

The following proof is taken from Leuschner & Fritzen [2017] with minor modifications. According to the implicit function theorem, a (local) inverse of the function $\mathfrak{M}$ defined in (7.57) exists if the matrix $\underline{\underline{\mathcal{M}}} = \partial \bar{\underline{\mathcal{F}}} / \partial \bar{\underline{\mathcal{I}}}$ is regular. As a result of the additive structure

---

[46]The FE gradient operator is specified in (6.37) for two-dimensional problems.

[47]It is recalled that elementwise uniform constitutive properties have been assumed in Section 6.2.

[48]Note that the tangent stiffness tensors at the integration points of one element are not equal in general.

assumed for the (local) Helmholtz free energy in the bulk in (7.2), $\underline{\mathcal{M}}$ is a block diagonal matrix with the diagonal blocks

$$\frac{\partial \underline{T}}{\partial \underline{\xi}} \stackrel{(7.55)}{=} \left\langle \underline{\underline{P}}^{\mathsf{T}} \frac{\partial \underline{\sigma}_{\mathrm{P}}}{\partial \underline{\xi}} \right\rangle_{\Omega} \stackrel{(7.84)}{=} \left\langle \underline{\underline{P}}^{\mathsf{T}} \underline{\underline{T}}_{\xi} \right\rangle_{\Omega} \stackrel{(7.83)}{=} -\left\langle \underline{\underline{P}}^{\mathsf{T}} \left(\underline{\underline{C}} + \underline{\underline{K}}_1 \right) \underline{\underline{P}} \right\rangle_{\Omega} \stackrel{(7.65)}{=} \underline{\underline{D}}_{\xi},$$

                                                  (B.7)

$$\frac{\partial \underline{R}^{[i]}}{\partial \underline{\lambda}^{[i]}} \stackrel{(7.55)}{=} \left\langle \left(\underline{\underline{Q}}^{[i]} \right)^{\mathsf{T}} \frac{\partial \underline{r}_{[i]}}{\partial \underline{\lambda}^{[i]}} \right\rangle_{\Omega} \stackrel{(3.1)}{=} -\left\langle \left(\underline{\underline{Q}}^{[i]} \right)^{\mathsf{T}} \frac{\partial^2 \psi_{[i]}}{\partial \underline{q}_{[i]}^2} \underline{\underline{Q}}^{[i]} \right\rangle_{\Omega} \stackrel{(7.72)}{=} \underline{\underline{\mathcal{H}}}^{[i]}$$

                                             $(i = 1, \ldots, N_{\mathrm{q}})$,   (B.8)

$$\frac{\partial \underline{Z}}{\partial \underline{\nu}} \stackrel{(7.55)}{=} \left\langle \underline{\underline{Y}}^{\mathsf{T}} \frac{\partial \underline{z}}{\partial \underline{y}} \right\rangle_{\mathscr{I}} \stackrel{(4.14)}{=} -\left\langle \underline{\underline{Y}}^{\mathsf{T}} \frac{\partial^2 \breve{\psi}}{\partial \underline{y}^2} \underline{\underline{Y}} \right\rangle_{\mathscr{I}} \stackrel{(7.70)}{=} \underline{\underline{\mathcal{G}}}.$$

                                                  (B.9)

It remains to show that each of these block matrices is regular, which is done taking the example $\partial \underline{T}/\partial \underline{\xi}$. To begin with, the observation

$$\underline{\xi}^{\mathsf{T}} \left(\underline{\underline{P}}(\boldsymbol{x}) \right)^{\mathsf{T}} \underline{\underline{C}}(\boldsymbol{x}) \, \underline{\underline{P}}(\boldsymbol{x}) \, \underline{\xi} \geq 0 \qquad \text{for all } \boldsymbol{x} \in \Omega \text{ and for all } \underline{\xi} \in \mathbb{R}^{N_{\xi}} \tag{B.10}$$

is made, where the fact has been exploited that the local stiffness tensor $\mathbb{C}$ has a positive definite matrix representation $\underline{\underline{C}}$. In order to prove the assertion, it is necessary to show for any $\underline{\xi} \neq \underline{0}$ that strict inequality is true in (B.10) on a subset of Ω which is not a null set. Such a set is given by

$$\mathscr{D}(\underline{\xi}) = \left\{ \boldsymbol{x} \in \Omega \mid \underline{\underline{P}}(\boldsymbol{x}) \underline{\xi} \neq \underline{0} \right\} \subset \Omega \tag{B.11}$$

for a fixed but arbitrary $\underline{\xi} \in \mathbb{R}^{N_{\xi}} \setminus \{\underline{0}\}$: the required strict inequality is obviously satisfied on $\mathscr{D}(\underline{\xi})$, and $\mathscr{D}(\underline{\xi})$ is not a null set due to

$$0 \neq \underline{\xi}^{\mathsf{T}} \underline{\xi} \stackrel{(7.28)}{=} \underline{\xi}^{\mathsf{T}} \left\langle \underline{\underline{P}}^{\mathsf{T}} \underline{\underline{P}} \right\rangle_{\Omega} \underline{\xi} = \frac{1}{|\Omega|} \int_{\mathscr{D}(\underline{\xi})} \underbrace{\left(\underline{\underline{P}}(\boldsymbol{x}) \underline{\xi} \right)^{\mathsf{T}} \underline{\underline{P}}(\boldsymbol{x}) \underline{\xi}}_{>0} \, \mathrm{d}V \tag{B.12}$$

$$+ \frac{1}{|\Omega|} \int_{\Omega \setminus \mathscr{D}(\underline{\xi})} \underbrace{\left(\underline{\underline{P}}(\boldsymbol{x}) \underline{\xi} \right)^{\mathsf{T}} \underline{\underline{P}}(\boldsymbol{x}) \underline{\xi}}_{=0} \, \mathrm{d}V. \tag{B.13}$$

Thus it is concluded that $\partial \underline{T}/\partial \underline{\xi}$ is negative definite. The proofs for $\partial \underline{R}^{[i]}/\partial \underline{\lambda}^{[i]}$ and $\partial \underline{Z}/\partial \underline{\nu}$ are conducted analogously. Note that the required positive definiteness of the involved second order gradients of $\psi_{[i]}$ and $\breve{\psi}$ is guaranteed by the strong convexity postulated in Section 7.2.

B.4 Weak form of Cauchy's fundamental lemma

Consider the first condition in (7.63) with attention drawn to the ith displacement jump mode:

$$0 \stackrel{!}{=} \frac{\partial \bar{\psi}}{\partial \zeta_i} = \left\langle \frac{\partial \psi}{\partial \boldsymbol{\varepsilon}} : \frac{\partial \boldsymbol{\varepsilon}}{\partial \zeta_i} \right\rangle_\Omega + \left\langle \frac{\partial \breve{\psi}}{\partial \boldsymbol{\delta}} \cdot \frac{\partial \boldsymbol{\delta}}{\partial \zeta_i} \right\rangle_{\mathscr{I}} = \left\langle \boldsymbol{\sigma} : \boldsymbol{\varepsilon}_\zeta^{(i)} \right\rangle_\Omega + \left\langle \breve{\boldsymbol{t}} \cdot \boldsymbol{\delta}^{(i)} \right\rangle_{\mathscr{I}}. \quad \text{(B.14)}$$

Exploiting Gauss's theorem (2.38), the Hill–Mandel condition (5.8), and the static equilibrium conditions (5.2), it is found that

$$\left\langle \boldsymbol{\sigma} : \boldsymbol{\varepsilon}_\zeta^{(i)} \right\rangle_\Omega = \left\langle \mathrm{div}\left(\boldsymbol{\sigma} \boldsymbol{u}_\zeta^{(i)} \right) \right\rangle_\Omega = -\left\langle \left[\!\left[(\boldsymbol{\sigma} \breve{\boldsymbol{n}}) \cdot \boldsymbol{u}_\zeta^{(i)} \right]\!\right] \right\rangle_{\mathscr{I}} = -\left\langle \langle\!\langle \boldsymbol{\sigma} \breve{\boldsymbol{n}} \rangle\!\rangle \cdot \boldsymbol{\delta}^{(i)} \right\rangle_{\mathscr{I}} \quad \text{(B.15)}$$

holds. Thereby, the condition

$$0 \stackrel{!}{=} \left\langle \left(\breve{\boldsymbol{t}} - \langle\!\langle \boldsymbol{\sigma} \rangle\!\rangle \, \breve{\boldsymbol{n}} \right) \cdot \boldsymbol{\delta}^{(i)} \right\rangle_{\mathscr{I}} \quad \text{(B.16)}$$

is obtained, which must be satisfied for every $i \in \{1, \dots, N_\zeta\}$.

B.5 Interpolation based on Gaussian kernels

Bilinear overall behavior of a hyperelastic composite material characterized by

$$\underline{\bar{\sigma}}(\bar{\varepsilon}) = \bar{\varepsilon} \, \underline{\bar{\sigma}}(\underline{x}) \qquad \text{for all} \quad \underline{\bar{\varepsilon}} = \bar{\varepsilon} \, \underline{x} \quad \text{with} \quad \bar{\varepsilon} \geq 0, \quad \underline{x} \in \mathbb{R}^6, \quad \|\underline{x}\|_2 = 1 \quad \text{(B.17)}$$

is assumed. The interpolation scheme considered in Section 7.9.1 [see also Fritzen & Leuschner, 2015] is based on N_t training points specified by the effective stresses and strains ($i = 1, \dots, N_\mathrm{t}$)

$$\underline{\bar{\sigma}}^{(i)}, \qquad \underline{\bar{\varepsilon}}^{(i)} = \bar{\varepsilon}^{(i)} \, \underline{x}^{(i)} \quad \text{with} \quad \bar{\varepsilon}^{(i)} > 0, \quad \underline{x}^{(i)} \in \mathbb{R}^6, \quad \left\|\underline{x}^{(i)}\right\|_2 = 1. \quad \text{(B.18)}$$

For two normalized six-dimensional vectors $\underline{x}$ and $\underline{x}'$ (representing loading directions), the Gaussian radial basis function kernel is defined as

$$k\left(\underline{x}, \underline{x}'; \gamma\right) = \exp\left(-\gamma \left\|\underline{x} - \underline{x}'\right\|_2^2\right) \quad \text{(B.19)}$$

with a positive real-valued parameter γ. Hereof, the symmetric positive definite Gram matrix

$$K_{ij}^\gamma = k\left(\underline{x}^{(i)}, \underline{x}^{(j)}; \gamma\right) \qquad (i, j = 1, \dots, N_\mathrm{t}) \quad \text{(B.20)}$$

is obtained by evaluation of all combinations of expansion centers (corresponding to the training directions). For a given effective strain $\underline{\bar{\varepsilon}}$, the effective stress is interpolated according to

$$(\bar{\sigma}(\underline{\bar{\varepsilon}}))_l = \bar{\varepsilon} \sum_{j=1}^{N_\mathrm{t}} y_{jl} \, k\left(\underline{x}, \underline{x}^{(j)}\right) \qquad (l = 1, \dots, 6) \quad \text{(B.21)}$$

with expansion coefficients y_{jl} determined via six systems of N_{t} linear equations given by

$$\sum_{j=1}^{N_{\mathrm{t}}} K_{ij}^{\gamma}\, y_{jl} = \frac{\bar{\sigma}_l^{(i)}}{\bar{\varepsilon}^{(i)}} \qquad (i = 1, \ldots, N_{\mathrm{t}},\ l = 1, \ldots, 6). \tag{B.22}$$

The conditions (B.22) guarantee that the training data are recovered exactly by the interpolation (B.21). Note that a reasonable choice of the width parameter γ is essential for the accuracy of the interpolated results and requires additional training points.

Appendix C:
Model parameters and load directions

C.1 Parameters of SDCZ models

basic	$k = 5\,\mathrm{GPa\,mm^{-1}}, \quad \tau_0 = 5\,\mathrm{MPa}$
power-law softening	$p = 10, \quad \gamma = 5.8\,\mathrm{mm^{-1}}$
bi-exponential softening	$\tau_1 = -4.38\,\mathrm{MPa}, \quad y_0 = 4.55\,\mathrm{mm}, \quad y_1 = 0.25\,\mathrm{mm}$
viscous regularization	$m = 10, \quad \dot{\delta}_0 = 1\,\mathrm{mm\,s^{-1}}, \quad \sigma_\mathrm{d} = 1\,\mathrm{kPa}$

Table C.1: Parameters of isotropic SDCZ damage models for large scale bridging in unidirectional carbon fiber/epoxy matrix composites in Section 4.8.1.

ratio of peak tractions	$R^\wedge$	$[-]$	$^1/_3$	$^2/_3$	1	$^3/_2$
stiffnesses	$k_\perp$	$[\mathrm{GPa\,\mu m^{-1}}]$	200	140	120	180
	$k_\parallel$	$[\mathrm{GPa\,\mu m^{-1}}]$	7	15	30	35
softening potential $\breve\psi_\perp^{\mathrm{s}}$	p	$[-]$		1		
	τ_0	$[\mathrm{MPa}]$	260	240	240	180
	γ	$[\mathrm{\mu m^{-1}}]$	142	66	30.3	29.8
softening potential $\breve\psi_\parallel^{\mathrm{s}}$	p	$[-]$		1		
	τ_0	$[\mathrm{MPa}]$	80	140	140	100
	γ	$[\mathrm{\mu m^{-1}}]$	5.8	15.6	42.7	30
coupling parameters	$\lambda_\perp$	$[-]$	0.93	0.58	0.42	0.27
	$\lambda_\parallel$	$[-]$	0.05	0.15	0.32	0.5
	$\alpha_\perp$	$[-]$	0.8	0.7	0.7	0.25
	$\alpha_\parallel$	$[-]$	0.2	0.3	0.3	0.5
stopping parameters	$\tau_\perp^{\mathrm{s}}$	$[\mathrm{MPa}]$	100	157	182	100
	$\tau_\parallel^{\mathrm{s}}$	$[\mathrm{MPa}]$	55	90	70	50
viscous regularization	m	$[-]$		8		
	$\dot\delta_0$	$[\mathrm{\mu m\,s^{-1}}]$		10^{-4}		
	σ_{d}	$[\mathrm{MPa}]$		1.5		

Table C.2: Parameters for transversely isotropic SDCZ damage models in Section 4.8.2.

stiffnesses	$k_\perp = 80\,\mathrm{GPa\,mm^{-1}}, \quad k_\parallel = 940\,\mathrm{MPa\,mm^{-1}}$
softening potential $\breve\psi_\perp^{\mathrm{s}}$	$\tau_0 = 10\,\mathrm{MPa}, \quad y_0 = 1.695\,\mathrm{\mu m}$
softening potential $\breve\psi_\parallel^{\mathrm{s}}$	$\tau_0 = 4\,\mathrm{MPa}, \quad y_0 = 15.625\,\mathrm{\mu m}$
viscous regularization	$m = 7, \quad \dot\delta_0 = 10^{-7}\,\mathrm{\mu m\,s^{-1}}, \quad \sigma_{\mathrm{d}} = 20\,\mathrm{Pa}$
stopping parameters	$\tau_\perp^{\mathrm{s}} = 2.7\,\mathrm{MPa}, \quad \tau_\parallel^{\mathrm{s}} = 0.7\,\mathrm{MPa}$
coupling parameters	$\lambda_\perp = 0.5 \quad \alpha_\perp = 0.4, \quad \lambda_\parallel = \alpha_\parallel = 0.1$

Table C.3: Parameters for transversely isotropic SDCZ damage models in Section 4.8.3.

C.2 Training and validation directions for Section 7.9

	D_1	D_2	D_3	D_4	D_5	D_6
1	0.57735027	0.57735027	0.57735027	0.00000000	0.00000000	0.00000000
2	0.52749012	-0.57421722	0.51623493	-0.22191417	0.03786000	-0.27358906
3	0.76533392	0.11268267	-0.42358059	-0.12910975	-0.13396597	-0.43304720
4	0.38671002	-0.14034493	-0.14112842	0.51663462	-0.73688109	0.03059990
5	0.14145381	-0.18207822	0.14572199	0.40974921	-0.07479493	-0.86724549
6	-0.03996835	-0.06716543	0.02463607	-0.87341309	0.05999014	-0.47627215
7	0.12945019	0.18521380	-0.66509616	0.54347488	0.45925365	0.01751393
8	-0.47740310	-0.17480181	-0.43554379	0.43444170	-0.29146398	0.52739110
9	-0.47180381	-0.46847107	0.09247093	0.69714265	0.22548478	-0.11195484
10	0.39068290	0.55873025	-0.33177153	0.15486959	-0.24499331	0.58404514
11	0.36225190	-0.80215918	-0.40784864	0.17328892	0.00954764	0.16986314
12	0.47943770	-0.17053503	0.22289332	-0.47707055	-0.56118103	0.38581786
13	-0.03153798	-0.29176894	0.42857267	0.02131670	0.85422545	0.00679686
14	-0.11408630	0.82823055	-0.37269777	-0.39674648	0.05825047	-0.03624841
15	-0.11888938	-0.51795544	-0.45101307	-0.16340697	0.47077891	-0.51559681
16	-0.26198765	0.12134716	-0.75920454	0.13258168	-0.34794698	-0.44899978
17	0.06930961	0.50406981	0.04421954	0.01484149	0.62270109	-0.59260233
18	-0.22938647	0.60419592	0.07963853	0.67019952	-0.27689949	-0.22393330
19	-0.07037790	-0.20037832	0.74027109	0.40484558	-0.38385071	0.30927801
20	-0.55261094	0.32119516	0.14899660	-0.20953694	-0.59175432	0.41854023
21	-0.09323021	0.31072759	0.47171653	-0.67052947	0.23063420	0.41162859
22	-0.92051398	0.14252784	-0.06971107	-0.09844336	0.12586603	-0.31929115
23	-0.33996381	-0.59259029	0.02353366	-0.10105834	-0.64150247	-0.33312057
24	0.21372598	-0.25003936	0.14171817	0.12819663	0.19213946	0.90463558
25	-0.47060315	-0.67546768	0.23714176	-0.39438021	0.06008537	0.32694628
26	-0.37896897	0.08762638	0.82311247	-0.09703488	0.02620547	-0.40135707
27	-0.43499485	0.01162948	-0.47635983	-0.25586087	0.58104601	0.42502505
28	-0.00124993	-0.17666739	-0.66972737	-0.58518043	-0.32011641	0.27448437
29	0.60992629	-0.05253448	0.21330820	0.69978015	0.29738695	0.03998011
30	0.07983631	0.42047851	0.18888961	-0.28203970	-0.69839087	-0.46243756
31	-0.36005493	0.52134452	0.29323793	0.37683942	0.42467163	0.43613978
32	0.63467190	0.02982604	-0.20998240	-0.42247880	0.56761479	0.22701208

Table C.4: Vector components of 32 training directions D. The first direction corresponding to hydrostatic tension was deliberately prescribed during the generation of the following 31 directions.

	D_1	D_2	D_3	D_4	D_5	D_6
1	-0.13286030	0.22733685	-0.21511770	-0.40396899	-0.07192162	0.84618367
2	0.32975831	-0.12050510	0.82261390	-0.08609665	0.24137122	0.36656739
3	-0.41408402	0.17955841	0.11380351	-0.52650413	0.68737574	-0.18343922
4	-0.27443814	0.26817521	-0.11453029	-0.21289174	-0.06266471	-0.88904377
5	-0.06218321	-0.46360149	-0.26460203	0.38936095	0.64319467	0.38195724
6	0.07747547	-0.37502612	-0.49297395	0.70295609	-0.10682347	-0.32368369
7	0.00683149	0.31591829	-0.44347256	-0.09040516	-0.82192654	0.14051595
8	0.46952493	-0.03184885	0.59424735	0.22758455	-0.50857425	-0.33905690
9	-0.54665061	0.57683393	-0.49234665	0.27157833	0.01512166	0.22813822
10	-0.37419543	-0.62082426	0.34722271	-0.12287390	0.21054549	-0.54273751
11	-0.19083400	-0.19800165	0.60954716	-0.57786253	-0.46745127	-0.01985445
12	0.03366990	0.13221460	0.02341862	0.85394875	-0.09208388	0.49308144
13	0.92417816	-0.13719074	-0.01856169	0.08735315	-0.10974966	0.32719006
14	0.58870914	-0.28215366	-0.11736915	0.14657594	0.58731550	-0.44001288
15	0.12994148	0.18318137	-0.77530096	-0.38282833	0.36645136	-0.26004633
16	0.51319553	0.45560243	-0.06457559	-0.70052513	-0.17622464	0.05564346
17	-0.07392308	-0.56973579	-0.00403558	0.00793929	-0.60009606	0.55654462
18	-0.60931578	-0.56430071	-0.55126315	-0.07016130	-0.03838555	-0.00344456
19	-0.34214183	0.81888726	0.42748092	-0.12398123	-0.04495085	-0.11059279
20	-0.05267468	0.20539464	0.61564241	0.61093392	0.34955188	-0.28389446
21	0.24608767	-0.61952395	-0.09669966	-0.67368217	0.23941379	0.18738591
22	-0.66536754	-0.03641005	0.23156345	0.41739625	-0.54017452	-0.19060582
23	-0.78301781	-0.11101250	0.42390201	0.15324310	0.09153166	0.40373868
24	0.36373767	-0.54491476	-0.28904001	-0.40952000	-0.39230683	-0.40694890
25	0.36043996	0.61861484	-0.03870440	0.12420499	0.61663568	0.30039016
26	0.47811324	0.69323743	-0.23100687	0.38835243	-0.01511480	-0.29397169
27	-0.62298313	-0.02237097	-0.18687718	-0.69009900	-0.31428804	-0.03814289
28	0.43801833	-0.07478907	-0.81457794	0.06042153	-0.00008769	0.36791106
29	0.06185347	-0.85545931	0.36735815	0.34711618	-0.08819220	0.03382308
30	0.53114421	0.17343248	0.37596750	-0.44225657	0.30032225	-0.51055960
31	-0.48701545	0.22528719	-0.18968701	0.51073940	0.53920615	-0.35282073
32	0.07896456	0.55385099	0.44769867	0.21417434	-0.43696268	0.49977250

Table C.5: Vector components of validation directions matching the training directions in Table C.4.

Bibliography

Alfano, G.: On the influence of the shape of the interface law on the application of cohesive-zone models. *Composites Science and Technology* **66** (2006), 723–730, Advances in statics and dynamics of delamination.

Alfano, G. & Crisfield, M. A.: Finite element interface models for the delamination analysis of laminated composites: mechanical and computational issues. *International Journal for Numerical Methods in Engineering* **50** (2001), 1701–1736.

Allix, O. & Corigliano, A.: Modeling and simulation of crack propagation in mixed-modes interlaminar fracture specimens. *International Journal of Fracture* **77** (1996), 111–140.

Allix, O.; Ladevéze, P. & Corigliano, A.: Damage analysis of interlaminar fracture specimens. *Composite Structures* **31** (1995), 61–74.

Amidi, S. & Wang, J.: Direct measurement of traction separation law of concrete epoxy interfaces subjected to moisture attack under mode-I loading. *Journal of Composites for Construction* **21** (2017), 04017028.

Armstrong, P. & Frederick, C.: *A mathematical representation of the multiaxial Bauschinger effect*. C.E.G.B. Report RD/B/N731, Berkeley Nuclear Laboratories, Berkeley, UK 1966.

Barenblatt, G. I.: The formation of equilibrium cracks during brittle fracture. General ideas and hypotheses. Axially-symmetric cracks. *Journal of Applied Mathematics and Mechanics* **23** (1959), 622–636.

Barenblatt, G. I.: *The Mathematical Theory of Equilibrium Cracks in Brittle Fracture*, Elsevier 1962, vol. 7 of *Advances in Applied Mechanics*. pp. 55–129.

Benzeggagh, M. L. & Kenane, M.: Measurement of mixed-mode delamination fracture toughness of unidirectional glass/epoxy composites with mixed-mode bending apparatus. *Composites Science and Technology* **56** (1996), 439–449.

Bertram, A.: *Elasticity and Plasticity of Large Deformations - an Introduction*. Springer-Verlag, Berlin Heidelberg 2008, 2nd edn.

Besson, J.; Blétry, M.; Cailletaud, G.; Chaboche, J. & Forest, S.: *Non-Linear Mechanics of Materials*. Solid Mechanics and Its Applications, Springer Netherlands 2009.

Biel, A. & Stigh, U.: Damage and plasticity in adhesive layer: an experimental study. *International Journal of Fracture* **165** (2010), 93–103.

Biot, M. A.: Theory of stress–strain relations in anisotropic viscoelasticity and relaxation phenomena. *Journal of Applied Physics* **25** (1954), 1385–1391.

Biot, M. A.: *Mechanics of incremental deformations: Theory of elasticity and viscoelasticity of initially stressed solids and fluids, including thermodynamic foundations and applications to finite strain*. John Wiley & Sons, Inc., New York 1965.

Borst, R. d.; Gutiérrez, M. A.; Wells, G. N.; Remmers, J. J. C. & Askes, H.: Cohesive-zone models, higher-order continuum theories and reliability methods for computational failure analysis. *International Journal for Numerical Methods in Engineering* **60** (2004), 289–315.

van den Bosch, M. J.; Schreurs, P. J. G. & Geers, M. G. D.: An improved description of the exponential Xu and Needleman cohesive zone law for mixed-mode decohesion. *Engineering Fracture Mechanics* **73** (2006), 1220–1234.

Brisard, S. & Dormieux, L.: FFT-based methods for the mechanics of composites: A general variational framework. *Computational Materials Science* **49** (2010), 663–671.

Brisard, S. & Dormieux, L.: Combining Galerkin approximation techniques with the principle of Hashin and Shtrikman to derive a new FFT-based numerical method for the homogenization of composites. *Computer Methods in Applied Mechanics and Engineering* **217–220** (2012), 197–212.

Budzik, M. K.; Pilawka, R.; Imielińska, K.; Jumel, J. & Shanahan, M. E. R.: Fracture of aluminium joints bonded with epoxy adhesive reinforced by MMT nanoparticles. *Advances in Materials Science* **9** (2009), 4–11.

Camacho, G. & Ortiz, M.: Computational modelling of impact damage in brittle materials. *International Journal of Solids and Structures* **33** (1996), 2899–2938.

Carlsson, L.; Gillespie, J. & Trethewey, B.: Mode II interlaminar fracture of graphite/epoxy and graphite/PEEK. *Journal of Reinforced Plastics and Composites* **5** (1986), 170–187.

Cazes, F.; Coret, M.; Combescure, A. & Gravouil, A.: A thermodynamic method for the construction of a cohesive law from a nonlocal damage model. *International Journal of Solids and Structures* **46** (2009), 1476–1490.

Cazes, F.; Simatos, A.; Coret, M. & Combescure, A.: A cohesive zone model which is energetically equivalent to a gradient-enhanced coupled damage-plasticity model. *European Journal of Mechanics - A/Solids* **29** (2010), 976–989.

Chaboche, J.: On some modifications of kinematic hardening to improve the description of ratchetting effects. *International Journal of Plasticity* **7** (1991), 661–678.

Chaboche, J.: *The application of the irreversible thermodynamics to the development of constitutive equations*, Springer Netherlands, Dordrecht 2002. pp. 87–100.

Chaboche, J.: A review of some plasticity and viscoplasticity constitutive theories. *International Journal of Plasticity* **24** (2008), 1642–1693, Special Issue in Honor of Jean-Louis Chaboche.

Chaboche, J. & Jung, O.: Application of a kinematic hardening viscoplasticity model with thresholds to the residual stress relaxation. *International Journal of Plasticity* **13** (1997), 785–807.

Chandra, N.; Li, H.; Shet, C. & Ghonem, H.: Some issues in the application of cohesive zone models for metal–ceramic interfaces. *International Journal of Solids and Structures* **39** (2002), 2827–2855.

Chaturantabut, S. & Sorensen, D. C.: Discrete empirical interpolation for nonlinear model reduction. In *Proceedings of the 48h IEEE Conference on Decision and Control (CDC) held jointly with 2009 28th Chinese Control Conference*, 2009, pp. 4316–4321.

Clausius, R.: Über verschiedene für die Anwendung bequeme Formen der Hauptgleichungen der mechanischen Wärmetheorie. *Annalen der Physik* **201** (1865), 353–400.

Coleman, B. D. & Gurtin, M. E.: Thermodynamics with internal state variables. *The Journal of Chemical Physics* **47** (1967), 597–613.

Comi, C. & Perego, U.: A unified approach for variationally consistent finite elements in elastoplasticity. *Computer Methods in Applied Mechanics and Engineering* **121** (1995), 323–344.

Cooley, J. W. & Tukey, J. W.: An algorithm for the machine calculation of complex Fourier series. *Mathematics of Computation* **19** (1965), 297–301.

Corigliano, A. & Mariani, S.: Parameter identification of a time-dependent elastic-damage interface model for the simulation of debonding in composites. *Composites Science and Technology* **61** (2001), 191–203.

Cosserat, E. & Cosserat, F.: *Théorie des corps déformables*. Hermann, Paris 1909.

da Costa Mattos, H. S. & Martins, S. d. A.: Plastic behaviour of an epoxy polymer under cyclic tension. *Polymer Testing* **32** (2013), 1–8.

Costanzo, F.: A continuum theory of cohesive zone models: deformation and constitutive equations. *International Journal of Engineering Science* **36** (1998), 1763–1792.

Costanzo, F. & Allen, D. H.: A continuum thermodynamic analysis of cohesive zone models. *International Journal of Engineering Science* **33** (1995), 2197–2219, The Edelen Symposium.

Covezzi, F.; de Miranda, S.; Marfia, S. & Sacco, E.: Homogenization of elastic–viscoplastic composites by the Mixed TFA. *Computer Methods in Applied Mechanics and Engineering* **318** (2017), 701–723.

Crisfield, M. A. & Alfano, G.: Adaptive hierarchical enrichment for delamination fracture using a decohesive zone model. *International Journal for Numerical Methods in Engineering* **54** (2002), 1369–1390.

Dauskardt, R.; Lane, M.; Ma, Q. & Krishna, N.: Adhesion and debonding of multi-layer thin film structures. *Engineering Fracture Mechanics* **61** (1998), 141–162.

Davies, P.: Influence of ENF specimen geometry and friction on the mode II delamination resistance of carbon/PEEK. *Journal of Thermoplastic Composite Materials* **10** (1997), 353–361.

Dollhofer, J.; Beckert, W.; Lauke, B. & Schneider, K.: Fracture mechanical characterisation of mixed-mode toughness of thermoplast/glass interfaces. *Computational Materials Science* **19** (2000), 223–228.

Dugdale, D.: Yielding of steel sheets containing slits. *Journal of the Mechanics and Physics of Solids* **8** (1960), 100–104.

Dumontet, H.: Homogénéisation par développements en séries de Fourier. *Comptes rendus de l'Académie des sciences. Série II, Mécanique, physique, chimie, astronomie* **296** (1983), 1625–1628.

Dvorak, G. J.: Transformation field analysis of inelastic composite materials. *Proceedings: Mathematical and Physical Sciences* **437** (1992), 311–327.

Dvorak, G. J. & Benveniste, Y.: On transformation strains and uniform fields in multiphase elastic media. *Proceedings of the Royal Society of London A: Mathematical, Physical and Engineering Sciences* **437** (1992), 291–310.

Einav, I.; Houlsby, G. & Nguyen, G.: Coupled damage and plasticity models derived from energy and dissipation potentials. *International Journal of Solids and Structures* **44** (2007), 2487–2508.

Eshelby, J. D.: The determination of the elastic field of an ellipsoidal inclusion, and related problems. *Proceedings of the Royal Society of London. Series A, Mathematical and Physical Sciences* **241** (1957), 376–396.

Eshelby, J. D.: The elastic field outside an ellipsoidal inclusion. *Proceedings of the Royal Society of London A: Mathematical, Physical and Engineering Sciences* **252** (1959), 561–569.

Espinosa, H. D. & Zavattieri, P. D.: A grain level model for the study of failure initiation and evolution in polycrystalline brittle materials. Part I: Theory and numerical implementation. *Mechanics of Materials* **35** (2003), 333–364.

Evans, A. & Hutchinson, J.: The thermomechanical integrity of thin films and multilayers. *Acta Metallurgica et Materialia* **43** (1995), 2507–2530.

Ferrante, J. & Smith, J. R.: Theory of the bimetallic interface. *Phys. Rev. B* **31** (1985), 3427–3434.

Fett, T.: Evaluation of the bridging relation from crack-opening-displacement measurements by use of the weight function. *Journal of the American Ceramic Society* **78** (1995), 945–948.

Feyel, F. & Chaboche, J.-L.: FE^2 multiscale approach for modelling the elastoviscoplastic behaviour of long fibre SiC/Ti composite materials. *Computer Methods in Applied Mechanics and Engineering* **183** (2000), 309–330.

Fink, D. & Ehlers, W.: Application and modification of the POD method and the POD-DEIM for model reduction in porous-media simulations. *PAMM* **15** (2015), 385–386.

Frassine, R.; Rink, M. & Pavan, A.: Viscoelastic effects on the interlaminar fracture behaviour of thermoplastic matrix composites: II. Rate and temperature dependence in unidirectional PEEK/carbon-fibre laminates. *Composites Science and Technology* **56** (1996), 1253–1260.

Frederick, C. & Armstrong, P.: A mathematical representation of the multiaxial Bauschinger effect. *Materials at High Temperatures* **24** (2007), 1–26.

Freed, Y. & Banks-Sills, L.: A new cohesive zone model for mixed mode interface fracture in bimaterials. *Engineering Fracture Mechanics* **75** (2008), 4583–4593.

Fries, T.-P. & Belytschko, T.: The extended/generalized finite element method: An overview of the method and its applications. *International Journal for Numerical Methods in Engineering* **84** (2010), 253–304.

Frigo, M. & Johnson, S. G.: The design and implementation of FFTW3. *Proceedings of the IEEE* **93** (2005), 216–231, Special issue on "Program Generation, Optimization, and Platform Adaptation".

Fritzen, F.: *Microstructural modeling and computational homogenization of the physically linear and nonlinear constitutive behavior of micro-heterogeneous materials.* Ph.D. thesis, KIT Scientific Publishing, Karlsruhe Institute of Technology, KIT Scientific Publishing (2011).

Fritzen, F.: *Introduction to model order reduction of mechanical systems.* Lecture notes, University of Stuttgart (2017).

Fritzen, F. & Böhlke, T.: Influence of the type of boundary conditions on the numerical properties of unit cell problems. *Technische Mechanik* **30** (2010), 354–363.

Fritzen, F. & Böhlke, T.: Reduced basis homogenization of viscoelastic composites. *Composites Science and Technology* **76** (2013), 84–91.

Fritzen, F.; Forest, S.; Kondo, D. & Böhlke, T.: Computational homogenization of porous materials of Green type. *Computational Mechanics* **52** (2013), 121–134.

Fritzen, F. & Hodapp, M.: The finite element square reduced (FE^{2R}) method with GPU acceleration: towards three-dimensional two-scale simulations. *International Journal for Numerical Methods in Engineering* **107** (2016), 853–881.

Fritzen, F.; Hodapp, M. & Leuschner, M.: GPU accelerated computational homogenization based on a variational approach in a reduced basis framework. *Computer Methods in Applied Mechanics and Engineering* **278** (2014), 186–217.

Fritzen, F. & Leuschner, M.: Reduced basis hybrid computational homogenization based on a mixed incremental formulation. *Computer Methods in Applied Mechanics and Engineering* **260** (2013), 143–154.

Fritzen, F. & Leuschner, M.: Nonlinear reduced order homogenization of materials including cohesive interfaces. *Computational Mechanics* **56** (2015), 131–151.

Fritzen, F.; Xia, L.; Leuschner, M. & Breitkopf, P.: Topology optimization of multiscale elastoviscoplastic structures. *International Journal for Numerical Methods in Engineering* **106** (2016), 430–453.

Geers, M. G. D.; Kouznetsova, V. G. & Brekelmans, W. A. M.: Multi-scale computational homogenization: Trends and challenges. *Journal of Computational and Applied Mathematics* **234** (2010), 2175–2182, Fourth International Conference on Advanced COmputational Methods in ENgineering (ACOMEN 2008).

Germain, P.; Nguyen, Q. S. & Suquet, P.: Continuum thermodynamics. *Journal of Applied Mechanics* **50** (1983), 1010–1020.

Geubelle, P. H. & Baylor, J. S.: Impact-induced delamination of composites: a 2D simulation. *Composites Part B: Engineering* **29** (1998), 589–602.

de Geus, T.; Vondřejc, J.; Zeman, J.; Peerlings, R. & Geers, M.: Finite strain FFT-based non-linear solvers made simple. *Computer Methods in Applied Mechanics and Engineering* **318** (2017), 412–430.

Glüge, R.; Weber, M. & Bertram, A.: Comparison of spherical and cubical statistical volume elements with respect to convergence, anisotropy, and localization behavior. *Computational Materials Science* **63** (2012), 91–104.

Gosz, M.; Moran, B. & Achenbach, J. D.: Effect of a viscoelastic interface on the transverse behavior of fiber-reinforced composites. *International Journal of Solids and Structures* **27** (1991), 1757–1771.

Gourgues, A. & Andrieu, E.: High-temperature, oxidation-assisted intergranular cracking resistance of a solid-solution-strengthened nickel base alloy. *Materials Science and Engineering: A* **351** (2003), 39–55.

Grasset-Bourdel, R.; Alzina, A.; Tessier-Doyen, N.; Schmitt, N.; Huger, M.; Chotard, T.; Gruber, D. & Harmuth, H.: Optimisation of 3D RVE for anisotropy index reduction in modelling thermoelastic properties of two-phase composites using a periodic homogenisation method. *Computational Materials Science* **50** (2011), 3136–3144.

Griffith, A. A.: The phenomena of rupture and flow in solids. *Philosophical Transactions of the Royal Society of London A: Mathematical, Physical and Engineering Sciences* **221** (1921), 163–198.

Gupta, A. & Steigmann, D. J.: Balance laws. In Merodio, J. & Saccomandi, G. (eds.): *Continuum Mechanics*. Eolss Publishers Co. Ltd., United Kingdom 2011.

Haasdonk, B.: Convergence rates of the POD-Greedy method. *ESAIM: M2AN* **47** (2013), 859–873.

Halphen, B. & Nguyen, Q. S.: Sur les matériaux standard généralisés. *Journal de Mécanique* **14** (1975), 39–63.

Hashemi, S.; Kinloch, A. & Williams, J.: The effects of geometry, rate and temperature on the mode I, mode II and mixed-mode I/II interlaminar fracture of carbon-fibre/poly(ether-ether ketone) composites. *Journal of Composite Materials* **24** (1990), 918–956.

Hashin, Z. & Shtrikman, S.: A variational approach to the theory of the elastic behaviour of multiphase materials. *Journal of the Mechanics and Physics of Solids* **11** (1963), 127–140.

Hernández, J.; Caicedo, M. & Ferrer, A.: Dimensional hyper-reduction of nonlinear finite element models via empirical cubature. *Computer Methods in Applied Mechanics and Engineering* **313** (2017), 687–722.

Hernández, J. A.; Oliver, J.; Huespe, A. E.; Caicedo, M. A. & Cante, J. C.: High-performance model reduction techniques in computational multiscale homogenization. *Computer Methods in Applied Mechanics and Engineering* **276** (2014), 149–189.

Hill, R.: A self-consistent mechanics of composite materials. *Journal of the Mechanics and Physics of Solids* **13** (1965), 213–222.

Hirschberger, C. B.; Ricker, S.; Steinmann, P. & Sukumar, N.: Computational multiscale modelling of heterogeneous material layers. *Engineering Fracture Mechanics* **76** (2009), 793–812.

Högberg, J. L.: Mixed mode cohesive law. *International Journal of Fracture* **141** (2006), 549–559.

Hutchinson, J. & Evans, A.: Mechanics of materials: top-down approaches to fracture. *Acta Materialia* **48** (2000), 125–135.

Idiart, M. I. & Vincent, P.-G.: A generalized-secant homogenization scheme for viscoplastic polycrystalline solids under imposed deformations. *Comptes Rendus Mécanique* **343** (2015), 179–186.

Javili, A.; McBride, A. & Steinmann, P.: Thermomechanics of solids with lower-dimensional energetics: On the importance of surface, interface, and curve structures at the nanoscale. A unifying review. *Applied Mechanics Reviews* **65** (2013), 010802.

Jöchen, K.: *Homogenization of the Linear and Non-linear Mechanical Behavior of Polycrystals*. Ph.D. thesis, Karlsruhe Institute of Technology (2013).

Jänicke, R. & Steeb: Minimal loading conditions for higher-order numerical homogenisation schemes. *Archive of Applied Mechanics* **82** (2012), 1075–1088.

Kaasschieter, E.: Preconditioned conjugate gradients for solving singular systems. *Journal of Computational and Applied Mathematics* **24** (1988), 265–275.

Kabel, M.; Fink, A. & Schneider, M.: The composite voxel technique for inelastic problems. *Computer Methods in Applied Mechanics and Engineering* **322** (2017), 396–418.

Kabel, M.; Merkert, D. & Schneider, M.: Use of composite voxels in FFT-based homogenization. *Computer Methods in Applied Mechanics and Engineering* **294** (2015), 168–188.

Keary, P. E.; Ilcewicz, L. B.; Shaar, C. & Trostle, J.: Mode I interlaminar fracture toughness of composites using slender double cantilevered beam specimens. *Journal of Composite Materials* **19** (1985), 154–177.

Khalili, S.; Shokuhfar, A.; Hoseini, S.; Bidkhori, M.; Khalili, S. & Mittal, R.: Experimental study of the influence of adhesive reinforcement in lap joints for composite structures subjected to mechanical loads. *International Journal of Adhesion and Adhesives* **28** (2008), 436–444, special Topic Issue on Structural Adhesive Joints.

Kim, B. C.; Park, S. W. & Lee, D. G.: Fracture toughness of the nano-particle reinforced epoxy composite. *Composite Structures* **86** (2008), 69–77, Fourteenth International Conference on Composite Structures.

Kochmann, J.; Wulfinghoff, S.; Ehle, L.; Mayer, J.; Svendsen, B. & Reese, S.: Efficient and accurate two-scale FE-FFT-based prediction of the effective material behavior of elasto-viscoplastic polycrystals. *Computational Mechanics* **61** (2018), 751–764.

Kolluri, M.; Hoefnagels, J. P. M.; van Dommelen, J. A. W. & Geers, M. G. D.: An improved miniature mixed-mode delamination setup for in situ microscopic interface failure analyses. *Journal of Physics D: Applied Physics* **44** (2011), 034005.

Kolluri, M.; Hoefnagels, J. P. M.; van Dommelen, J. A. W. & Geers, M. G. D.: Irreversible mixed mode interface delamination using a combined damage-plasticity cohesive zone enabling unloading. *International Journal of Fracture* **185** (2014), 77–95.

Kolluri, M.; Hoefnagels, J. P. M.; Samimi, M.; van Dommelen, H.; van der Sluis, O. & Geers, M. G. D.: An in situ experimental-numerical approach for characterization and prediction of interface delamination: Application to CuLF-MCE systems. *Advanced Engineering Materials* **14** (2012), 1034–1041.

Kolluri, M.; Thissen, M. H. L.; Hoefnagels, J. P. M.; van Dommelen, J. A. W. & Geers, M. G. D.: In-situ characterization of interface delamination by a new miniature mixed mode bending setup. *International Journal of Fracture* **158** (2009), 183–195.

Konyukhov, A. & Schweizerhof, K.: *Computational Contact Mechanics*, vol. 67 of *Lecture Notes in Applied and Computational Mechanics*. Springer-Verlag Berlin Heidelberg 2013, 1st edn.

Kouznetsova, V.; Geers, M. G. D. & Brekelmans, W. A. M.: Multi-scale constitutive modelling of heterogeneous materials with a gradient-enhanced computational homogenization scheme. *International Journal for Numerical Methods in Engineering* **54** (2002), 1235–1260.

Kriz, R. D. & Stinchcomb, W. W.: Elastic moduli of transversely isotropic graphite fibers and their composites. *Experimental Mechanics* **19** (1979), 41–49.

Lahellec, N. & Suquet, P.: On the effective behavior of nonlinear inelastic composites: I. Incremental variational principles. *Journal of the Mechanics and Physics of Solids* **55** (2007a), 1932–1963.

Lahellec, N. & Suquet, P.: On the effective behavior of nonlinear inelastic composites: II: A second-order procedure. *Journal of the Mechanics and Physics of Solids* **55** (2007b), 1964–1992.

Lebensohn, R. A. & Needleman, A.: Numerical implementation of non-local polycrystal plasticity using fast fourier transforms. *Journal of the Mechanics and Physics of Solids* **97** (2016), 333–351, SI: Pierre Suquet Symposium.

Lee, D. D. & Seung, H. S.: Algorithms for non-negative matrix factorization. In *NIPS*, MIT Press 2000, pp. 556–562.

Lee, H. Y. & Park, G. S.: Failure paths at copper-base leadframe/epoxy molding compound interfaces. *Journal of Materials Science* **37** (2002), 4247–4257.

Lee, Y. & Basaran, C.: A multiscale modeling technique for bridging molecular dynamics with finite element method. *Journal of Computational Physics* **253** (2013), 64–85.

Leuschner, M. & Fritzen, F.: Reduced order homogenization for viscoplastic composite materials including dissipative imperfect interfaces. *Mechanics of Materials* **104** (2017), 121–138.

Leuschner, M. & Fritzen, F.: Fourier-Accelerated Nodal Solvers (FANS) for homogenization problems. *Computational Mechanics* **62** (2018), 359–392.

Leuschner, M.; Fritzen, F.; van Dommelen, J. A. W. & Hoefnagels, J. P. M.: Potential-based constitutive models for cohesive interfaces: Theory, implementation and examples. *Composites Part B: Engineering* **68** (2015), 38–50.

Li, J.; Tian, X.-X. & Abdelmoula, R.: A damage model for crack prediction in brittle and quasi-brittle materials solved by the FFT method. *International Journal of Fracture* **173** (2012), 135–146.

Li, S.; Thouless, M.; Waas, A.; Schroeder, J. & Zavattieri, P.: Mixed-mode cohesive-zone models for fracture of an adhesively bonded polymer–matrix composite. *Engineering Fracture Mechanics* **73** (2006), 64–78.

Li, V. C. & Ward, R. I.: A novel testing technique for post-peak tensile behaviour of cementitious materials. In H. Mihashi, H. T. & Wittmann, F. H. (eds.): *Fracture Toughness and Fracture Energy—Testing Methods for Concrete and Rocks*. A. A. Balkema, Rotterdam 1989, pp. 183–195.

Linder, C. & Armero, F.: Finite elements with embedded strong discontinuities for the modeling of failure in solids. *International Journal for Numerical Methods in Engineering* **72** (2007), 1391–1433.

Littell, J. D.; Ruggeri, C. R.; Goldberg, R. K.; Roberts, G. D.; Arnold, W. A. & Binienda, W. K.: Measurement of epoxy resin tension, compression, and shear stress–strain curves over a wide range of strain rates using small test specimens. *Journal of Aerospace Engineering* **21** (2008), 162–173, Special Issue: Impact Mechanics of Composite Materials for Aerospace Application.

Lubliner, J.: *Plasticity Theory*. Dover books on engineering, Dover Publications, New York 2008.

Marsden, J. & Hughes, T.: *Mathematical Foundations of Elasticity*. Dover Civil and Mechanical Engineering Series, Dover Publications, New York 1994.

Marzi, S.; Hesebeck, O.; Brede, M. & Kleiner, F.: A rate-dependent, elasto-plastic cohesive zone mixed-mode model for crash analysis of adhesively bonded joints. In *7th European LS-DYNA conference*, 2009.

Matouš, K.; Kulkarni, M. G. & Geubelle, P. H.: Multiscale cohesive failure modeling of heterogeneous adhesives. *Journal of the Mechanics and Physics of Solids* **56** (2008), 1511–1533.

Michel, J. C.; Galvanetto, U. & Suquet, P.: Constitutive relations involving internal variables based on a micromechanical analysis. In Maugin, G. A.; Drouot, R. & Sidoroff, F. (eds.): *Continuum Thermomechanics: The Art and Science of Modelling Material Behaviour*. Kluwer Academic Publishers, Dordrecht 2000, pp. 301–312.

Michel, J.-C. & Suquet, P.: Nonuniform transformation field analysis. *International Journal of Solids and Structures* **40** (2003), 6937–6955, Special issue in Honor of George J. Dvorak.

Michel, J.-C. & Suquet, P.: Computational analysis of nonlinear composite structures using the nonuniform transformation field analysis. *Computer Methods in Applied Mechanics and Engineering* **193** (2004), 5477–5502, Advances in Computational Plasticity.

Michel, J.-C. & Suquet, P.: A model-reduction approach in micromechanics of materials preserving the variational structure of constitutive relations. *Journal of the Mechanics and Physics of Solids* **90** (2016a), 254–285.

Michel, J.-C. & Suquet, P.: A model-reduction approach to the micromechanical analysis of polycrystalline materials. *Computational Mechanics* **57** (2016b), 483–508.

Michel, J.-C. & Suquet, P.: Effective potentials in nonlinear polycrystals and quadrature formulae. *Proceedings of the Royal Society of London A: Mathematical, Physical and Engineering Sciences* **473** (2017), 20170213.

Miehe, C.: Strain-driven homogenization of inelastic microstructures and composites based on an incremental variational formulation. *International Journal for Numerical Methods in Engineering* **55** (2002), 1285–1322.

Miehe, C.: A multi-field incremental variational framework for gradient-extended standard dissipative solids. *Journal of the Mechanics and Physics of Solids* **59** (2011), 898–923.

Miehe, C.: Variational gradient plasticity at finite strains. Part I: Mixed potentials for the evolution and update problems of gradient-extended dissipative solids. *Computer Methods in Applied Mechanics and Engineering* **268** (2014), 677–703.

Miehe, C.; Welschinger, F. & Hofacker, M.: Thermodynamically consistent phase-field models of fracture: Variational principles and multi-field FE implementations. *International Journal for Numerical Methods in Engineering* **83** (2010), 1273–1311.

Moeckel, G. P.: Thermodynamics of an interface. *Archive for Rational Mechanics and Analysis* **57** (1975), 255–280.

Mori, T. & Tanaka, K.: Average stress in matrix and average elastic energy of materials with misfitting inclusions. *Acta Metallurgica* **21** (1973), 571–574.

Mosler, J. & Scheider, I.: A thermodynamically and variationally consistent class of damage-type cohesive models. *Journal of the Mechanics and Physics of Solids* **59** (2011), 1647–1668.

Moulinec, H. & Suquet, P.: A fast numerical method for computing the linear and nonlinear mechanical properties of composites. *Comptes rendus de l'Académie des sciences. Série II, Mécanique, physique, chimie, astronomie* **318** (1994), 1417–1423.

Moulinec, H. & Suquet, P.: A FFT-based numerical method for computing the mechanical properties of composites from images of their microstructures. In Pyrz, R. (ed.): *IUTAM Symposium on Microstructure-Property Interactions in Composite Materials*. Springer Netherlands 1995, vol. 37 of *Solid Mechanics and Its Applications*, pp. 235–246.

Moulinec, H. & Suquet, P.: A numerical method for computing the overall response of nonlinear composites with complex microstructure. *Computer Methods in Applied Mechanics and Engineering* **157** (1998), 69–94.

de Moura, M. & de Morais, A.: Equivalent crack based analyses of ENF and ELS tests. *Engineering Fracture Mechanics* **75** (2008), 2584–2596.

Moës, N.; Dolbow, J. & Belytschko, T.: A finite element method for crack growth without remeshing. *International Journal for Numerical Methods in Engineering* **46** (1999), 131–150.

Musto, M. & Alfano, G.: A novel rate-dependent cohesive-zone model combining damage and visco-elasticity. *Computers & Structures* **118** (2013), 126–133, Special Issue: UK Association for Computational Mechanics in Engineering.

Needleman, A.: A continuum model for void nucleation by inclusion debonding. *Journal of Applied Mechanics* **54** (1987), 525–531.

Needleman, A.: An analysis of decohesion along an imperfect interface. *International Journal of Fracture* **42** (1990a), 21–40.

Needleman, A.: An analysis of tensile decohesion along an interface. *Journal of the Mechanics and Physics of Solids* **38** (1990b), 289–324.

Needleman, A.: Micromechanical modelling of interfacial decohesion. *Ultramicroscopy* **40** (1992), 203–214.

Obnosov, Y. V.: Periodic heterogeneous structures: New explicit solutions and effective characteristics of refraction of an imposed field. *SIAM Journal on Applied Mathematics* **59** (1999), 1267–1287.

Ortiz, M. & Pandolfi, A.: Finite-deformation irreversible cohesive elements for three-dimensional crack-propagation analysis. *International Journal for Numerical Methods in Engineering* **44** (1999), 1267–1282.

Ortiz, M. & Stainier, L.: The variational formulation of viscoplastic constitutive updates. *Computer Methods in Applied Mechanics and Engineering* **171** (1999), 419–444.

Ortiz, M. & Suresh, S.: Statistical properties of residual stresses and intergranular fracture in ceramic materials. *Journal of Applied Mechanics* **60** (1993), 77–84.

Oskay, C. & Fish, J.: Eigendeformation-based reduced order homogenization for failure analysis of heterogeneous materials. *Computer Methods in Applied Mechanics and Engineering* **196** (2007), 1216–1243.

Ostoja-Starzewski, M.: Towards stochastic continuum thermodynamics. *Journal of Non-Equilibrium Thermodynamics* **27** (2002), 335–348.

Ostoja-Starzewski, M.: Material spatial randomness: From statistical to representative volume element. *Probabilistic Engineering Mechanics* **21** (2006), 112–132.

Ottosen, N. S.; Ristinmaa, M. & Mosler, J.: Fundamental physical principles and cohesive zone models at finite displacements – Limitations and possibilities. *International Journal of Solids and Structures* **53** (2015), 70–79.

Pan, F. M.; Horng, S. R.; Yang, T. D. & Tang, V.: Studies of the interface between the epoxy molding compound and the copper leadframe by x-ray photoelectron spectroscopy, Auger electron spectroscopy, and secondary electron microscopy. *Journal of Vacuum Science & Technology A: Vacuum, Surfaces, and Films* **8** (1990), 4074–4078.

Park, K. & Paulino, G. H.: Cohesive zone models: A critical review of traction-separation relationships across fracture surfaces. *Applied Mechanics Reviews* **64** (2013), 060802.

Park, K.; Paulino, G. H. & Roesler, J. R.: A unified potential-based cohesive model of mixed-mode fracture. *Journal of the Mechanics and Physics of Solids* **57** (2009), 891–908.

Perzyna, P.: The constitutive equations for rate sensitive plastic materials. *Quarterly of Applied Mathematics* **20** (1963), 321–332.

Perzyna, P.: Fundamental problems in viscoplasticity. *Advances in Applied Mechanics* **9** (1966), 243–377.

Ponte Castañeda, P.: The effective mechanical properties of nonlinear isotropic composites. *Journal of the Mechanics and Physics of Solids* **39** (1991), 45–71.

Ponte Castañeda, P.: New variational principles in plasticity and their application to composite materials. *Journal of the Mechanics and Physics of Solids* **40** (1992), 1757–1788.

Ponte Castañeda, P.: Exact second-order estimates for the effective mechanical properties of nonlinear composite materials. *Journal of the Mechanics and Physics of Solids* **44** (1996), 827–862.

Ponte Castañeda, P.: Fully optimized second-order variational estimates for the macroscopic response and field statistics in viscoplastic crystalline composites. *Proceedings of the Royal Society of London A: Mathematical, Physical and Engineering Sciences* **471** (2015), 20150665.

Portillo, O. & Cebon, D.: Modeling failure of bitumen films in tension. *Journal of Engineering Mechanics* **138** (2012), 1357–1371.

Portillo, O. & Cebon, D.: Modeling mode I fracture of bitumen films. *Journal of Materials in Civil Engineering* **25** (2013), 1403–1414.

Prager, W.: Recent developments in the mathematical theory of plasticity. *Journal of Applied Physics* **20** (1949), 235–241.

Radermacher, A. & Reese, S.: POD-based model reduction with empirical interpolation applied to nonlinear elasticity. *International Journal for Numerical Methods in Engineering* **107** (2016), 477–495.

Rahulkumar, P.; Jagota, A.; Bennison, S. & Saigal, S.: Cohesive element modeling of viscoelastic fracture: application to peel testing of polymers. *International Journal of Solids and Structures* **37** (2000), 1873–1897.

Redeker, M. & Haasdonk, B.: A POD-EIM reduced two-scale model for crystal growth. *Advances in Computational Mathematics* **41** (2015), 987–1013.

Reeder, J. R. & Crews, J. H.: Mixed-mode bending method for delamination testing. *AIAA Journal* **28** (1990), 1270–1276.

Reeder, J. R. & Crews, J. H.: *Nonlinear Analysis and Redesign of the Mixed-Mode Bending Delamination Test*. Tech. rep. 1991.

Reina-Romo, E. & Sanz-Herrera, J.: Multiscale simulation of particle-reinforced elastic–plastic adhesives at small strains. *Computer Methods in Applied Mechanics and Engineering* **200** (2011), 2211–2222.

Rempler, H.-U.; Wieners, C. & Ehlers, W.: Efficiency comparison of an augmented finite element formulation with standard return mapping algorithms for elastic-inelastic materials. *Computational Mechanics* **48** (2011), 551–562.

Reuss, A.: Berechnung der Fließgrenze von Mischkristallen auf Grund der Plastizitätsbedingung für Einkristalle. *ZAMM - Journal of Applied Mathematics and Mechanics / Zeitschrift für Angewandte Mathematik und Mechanik* **9** (1929), 49–58.

Rice, J. R. & Wang, J.-S.: Embrittlement of interfaces by solute segregation. *Materials Science and Engineering: A* **107** (1989), 23–40, Poceedings of the Symposium on Interfacial Phenomena in Composites: Processing Characterization and Mechanical Properties.

Rockafellar, R. T.: *Convex analysis*. Princeton University Press, Princeton 1970.

Rose, J. H.; Ferrante, J. & Smith, J. R.: Universal binding energy curves for metals and bimetallic interfaces. *Phys. Rev. Lett.* **47** (1981), 675–678.

Rose, J. H.; Smith, J. R. & Ferrante, J.: Universal features of bonding in metals. *Phys. Rev. B* **28** (1983), 1835–1845.

Russell, A. J.: *On the measurement of mode II interlaminar fracture energies*. Tech. Rep. MAT–R–82–0, Defence Research Establishment Pacific, Victoria BC (CAN) 1982.

Ryckelynck, D.: A priori hyperreduction method: an adaptive approach. *Journal of Computational Physics* **202** (2005), 346–366.

Ryckelynck, D.; Vincent, F. & Cantournet, S.: Multidimensional a priori hyper-reduction of mechanical models involving internal variables. *Computer Methods in Applied Mechanics and Engineering* **225–228** (2012), 28–43.

Samimi, M.; van Dommelen, J.; Kolluri, M.; Hoefnagels, J. & Geers, M.: Simulation of interlaminar damage in mixed-mode bending tests using large deformation self-adaptive cohesive zones. *Engineering Fracture Mechanics* **109** (2013), 387–402.

Samimi, M.; van Dommelen, J. A. W. & Geers, M. G. D.: An enriched cohesive zone model for delamination in brittle interfaces. *International Journal for Numerical Methods in Engineering* **80** (2009), 609–630.

Scheider, I. & Brocks, W.: Simulation of cup–cone fracture using the cohesive model. *Engineering Fracture Mechanics* **70** (2003), 1943–1961.

Schellekens, J. C. J. & Borst, R. D.: On the numerical integration of interface elements. *International Journal for Numerical Methods in Engineering* **36** (1993), 43–66.

Schneider, M.; Merkert, D.; Kabel, M.; Schneider, M.; Merkert, D. & Kabel, M.: FFT-based homogenization for microstructures discretized by linear hexahedral elements. *International Journal for Numerical Methods in Engineering* **109** (2017), 1461–1489.

Schneider, M.; Ospald, F. & Kabel, M.: Computational homogenization of elasticity on a staggered grid. *International Journal for Numerical Methods in Engineering* **105** (2016), 693–720.

Seagraves, A. & Radovitzky, R.: *Advances in Cohesive Zone Modeling of Dynamic Fracture*, Springer US, Boston, MA 2010. pp. 349–405.

Smiley, A. & Pipes, R.: Rate effects on mode I interlaminar fracture toughness in composite materials. *Journal of Composite Materials* **21** (1987), 670–687.

Soboyejo, W. O.; Lu, G.-Y.; Chengalva, S.; Zhang, J. & Kenner, V.: A modified mixed-mode bending specimen for the interfacial fracture testing of dissimilar materials. *Fatigue & Fracture of Engineering Materials & Structures* **22** (1999), 799–810.

Sørensen, B. F. & Jacobsen, T. K.: Large-scale bridging in composites: R-curves and bridging laws. *Composites Part A: Applied Science and Manufacturing* **29** (1998), 1443–1451.

Sørensen, B. F. & Jacobsen, T. K.: Determination of cohesive laws by the J integral approach. *Engineering Fracture Mechanics* **70** (2003), 1841–1858.

Steinmann, P. & Häsner, O.: On material interfaces in thermomechanical solids. *Archive of Applied Mechanics* **75** (2005), 31–41.

Suo, Z.; Bao, G. & Fan, B.: Delamination R-curve phenomena due to damage. *Journal of the Mechanics and Physics of Solids* **40** (1992), 1–16.

Suquet, P. M.: Local and global aspects in the mathematical theory of plasticity. *Plasticity today: modelling, methods and applications* (1985), 279–310.

Suquet, P. M.: Elements of homogenization for inelastic solid mechanics. In Sanchez-Palencia, E. & Zaoui, A. (eds.): *Homogenization Techniques for Composite Media*, Springer, Berlin Heidelberg 1987, pp. 193–198.

Swenson, D. V. & Ingraffea, A. R.: Modeling mixed-mode dynamic crack propagation using finite elements: Theory and applications. *Computational Mechanics* **3** (1988), 381–397.

Thijsse, J.; van der Sluis, O.; van Dommelen, J.; van Driel, W. & Geers, M.: Characterization of semiconductor interfaces using a modified mixed mode bending apparatus. *Microelectronics Reliability* **48** (2008), 401–407.

Truesdell, C.: *The Elements of Continuum Mechanics*. Springer, Berlin Heidelberg 1966.

Turon, A.; Camanho, P.; Costa, J. & Dávila, C.: A damage model for the simulation of delamination in advanced composites under variable-mode loading. *Mechanics of Materials* **38** (2006), 1072–1089.

Tvergaard, V.: Effect of fibre debonding in a whisker-reinforced metal. *Materials Science and Engineering: A* **125** (1990), 203–213.

Tvergaard, V. & Hutchinson, J. W.: The relation between crack growth resistance and fracture process parameters in elastic-plastic solids. *Journal of the Mechanics and Physics of Solids* **40** (1992), 1377–1397.

Tvergaard, V. & Hutchinson, J. W.: The influence of plasticity on mixed mode interface toughness. *Journal of the Mechanics and Physics of Solids* **41** (1993), 1119–1135.

Valoroso, N. & Champaney, L.: A damage-mechanics-based approach for modelling decohesion in adhesively bonded assemblies. *Engineering Fracture Mechanics* **73** (2006), 2774–2801.

Veroy, K.; Prud'Homme, C.; Rovas, D. V. & Patera, A. T.: A posteriori error bounds for reduced-basis approximation of parametrized noncoercive and nonlinear elliptic partial differential equations. In *16th AIAA Computational Fluid Dynamics Conference*, Orlando, United States 2003.

Voce, E.: A practical strain hardening function. *Metallurgia* **51** (1955), 219–226.

Voigt, W.: *Lehrbuch der Kristallphysik*. Teubner, Berlin 1910.

Volokh, K. Y.: Comparison between cohesive zone models. *Communications in Numerical Methods in Engineering* **20** (2004), 845–856.

Vossen, B.; Schreurs, P.; van der Sluis, O. & Geers, M.: On the lack of rotational equilibrium in cohesive zone elements. *Computer Methods in Applied Mechanics and Engineering* **254** (2013), 146–153.

Wang, H. & Vu-Khanh, T.: Use of end-loaded-split (ELS) test to study stable fracture behaviour of composites under mode II loading. *Composite Structures* **36** (1996), 71–79.

Warrior, N. A.; Pickett, A. K. & Lourenço, N. S. F.: Mixed-mode delamination – experimental and numerical studies. *Strain* **39** (2003), 153–159.

Wells, G. N. & Sluys, L. J.: A new method for modelling cohesive cracks using finite elements. *International Journal for Numerical Methods in Engineering* **50** (2001), 2667–2682.

Whitney, J.; Browning, C. & Hoogsteden, W.: A double cantilever beam test for characterizing mode I delamination of composite materials. *Journal of Reinforced Plastics and Composites* **1** (1982), 297–313.

Wiechert, E.: Gesetze der elastischen Nachwirkung für constante Temperatur. *Annalen der Physik* **286** (1893), 546–570.

Willot, F.: Fourier-based schemes for computing the mechanical response of composites with accurate local fields. *Comptes Rendus Mécanique* **343** (2015), 232–245.

Willot, F.; Abdallah, B. & Pellegrini, Y.-P.: Fourier-based schemes with modified Green operator for computing the electrical response of heterogeneous media with accurate local fields. *International Journal for Numerical Methods in Engineering* **98** (2014), 518–533.

Wirtz, D.; Karajan, N. & Haasdonk, B.: Surrogate modeling of multiscale models using kernel methods. *Int. J. Numer. Meth. Engng* **101** (2015), 1–28.

Wriggers, P. & Laursen, T. A. (eds.): *Computational Contact Mechanics*, vol. 498 of *CISM International Centre for Mechanical Sciences: Courses and Lectures*. Springer-Verlag Wien 2007, 1st edn.

Wulfinghoff, S.; Cavaliere, F. & Reese, S.: Model order reduction of nonlinear homogenization problems using a Hashin–Shtrikman type finite element method. *Computer Methods in Applied Mechanics and Engineering* **330** (2018), 149–179.

Xu, X. P. & Needleman, A.: Void nucleation by inclusion debonding in a crystal matrix. *Modelling and Simulation in Materials Science and Engineering* **1** (1993), 111–132.

Xu, X.-P. & Needleman, A.: Numerical simulations of fast crack growth in brittle solids. *Journal of the Mechanics and Physics of Solids* **42** (1994), 1397–1434.

Yvonnet, J. & He, Q.-C.: The reduced model multiscale method (R3M) for the nonlinear homogenization of hyperelastic media at finite strains. *Journal of Computational Physics* **223** (2007), 341–368.

Zbib, H. M.; Hiratani, M. & Shehadeh, M.: *Multiscale Discrete Dislocation Dynamics Plasticity*, Wiley-VCH Verlag GmbH & Co. KGaA 2005. pp. 201–229.

Zeman, J.; Vondřejc, J.; Novák, J. & Marek, I.: Accelerating a FFT-based solver for numerical homogenization of periodic media by conjugate gradients. *Journal of Computational Physics* **229** (2010), 8065–8071.

Zhang, Z. J.; Paulino, G. H. & Celes, W.: Extrinsic cohesive modelling of dynamic fracture and microbranching instability in brittle materials. *International Journal for Numerical Methods in Engineering* **72** (2007), 893–923.

Ziegler, H.: Some extremum principles in irreversible thermodynamics with application to continuum mechanics. In Sneddon, I. & Hill, R. (eds.): *Progress in Solid Mechanics*. North-Holland Publishing Company, Amsterdam 1963, vol. IV.

Emmy Noether Research Group

Efficient Methods for
Mechanical Analysis

Many engineering materials exhibit heterogeneous microstructures, whose compositions and formations may to some extend be controlled during manufacturing processes. Homogenization methods predicting effective macroscopic properties of micro-heterogeneous materials are important tools for the development of high performance materials and for multiscale analyses of structures made thereof.

Conventional computational homogenization techniques usually suffer from long computing times. For microstructures represented by pixel or voxel images, a reduction of computational effort can be achieved using fast Fourier transform algorithms. A method combining Fourier-based acceleration with a finite element discretization is presented with numerical examples of thermal and mechanical homogenization. In addition, a reduced basis approach for materials with viscoplastic constituents and imperfect interfaces at the phase boundaries is developed. Systematic offline analyses of precomputed training data allow for efficient online algorithms, which yield good predictions for test scenarios that deviate moderately from the training cases.